# DETERMINATION OF SELECTIVE LASER MELTING PROCESS PARAMETERS FOR A NOVEL MATERIAL SYSTEM: WITH APPLICATIONS IN THERMOELECTRICS

# DETERMINATION OF SELECTIVE LASER MELTING PROCESS PARAMETERS FOR A NOVEL MATERIAL SYSTEM: WITH APPLICATIONS IN THERMOELECTRICS

Ву

MICHAEL CINO, M.A.Sc.

A Thesis Submitted to the School of Graduate Studies in Partial Fulfilment of the Requirements for the Degree of Doctor of Philosophy

**McMaster University** 

© Copyright by Michael Cino, October 2025

Doctor of Philosophy (2025) McMaster University

Department of Engineering Physics Hamilton, Ontario

TITLE: Determination of Selective Laser Melting Process Parameters for a Novel Material

System: With Applications in Thermoelectrics

AUTHOR: Michael Vincent Cino, M.A.Sc., (McMaster University)

SUPERVISOR: Dr. John S. Preston

NUMBER OF PAGES: xix, 231

#### **Abstract**

The application of additive manufacturing (AM) to multiple technological industries has become extremely prevalent in recent years. With this move, there has been a need to qualify new materials for first time use within a conventional AM system. One such common system is that of laser powder bed fusion (LPBF). It is also known as Selective Laser Melting (SLM). As it is already extensively used with metals, LPBF is an excellent tool for exploratory research with powdered materials such as semiconductors and semimetals that are traditionally used in electronic devices in bulk crystalline form. An excellent candidate in this subset of materials is thermoelectrics. The work in this thesis focuses on the use of AM to produce thermoelectric devices with the bismuth telluride semimetal alloy, and to use the knowledge of laser-material interactions to develop a framework that can forecast optimal process parameters for this material system, and ultimately, any system that is conducive to LPBF.

An EOSINT M280 Direct Metal Laser Sintering machine was used to carry out experiments on the powdered bismuth telluride alloys. These were unfit to be readily used within the machine due to their nonspherical morphology and wide particle distribution. A sieving of the powder, followed by optical and thermal characterization and a consultation of literature, provided the necessary information to create the necessary manufacturing jig and semi-analytical model to explore appropriate laser powers and

speeds to use. A custom powder delivery system was developed in order to overcome flowability issues, and to obtain uniform layer height within a build. The delivery system used metallic solder stencil masks of a fixed 76µm thickness, that were able to be stacked with relative ease. The substrates upon which the AM took place were prefabricated printed circuit boards that were designed to have the electrode layout of a conventional thermoelectric module. The developed model used a semi-analytical energy balance to determine laser power/speed pairs that satisfy the thermal requirements of the melt process with some associated losses. It uses an approach to divide the incident beam into solid- and liquid- interacting components, to attempt to deliver power at a rate that would allow for melting to the bottom of the powder bed with minimal evaporative loss.

Both p-type and n-type bismuth telluride elements were successfully manufactured on PCB substrates and showed interesting triangular microstructures upon their rapid solidification after laser melting. They also maintained their stoichiometry to the point that their alloy types did not change. The p-type bismuth telluride was tested using the Harman Technique and was determined to have a room temperature ZT of 1.1. For an understanding of the optimal process parameters, the semi-analytical model was compared to two widely different material systems in literature, the well-characterized Ti6Al4V metallic alloy and other attempts at AM of bismuth telluride. It was able to provide a good approximation to the

empirically observed process windows for each material that used the metric of maximal relative density.

# **Acknowledgements**

"It's been a long, long, long time running."

The Tragically Hip

There has been no greater feat in my life that has at times, felt so insurmountable than seeing this thesis come to completion. Amidst marriage, children, new employment, personal tragedy, a worldwide pandemic, and other life events, I persisted to create this document with the help of *lots* of encouragement along the way. Although it has taken me much longer than expected to reach this point, I am excited to be here and owe much of it to the contributions of the following individuals:

Firstly, I am eternally grateful for the foundation set by Dr. John Preston and Dr. Jim Cotton. Both have trusted in me to bring my vision of this thesis into reality, and I could not ask for more knowledgeable, wise, and especially, understanding supervisors. You both have helped me to shape the foundation of my academic and professional career and for that I will be eternally grateful. I would also like to thank Dr. Peter Mascher for being an additional voice of guidance during my research that allowed me to frame my work in a meaningful way. The inputs from all three members of this supervisory committee have led me to the culmination of this document and I am extremely proud of it. An honorable mention is extended to Dr. Mo Elbestawi, for being an invaluable resource in the world of Additive Manufacturing and introducing me to many key concepts that influenced this thesis.

Dr. Vickram Lakhian, thank you for your continued leadership and for being a great friend. Your wisdom and help throughout my research have allowed me to keep my optimism and to see this through to the end. Thank you for your academic and moral support throughout the years.

Dr. Ahmed Ali Abdelnabi, thank you for taking this thermoelectric manufacturing ride with me. From sharing the same coop placement, to having great conversations about our research, you too are an integral part of my success and I thank you for your friendship and your perpetual kind demeanour.

Dr. Stephen Jovanovic, an Übermensch if there ever was one. The years spent in the basement of ABB, and the years since spent apart abroad are full of memories, laughs, insight and discussions. Whether here in Hamilton, or from the other side of this continent, you have always been taking me to task to see this thesis to completion and to act as the ultimate

sounding board whenever I felt in despair. Thank you for helping me realize that *part of the journey is the end*, and for helping me get here.

Gerard Campeau, thank you for the years of hands on experience, guidance, and providing me the opportunity to set foot into the thermoelectrics industry.

Fellow graduate students from the departments of Engineering Physics and Mechanical Engineering: Dr. Tahereh Majdi, Dr. Abhi Rampal, Dr. Raf Hirmiz, Jeff Girard, Dr. Isaac Jackiw and Dr. Sarah Nangle-Smith, thank you for engaging conversations and helping me push the boundaries of my research to the next level.

To the staff that have helped me through the years:

- Sarah Novosedlik, thank you for facilitating what needed facilitating, when I needed it most. Your help has been most valuable, and I am grateful for all that you have done.
- Jim Garrett master tinkerer and fabricator extraordinaire. Thank you for your help over the years, and for imparting many skills upon me that I have taken and applied in my research and professional life.
- Dr. Jim Britten and Victoria Jarvis of the McMaster X-ray Crystallography Facility, thank you for your help to broaden my understanding of XRD and for supporting me during my research
- Doris Stevanovic and Dr. Shahram Ghanad-Tavakoli of the CEDT, thank you for your continued help providing me with many research tools to succeed, especially in the area of thin films.
- Zhilin Peng of the CANS Facility, thank you for accommodating my needs for microscopy and allowing me to capture such great images for use in this work
- Peter Jonasson and Glen Leinweber, Eng Phys laboratory technicians and beacons of knowledge. Thank you for all your help and guidance with instrumentation over the years and really allowing me to make something from nothing.
- Simon Coulson of the Mohawk College Additive Manufacturing Innovation Centre for providing a facility to explore this material with, and get meaningful data.

To my friends that I have not seen as much of in the recent years, I hope to remedy that soon. My cousin Carm Milioto and his wife Micaela Milioto, my friends, Dr. Paul Kuyanov, Harrison King-McBain, Jeff Serradeiro, Anthony Indelicato, Nicholas Cappelletti, Rachael D'Souza and Daniel D'Souza. I have many fantastic memories with you all and am excited to make many more as the years continue. Thank you for sticking around while I figured this out!

Over the years, the love of my family has been steadfast and has kept me motivated also. They say it takes a village to raise a child, and from the earliest age, I have had the support of wonderful grandparents, uncles and aunts, and cousins. Thank you to all of you, my grandmothers the late Lidia Rastelli and the late Concetta Cino, Uncle Tony Rastelli, Aunt Laura Rastelli, Jessica Rastelli (Marc Gillespie), Alex Rastelli, Aunt Carm Rastelli, Uncle Mike Barbera, Lidia Barbera, Rebecca Barbera, Katelyn Barbera, and aunt, Dr. Maria Cino. An honorable mention to my cousins, the entire Milioto family, for also being a great source of love throughout my life.

For those I have lost during the pursuit of this thesis, who were here when it began but are not now when it ends. I will miss you always and want this to be a testament to the legacy you left upon me. For my close family friend and neighbour, Jude D'Souza, my grandmother-in-law, Maria Salis, my grandfathers Vincent Cino and Alessandro Rastelli, my cousin Grazia Milioto, my cousin Calogera Cino, and my aunt Emilia Rastelli. Thank you for your love and kindness throughout my life. Although you are no longer here, I hope to honour your memories, and will never forget you. And although they have long since been gone, I dedicate this to my grandmothers Lidia Rastelli and Concetta Cino as well.

My in-laws, Tony and Joanne DiTommaso, brothers and sisters-inlaw Anthony DiTommaso, Jenn DiTommaso, Daniel DiTommaso and Victoria Martin, my niece and nephews Norina and Noah DiTommaso, and Arthur DiTomasso, thank you for welcoming me into your family and for providing so much love and support over the years.

My sister, Catherine Cino, her partner Mark Jones and their baby and my nephew Michael Jones. Catherine, I am very proud of who you are and who you have become. I am happy to have shared so many experiences with you as we grew up and continue to laugh with you even to this day about all that we have done. Thank you for always being there.

To my mother, Ivania Rastelli Cino. I am who I am today because of you, and your wisdom. I try to model myself the best I can on the example you have provided me, and I will never be able to repay to you all that you have done and continue to do for me, Sara, Julian and Aria. Thank you mom, I love you.

To my wife, Sara Cino. Oh, what a journey we have been on with this thesis! Your support in every way made its completion possible. You have helped us navigate times of great happiness and sorrow, have put up with me working through weekends and late nights, and your help has been unwavering. You have given me the most wonderful children, who would not exist without you. I share this success with you and love you deeply. Thank you.

We are nothing, if not the sum of our experiences. For any family, friends, colleagues, and teachers of the past and present that I have not named, I dedicate this to you as well. Every interaction in my life has led to me reaching this moment, and I thank you as well.

Finally, to my two children, Julian Anthony Cino and Aria Ivania Cino. Both born into a world that was changed by a global pandemic. Both rays of sunshine through a cloudy sky. As I write this, Julian is obsessed with planets and outer space, and Aria is just learning to talk. I am so proud of both of you and can't wait to see the incredible people that you become. *This is for you*.

For Julian and Aria

# Contents

Abstract	iii
Acknowledgements	V
List of Figures and Tables	xiv
List of Abbreviations and Symbols	xix
1. Introduction	1
1.1 Scope of Work	4
1.2 Thesis Outline	5
2. Background and Literature Review	6
2.1 Argument for the Additive Manufacturing of TEGs	6
2.1.1 Conventional TEG Manufacturing Process	6
2.1.2 Segmented Thermoelement Compositions	9
2.1.3 Geometry Enhancement	13
2.2 Current State-of-the-Art in TEG AM	15
2.2.1 Process	16
2.2.2 Structure	19
2.2.3 Property	21
2.3 The Modeling of Laser-Material Interactions	23
2.4 Research Implications	31
3. Model Setup	33
3.1 Semi-Analytical Component	33
3.1.1 Relevant Physical Properties	33
3.1.1.1 Optical Properties	34
3.1.1.1.1 Powder Absorption Coefficient (β)	34
3.1.1.1.2 Powder Absorptivity (B <sub>p</sub> )	44
3.1.1.1.3 Liquid Absorptivity (A <sub>L</sub> )	45
3.1.1.2 Thermal Properties	47
3.1.1.2.1 Powder Thermal Conductivity (kp)	47
3.1.1.2.2 Effective Boiling Point (T <sub>b</sub> )	48
3.1.1.2.3 Latent Heat of Vaporization ( $\Delta H_{\nu}$ )	48
3.1.2 Model Assumptions	50
3.1.3 Laser Parameter Determination	52
3 1 3 1 Gaussian Ream Profile	53

		3.1.3.2	Solid and Liquid-Interacting Beam Components	56
		3.1.3.3	Process Windows	68
4.		Experim	ental Method	74
	4.1	Custo	m Powder Delivery System	74
	4.2	Morph	ology	81
		4.2.1	Scanning Electron Microscopy (SEM)	81
		4.2.2	Transmission Electron Microscopy (TEM)	81
		4.2.3	Particle Size Analysis	83
	4.3	Comp	osition	84
		4.3.1	X-Ray Diffraction (XRD)	84
	4.4	Therm	nal Properties	86
		4.4.1	Differential Scanning Calorimetry (DSC)	86
5.	F	Results .		89
	5.1	Comp	osition	89
		5.1.1	Energy Dispersive Spectroscopy (EDS)	91
		5.1.2	X-Ray Diffraction (XRD)	92
		5.1.2.1	P-Type Results	92
		5.1.2.2	N-Type Results	96
	5.2	Relati	ve Density	99
		5.2.1	Porosity	99
		5.2.1.1	Archimedes Density	99
		5.2.1.2	Image Processing	100
	5.3	Morph	ology	102
		5.3.1	Optical Microscopy	103
		5.3.2	Scanning Electron Microscopy	107
	5.4	Comp	arison to Model	112
	5.5	Therm	noelectric Characterization	125
6.	. (	Conclus	ions and Future Work	126
	6.1	Contri	butions to Knowledge	126
	6.2	Future	Work	131
		6.2.1	Proposed Modifications to the Semi-Analytical Model	131
		6.2.2	Considerations for TEG Fabrication	133
7.			ces	
8.		Appendi	ces	147
	Δ1	Solutio	on to the Radiative Transfer Equation	147

	A.1.1. Collimated Component	
	A.1.2. Diffuse Component	
	A.1.3. Full RTE Solution	
A.2	? Green's Function Solution Derivation	
	A.2.1. Dimensionless Numbers	
	A.2.2. 1-D Green's Function in an Infinite Domain in Dimensionless Coordinates 177	
	A.2.3. 1-D Green's Function in a Finite Domain in Dimensionless Coordinates 185	
	A.2.4. Green's Function Solution Equation (GFSE) in Dimensionless Coordinates 197	
	A.2.5. GFSE for a Moving Coordinate System in Dimensionless Coordinates 210	
	A.2.6. Laser Source Term in Dimensionless Coordinates	
	A.2.7. Final Form of the GFSE	

# **List of Figures and Tables**

Figure 1: Semi cross-sectional view of a flat-plate commercial TEG module with inse showing the different layers within the module, as recreated from [6]
Figure 2: Conventional TEG Process flow, adapted from [4]
Figure 3: Segmented TEG proposed by the JPL, recreated from [10]
Figure 4: Compatibility factors for different p-type materials as recreated from [13]12
Figure 5: Different annular TEG designs recreated from literature. Top view is isometric bottom view is a cross section of the isometric view; (a) Rowe et al [15] (b) Schmitz [16].
Figure 6: Basic representation of a model as recreated from [54]25
Figure 7: Different phenomena present during the PBF process, as recreated from [56]
Figure 8: Incident laser radiation $Io$ on a powder bed surface at z=0. The radiation propagates through the powder to the substrate which begins at z=L. The intensity is both absorbed by the system and scattered by the particles at angle $\Theta$ to a resultan intensity $Iz$ , $\Theta$ . This image is recreated from [64]
Figure 9: a) Characteristic volume $Vc$ which represents the minimal bounding volume that can be repeated. The colour blue represents the gaseous environment that the particles inhabit. b) A distribution of particles of different diameters, indicated both by their sizes and fill texture. The sum of the volumes of these spheres is denoted as $Vs$ c) The spheres are placed within their characteristic volume, where the packing factor given as $PFp = VsVc$ . Thus the volume of spheres with respect to the characteristic volume is equal to $Vs = PFpVc$ . d) The particles have been omitted and the remaining blue region is the volume of gas that is present in $Vc$ after the particles have been added and displace their volume in gas. This remaining volume is equal to $Vc - Vs$ making the volume of gas within a characteristic volume of particles equal to $Vgas = 1 - PFpVc$ .
Figure 10: Surface plot trend of optical penetration depth vs. changing equivalent particle diameter and powder packing factor43
Figure 11: (Top) Gaussian intensity profile of a laser beam as a function of radius. (Bottom Projection of the beam on a surface with specific radii labelled
Figure 12: Starting point of laser beam before entering the ROI. (Top) Setting up the lase scan path along the positive x-direction in the xy plane. The view in the xy plane exists between ω and 3ω. (Bottom) The depth in the xz direction is shown to be the length of the powder layer. The subscript x has been dropped for clarity.

Figu	re 13: (a) through (f) portrays the path of a laser beam as it traverses a distance of two
	diameters (or four radii). The top portion of each frame is referenced to the xy plane,
	while the bottom is a side view of the xz plane, looking at a cross section of the powder
	layer ROI. (a) The laser begins at (0,0) and at time t=0s. (b) The laser has moved a
	distance of $v\tau s$ , enough such that a portion of its beam will pass into the ROI. (c) The
	red line that appears at the left side of the ROI represents the beginning of the melt
	front. The melt is assumed to have zero initial lateral width and has a depth equal to
	the solid optical penetration depth, lOS. (d) The beam has moved fully into the ROI
	now, and it leads with a portion that only interacts with solid powder, while the
	remaining portion of the beam is incident upon liquid. The portion absorbed in the
	liquid reaches the liquid optical penetration depth, <i>lOL</i> . (e) The beam has begun to
	exit the ROI, and only the portion of the beam interacting with a liquid interface
	remains inside, however there is still solid material inside the cell that the melt front
	has not reached. (f) The laser beam has left the ROI entirely, and the melt front has
	propagated completely through the powder depth, $lP$ , and the process repeats. The
	laser scan vector, indicated by the black arrow joining the start and end positions of
	the beam is assumed to have lasted for the same amount of time as the melt
	propagation vector, which moves from the beginning of the melt front position at the
	top left of the ROI, down to the opposite corner
Figu	re 14: Determination of the fraction of the beam that interacts with solid powder, $fs$ .
Ū	61
Figu	re 15: Solid- and liquid-interacting beam components of the laser, applied
	mathematically via the Heaviside function. The energy delivered from the entire beam
	is the sum of both components, acting volumetrically within each medium's absorption
	depth. The ROI used here is the same as in Figure 13 and Figure 14, and the area
	fraction interacting with the solid, fs, is defined in equation (48)65
Figu	re 16: Calculated process windows of power and speed that attempt to yield full melting
	to the bottom of a powder depth, and to the width of one laser diameter. Calculations
	performed for bismuth telluride and for Ti6Al4V alloy
Figu	re 17: <i>(Top)</i> Comparison between the Lambert-Beer (LB) and the Radiative Transfer
	Equation (RTE) methods for treating the powder-interacting portion of the beam.
	(Bottom) Percent difference between the calculated laser power values obtained by
	both of the aforementioned methods
	40 4 6 5 1 1 1 1 1 1 1 1 1 1 1 1 1 1 1 1 1 1
Figu	re 18: Left: Exploded assembly of the custom build plate insert. (a) Mask guide
	threaded rods. (b) Fastening screws. (c) Quick release nuts to allow for the immediate
	addition of subsequent masks. (d) 76µm stainless steel mask to allow powder to sit
	within its exposed areas. (e) Metallized substrate upon which powder will be melted.
	(f) Substrate holder. (g) Sample-centering jig piece. (h) Milled double-sided PCB used
	for machining guide holes that contains thermal vias and offers a flat surface for the
	substrate to be set upon. (i) Aluminum base plate. Right: Isometric view of assembled
	build plate insert75

Figure 19: (a) Stainless steel mask of thickness 76µm from Figure 18(e). (b) Magnified view of mask regions that receive powder, with sample cross section selected in receive (c) Simplified cross section of a single mask region introduced in (b). The corresponding red line indicates the cut view from (b)	d. ne
Figure 20: Powder deposition and growth processes of the additive manufacturing of TEG.  Two layers of deposition are shown, and this process is repeated with up to for masks	ur
Figure 21: (a) Insertion of the PCB substrate into the TEG manufacturing assembly. (In Application of the mask to the substrate. (c) Deposition of a single powder layer of top of the mask. (d) Resolidified regions of the single powder layer after additional manufacturing. (e) Resolidified powder on substrate with mask removed	on ⁄e
Figure 22: SEM images of (Left) p-type (Bi <sub>0.15</sub> Sb <sub>0.85</sub> ) <sub>2</sub> Te <sub>3</sub> and (Right) n-type Bi <sub>2</sub> (Se <sub>0.17</sub> Te <sub>0.83</sub> ) <sub>3</sub>	
Figure 23: Images of (a)-(b) n-type and (c)-(d) p-type grains. Amorphous regions consisted with oxide growth are outlined in the dotted yellow lines.	
Figure 24: Powder particle diameter distribution according to percentage total volume of the observed sample	
Figure 25: XRD powder pattern of (Bi <sub>0.15</sub> Sb <sub>0.85</sub> ) <sub>2</sub> Te <sub>3</sub> for unmelted powder compared reference [91].	
Figure 26: XRD powder pattern of Bi <sub>2</sub> (Se <sub>0.17</sub> Te <sub>0.83</sub> ) <sub>3</sub> for unmelted powder compared reference [92]	
Figure 27: DSC of p-type (Bi <sub>0.15</sub> Sb <sub>0.85</sub> ) <sub>2</sub> Te <sub>3</sub> for the determination of $\Delta H_m$	37
Figure 28: DSC of n-type $Bi_2(Se_{0.17}Te_{0.83})_3$ for the determination of $\Delta H_m$	38
Figure 29: Vapor pressures of Bi, Sb, Se and Te vs. Temperature taken from [93]. Ambier pressure and the melt temperature are denoted as horizontal and vertical line respectively.	s,
Figure 30: (Bi <sub>x</sub> Sb <sub>1-x</sub> ) <sub>2</sub> Te <sub>3</sub> powder pattern comparison from literature data [91,94–96]9	)3
Figure 31: Bi-Sb-Te alloy powder pattern comparison from literature with reduced T content [95,97].	
Figure 32: Powder patterns of resolidified p-type material at 17W, 0.071m/s and 18V 0.075m/s overlaid with the pattern of the unmelted powder of stoichiometric (Bi <sub>0.15</sub> Sb <sub>0.85</sub> ) <sub>2</sub> Te <sub>3</sub>	ry
Figure 33: Overlay of Figure 32 with peak positions of Figure 31 to show the transition to reduced Te alloy system during the melt process at the listed powers and speed [95,97].	ds

Figu	re 34: Bi <sub>2</sub> (Se <sub>y</sub> Te <sub>1-y</sub> ) <sub>3</sub> powder pattern comparison from literature data [92,94,98–100].
Figu	ore 35: Powder patterns of resolidified n-type material at 16W, 0.067m/s, 17W, 0.071m/s and 18W, 0.075m/s overlaid with the pattern of the unmelted powder of stoichiometry Bi <sub>2</sub> (Se <sub>0.17</sub> Te <sub>0.83</sub> ) <sub>3</sub>
Figu	re 36: Overlay of Figure 35 with peak positions of Figure 34 to show the effects of varying the ratio of Se to Te during the melt process at the listed powers and speeds [92,94,98–100]
Figu	detached, leaving five. (b) Sample image of site 5 processed in ImageJ. Here the areas of the porous regions were summed and compared to the nonporous region. (c) Nonporous area fraction per site compared to the relative density determined by the Archimedes method
Figu	re 38: (a) P-type bismuth telluride on PCB, manufactured at P=17W and v=70mm/s.  (b) N-type bismuth telluride on PCB, manufactured at P=17W and v=70mm/s.  Designed to form a complete TEG when sandwiched together
Figu	TEG element on a PCB substrate, with (c) and (d) being the respective enhanced regions denoted by their coloured outlines. Images were taken in segments using an Olympus DSX500 microscope and joined together with its accompanying software. (c) and (d) are corresponding to the selected regions in (a) and (b), respectively. 104
Figu	re 40: Stacked composite image of p-type sample created with 17W power and 70mm/s speed. Images taken at different focus levels using a Zeiss Axioplan 2 optical microscope. 15 images in total were taken and stack focused using ImageJ software
Figu	re 41: (a) Interface of detached p-type element made at 17W, 70mm/s at 5X zoom. (b) 20X zoom of element in (a). Melt tracks clearly visible on initial layer with average track width of 33µm, measured using ImageJ software. Images were taken with a Zeiss Axioplan 2 optical microscope
Figu	re 42: Lower resolution p-type samples manufactured at a) 50W, 1500 mm/s b) 50W, 2500mm/s c) 250W, 1500mm/s d) 250W, 2500mm/s
Figu	re 43: Higher resolution p-type samples manufactured at a) 50W, 1500 mm/s b) 50W, 2500mm/s c) 250W, 1500mm/s d) 250W, 2500mm/s109
Figu	re 44: Lower resolution n-type samples manufactured at a) 50W, 1500 mm/s b) 50W, 2500mm/s c) 250W, 1500mm/s d) 250W, 2500mm/s
Figu	are 45: Higher resolution n-type samples manufactured at a) 50W, 1500 mm/s b) 50W,

Figu	ure 46: Experimental process parameters attempted in this work, as well as modelled process window. (Top) All parameters included, (Bottom) Enhanced reshown in Top.	gior
Figu	ure 47: Semi-analytical model comparison to [25]	117
Figu	ure 48: Semi-analytical model comparison to [26]	118
Figu	ure 49: Semi-analytical model comparison to numerically modelled (COMSOL) va and the decided upon optimal experimental set [35].	
Figu	ure 50: Semi-analytical model comparison to experimental, empirically modelled, vendor-recommended parameters for Ti6Al4V [88,109,110]	
Figu	ure 51: Combination of Bismuth Telluride and Ti6Al4V modeled process windows corresponding experimental results from literature	
Figu	ure 52: Comparison of room temperature ZT for p-type bismuth telluride sam manufactured by selective laser melting [21,35]. The error bar given represents ±	9%.
Figu	The hatched regions signify the only direction considered is the positive z-direction which in this case moves downwards from the top surface	tion

# **List of Abbreviations and Symbols**

Symbol	Description	Units
$A_L$	Liquid Absorptivity	
$B_p$	Powder Bed Absorptivity	
$T_b$		
$T_m$		
$v_a$	Ablation Velocity	m/s
$\omega_{\chi}$	Beam Radius of the 1/χ Intensity Profile	m
AM	Additive Manufacturing	
DMLS	Direct Metal Laser Sintering	
LPBF	Laser Powder Bed Fusion	
PF Packing Factor		
SEM Scanning Electron Microscopy		
SLM	Selective Laser Melting	
TEM	M Transmission Electron Microscopy	
XRD X-Ray Diffraction		
ZT Thermoelectric Figure of Merit		
I	Intensity	W/m <sup>2</sup>
P	Laser Power	W
r	Radius	m
v	Laser Speed	m/s
$\Delta H_v$	Latent Heat of Vaporization	J/kg
β	Powder Absorption Coefficient	m <sup>-1</sup>
ρ	Density	kg/m³
χ	Laser Beam Intensity Parameter	

## 1. Introduction

One of the largest driving forces in a country's infrastructure is its production of energy. Unfortunately, the total amount that is accessible to the end users is a fraction of the total produced, yet the latter amount is what is paid for. For example, during 2018 in the United States alone, over 68% of the energy that was generated was lost [1]. This loss manifests itself as waste heat during the generation and delivery stages and is regrettably included in the final cost to the end user. Since it is already paid for, it would be advantageous to reclaim some of this lost energy and divert it to other useful processes. The technology that can facilitate this task is known as thermoelectrics. As their namesake implies, thermoelectrics convert thermal energy delivered via a temperature gradient into electrical energy. Thermoelectric materials and devices are ranked based on their figure of merit, ZT, as given in equation (1):

$$ZT = \frac{\alpha^2}{\rho \kappa} T \tag{1}$$

Where  $\alpha$  is the Seebeck coefficient in (V/K),  $\kappa$  is the thermal conductivity in (W/m·K),  $\rho$  is the electrical resistivity in ( $\Omega$ ·m) and T is the absolute, average temperature of operation between the hot and cold sides of the device, in (K). The ratio of  $\frac{\alpha^2}{\rho}$  is known as the power factor and is responsible for the

maximum output power of a thermoelectric material. Improving this factor alone increases the total output power of the device. The higher ZT, the better the thermoelectric material is deemed. For reference, thermoelectric generators (TEGs) that are considered viable for commercial applications are fabricated with a ZT of approximately unity [2]. In addition to the optimization of ZT, however, there are other aspects of TEG production that contribute to their overall performance. These include their manufacturing method and geometry, both of which exhibit room for improvement. The prevalent configuration of a TEG module is that of the flat-plate design. This type of module is shown in Figure 1. The module is composed of a series of thermocouples, which are p-type and n-type semiconductor materials that are joined electrically in series and thermally in parallel. The semiconductors used are typically p-type and n-type bismuth telluridebased alloys. The electrical contacts between adjacent semiconductor materials are made from metals such as copper and zinc, and the entire arrangement is sandwiched in between two ceramic plates to accept heat flow.

One of the drawbacks of manufacturing flat-plate TEGs is the excessive material loss due to the dicing process of the thermocouple legs. These materials are grown as polycrystalline ingots and then diced into the cubic leg structures observed in Figure 1. A nonlinear temperature gradient during growth coupled with the anisotropic thermal expansion of the

randomly oriented polycrystalline grains lead to the formation of microcracks in the ingot [3]. Regions of the growth in which these are prevalent are therefore discarded and unusable in finalized TEG modules. This intentionally discarded amount is added to the kerf losses from dicing the cubes TEG legs, which can be up to 50% [4,5]. Thus, a switch to a less wasteful manufacturing process would be important if devices can be made to the current commercial performance standards.

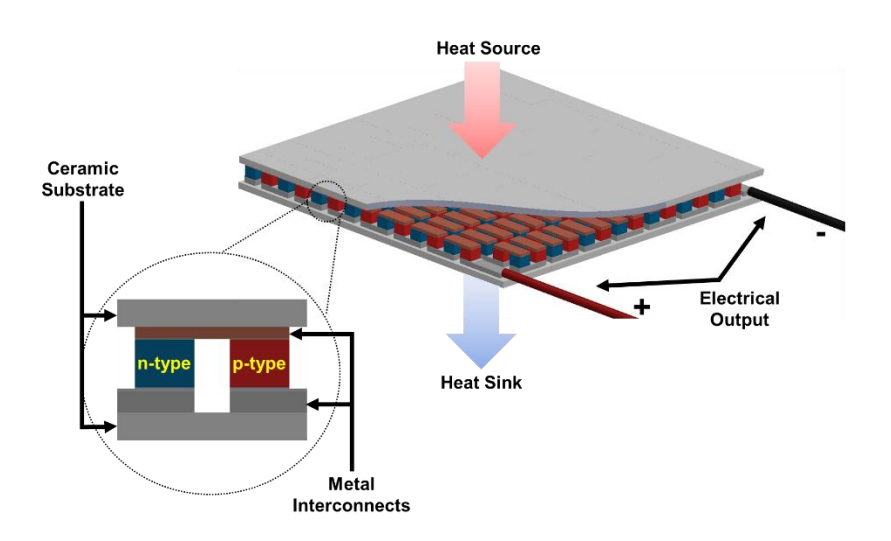


**Figure 1**: Semi cross-sectional view of a flat-plate commercial TEG module with inset showing the different layers within the module, as recreated from [6].

Additionally, small dimensional variations in each layer during manufacturing induce an inherent mechanical stress in the device when it is fully assembled between its outer ceramic surfaces. As such, the largest a device can be made is roughly 100 x 100 mm<sup>2</sup>. Since this arrangement is

connected between a heat source and a heat sink, it needs to be applied pressure from both sides such that the external thermal contact resistance is minimized. Once heat begins to flow and a temperature gradient is developed, the differences in the temperature-dependent thermal expansion coefficient in each layer provide additional stresses [7]. This in turn causes fluctuations in the thermal conductance which lead to different thermal gradients across the device than those predicted for a given heat input. The result is the slow degradation of the TEG module and thus a diminished electrical output over time. It would therefore be preferable to design thermoelectric devices for manufacture with a low waste, high volume method that can maintain or improve upon the performance of those currently available. One such method that meets these criteria and has gained much attention in recent years is additive manufacturing (AM).

# 1.1 Scope of Work

The insights gained from the current research apply to not only thermoelectrics, but additive manufacturing at large. The objective of this work was two-fold in that there was a desire to attempt to manufacture a TEG using SLM. This relied on a material system that, until recently, had not been used in commercial AM machines. The second part of this objective was to develop a model that could predict a process window for a previously unused material system in the additive manufacturing space.

#### 1.2 Thesis Outline

The content of this thesis is structured into six chapters, each containing numerous subsections. This first chapter provides the reader an insight into the initial motivating factors that led to the pursuit of this research. It introduces the existence of an aging technology - thermoelectrics - that can by significantly improved with the help of additive manufacturing. The second chapter provides context and support for the claim of the additive manufacturing of thermoelectric devices while also examining their current state-of-the-art. The third chapter describes the proposed coarse semianalytical model for determining an initial process window for any powder system. The fourth chapter details the experimental methods used in characterizing both the powder and the additively-manufactured samples that were produced in this thesis. It also describes the custom powder delivery system that was constructed to overcome the challenges of using a powder with low flowability and an irregular morphology. The fifth chapter provides both the experimental results of the characterized, additivelymanufactured thermoelectric material, and also a validation of the proposed model with sources in literature. Finally, the sixth chapter provides conclusions based on the work contained herein and offers guidance as to potential paths that this research could take in the future.

# 2. Background and Literature Review

# 2.1 Argument for the Additive Manufacturing of TEGs

## 2.1.1 Conventional TEG Manufacturing Process

Flat-plate TEGs like those observed in Figure 1 are generally fabricated the same way by all manufacturers. The current process flow is outlined below.

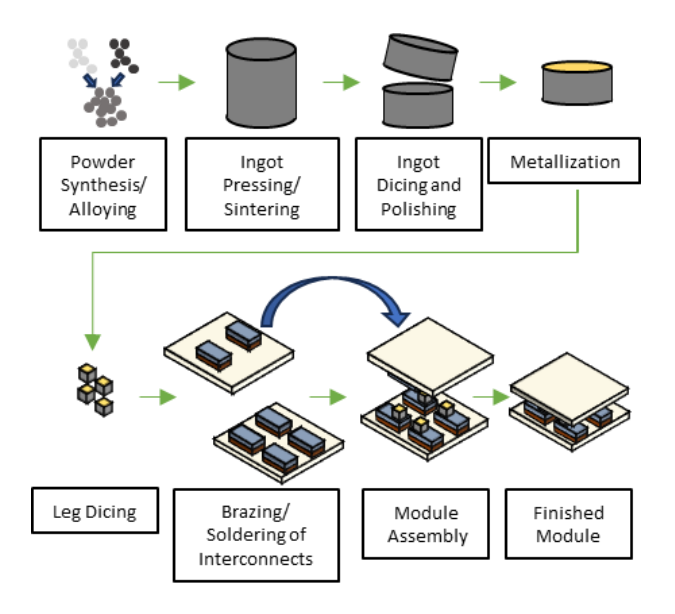


Figure 2: Conventional TEG Process flow, adapted from [4].

In Figure 2, the semiconductor material is mechanically alloyed from the stoichiometric components needed for the desired thermoelectric material properties. An example of this is Bi and Te in a 2:3 mass ratio creating Bi<sub>2</sub>Te<sub>3</sub>. This alloyed powder is then pressed and sintered into an ingot and

then diced and polished to the thickness that will be used in the module. The diced pieces are then metalized for contacting to the electrical connections, and then diced again into cubes that are of the final dimensions within the TEG. These are typically 1mm³. The ceramic substrates are then prepared with the electrical contact materials, typically Zn on one side and Cu on the other to allow for a flame brazing and soldering process, respectively. This ensures that one side can withstand hotter temperatures than the other during the module assembly, so that the TEG legs can be held in place during the bonding of the top substrate to the bottom. As mentioned previously, the combination of kerf, chipping, and cracking losses that can occur during the dicing has been approximated to be up to 50% of the overall ingot that was used originally [4,5]. This is significant when viewing the raw and processed material costs for different semiconductors used in thermoelectric modules, as given in Table 1.

Material Type	Material Name	Material Cost (\$USD/kg)	
waterial Type		Raw	Pure
Chalcogenide	Bi <sub>2</sub> Te <sub>3</sub>	110	806
Gilaloogoillao	AgPb <sub>18</sub> SbTe <sub>20</sub>	84	581
SiGe	Si <sub>0.8</sub> Ge <sub>0.2</sub>	371	7081
Clathrate	Ba <sub>8</sub> Ga <sub>16</sub> Ge <sub>28</sub> Zn <sub>2</sub>	615	3973
Skutterudite	Yb <sub>0.2</sub> In <sub>0.2</sub> Co <sub>4</sub> Sb <sub>12</sub>	24	204
Half-Heusler	Ti <sub>0.8</sub> Hf <sub>0.2</sub> NiSn	11	530
Silicide	Mg <sub>2</sub> Si <sub>0.85</sub> Bi <sub>0.15</sub>	7	191
Oxide	(Zn <sub>0.98</sub> Al <sub>0.02</sub> )O	2	50

**Table 1**: Comparison of different semiconductors used in TEG manufacturing. Their raw material constituents and processed (pure) costs are given in \$USD/kg. Recreated from [4].

The most industrially mature devices use chalcogenide materials which can be found in the first two rows of the above table. It is startling to see that the material cost is between \$581-\$806 per kilogram for the processed material. These numbers are paramount to the understanding that the manufacturing of TEG modules is by no means inexpensive and none of the source material that is produced can afford to be wasted through the previously mentioned losses.

In addition to the semiconductor materials, the costs associated with the fabrication of the module and the heat exchanger also need to be considered when selecting thermoelectrics as a viable option for waste heat recovery. For the mostly common, Chalcogenide materials that were previously mentioned, Leblanc *et al* [4] outlined the cost per watt of this renewable energy source ranges from \$60/W to \$75/W. This is due to the associated back end costs of manufacturing the heat exchanger, surrounding ceramic plates for the module, and all of the preparation such as dicing, polishing, and metalizing the semiconductor material (areal manufacturing). As a reference, the photovoltaic industry strives to reduce its costs for the final module price of \$1/W [8]. Therefore, to compete in the renewable energy market either significant improvements to the device performance must be made, or its cost of manufacturing must decrease.

One potential solution is to focus on additive manufacturing of the entire device and its associated system from the bottom-up. The most

logical starting point would be to selectively melt the powder of the semiconductor material on to a prepared ceramic substrate that already contains metal interconnects [6]. However, since all of the constituent materials of the system – metals and ceramics – are current materials that are used in AM today, the entire module can eventually theoretically be made using an AM process such as powder bed fusion (PBF) from top to bottom.

## 2.1.2 Segmented Thermoelement Compositions

Thermoelectric devices composed of a single material system are optimized for use in a specific temperature range. Outside of this range, their electrical output for a given thermal input will decrease, or they may have a melt temperature that is lower than the application they are to be used in. Thus, based on the temperature dependence of thermoelectric material properties, there is no single material that is optimized over a large temperature range [9]. A solution to this is the segmentation of thermoelements within a device. This was first proposed by the NASA Jet Propulsion Lab (JPL) as shown in Figure 3.

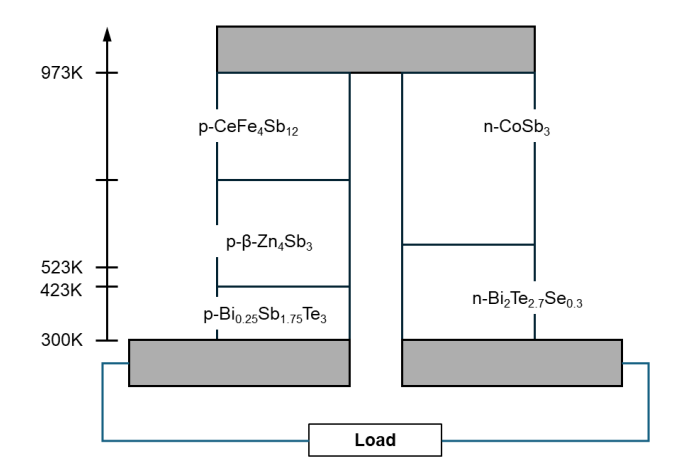


Figure 3: Segmented TEG proposed by the JPL, recreated from [10].

Each of the segments is optimized for the portion of the overall temperature gradient it is subjected to. There are a few caveats to overcome, however, in order to make a successful device using this principle.

The materials under consideration should have similar coefficients of thermal expansion such that any stresses caused by thermal mismatch can be negated. This will increase the lifetime and durability of the device. They should also be chemically compatible such that the electrical and thermal resistances are minimized between adjacent materials, as well as mass diffusion between the two [2]. The latter situation can be prevented by the intermediate application of a diffusion barrier, however. There is also the aspect of thermoelectric compatibility, s, determined by Snyder  $et\ al\ [11]$  and given in the following equation:

$$s(T) = \frac{\sqrt{1 + ZT} - 1}{\alpha T} \tag{2}$$

This parameter was determined from an efficiency optimization of a segmented module and is temperature dependent like the figure of merit. If *s* differs more than a factor of two for a given pair of materials, they are deemed thermoelectrically incompatible and would decrease the efficiency and ZT of the device they are implemented in. A notable example of this is the incompatibility between TAGS (compounds containing a combination of Te, Ag, Ge and Sb) and SiGe for high temperature space applications [12]. The replacement of the SiGe segment with Yb<sub>14</sub>MnSb<sub>11</sub> provided an efficiency increase from 4.5% to 18.6% over a 975 K temperature difference [13]. The compatibility factors for the aforementioned materials, as well as some other p-type thermoelectrics are given in Figure 4.

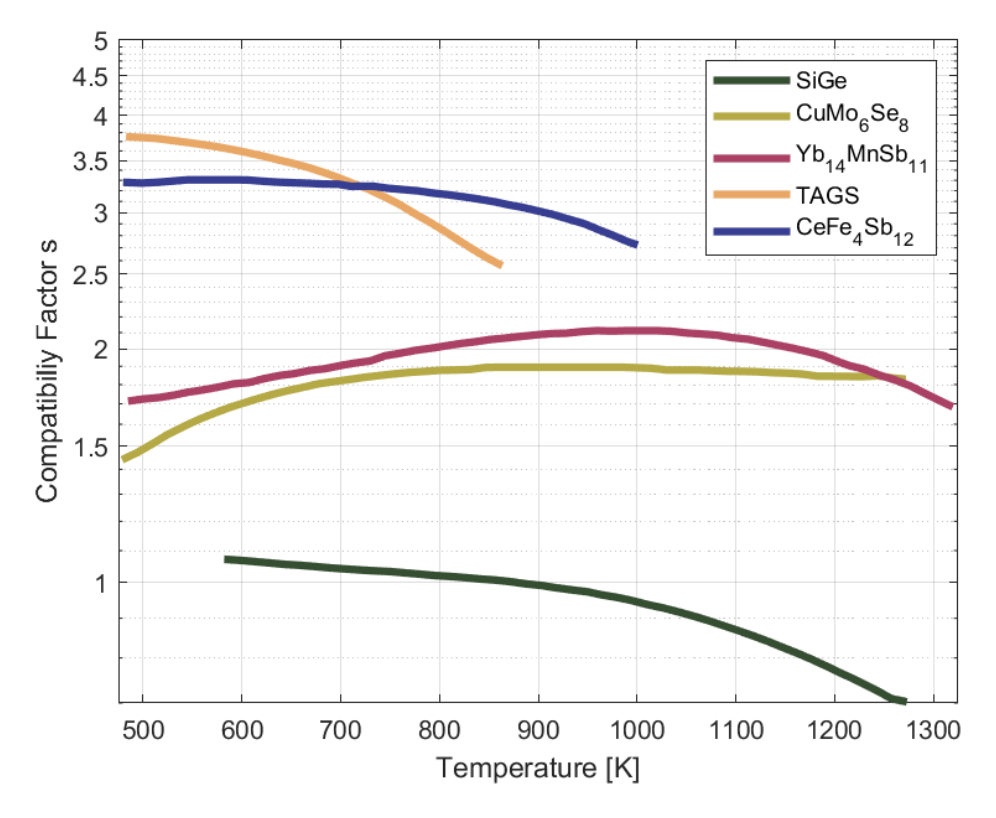


Figure 4: Compatibility factors for different p-type materials as recreated from [13].

A fully comprehensive model was created by Ouyang *et al* that incorporated the highest performing materials currently available. It accounted for thermoelectric compatibility between the materials as well as all potential thermal and electrical losses inherent to the module. In the industrial waste heat regime with a temperature difference of 200K, T<sub>HOT</sub> = 500K, a TEG efficiency of 10.6% was predicted [14]. This value shows great promise as commercially available TEG modules composed of single materials have an efficiency of roughly 3%. For a higher temperature range of 700K, T<sub>HOT</sub> = 1000K, 20.9% with a power density of 2.1 W/cm<sup>2</sup> for a [14].

The selected materials for the simulation were analytically solved to each be within the required factor of two envelope of thermoelectric compatibility.

If the appropriate resources are available, the process of segmentation should be the standard to which high performance TEGs are created. This principle can be taken from the standard flat-plate thermocouple configuration and applied to other unique geometries which can receive a higher heat flux. The coupling of these two aspects could produce reliable TEGs that overshadow those currently available. The use of SLM to combine different materials in a vertical arrangement is conducive to the development of segmented TEGs.

# 2.1.3 Geometry Enhancement

The thermal and mechanical stresses associated with a flat-plate TEG are limiting factors to its lifecycle. Since the device is subjected to thermal gradients, its parallel plate structure will undergo much expansion and contraction upon heating and cooling. Other designs have been suggested to ease this stress, including the annular TEG. Two of these are shown in Figure 5.

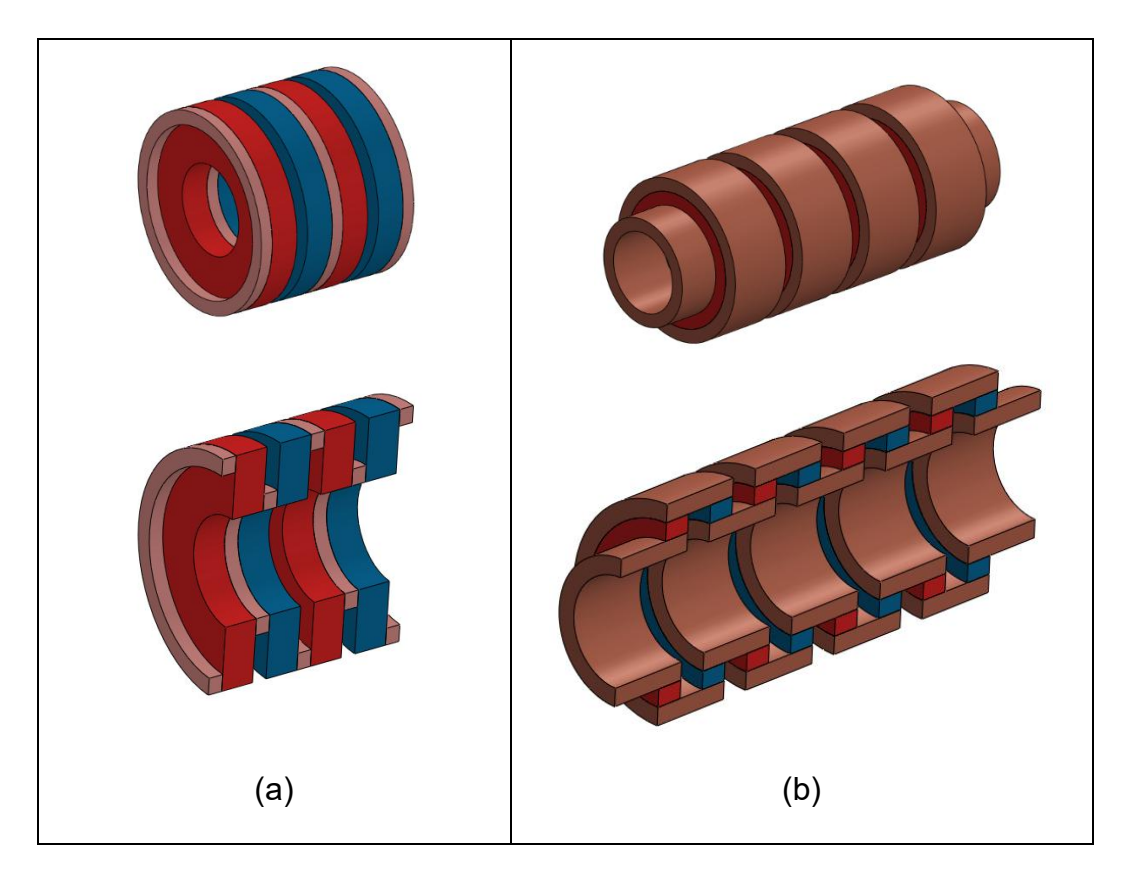


**Figure 5**: Different annular TEG designs recreated from literature. Top view is isometric, bottom view is a cross section of the isometric view; (a) Rowe et al [15] (b) Schmitz [16].

The annular designs are meant to fit around pipes to alleviate the thermal stresses associated with the flat-plate design. Their geometry would enable them to receive all escaping heat since it travels radially by nature. The design from Rowe *et al* uses spark plasma sintered (SPS) ring structures bonded between adjacent metal conducting rings [15]. The design from Schmitz also uses SPS-manufactured rings of thermoelectric material with sintered metal interconnects, in a structure that resembles the flat plate TEG

cross section that is rotated about an axis [16]. It is evident that both of these designs are extremely difficult to manufacture, and in the case of Schmitz, a more exotic method of SPS was needed. However, the versatility of additive manufacturing could allow these, and other unconventional designs to be made in a single process. An initial attempt at an annular geometry was performed by Su *et al* [17] using direct writing and a thermoelectric powder slurry. This showcases the potential of TEG technology uninhibited by manufacturing constraints and is where the research in this field will ultimately lead.

#### 2.2 Current State-of-the-Art in TEG AM

In recent years, additive manufacturing techniques have become increasingly more commonplace since the mainstream integration of the 3D printer. Metals are commonly 3D printed via SLM. In recent years, some research groups have attempted to see the effectiveness of SLM on the consolidation of thermoelectric powders [6,18–26]. SLM has advantages over other additive manufacturing techniques in that it allows for direct assembly onto a variety of substrates, in virtually any geometry, with an ever-growing number of materials [6].

A useful method to evaluate the state-of-the-art of the additive manufacturing of thermoelectrics is to examine the Process-Structure-Property relationship that is referenced in AM literature [27–29]. This methodology, seemingly first mentioned by Olson [30], describes a process

flow wherein a comprehensive understanding of the manufacturing process and its limitations resulted in the control of a material's microstructure, and this in turn affected the magnitude of many of its physical properties.

#### 2.2.1 Process

In order to process a powder in a PBF system, the limitations of its material system must be understood. The major such limitation being poor powder flowability. In general, poor flowability leads to non-uniform layer thicknesses during the PBF process [31]. The bismuth telluride alloys that are commercially available have, for the most part been mechanically alloyed. The particle size ranges from the nm to the 100µm range, with a wide distribution between the two, unfortunately. Attempts have been made to make gas atomized (GA) bismuth telluride, however the infrastructure and demand for that material is not as prevalent as those in the fields of metallurgy so it is not currently cost effective to produce it in this manner for mass production [32-34]. Recently, one group showed promise in using radio-frequency plasma high-energy spheroidization and created a narrow spherical powder distribution for both p-type and n-type alloys [35]. The poor quality of the powder for AM standards has led to researchers finding other methods of additive manufacturing for thermoelectrics including inkiet printing [19,36-38], thermal spray methods [39-41], and the use of stereolithography apparatus (SLA) printing [22].

In terms of first using powder, El-Desouky *et al* [18] published initial attempts at melting bismuth telluride using an SLM machine. They used an Nd:YLF 5kHz pulsed laser to melt lines into pressed compacts of bismuth telluride powder to observe melt morphology. The power and speed were studied in the space of 1 to 2 W and from 5 to 20mm/s, respectively. The initial low power and speed range was likely selected due to the low melting temperature of Bi<sub>2</sub>Te<sub>3</sub> of 585°C, which is much lower than almost all of the metal powders used in AM today [42]. A trend of lower material ejection was observed at higher speeds. They continued this investigation in a higher power range from 3 to 5 W while fixing the speed to 40 mm/s [6]. These initial results indicated that the powder can be melted without significant ablation, and that a parameter space in the low power, low speed range seemed promising for manufacturing in the Bi<sub>2</sub>Te<sub>3</sub> alloy system.

As the research evolved, attempts were made to print with loose powder or slurries as opposed to processing upon powder compacts. Greifzu *et al* [43] used a syringe deposition system for 15µm particle size bismuth telluride suspended in an organic binder and printed samples using a fiber laser with a wavelength of 1064nm. Shi *et al* [21] utilized SLM to print Bi<sub>0.5</sub>Sb<sub>1.5</sub>Te<sub>3</sub> powder with an average particle size of 100µm, using a custom-built screening apparatus that acted as an in-situ dry sieve to ensure only grains less than or equal to the desired maximum particle size were incorporated into the build. This process was aimed at maximizing

porosity in the finished part, so that thermal conductance could be minimized. Zhang and LeBlanc [44] characterized mechanically alloyed bismuth telluride powder by its angle of repose and compared it to a stainless steel powder with good flowability for a reference metric. They sieved and continually mixed the powder until it showed an angle approaching that of the reference and built a custom powder delivery system to create sample thermoelectric elements. Most recently, Bian [24] fabricated thermoelectric devices based on a slurry with a gel-like organic binder that contained Cu particles for increased electric conductivity. These were created on custom Al substrates.

Currently, the poor flowability of mechanically alloyed bismuth telluride does present a processing issue for SLM. The aforementioned solutions ranging from melting lines in powdered compacts to using slurries with binding agents, provide a foundation for exploration. With such a powder, there is an importance to develop a process that can produce repeatable layer thicknesses. Also, since this is an electronically functional material, it would be beneficial to print directly onto a device-ready substrate as opposed to a generic metallic build plate. These items, in addition to quantifying a laser power and speed process window based on material properties, are aspects of investigation in the upcoming chapters of this thesis.

#### 2.2.2 Structure

The microstructure of AM produced Bi<sub>2</sub>Te<sub>3</sub> alloys has been demonstrated in the literature as well. The initial attempts by El-Desouky [18] showed the formation of microcracks in the melted region. The formation of these cracks is detrimental to future device development, as it will compromise its mechanical stability when used in an industrial setting. The authors postulated that the cracks were a result of performing the lasing at room temperature rather than at an elevated bed temperature as observed in PBF processes.

Zhang *et al* [19] showed the melting of nanopowder bismuth telluride on a glass surface using a 532nm CW laser. The power and speed were not given in the publication. The results showed a coalescing of the grains for thicker regions of the deposited nanoparticles, and a lateral film formation for thinner regions. This early work aided in the knowledge that the Bi<sub>2</sub>Te<sub>3</sub> material system could be processed with a laser.

Further work of EI-Desouky *et al* [45] increased the power and speed, as well as scanned areas of bismuth telluride to incorporate hatch spacing. They again used pressed compacts and observed the effects on the microstructure in the parameter space of 10 to 25 W, with a constant speed of 350mm/s and hatch spacing of 70µm. In this power range, the melt depth grew deeper into the specimen as the power was increased. There were large granular structures present as well, indicating a polycrystalline nature

of the sample. The stoichiometry and crystallinity were tested in and showed that between different power ranges, no new phases of the material were formed, and the stoichiometry of the powder remained consistent between specimens. This is evident from the fact that there are not any new peak locations between each of the four measurements. Also, the crystallinity improved in the (0015) and (0018) directions, as the peaks became taller and narrower with increasing laser power. This represents a large number of counts received in the XRD system due to the large concentration of crystallites oriented in these directions present within the sample.

Mao *et al* [46] performed XRD on the powder before and after the SLM process, and showed that the melting did not cause significant evaporation of one of the constituents of the thermoelectric alloy, keeping the stoichiometry between the unmelted and melted powder intact. The power was 6W, speed 200mm/s, layer thickness 50µm and hatch spacing 30µm. The microstructure of the powder is paramount to the final device performance. It is undoubtedly tied to the process and the underlying powder that is used. With such a low melting-point alloy, it is necessary to confirm that the stoichiometry of the initial powder is not drastically changed during the laser interaction.

Welch *et al* [23] used SLM to manufacture samples of Bi<sub>2</sub>Se<sub>0.3</sub>Te<sub>2.7</sub> using a customized setup and observed a grain structure similar to that of El-Desouky. They analyzed the microstructure and determined that low

angle grain boundaries of approximately two degrees formed along the scan path during the solidification process. They noticed that microcracking was more prevalent in areas of higher angle grain boundaries, which occurred in the growth direction, perpendicular to the scan path. They also performed EDS mapping during TEM and observed the presence of oxide formation at the nanoscale, indicating the need for material purity and potential post-processing efforts.

## 2.2.3 Property

In addition to the standard high strength and toughness mechanical quantities that are always desired in AM parts, the thermoelectric materials manufactured need to exhibit the enhanced thermal and electrical properties that allow them to function in a waste heat recovery device. The Figure of Merit (ZT) given at the beginning of this report in equation (1), is composed of the Seebeck coefficient, thermal conductivity and electrical resistivity of the material. Commercial devices are generally manufactured with a ZT on the order of unity for their temperature specific application.

Earlier work by Mao et al [46] provided a comparison between SLM and zone melted (ZM) materials. The ZM method is a popular method to grow the semiconductor element by using a traveling heater to traverse across a region of unmelted material, slowly melting and solidifying it into a polycrystalline ingot. Here, electrical conductivity (the inverse of resistivity) is given and is shown to be lower in the SLM sample. The Seebeck

coefficient also is not as high as in the ZM sample on average, while the inplane and cross-plane thermal conductivities are lower. The in-plane
thermal conductivity is decreased by a factor of 2. The peak ZTs for the inand cross-plane measurements were respectively increased to 0.85 and
decreased to 0.45 from the ZM peak of 0.8. As observed in the equation for
ZT, performance improvements come with enhanced Seebeck coefficient
and electrical conductivity and reduced thermal conductivity. The SLM
manufactured specimen was able to at least reduce the thermal conductivity
of the Bi<sub>2</sub>Te<sub>3</sub> in one crystallographic direction substantially. This in turn
yielded a better thermoelectric material than its zone-melted counterpart.

Bismuth telluride is an extremely brittle alloy and so much of the effort to manufacture it using SLM are heavily focused on both approaching theoretical density and having high-performing thermoelectric properties. Recent work by Hu *et al* [35] showed that they managed to obtain 97.4% relative density for the p-type alloy, and 96.4% for the n-type alloy. They also observed a ZT of 1.2 and 0.9, respectively, for these alloys at room temperature. They reasoned that multiscale defects introduced by the layering process during AM are responsible for reducing the thermal conductivity of the manufactured part, and therefore increasing its ZT. Additionally, Headley *et al* [25] used machine learning to predict optimal parameters that resulted in an experimentally low porosity of 0.9%. This corresponded to a relative density of 99.1%. Models involving numerical

software or machine learning were used in these references to determine the process window. While excellent results were achieved using these methods, they can be resource intensive and thus there is an opportunity to investigate the creation of a closed form model for novel material systems.

## 2.3 The Modeling of Laser-Material Interactions

The current state of the additive manufacturing (AM) process known as powder bed fusion (PBF) has allowed it to shift from being used solely as a rapid-prototyping technology, to a mainstream production method. Since parts can be manufactured with mechanical properties similar to those made from traditional manufacturing techniques, the evolving attractiveness of additive manufacturing continues to move in the positive direction. Despite this however, sources such as [47] have reported that approximately 47% of surveyed manufacturers have expressed concern that uncertainty in the quality of the completed part has provided a barrier to entry of AM into their production run. PBF involves many complex physical phenomena that are difficult to model. This is due to the severely coupled thermal, optical, and physical properties that are present within the powder material in the presence of applied laser energy. Thus, a focused effort must be made on modeling the process to remove this concern.

The three main user-defined parameters that influence the melting behaviour of a material during SLM are the laser power P, speed v, and

hatch spacing h. Together, along with the powder layer thickness l, they comprise a number that is used to qualitatively classify the energy requirements for melting. This is known as the volumetric energy density and is given in equation (3) [48–50].

$$E_d = \frac{P}{vhl} \tag{3}$$

The volumetric energy density is heavily used in parameterization studies where any or all the above are permutated about a test matrix. Functional relationships are made between  $E_d$  and properties of interest (ie. chemical, physical, mechanical), such that a process window can be obtained for that specific material. The experimental process of doing this can be time consuming and costly, and does not guarantee that optimal parameters will be obtained [51]. In fact some authors have stated that  $E_d$  should not be used as a metric for production as it does not adequately represent all of the physics of the melt process [52,53]. Therefore, an effort to model as much of the physics within the melt process as possible will allow for a better understanding of the correct parameters to use during SLM.

The necessity of modeling is paramount to the optimization of any manufacturing process. It can save time, money and resources that would otherwise be spent on producing numerous iterations of a product to obtain its best characteristics by brute force – although as it will be seen later, this

process is itself a form of modeling. The simplest depiction of a model is given in Figure 6.



Figure 6: Basic representation of a model as recreated from [54].

As observed above, a model is used to forecast an output given a set of inputs. These inputs can be experimentally determined or simply estimated and are generally related to the perceived output through a mathematical relationship. The fundamental structure of this relationship is in the form of equation (1):

$$y = f(x) + \varepsilon \tag{4}$$

This represents a response, y, to an unknown relation, f, of process parameter x, with an associated error,  $\varepsilon$  [51]. This is the basic formulism for any model that can be used to predict an outcome based on given inputs and it is the skeleton of the three types of models discussed in this report.

Steen *et al* [54] summarize modeling three levels. The first is to obtain a semiquantitative understanding of the physical mechanisms of the process for the design of experiments. This is the creation of the so called, "order of magnitude" calculations that describe the feasibility of the proposed model. At the second level, it is expected that one must gain a parametric

understanding of the process so that it can be controlled and modified for different material systems and conditions. The final level is to detailed understanding of the process mechanisms so that prediction of outcomes and potential improvement can be applied. This is the point at which the analytical and numerical models can be tested.

The physics of the melt process are coupled between one another through various types of phenomena, thus it is important for the experimenter to determine what they wish to obtain from their model. The interaction of the laser with the material is impacted by numerous effects, many of which are given in Figure 7. As many of these effects as possible are taken into account so that the melt and solidification process can be understood, as well as an investigation into modeling the desired properties of the manufactured part [55].

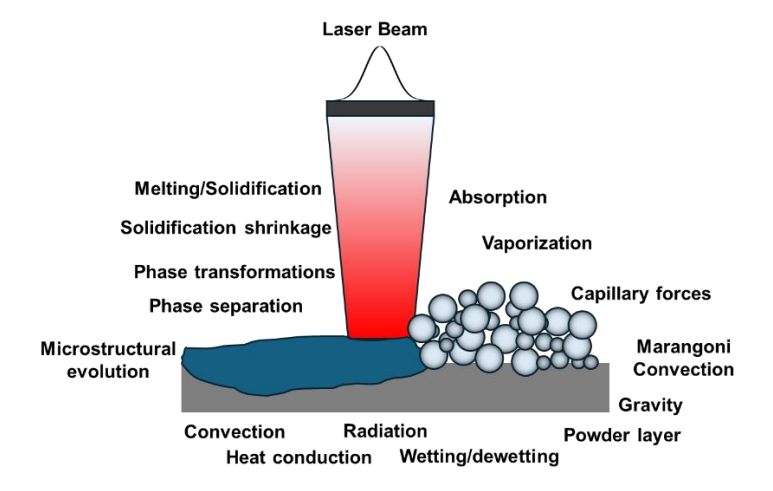


Figure 7: Different phenomena present during the PBF process, as recreated from [56].

Fortunately for laser-based AM, much of the physics surrounding the process is identical to other laser processes that preceded it. These include laser hardening, cutting, welding, and ablation. Initial modeling of laser melting can be traced back to Rosenthal's solution of a moving point source model for cutting and welding metal using an arc welder [57]. He developed solutions to the heat equation that incorporated a moving line and point sources on the surface of a semi-infinite medium to visualize the threedimensional isotherms created as the source propagated. This analytical solution did not incorporate any losses due to convection, radiation, evaporation, or even phase change upon melting. The Rosenthal solution has been noted to provide a good benchmark for laser melting, although as coordinates closer to the beam center are evaluated the temperature tends toward infinity due to a singularity at this point. Building upon this work, the analytical solution for a moving Gaussian beam was developed using a similar approach by Cline and Anthony [58]. They also considered a semiinfinite medium but included a volumetric heat source rather than a surface source.

The types of modeling that exist are empirical, numerical and analytical. All three modeling schemes contain inherent advantages and disadvantages. The empirical model, while simplest to perform, requires the physical production of numerous parts by means of applying a build parameter matrix. Here, many experiments are essentially performed and

their outcomes are correlated to produce a trend that can be validated by further experimentation. An understanding of the underlying physics is not necessarily required for the implementation of an empirical model, but this would be useful in determining the magnitude and placement of the constants that fit the relation [59]. Numerical simulations require the use of specialized software or a coding language to perform FEM approximations. Depending on the complexity of the solving mechanism, the user can be met with an easy-to-use graphical user interface or become consumed with debugging code. Also, many of the software suites, such as ANSYS require the purchasing of a license which can be expensive. Furthermore, some software may be proprietary therefore it is impossible to be provided to the research community at large, which can impede advancements in this field, such as the case for the ALE3D software designed by Lawrence Livermore National Laboratory [56].

The numerical and analytical approaches can be performed without the need to manufacture parts, but do require knowledge of the optical, thermal, and physical mechanisms of the melt process to provide a physically relevant result. This is the trade-off between these two methodologies and the empirical model, as it is possible to become lost in the minutiae of the physics by consistently trying to improve upon the model before testing it [54].

Despite the previous points however, it is the analytical approach that has the industrial advantage, if it exists. This is because a closed form solution can be obtained, and the results of the temperature profile obtained using this method can be passed into the AM process control system during a live build to monitor the part quality in-situ by adjusting the build parameters accordingly. Unfortunately, there exists no fully complete analytical model that can predict the quality of an additively manufactured part with 100% accuracy yet. This shortcoming can be a result of the type and number of assumptions surrounding the analytical approach [59].

One such set of assumptions is the universal use of the heat equation for the determination of the thermal history of the part. In [60], Bäuerle describes limits to the validity of this equation for modeling purposes. For example, the relevant optical and thermal properties are usually taken from data that utilized test methods to obtain these properties where small thermal gradients were applied across the sample. This is not the case in laser processing, however, since there is a lot of energy delivered in such a short amount of time. In fact, since the dominant mechanisms involve conduction and absorption, laser processing of materials usually lead to the creation of large thermal gradients whereby the expected contribution of the input parameters may deviate from their perceived values. These properties also depend on the crystallinity and surface morphology of the material to be melted. Since the PBF process uses powder as a medium, its optical

absorption and thermal conductivity, for example, will be radically different than for a homogeneous and isotropic slab of the same material of equivalent thickness. Finally, the coupling between different aspects of the melt phenomenon, such as the local temperature and density of the powder, can lead to the necessity of solving coupled non-linear equations that will only add further complexity to the model and a source of error if not properly understood.

Some models neglect certain physical phenomena for simplicity. The numerical model proposed by King et al [47] describes the omission of characteristics such as the interaction of intensely vaporized material with the incident laser beam and the convective losses to the surrounding gas medium. The intense vaporization of material is typically observed during the process of keyhole welding, where this vaporization is caused by the creation of a plasma due to the extremely high laser energy. There exist models for this laser-plasma interaction however the authors determined that as the laser energy approaches the welding regime the build quality would begin to deteriorate. In the matter of the gas-driven convective losses, their neglect from the model is due to limits in computational power. The software they used would only allow for the modeling of extremely small regions of the build area at a time, over small timescales on the order of a few milliseconds. They reasoned that within these conditions heat losses from the melt track due to evaporation, radiation and conduction into the

substrate would dominate over convection and that modeling convection would only be advantageous when they could accommodate the computation of a larger region of the build area.

These limitations are not by any means exhaustive and may be exceeded as the current state-of-the-art in PBF modeling practices continue to develop.

## 2.4 Research Implications

The remainder of this thesis provides experimental and modeling efforts to emphasize the role that additive manufacturing can play in thermoelectrics, as well as the benefits of modeling an uncharacterized material system for first time use with SLM. In Chapter 3, a semi-analytical model is developed to provide an elementary process window based on some coarse physical assumptions of the laser interaction. It employs a novel approach of separating the beam into two portions; one that is incident on powder and the remainder that is incident on the lagging melt pool as the beam traverses across the powder bed. The material properties of both the powder bed and the liquid are taken into account, and often additional modeling from known physical relationships was employed to determine properties that were either unknown or difficult to measure. The process window that is created via this model is a first approximation to allow an experimenter to begin processing their material with a laser power and

speed that should facilitate melting with minimal evaporative loss, and provide values that would be consistent with the conduction regime of laser processing. This window acts as an initial guide and is meant to be improved upon as experimentation develops. Chapter 4 outlines the experimental challenges of getting an unfit-for-AM powder into a commercial LPBF system. It details the powder and bulk characterization techniques as custom powder delivery system used to overcome these challenges. This custom system acts as a foundation to allow for further experimentation with the AM of metallic powders of different morphology, by allowing for the manual stackability of powder layers of repeatable thickness. The fifth chapter combines the successful experimental efforts of producing an AM-manufactured thermoelectric device, with the validation of the semi-analytical model to act as a guide for future experimentation in the semiconductor or semimetal space, where the preservation of both stoichiometry and crystal structure of the underlying powder are of paramount importance.

# 3. Model Setup

# 3.1 Semi-Analytical Component

# 3.1.1 Relevant Physical Properties

The powder and liquid properties required for effective modeling of the laser melting process are organized into optical, thermal, and physical property categories. In this thesis, when a measurement was unable to be performed or data did not exist in literature, the property was modelled based on related physical processes. This is meant to emphasize overcoming the challenges of obtaining reasonable values for difficult-to-obtain material properties. Below is a table of all necessary properties for the modeling of Bi<sub>2</sub>Te<sub>3</sub> noting those which were estimated. The properties for both the powder and the bulk solid are both categorized under "powder".

	Necessary Properties for the Modeling of SLM of Bi₂Te₃ (Symbol for Powder/Symbol for Liquid)  • = Modeled		
	Property	Powder	Liquid
Optical	Absorption Coefficient $(\beta/\alpha)$	•	N/A
	Reflectivity $(R_p/R_L)$	•	•
	Absorptivity $(B_p/A_L)$	•	•
	Thermal Conductivity $(k_p/k_L)$	•	
	Heat Capacity $(cp_{\scriptscriptstyle S}/cp_{\scriptscriptstyle L})$		
	Melt Temperature $(T_m)$		
Thermal	Effective Boiling Temperature $(T_b)$	N/A	•
	Latent Heat of Fusion ( $\Delta H_m$ )		N/A
	Latent Heat of Vaporization $(\Delta H_v)$	N/A	•
	Emissivity = Absorptivity [61]	•	•

Table 2: Necessary properties for the Modeling of the SLM of Bi<sub>2</sub>Te<sub>3</sub>.

# 3.1.1.1 Optical Properties

# 3.1.1.1.1 Powder Absorption Coefficient (β)

Light is absorbed to a depth into a homogeneous body via the Lambert-Beer Law. For an incident intensity, such as one provided by a laser, the absorbed radiation in the z-direction will follow equation (5)

$$\frac{dI(x,y,z,t)}{dz} = -\alpha I(x,y,z,t) \qquad \left[\frac{W}{m^3}\right] \quad (5)$$

where I(x,y,z,t) is the intensity [W/m²] and  $\alpha$  is the absorption coefficient in [m¹¹] that determines the attenuation of that intensity at a depth in the z-direction [62]. However when the medium is nonhomogeneous and contains voids, as is the case with a powder bed used in additive manufacturing, the absorption of light is characterized by the Radiative Transfer Equation (RTE) [63–66]. This equation considers the analogous absorption from the Lambert-Beer law, while also considering the effects of scattering from the particles in the system internally. The equation is given below and the additional coordinate notation for x, y, and t have been dropped for simplicity but are implied in the intensity equation [64,67].

$$\mu \frac{dI(z,\mu)}{dz} = \beta \left\{ \frac{\omega}{2} \int_{-1}^{1} I(z,\mu') P(\mu',\mu) d\mu' - I(z,\mu) \right\} \qquad \left[ \frac{W}{m^3} \right] \quad (6)$$

Where  $\mu=\cos\theta$ ,  $\omega$  is the scattering albedo,  $\beta$  in [m<sup>-1</sup>] is the powder absorption coefficient similar to  $\alpha$  in the Lambert-Beer law, and  $P(\mu',\mu)$  is the scattering phase function. This phase function is assumed equal to unity to provide isotropic scattering from the spherical particles [64]. A sample powder bed system showing powder placed upon a substrate is given in Figure 8 that illustrates the effects of the RTE. The solution to this equation will be revisited in the derivation of the powder bed absorptivity in the next section.

The absorption coefficient  $\beta$  first needs to be determined for a powder bed system, and will be shown to be explicitly based on the geometry of the powder bed particles alone, and have no dependence on wavelength or material properties [63]. Thus, it is first important to understand the geometry of the particles present within a powder bed. A powder size distribution is given in Figure 24 for a p-type bismuth telluride ternary alloy.

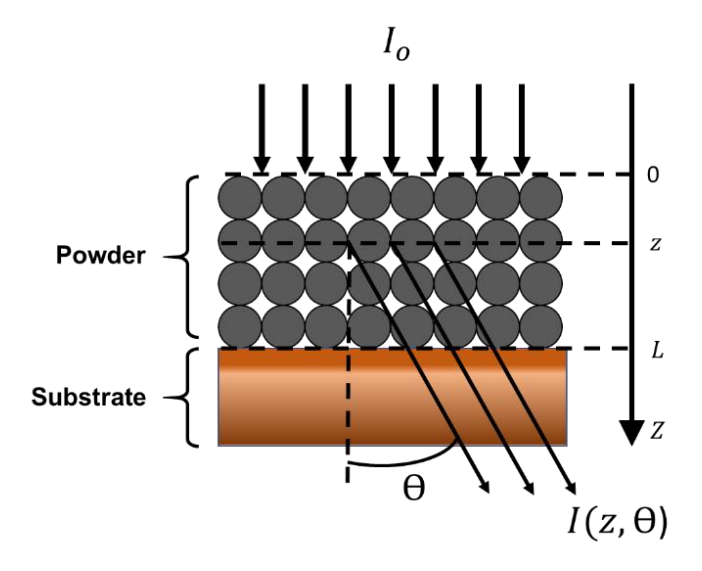


**Figure 8:** Incident laser radiation  $I_o$  on a powder bed surface at z=0. The radiation propagates through the powder to the substrate which begins at z=L. The intensity is both absorbed by the system and scattered by the particles at angle  $\Theta$  to a resultant intensity  $I(z, \theta)$ . This image is recreated from [64].

The powder packing factor  $PF_p$  is equal to the sum volume of particles divided by a fixed bounding volume. This value can be measured experimentally and evaluated using the following equation.

$$PF_p = \frac{m_{measured}}{V_{fixed} \cdot \rho_{bulk}} = \frac{\rho_{powder}}{\rho_{bulk}} = \frac{V_{powder}}{V_{fixed}}$$
 (7)

Where the measured mass  $m_{measured}$  of powder in [kg] that is contained within some fixed volume  $V_{fixed}$  in [m³] provides the powder density  $\rho_{powder}$  in [kg/m³]. This value is then divided by the theoretical bulk density of the powder material  $\rho_{bulk}$  in [kg/m³] that can be obtained from literature. The packing factor is scalable to a powder distribution where the sum of the particle volumes  $V_s$  in [m³] can be divided by a minimal characteristic volume  $V_c$  in [m³] that is representative of the powder packing on a larger scale.

$$PF_{p} = \frac{\sum_{i=1}^{N} V_{s_{i}}}{V_{c}} = \frac{V_{s}}{V_{c}}$$
 (8)

The concept of a packing factor defined by characteristic volume is provided in Figure 9, with definitions of the volume of spheres and the volume of the surrounding gas with respect to the characteristic volume,  $V_G$ .

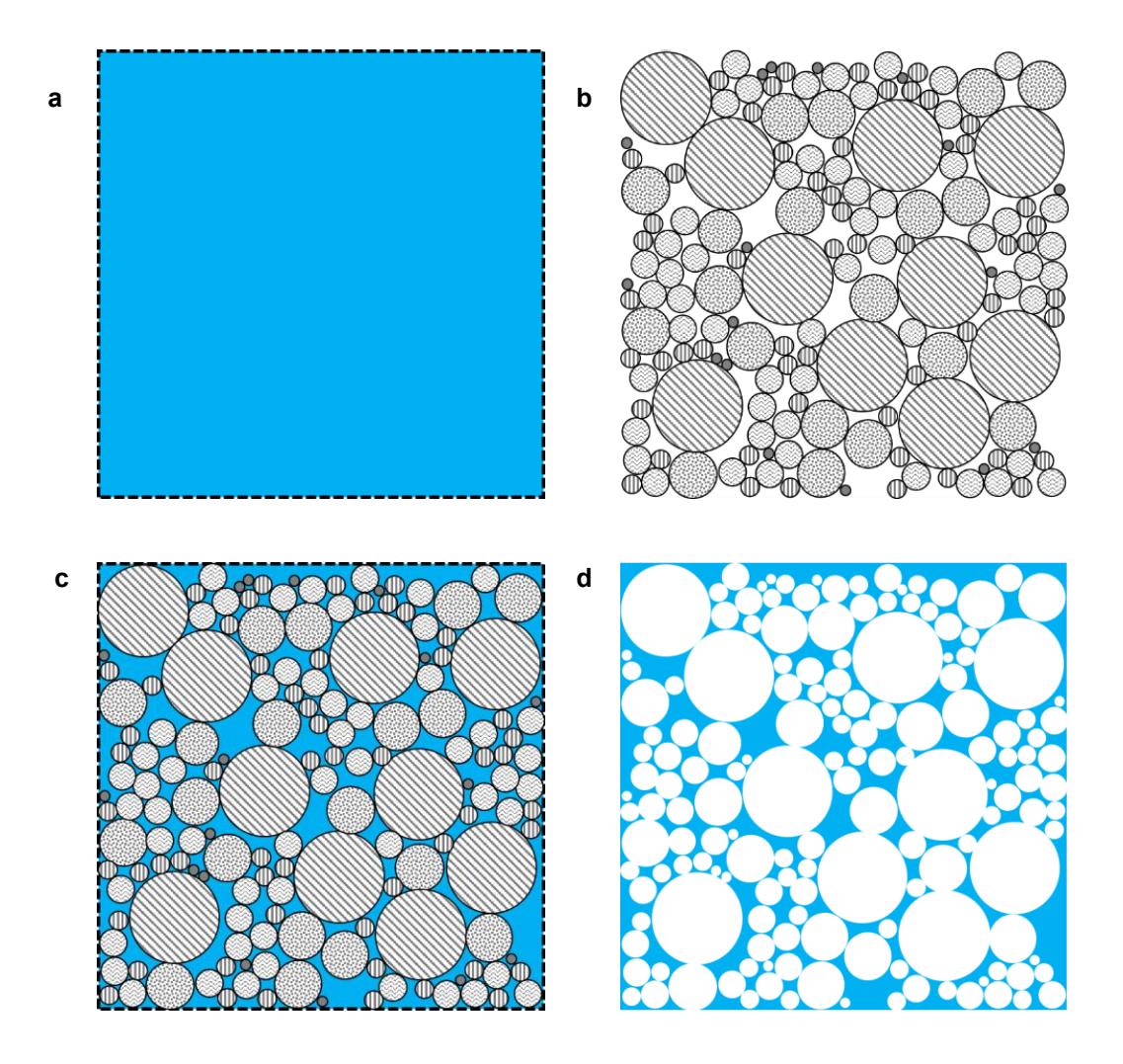


Figure 9: a) Characteristic volume  $V_c$  which represents the minimal bounding volume that can be repeated. The colour blue represents the gaseous environment that the particles inhabit. b) A distribution of particles of different diameters, indicated both by their sizes and fill texture. The sum of the volumes of these spheres is denoted as  $V_s$ . c) The spheres are placed within their characteristic volume, where the packing factor given as  $PF_p = \frac{V_s}{V_c}$ . Thus the volume of spheres with respect to the characteristic volume is equal to  $V_s = (PF_p)V_c$ . d) The particles have been omitted and the remaining blue region is the volume of gas that is present in  $V_c$  after the particles have been added and displace their volume in gas. This remaining volume

is equal to  $V_c - V_s$  making the volume of gas within a characteristic volume of particles equal to  $V_{gas} = (1 - PF_p)V_c$ .

For a given powder size distribution such as that given in Figure 24, the total volume of all particles in a given sample is given by equation (9).

$$V_{s} = \sum_{i=1}^{N} V_{s_{i}} = \sum_{i=1}^{N} N_{s}(d_{i}) \cdot \frac{\pi}{6} d_{i}^{3}$$
 [m<sup>3</sup>] (9)

where in a multimodal powder of N different diameters the number of spheres in the i<sup>th</sup> diameter size is given by  $N_s(d_i)$  with  $d_i$  being the diameter in [m]. The multimodal powder in Figure 24 provides these diameters, although they are given in [ $\mu$ m] and therefore must be converted to [m] for all subsequent calculations. For single mode powders, N=1 and the summation vanishes. The distribution in Figure 24 is given as percent volume per diameter size. This percentage is calculated by equation (10).

$$(\%)_{i} = \frac{V_{s_{i}}}{\sum_{i=1}^{N} V_{s_{i}}} = \frac{N_{s}(d_{i}) \cdot \left(\frac{\pi}{6} d_{i}^{3}\right)}{V_{s}}$$
(10)

Solving equation (10) for  $N_s(d_i)$  yields equation (11):

$$N_s(d_i) = \frac{6V_s}{\pi} \cdot \frac{(\%)_i}{d_i^3} \tag{11}$$

With these values in place, it is important to return to the characteristic volume to once again state the volume of gas present in between the

particles. Within the Figure 9 description, this volume is denoted as  $V_{gas}$ . It can be formally defined in terms of the packing factor and  $V_c$  by equations (12) – (14) with the help of the substitution of equation (8) into equation (13).

$$V_{qas} = V_c - V_s$$
 [m<sup>3</sup>] (12)

$$\frac{V_{gas}}{V_c} = \frac{V_c}{V_c} - \frac{V_s}{V_c} = 1 - \frac{V_s}{V_c} = 1 - PF_p \tag{13}$$

$$V_{gas} = (1 - PF_p)V_c$$
 [m<sup>3</sup>] (14)

Even with the specific particle and characteristic volumes unknown, there is now enough information to calculate  $\beta$  using knowledge of the powder distribution of volumes and the measured packing factor. The powder absorption coefficient is defined in the literature as the ratio of the surface area of a particle population to the volume of its voids, multiplied by a factor of  $\frac{1}{4}$ . The void volume is the volume of the gas between particles, given by equation (14). Further information about its derivation can be found in numerous sources [63–68]. Using equation (11) for the number of particles in the distribution of a certain diameter, the surface area of this subset can be calculated in equation (15) with the surface area of a single particle equal to that of a sphere.

$$SA_i = N_s(d_i) \cdot \pi d_i^2 = \left(\frac{6V_s}{\pi} \cdot \frac{(\%)_i}{d_i^3}\right) \cdot \pi d_i^2 = 6V_s \cdot \frac{(\%)_i}{d_i}$$
 [m<sup>2</sup>] (15)

The description of  $\beta$  given in the preceding paragraph can now be formulated using both equations (14) and (15).

$$\beta = \frac{1}{4} \cdot \frac{\sum_{i=1}^{N} SA_i}{V_{gas}} = \frac{1}{4} \cdot \frac{6V_s \cdot \sum_{i=1}^{N} \frac{(\%)_i}{d_i}}{(1 - PF_p)V_c}$$

$$= \frac{3}{2} \cdot \frac{V_s}{V_c} \cdot \frac{1}{1 - PF_p} \cdot \sum_{i=1}^{N} \frac{(\%)_i}{d_i}$$
[m²] (16)

Finally, with the definition of the packing factor provided in equation (8), equation (16) can be further simplified to remove the two unknowns of  $V_s$  and  $V_c$  and leave  $\beta$  only in terms of experimentally determined quantities. The equation value for  $\beta$  is given for a powder distribution in [63].

$$\beta = \frac{3}{2} \cdot \frac{PF_p}{1 - PF_p} \cdot \sum_{i=1}^{N} \frac{(\%)_i}{d_i} \qquad \left[\frac{1}{m}\right] \quad (17)$$

All of the necessary values needed to calculate  $\beta$  in equation (17) have been provided; the packing factor can be experimentally determined from a simple mass and containing volume measurement, and the volume percentage per diameter (%) $_i$  as well as the diameters of the particles themselves  $d_i$  are given in the distribution shown in Figure 24, where the values in the y-axis need to be divided by 100 to be used in the calculation above.

For the powder distribution of p-type (Bi<sub>0.15</sub>Sb<sub>0.85</sub>)<sub>2</sub>Te<sub>3</sub> given in Figure 24, the absorption coefficient  $\beta$  calculated using equation (17) is equal to 3.36·10<sup>5</sup> m<sup>-1</sup>. This yields an optical penetration depth of  $\frac{1}{\beta}$  equal to 2.98  $\mu$ m.

It is evident in equation (17) that the powder absorption coefficient is not dependent on the incident light wavelength or the reflectivity of the bulk powder material itself, but rather simply on geometrical factors. These factors are clearly the packing factor and diameter distribution of the powder. In order to forecast the effects of changing these parameters in  $\beta$ , a substitution for the sum in this equation can be provided by equation (18).

$$\frac{1}{d_{eq}} = \sum_{i=1}^{N} \frac{(\%)_i}{d_i}$$
  $\left[\frac{1}{m}\right]$  (18)

The above equation converts the diameter distribution into a single equivalent powder diameter  $d_{eq}$ . Again, for a single mode powder where there is only one diameter grain size present, this equivalent diameter is equal to that single mode diameter of the distribution. Making the above substitution, the absorption coefficient can be parametrized for PF and  $d_{eq}$  using the following equation.

$$\beta = \frac{3}{2} \cdot \frac{PF_p}{1 - PF_p} \cdot \frac{1}{d_{eq}}$$
 
$$\left[ \frac{1}{m} \right]$$
 (19)

The relationship between  $\beta$ ,  $PF_p$  and  $d_{eq}$  are shown in Figure 10. To make the results more meaningful, the plot is shown as  $\frac{1}{\beta}$ , the optical penetration depth of the powder.

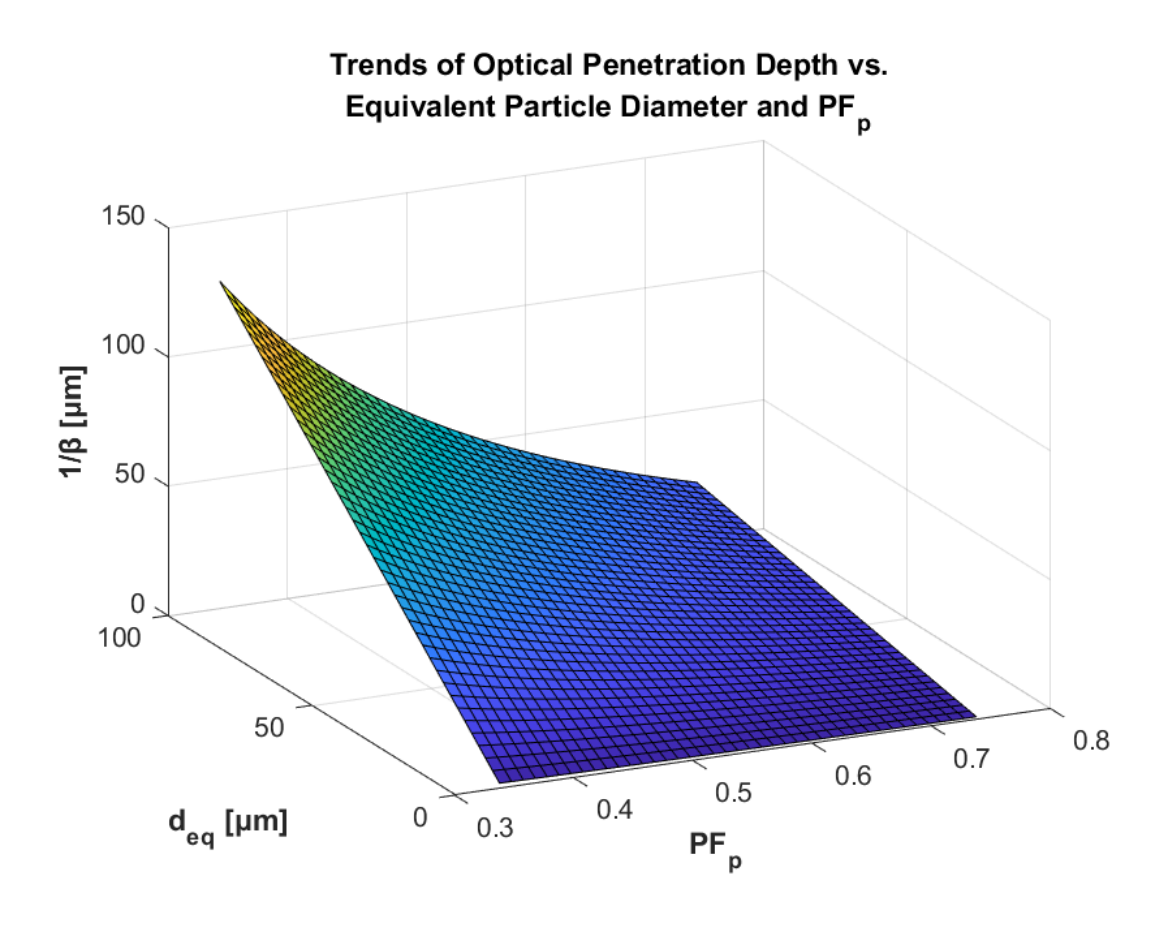


**Figure 10**: Surface plot trend of optical penetration depth vs. changing equivalent particle diameter and powder packing factor.

The general trend is understood to be that the optical penetration depth increases with increasing equivalent particle size and decreasing packing factor. It is important to note, however, that a nonspherical powder containing a wide distribution of sizes from the nano to macro scale will not

interact with light in the same manner as a narrow distribution of spherical particles. The irregular powder morphology implemented in the layer thicknesses used in this research create optically thick powder layers that are estimated to be better at isotropic scattering within the powder bed. A narrow distribution of spherical particles that have high flowability will arrange themselves in such a way that that they are not uniformly distributed and thus the concept of the equivalent diameter will be a less accurate representation of the powder particle size. It will also decrease the accuracy of the powder absorption coefficient. Nevertheless, the initial assumptions and the aforementioned calculation methodology still lead to the production of a process window that suitable for first-time use with a novel powder system.

#### 3.1.1.1.2 Powder Absorptivity (B<sub>p</sub>)

Since part of the beam will interact with powder and part will interact with liquid, both the solid and liquid absorptivities will be discussed. Beginning with the solid absorptivity, this is the effective absorptivity of the powder that is determined from the RTE solution of the heat flux as a function of depth. This solution is given in Appendix A.1 with the final equation of heat flux  $q(\xi)$  provided in subsection A.1.3, where the dimensionless variable  $\xi = \beta z$ . The powder absorptivity was completely derived also in the same appendix, with its equation restated below:

$$B_{p} = \frac{A}{2} \left( 1 - e^{-2a\lambda} \right) + \frac{B}{2} \left( 1 - e^{2a\lambda} \right) + \left( \frac{R_{b}}{4R_{b} - 3} - 1 \right) \left( R_{s}e^{-2\lambda} + e^{-\lambda}(1 - R_{s}) - 1 \right)$$
(20)

The absorptivity of the powder – the amount of energy absorbed only in the powder layer,  $B_p$  – is the difference between the powder-substrate and substrate absorptivities [63,64]:

$$B_p = B_{ps} - B_s = q(0) - q(\lambda)$$
 (21)

where in the equations above,  $a=\sqrt{1-R_b}$ ,  $\lambda=\beta\Delta z_p$ , and A and B are respectively defined in equations (A1.103) and (A1.102) . For a powder depth of 76µm,  $R_s=0.97$  for a copper substrate,  $R_b=0.72$  for bulk bismuth telluride and  $\beta$  of **3.36·10**<sup>5</sup> m<sup>-1</sup>, the powder absorptivity was calculated to be **0.77**.

#### 3.1.1.1.3 Liquid Absorptivity (A<sub>L</sub>)

For conductive materials, the liquid absorptivity can be derived from the implementation of the DC electrical conductivity in the Fresnel equations for the real component of the refractive index (n) and the extinction coefficient (k). The relevant equations are [69]:

$$n^2 - k^2 = 1 (22)$$

$$2nk = \frac{\sigma}{\varepsilon_0 \omega} \tag{23}$$

where  $\sigma$  is the DC electrical conductivity in  $[\Omega \cdot m]^{-1}$ ,  $\omega$  is the frequency of the incident light in rad/s, and  $\varepsilon_o$  is the permittivity of free space. Isolating both n and k separately and using temperature-dependent values for the electrical conductivity, the resulting equations yield a temperature dependency in the optical properties as well.

$$n(T) = \sqrt{\frac{1}{2} + \frac{1}{2} \sqrt{1 + \left(\frac{\sigma(T)}{\varepsilon_o \omega}\right)^2}}$$
 (24)

$$k(T) = \sqrt{-\frac{1}{2} + \frac{1}{2}\sqrt{1 + \left(\frac{\sigma(T)}{\varepsilon_o \omega}\right)^2}}$$
 (25)

With these coefficients determined vs. temperature, the reflectivity can be subsequently calculated as shown below.

$$R_L(T) = \frac{(n(T) - 1)^2 + k(T)^2}{(n(T) + 1)^2 + k(T)^2}$$
 (26)

Finally, with the assumption that light is only absorbed or reflected, the absorptivity as a function of temperature is equal to  $A_L(T) = 1 - R_L(T)$  and can be temperature averaged between the melt temperature  $T_m$  and the boiling temperature  $T_b$  in the following equation.

$$A_{L} = \frac{1}{T_{b} - T_{m}} \int_{T_{m}}^{T_{b}} (1 - R_{L}(T)) dT$$
 (27)

Using temperature-dependent values for the DC electrical conductivity of liquid  $Bi_2Te_3$  from [70] and equations (24) to (27), the value of  $A_L$  calculated for bismuth telluride was **0.50**.

#### 3.1.1.2 Thermal Properties

#### 3.1.1.2.1 Powder Thermal Conductivity (kp)

The effective thermal conductivity of the powder was estimated using the model put forward by Thümmler and Oberacker:

$$k_p = k_s (1 - \phi) \qquad \left[ \frac{W}{m \cdot K} \right] \tag{28}$$

where  $k_s$  is the thermal conductivity of the bulk solid material and  $\phi=1-PF_p$  is the porosity of the powder [71]. It neglects the thermal conductivity of the surrounding gaseous medium as its thermal conductivity is much less than the bulk solid material. This method of determination was used extensively in the literature, see for example [72–74], and was selected over more complex empirical models [75–77] based on its simplistic formation and its justification to be a good first order estimate of the effective thermal conductivity of a porous medium.

With a bulk thermal conductivity  $k_s = 0.945$  W/(m·K) and  $PF_p = 0.41$ , the thermal conductivity of the powder bed was calculated for bismuth telluride to be roughly **0.39** W/(m·K).

#### 3.1.1.2.2 Effective Boiling Point (T<sub>b</sub>)

Due to the different evaporative pressures for components in alloys, a single effective boiling temperature for the bulk material must be approximated. This is approximated by the effusion pressure-temperature relationship. For example, for bismuth telluride, this is given in the literature as [78]:

$$\log(p) = 7.579 - \frac{1.020 \cdot 10^4}{T} \tag{29}$$

where p is the pressure in atm and T is the temperature in Kelvin. Since processing occurs at roughly 1 atm of pressure, the corresponding temperature can be solved for by equating the left side of equation (29) to zero and solving for temperature. For bismuth telluride, this effective boiling temperature was determined to be **1346** K.

### 3.1.1.2.3 Latent Heat of Vaporization ( $\Delta H_{\nu}$ )

That latent heat of vaporization is difficult to obtain for nonhomogeneous materials because different components may evaporate at different pressures. However, an acceptable approximation can be made from the ablation threshold of the material [79]. An energy balance with the ablation threshold must first be evaluated.

$$\rho_s(cp_s(T_m - T_o) + \Delta H_m) + \rho_L(cp_L(T_b - T_m) + \Delta H_v) = F_{th}\alpha_s \quad \left[\frac{J}{m^3}\right] \quad (30)$$

Rearranging (30) and solving for  $\Delta H_v$ , the latent heat of vaporization is given below.

$$\Delta H_v = \frac{F_{th}\alpha_s - \rho_s(cp_s(T_m - T_o) + \Delta H_m) - \rho_L cp_L(T_b - T_m)}{\rho_L} \qquad \left[\frac{J}{kg}\right] \quad (31)$$

The ablation threshold is denoted as  $F_{th}$ , the absorption coefficient for solid bulk material is  $\alpha_s$ , the latent heat of melting is  $\Delta H_m$ , and the remaining symbols have their usual meanings. To calculate the latent heat of vaporization for generic Bi<sub>2</sub>Te<sub>3</sub> using equation (31), the following properties are used which yields  $\Delta H_v = 4.37 \times 10^6 \text{ J/kg}$  for Bi<sub>2</sub>Te<sub>3</sub>:

Property	Value	Reference	
$F_{th}$	350 [J/m²]	[80]	
$\alpha_s$	9.81x10 <sup>7</sup> [m <sup>-1</sup> ]	Calculated at 800nm corresponding to laser used in [80] ,from [81]	
$ ho_s$	7.64 x10 <sup>3</sup> [kg/m <sup>3</sup> ]	Temperature averaged from [70]	
$cp_s$	172 [J/(kg·K)]	Temperature averaged from [82]	
$T_m$	858 [K]	[42]	
$\Delta H_m$	1.51 x10⁵ [J/kg]	[42]	
$ ho_L$	7.09 x10 <sup>3</sup> [kg/m <sup>3</sup> ]	Temperature averaged from [70]	
$cp_L$	407 [J/(kg·K)]	Temperature averaged from [82]	
$T_b$	1.35 x10 <sup>3</sup> [K]	Effectively approximated from [78]	
T <sub>o</sub>	300 [K]	[80]	

**Table 3**: Thermal properties used for the approximation of the latent heat of vaporization for  $Bi_2Te_3$ .

## 3.1.2 Model Assumptions

The output of this model acts as a starting point for experimentation, in a parameter space that spans hundreds of watts of power and thousands of mm/s. It contains many coarse assumptions that will lead to the formation of an elementary process window that will reduce the planning time before initial experimentation in a new material system can occur. The following is a list of assumptions made to simplify the analysis and close the form of the solution:

- The laser beam will travel along the x-axis.
- The beam area will be split into two parts; one that interacts volumetrically with the powder and one that acts volumetrically with the liquid.
- The portion of the beam that interacts with the powder will utilize
  a simplified approach of the Radiative Transfer Equation. It will
  be Lambert-Beer in application, but its absorption coefficient will
  come from the Radiative Transfer Equation.
- The beam radius is defined by its  $\frac{1}{e^{\chi}}$  intensity waist, denoted as  $\omega_{\chi}$ .
- The beam will start at time t = 0 at position (0,0,0) and move with velocity v in the positive x-direction.

- There exists a time  $t=\tau_s>0$  when the beam will have deposited enough energy at  $(\omega_\chi,0,0)$  such that a liquid melt front will begin to form that can begin to be evaluated by the Stefan formulation.
  - $\sigma_s$  is solved for semi-analytically from an energy balance that meets the requirements for the laser to begin melting the surface. There are combinations of laser power and speed that do not allow for this initial surface melting and therefore would not be appropriate for experimentation.
  - This is assumed to be the time at which the optical penetration depth of the powder is melted.
- P and v are solved for by considering the melt requirements for the powder contained within the powder layer, at τ<sub>s</sub> as well as an overall energy balance for the system that necessitates melting to the bottom of the powder layer for the center point of the beam.
  - The power and speed combinations are determined for melt requirements on a cubical region of powder that has a top surface side length of the laser diameter, and the depth of the powder bed. The melt requirements are assumed to be the amount of energy deposited into the absorption depths of the liquid and solid media to satisfy the sensible and latent heats of the material system

accounting for surface losses such as radiation and evaporation.

- o Only the melt requirements of the powder contained within the powder layer are considered. The additional energy needed for the remelting of the solid layer beneath was omitted in this approximation in order to provide a window as close to the conduction regime as possible. Future considerations for the energy component associated with remelting of the layer beneath are recommended.
- Convection, both in the ambient medium and within the melt are neglected but could be included in the future.

#### 3.1.3 Laser Parameter Determination

The goal of the semi-analytical model is to outline an elementary process window for laser power and speed that can then be further verified with more in-depth modeling or experimentation. This model is based upon an energy balance that recognizes the laser beam can be divided into two portions; one that interacts solely with solid powder and the other that interacts with liquid.

#### 3.1.3.1 Gaussian Beam Profile

A stationary Gaussian beam has an intensity profile described by equation (32) which is given in radial dimensions.

$$I(r) = I_0 e^{-\frac{r^2}{\omega_1^2}} \qquad \left[\frac{W}{m^2}\right] \quad (32)$$

where  $\omega_1$  is the radius at which the intensity drops to 1/e of its maximum value near the focal plane. The intensity is related to the total laser power P through equation (33).

$$P = \int_{r=0}^{r=\infty} I(r)dA \qquad [W] \quad (33)$$

where the infinitesimally small area dA is related to the shape of the circular beam area by:

$$A = \pi r^2 \tag{34}$$

$$dA = 2\pi r dr [m^2] (35)$$

Thus, the total power in equation (33) can be rewritten and the maximum intensity  $I_0$  can be solved for:

$$P = 2\pi \int_{r=0}^{r=\infty} I(r)rdr \qquad [W] \quad (36)$$

$$P = 2\pi \int_{r=0}^{r=\infty} I_0 r e^{-\frac{r^2}{\omega_1^2}} dr = I_0 \pi \omega_1^2$$
 [W] (37)

$$I_O = \frac{P}{\pi \omega_1^2} \qquad \left[ \frac{W}{m^2} \right] \tag{38}$$

This allows the intensity to be written in terms of laser power and beam radius:

$$I(r) = \frac{P}{\pi\omega_1^2} e^{-\frac{r^2}{\omega_1^2}} \qquad \left[\frac{W}{m^2}\right] \quad (39)$$

If the upper limit of integration in equation (33) was changed from infinity to the 1/e beam radius,  $\omega_1$ , the integral would equal 0.63P. This indicates that only 63% of the total beam power is present within that radius. In order to encompass more of the beam, a larger radius can be chosen such that:

$$\omega_{\gamma} = \omega_1 \sqrt{\chi} \tag{40}$$

where  $\chi$  can be any number greater than zero, however practically integer values are used. This creates a new radius of  $1/e^{\chi}$  intensity. Figure 11 shows a Gaussian beam that is labelled with the 1/e, 1/e², 1/e³, and 1/e⁴ intensity radii. These correspond to 63%, 86%, 95% and 98% of the total beam power, respectively. In general, the sensitivity of the radius selection can be taken into account with a modification to the intensity equation as a result of equation (40). The generalized intensity equation is then given below:

$$I(r) = \frac{\chi P}{\pi \omega_{\chi}^{2}} e^{-\frac{\chi r^{2}}{\omega_{\chi}^{2}}} \qquad \left[\frac{W}{m^{2}}\right] \quad (41)$$

Equation (41) can be modified to represent a moving beam but must first be converted into Cartesian coordinates from the familiar relationship:

$$r^2 = x^2 + y^2 [m^2] (42)$$

$$x = x - v_x t, \quad y = y - v_y t$$
 [m] (43)

with the Cartesian intensity equation equal to:

$$I(x,y,t) = \frac{\chi P}{\pi \omega_{\chi}^{2}} e^{-\left(\frac{\chi(x-v_{\chi}t)^{2}}{\omega_{\chi}^{2}}\right)} e^{-\left(\frac{\chi(y-v_{\chi}t)^{2}}{\omega_{\chi}^{2}}\right)} \left[\frac{W}{m^{2}}\right]$$
(44)

When integrating the above equation for a heat balance, it is convenient to assume the beam travels solely in the x-direction with speed  $v_x = v$ . This causes  $v_y$  to equal zero and simplifies the equation.

$$I(x,y,t) = \frac{\chi P}{\pi \omega_{\chi}^2} e^{-\left(\frac{\chi(x-vt)^2}{\omega_{\chi}^2}\right)} e^{-\left(\frac{\chi y^2}{\omega_{\chi}^2}\right)} \left[\frac{W}{m^2}\right]$$
(45)

A value of  $\chi=2$  is used in the literature and is standard in industry as well [62,83].

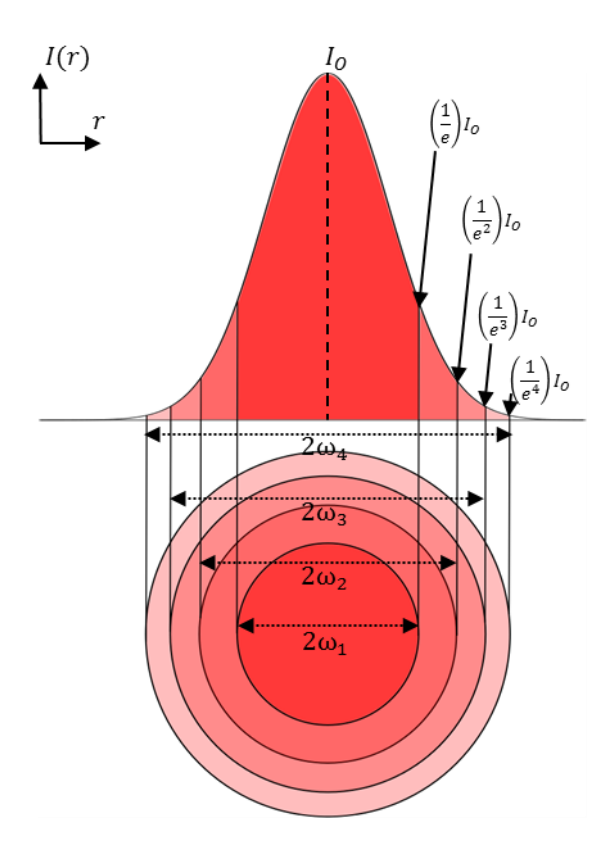


**Figure 11:** (Top) Gaussian intensity profile of a laser beam as a function of radius. (Bottom) Projection of the beam on a surface with specific radii labelled.

#### 3.1.3.2 Solid and Liquid-Interacting Beam Components

In the proposed model, the beam is assumed to start at the origin in the xy-plane at time t=0s. The melt region of interest (ROI) is a cube with dimensions of the square of the beam diameter in the xy plane, multiplied by the powder depth in the z plane. A diagram of the laser starting position is given below.

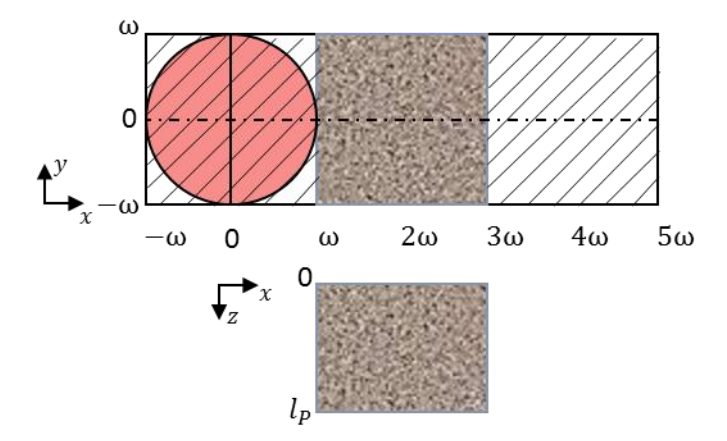


**Figure 12**: Starting point of laser beam before entering the ROI. (Top) Setting up the laser scan path along the positive x-direction in the xy plane. The view in the xy plane exists between  $\omega$  and  $3\omega$ . (Bottom) The depth in the xz direction is shown to be the length of the powder layer. The subscript  $\chi$  has been dropped for clarity.

As observed in Figure 12 the laser begins just outside of the ROI, in fact it is one beam radius from entering the region of interest. It will traverse along the dotted path with some speed, v, until it reaches its end point at  $(4\omega, 0)$  in the xy plane. The total time taken for the laser to enter, pass through and exit the ROI entirely is given in equation (46).

$$\tau_L = \frac{4\omega}{v}$$
 [s] (46)

It is important to note that the energy contributions in the hatched regions in Figure 12 are not considered in the model, and any energy deposited in those regions are neglected. They are simply included to show the path that the laser will take in order to traverse across the ROI.

It is assumed that along a given scan path, part of the beam will begin to melt the powder while the remaining part will encounter a liquid interface. This is illustrated in Figure 13. The portion of the beam that interacts with the solid enters the ROI at time  $\tau_S$ . The portion of the beam area that crosses into the ROI,  $f_S$ , can be calculated from equation (48) which was derived from simple trigonometry in Figure 14.

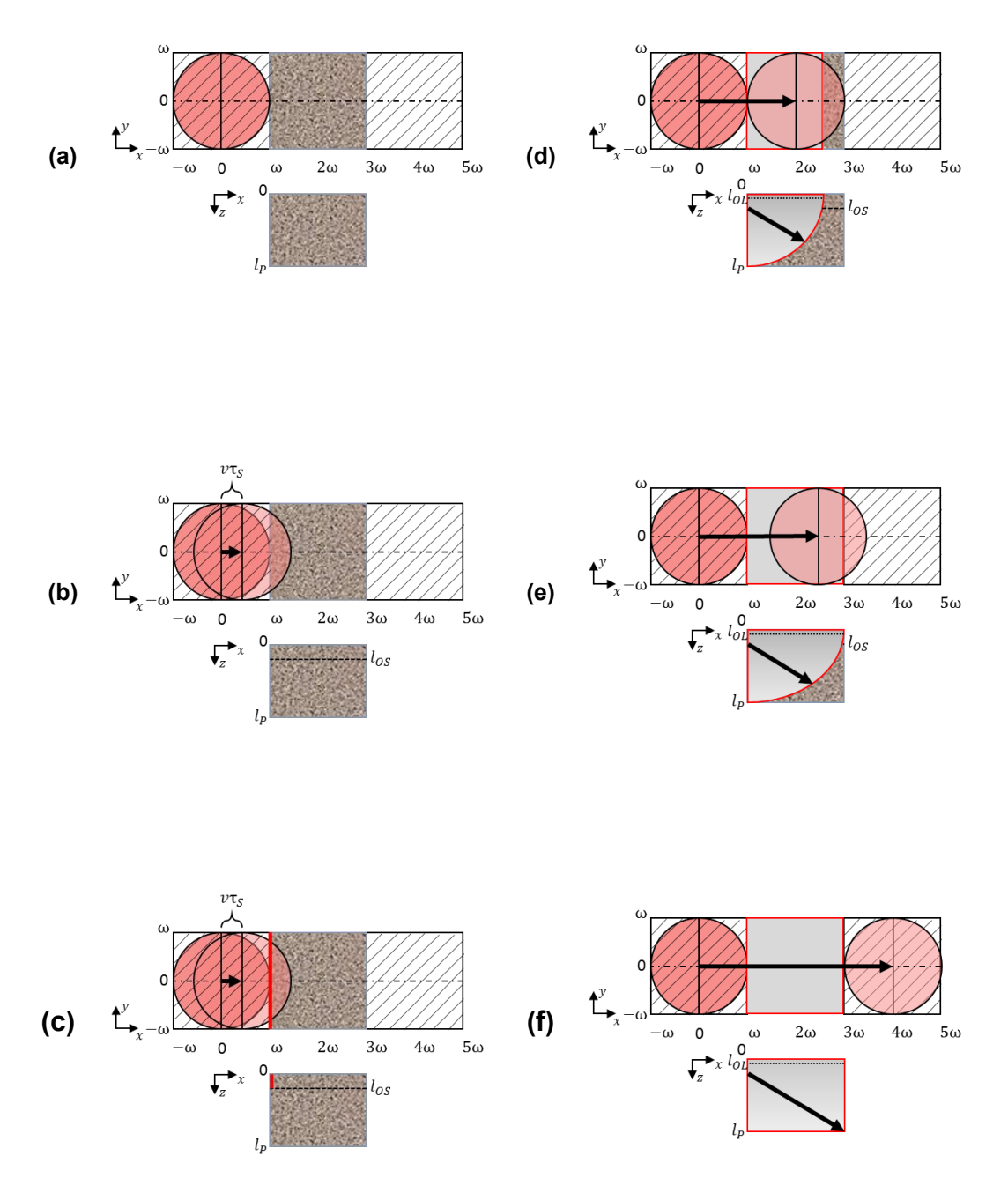


**Figure 13:** (a) through (f) portrays the path of a laser beam as it traverses a distance of two diameters (or four radii). The top portion of each frame is referenced to the xy plane, while the bottom is a side view of the xz plane, looking at a cross section of

the powder layer ROI. (a) The laser begins at (0,0) and at time t=0s. (b) The laser has moved a distance of  $v\tau_s$ , enough such that a portion of its beam will pass into the ROI. (c) The red line that appears at the left side of the ROI represents the beginning of the melt front. The melt is assumed to have zero initial lateral width and has a depth equal to the solid optical penetration depth,  $m{l}_{\it{OS}}$ . (d) The beam has moved fully into the ROI now, and it leads with a portion that only interacts with solid powder, while the remaining portion of the beam is incident upon liquid. The portion absorbed in the liquid reaches the liquid optical penetration depth,  $l_{oL}$ . (e) The beam has begun to exit the ROI, and only the portion of the beam interacting with a liquid interface remains inside, however there is still solid material inside the cell that the melt front has not reached. (f) The laser beam has left the ROI entirely, and the melt front has propagated completely through the powder depth,  $l_p$ , and the process repeats. The laser scan vector, indicated by the black arrow joining the start and end positions of the beam is assumed to have lasted for the same amount of time as the melt propagation vector, which moves from the beginning of the melt front position at the top left of the ROI, down to the opposite corner.

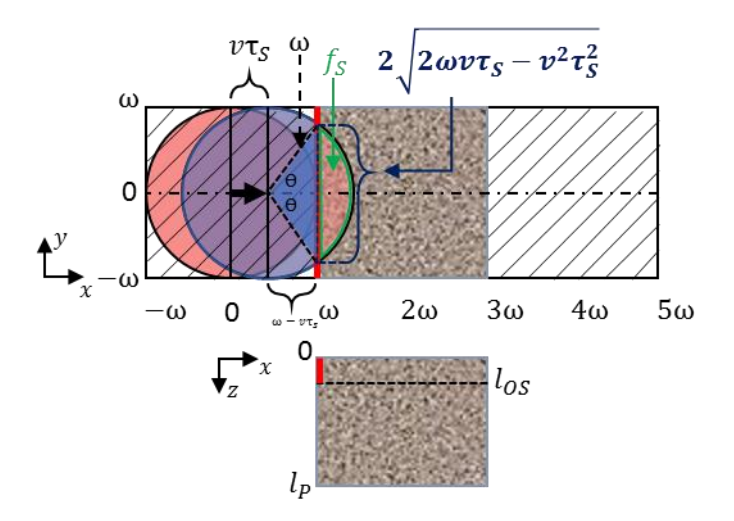


**Figure 14:** Determination of the fraction of the beam that interacts with solid powder,  $f_s$ .

$$\theta = \cos^{-1}\left(\frac{\omega - v\tau_{S}}{\omega}\right)$$
 [rad] (47)

$$f_S = \frac{\omega^2 \cos^{-1} \left( \frac{\omega - v\tau_S}{\omega} \right) - (\omega - v\tau_S) \cdot \sqrt{2\omega v\tau_S - v^2 \tau_S^2}}{\pi \omega^2}$$
(48)

where v is again the laser speed and  $\tau_S$  the time taken for the beam to enter into the ROI and for the melt front to begin. It is the time taken for powder of the optical absorption depth to begin melting. Conversely, the portion of the beam that interacts with the liquid is therefore  $(1 - f_S)$ . This implies that both liquid and effective solid optical properties are needed for the laser source term, and it will have to be modified to contain both components of the beam, as will be observed later.

The propagation of the melt front in Figure 13 should coincide with one whole beam width entering and exiting the ROI. Thus, in the time it takes for the laser to travel  $4\omega$  in the x-direction, the melt front must move throughout the entire cell, indicating that all the energy supplied by the beam should be used to melt the entire powder volume. Recalling the definition of  $\tau_L$  as the total time for the laser to travel  $4\omega$  metres, and introducing  $\tau_M$  as the length of time it takes for the melt front to cross the diagonal of the ROI, then the portion of time spent by the beam interacting with the solid powder,  $\tau_S$ , is related to both times in the following manner:

$$\tau_L = \tau_S + \tau_M \tag{49}$$

Rearranging for  $\tau_S$  and substituting equation (46) for  $\tau_L$  we get

$$\tau_S = \frac{4\omega}{v} - \tau_M \tag{50}$$

An appropriate estimate for  $\tau_M$  would be the thermal diffusion time of the melt front across the diagonal distance of the ROI. Since the dimensions of the ROI are known,  $\tau_M$  can be calculated by [84]

$$\tau_M = \frac{(l_P - l_{OS})^2 + (2\omega)^2}{4D_L}$$
 [s] (51)

where, as observed in the bottom portion of Figure 14,

$$l_P = \Delta z_p \tag{52}$$

$$l_{OS} = \frac{1}{\beta} \tag{53}$$

 $D_L$  is the liquid thermal diffusivity as taken from [85]. Equations (49) through (51) can be combined to provide the two unknowns, the solid interaction time  $\tau_S$  and the laser speed v into a single equation:

$$\tau_S = \frac{4\omega}{v} - \frac{(l_P - l_{OS})^2 + (2\omega)^2}{4D_L}$$
 [s] (54)

All the necessary background has now been covered to approach the solid- and liquid-interacting beam portions. It is important to note that for the solid-interacting portion, a simplified approach to the RTE will be taken such that the applied laser source will be Lambert-Beer in nature, but will contain a powder absorptivity and absorption coefficient that are derived from the RTE. This simplified approach is best applied to optically thick powder beds, where the beam is expected to be almost fully attenuated by the time it penetrates to the bottom of the powder layer, acting similarly to a laser encountering a homogeneous material under the Lambert-Beer Law. The effects on the accuracy of the results due to this substitution is addressed at the end of section 3.1.3.3.

The energy contents in the beam portions are described as quadruple integrals over the observed powder region in Figure 14.

For the solid-interacting portion:

$$\int_{0}^{\frac{1}{\beta}} \int_{-\omega}^{\omega} \int_{0}^{3\omega} \int_{-\infty}^{\infty} B_{p} \beta I(x, y, t + \tau_{s}) e^{-\beta z} \cdot H(x - vt - \omega) dt dx dy dz$$
 [J] (55)

and for the liquid-interacting portion:

$$\int_{0}^{\frac{1}{\alpha}} \int_{-\omega}^{\omega} \int_{0}^{3\omega} \int_{-\infty}^{\infty} A_{L}\alpha I(x, y, t + \tau_{s}) e^{-\alpha z} \cdot H(-(x - vt - \omega)) dt dx dy dz$$
 [J] (56)

where  $B_p$  and  $A_L$  are the powder and liquid absorptivities, and  $\beta$  and  $\alpha$  are the powder and liquid absorption coefficients, respectively. Each of the integrals in (55) and (56) are evaluated over a square shaped spatial region, with side length equal to the laser diameter. The integral in the z-direction is from the top surface of the powder to the absorption depth determined by the solid or liquid absorption coefficient. The temporal integral from  $-\infty$  to  $+\infty$  signifies the use of an infinite scan vector, as mentioned previously in the assumptions. The Heaviside step function is also used in each equation to permit only one part of the laser source to deposit energy, depending on the medium of interaction. It helps to separate the energy contributions from each beam portion, belonging to the same source. The desired effect of the Heaviside function is illustrated in the following figure.

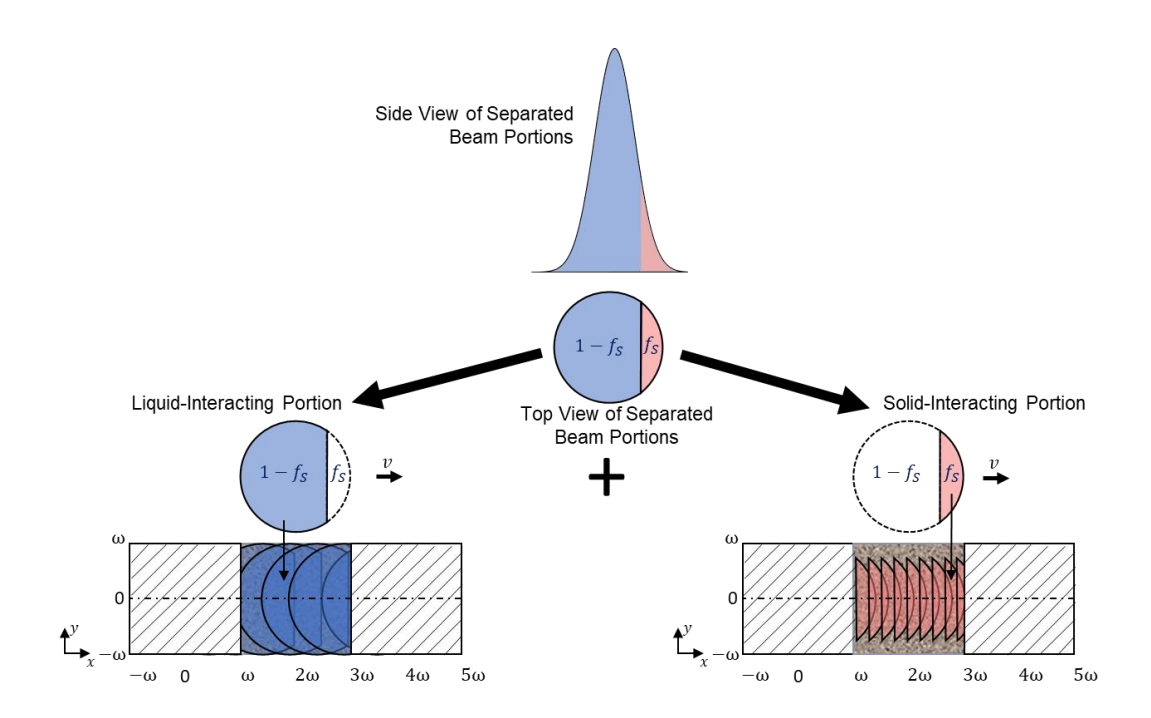


**Figure 15**: Solid- and liquid-interacting beam components of the laser, applied mathematically via the Heaviside function. The energy delivered from the entire beam is the sum of both components, acting volumetrically within each medium's absorption depth. The ROI used here is the same as in Figure 13 and Figure 14, and the area fraction interacting with the solid,  $f_s$ , is defined in equation (48).

In addition to the laser energy portions, the melt requirements must also be defined for each medium. It is important to note that the *delivered* energy from the laser was evaluated to guarantee a certain energy content to the absorption depth of the medium of interaction. Conversely, the energy sinks that comprise the melt requirements are evaluated for the entire powder volume. The premise here is that there needs to be sufficient energy deposited within the absorption depth to meet the basic melt requirements of the powder within the powder volume. These requirements at least

confine the associated parameters of laser power and speed to the dimensionality and material parameters of the powder system and allow for the development of material-specific process windows. For the solid-interacting region:

$$E_{solid} = \rho_s (cp_s (T_m - T_o) + \Delta H_m) (2\omega_\chi)^2 (l_p)$$

$$+ f_s \sigma_B B_p (T_m^4 - T_a^4) (2\omega_\chi)^2 \left(\frac{2\omega_\chi}{v}\right)$$
[J] (57)

Equation (57) is composed of two terms; the first being the sensible heat and latent heat of fusion for the solid material, multiplied by the ROI volume. The second is the radiative loss at the top surface which is combined with the product of the top surface total area, the fraction of solid-interaction, and the laser interaction time for the ROI. The liquid-interacting region, contains an additional term:

$$E_{liquid} = \rho_{L} \left( cp_{L} (T_{b} - T_{m}) \right) \left( 2\omega_{\chi} \right)^{2} \left( l_{p} \right)$$

$$+ (1 - f_{s}) \left[ \sigma_{B} A_{L} (T_{b}^{4} - T_{a}^{4}) + \rho_{L} v_{a} \Delta H_{v} \right] \left( 2\omega_{\chi} \right)^{2} \left( \frac{2\omega_{\chi}}{v} \right)$$
[J] (58)

Here, the remaining beam fraction is multiplied into the areal term, which is composed of both radiative and evaporative losses. Also, the upper temperature limit of the system is assumed to be the liquid's boiling temperature. This is a starting approximation that can also be modified in the future. The ablation velocity,  $v_a$ , is determined via the Hertz-Knudsen

equation that is referenced in the literature [62,79,86]. It is given below for a surface at an arbitrary temperature,  $T_s$ :

$$v_{a} = \frac{p_{o} \exp\left(-\left(\frac{Ma\Delta H_{v}}{R}\right)\left(\frac{1}{T_{s}} - \frac{1}{T_{b}}\right)\right)}{\rho_{L}\sqrt{\frac{2\pi RT_{s}}{Ma}}} \qquad \left[\frac{m}{s}\right] \quad (59)$$

where  $p_o$  is the ambient pressure, Ma is the molar mass of the ablated product, and R is the gas constant. For this model, the assumed surface temperature is equal to the boiling point of the material, which significantly simplifies the numerator of equation (59). It should be emphasized that the melt requirements in equations (57) and (58) are by no means exhaustive and can be modified with additional energy sinks such as convective losses to the surroundings, ablation above the material boiling point, and conduction to the laser bed to further refine the model in the future.

Equating the sum of (55) and (56) to the sum of (57) and (58) and isolating for laser power provides the main governing equation for the process window:

$$P = \frac{\left(E_{solid} + E_{liquid}\right)v}{\left(\left(B_p - A_L\right)\operatorname{erf}\left(\frac{\sqrt{\chi}(v\tau_s - \omega_\chi)}{\omega_\chi}\right) + B_p + A_L\right)(1 - e^{-1})\operatorname{erf}(\sqrt{\chi})\omega_\chi}$$
 [W] (60)

The above equation produces recommended power values to corresponding speed values for a given material system. The methodology

to arrive at this point assumes sufficient energy is delivered to a representative volume of powder within the time scale of one laser pass, to fully melt to the bottom of the powder layer. Although there were many assumptions made regarding dimensions, beam profile, and surface temperature, the process windows that can be developed using this method will be shown to be material system-dependent and have use for a first order approximation to laser parameter selection.

#### 3.1.3.3 Process Windows

The objective of the semi-analytical model is to create material-specific process windows for the laser power and speed, to act as a guide for initial additive manufacturing endeavours in a relatively uncharacterized material system. The material process window was created by evaluating equation (60) at parameterized values of laser speed, v. The speed variable was cycled from the lowest to the highest achievable speeds for the AM system in use. In this case, these values were between 0.05 to 7 m/s for the EOSINT M280 system. For reference, this system also has a laser power upper limit of 400W. Since equation (60) contains the variable  $f_s$  defined by equation (48), it contains a dependency on a square root term that can produce imaginary values depending on the selected value of laser speed. Thus, the window is created by only taking the corresponding speeds that produce real values of power within the evaluation limits. Figure 16 displays

the calculated process windows using the semi-analytical model for two vastly different material systems; bismuth telluride and Ti6Al4V.

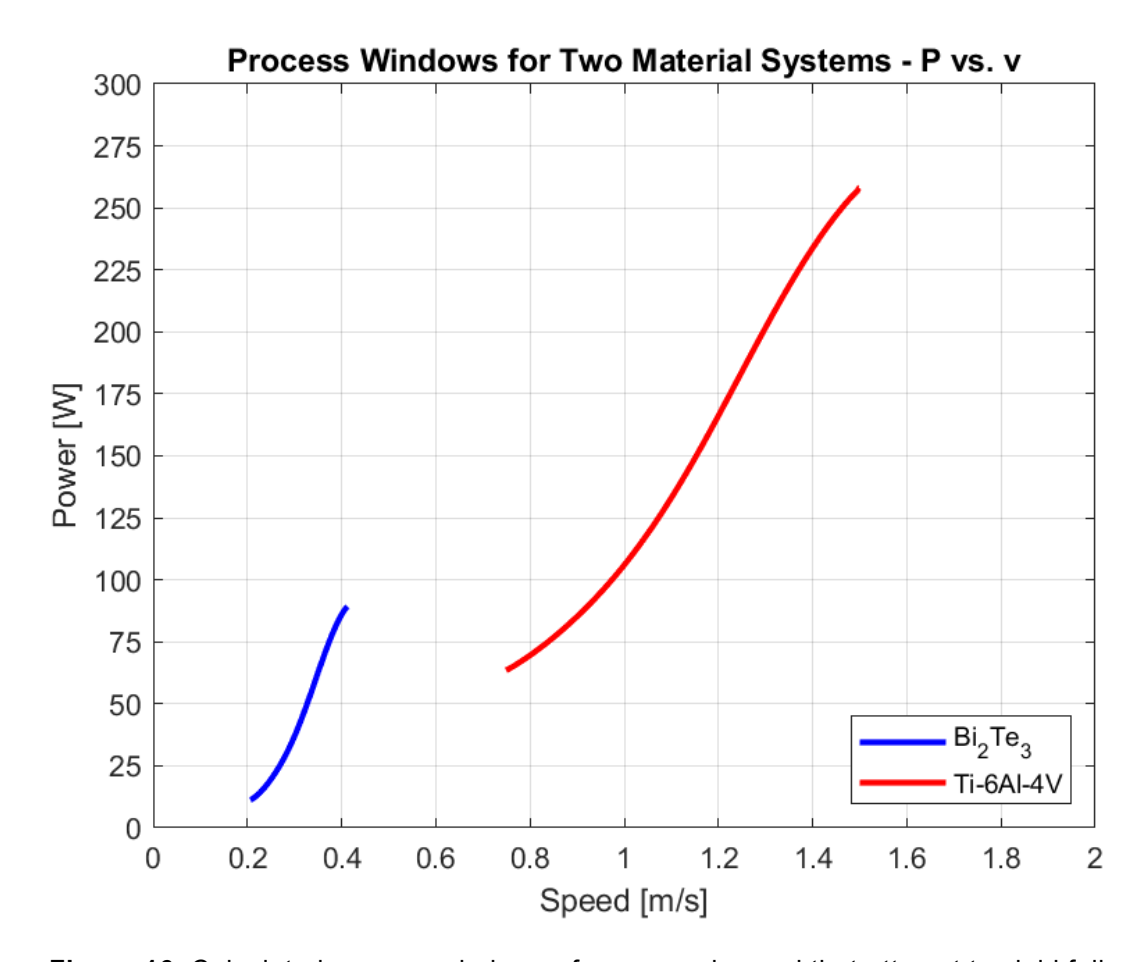


**Figure 16**: Calculated process windows of power and speed that attempt to yield full melting to the bottom of a powder depth, and to the width of one laser diameter. Calculations performed for bismuth telluride and for Ti6Al4V alloy.

Taking the optical, thermal, and dimensional properties of each system into account, the semi-analytical model was able to produce two distinctly different domains for speed and ranges for laser power. The properties for bismuth telluride were those determined in section 3.1.1, for a powder depth,  $l_p$ , of 76 $\mu$ m and are summarized again in Table 4. They represent

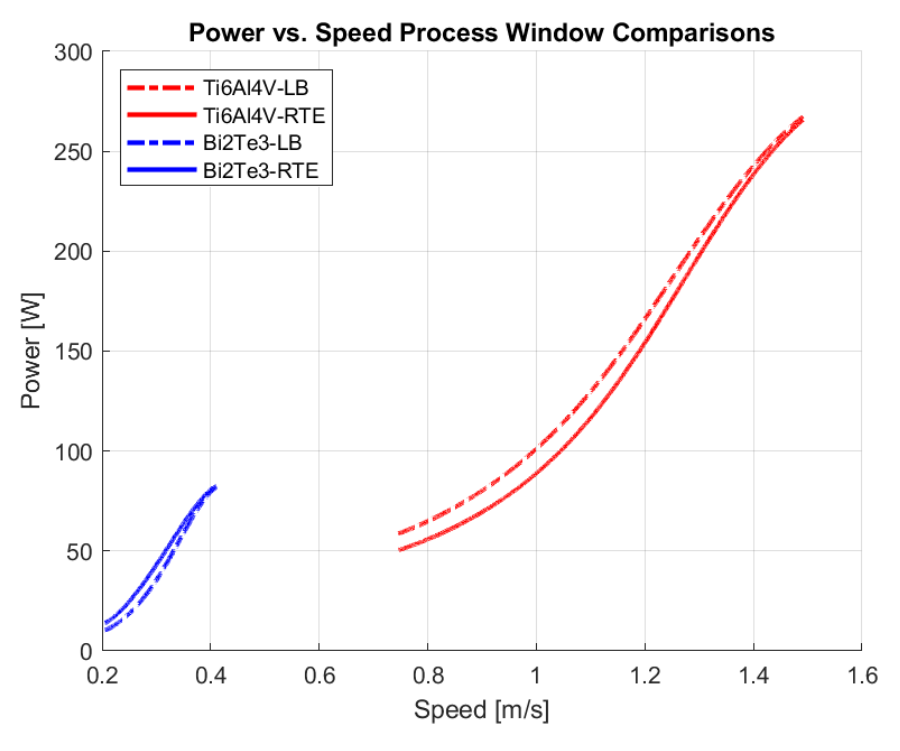
the alloy used experimentally as best as possible. The properties used for Ti6Al4V were taken from literature for a powder depth of 30µm [87], with the particle size distribution from [88] analyzed in ImageJ and used to estimate the powder absorption coefficient and the powder absorptivity. These windows can change based on material system, powder thickness, particle size distribution, particle shape, presence of surfactants, laser wavelength, and other experimental factors.

Bi <sub>2</sub> Te <sub>3</sub>				
Property	Value	Reference		
β	3.36·10 <sup>5</sup> [m <sup>-1</sup> ]	Calculated in section 3.1.1.1.1 with $PF_p = 0.41$ and $d_{eq} = 3.10E-6$ from the experimental powder distribution in Figure 24.		
$R_b$	0.72	Calculated using equation (26) with room temperature $n$ and $k$ values at 1080nm from [81]		
$B_p$	0.77	Calculated in section 3.1.1.1.2		
$A_L$	0.50	Calculated in section 3.1.1.1.3		
$ ho_s$	7.64 x10³ [kg/m³]	Temperature averaged from [70]		
$cp_s$	172 [J/(kg·K)]	Temperature averaged from [82]		
$T_m$	858 [K]	[42]		
$\Delta H_m$	1.51 x10 <sup>5</sup> [J/kg]	[42]		
$ ho_L$	7.09 x10 <sup>3</sup> [kg/m <sup>3</sup> ]	Temperature averaged from [70]		
$cp_L$	407 [J/(kg·K)]	Temperature averaged from [82]		
$T_b$	1.35 x10 <sup>3</sup> [K]	Effectively approximated from [78]		
$T_o$	473.15 [K]	Assumed base plate temperature		
$l_p$	76 [µm]	Used experimentally		
$\Delta H_v$	4.37 x10 <sup>6</sup> [J/kg]	Calculated in section 3.1.1.2.3		

**Table 4**: Collected properties of bismuth telluride used to generate its process window.

As mentioned the previous section, this model uses a hybridized approach to solving the energy balance in that the portion of the beam that interacts with the powder is mathematically treated with the Lambert-Beer law whilst using an absorption coefficient and an effective absorptivity that were derived from the RTE. It was assumed that this could keep the process

window equations more compact and that the predicted parameters would be similar between the methods. To quantify this, the model was evaluated twice; once with the effective Lambert-Beer approximation for the solid-interacting beam, and then with the solution to the Radiative Transfer Equation for the aforementioned beam portion. The liquid-interacting beam was treated with the Lambert-Beer model in both cases, as the dominant mechanism that necessitated the use of the RTE, scattering, was not considered when interacting with the liquid. The comparison between the models for both the bismuth telluride and Ti6Al4V material systems is provided in Figure 17.



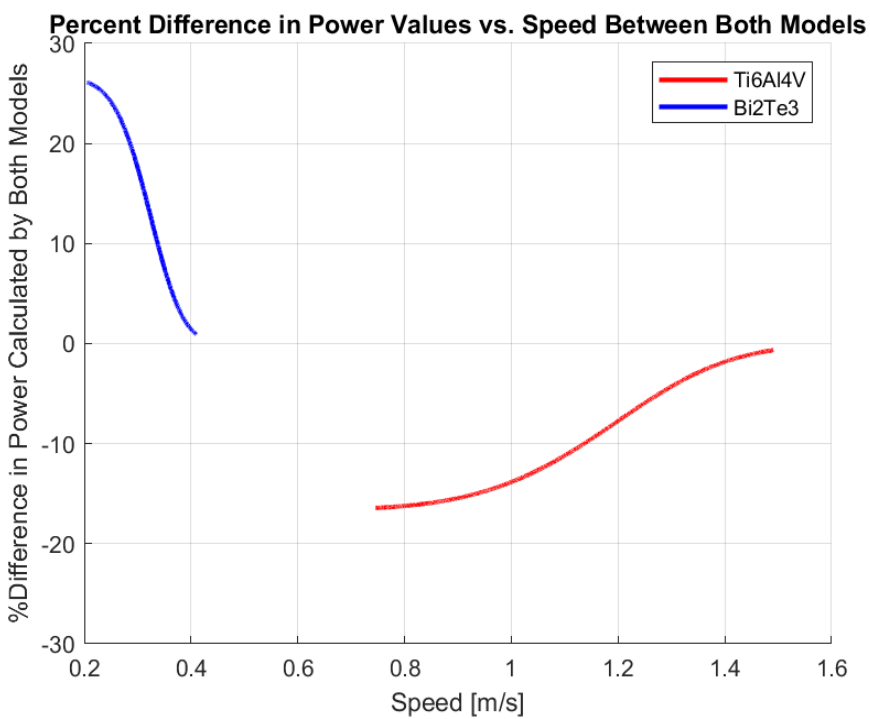


**Figure 17**: *(Top)* Comparison between the Lambert-Beer (LB) and the Radiative Transfer Equation (RTE) methods for treating the powder-interacting portion of the beam. *(Bottom)* Percent difference between the calculated laser power values obtained by both of the aforementioned methods.

The above comparison shows the difference in predicted laser power for the same speed using both models. The maximum deviation was calculated as 26% and occurred in the Bi2Te3 system. As speed increased within each process window, the percent deviation approached less than 1% for both materials. This overall low deviation between the models, observed for two vastly different material systems, supports the effort to use the hybridized Lambert-Beer approximation with RTE-derived absorption parameters.

## 4. Experimental Method

#### 4.1 Custom Powder Delivery System

Thermoelectric p-type (Bi<sub>0.15</sub>Sb<sub>0.85</sub>)<sub>2</sub>Te<sub>3</sub> and n-type Bi<sub>2</sub>(Se<sub>0.17</sub>Te<sub>0.83</sub>)<sub>3</sub> bulk structures were produced from the melting of powder layers using an EOSINT M280 SLM machine. The ternary alloy powders were first wet sieved in acetone using a pore diameter of 70µm to limit the maximum particle size. The powder-acetone slurry was kept in individual containers to be removed and applied to the build plate via a syringe.

A custom build plate assembly was implemented in order to repeatedly apply limited amounts of powder to the same area for multiple layer processing. This assembly is given in Figure 18.

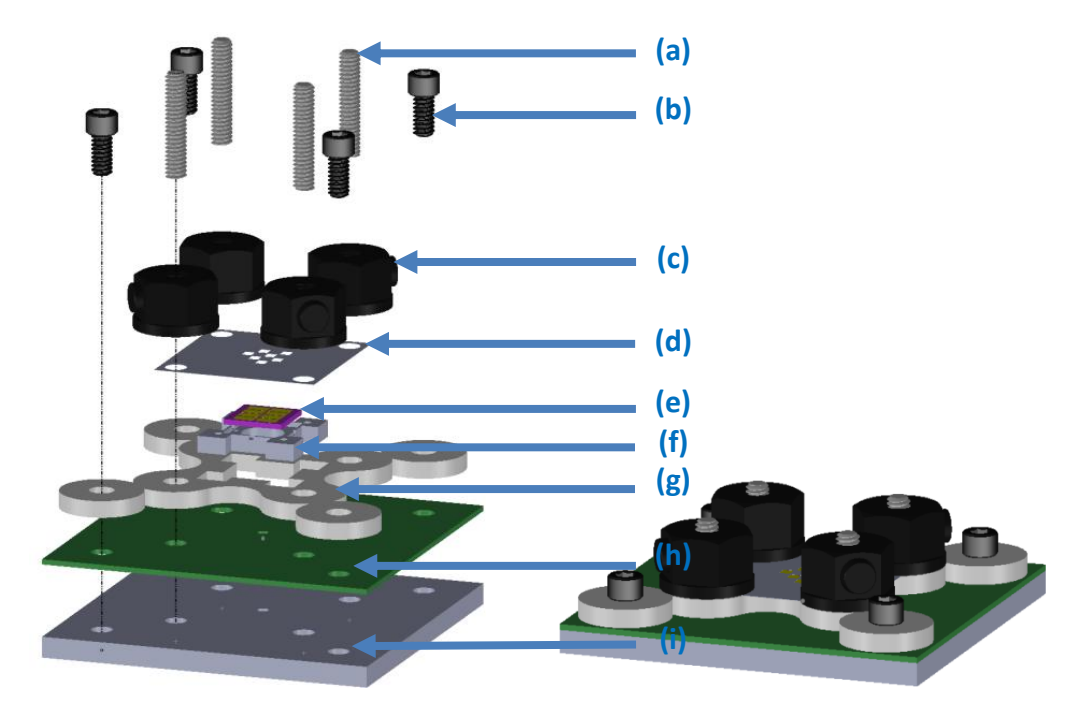
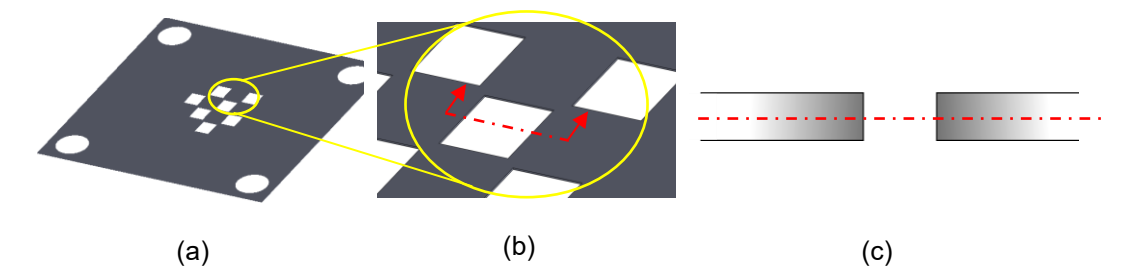


Figure 18: Left: Exploded assembly of the custom build plate insert. (a) Mask guide threaded rods. (b) Fastening screws. (c) Quick release nuts to allow for the immediate addition of subsequent masks. (d) 76μm stainless steel mask to allow powder to sit within its exposed areas. (e) Metallized substrate upon which powder will be melted. (f) Substrate holder. (g) Sample-centering jig piece. (h) Milled double-sided PCB used for machining guide holes that contains thermal vias and offers a flat surface for the substrate to be set upon. (i) Aluminum base plate. *Right:* Isometric view of assembled build plate insert.

Multiple layers of powder were able to be deposited at relatively constant thicknesses with the help of the stainless steel masks (Figure 18(e)). The amount of powder melted after each laser exposure is dictated by the mask thickness. The mask with its exposed regions is highlighted in Figure 19 with an illustrated view of its cross section.



**Figure 19**: (a) Stainless steel mask of thickness 76μm from Figure 18(e). (b) Magnified view of mask regions that receive powder, with sample cross section selected in red. (c) Simplified cross section of a single mask region introduced in (b). The corresponding red line indicates the cut view from (b).

The powder deposition and melting processes are shown in Figure 20. After the insertion of the substrate, a stainless steel mask of thickness 76µm was placed over it. The powder slurry was applied via a syringe and the excess was scraped off with a razor blade. Once the areas of interest were covered with a uniform layer of powder, the print chamber was sealed and purged with N<sub>2</sub> gas at roughly 1 atm until less than one percent of oxygen was detected in the environment. The print bed was also brought to a temperature of 150°C through its internal heater. The laser was then scanned over the areas of interest with a specific power, speed and hatch spacing. After the powder was melted, the excess powder was wiped from the areas of interest. The consolidated powder regions were roughly half the thickness in the z-direction than they were before melting. Thus before adding a second mask, powder was deposited onto these regions once more and levelled using a razor blade. The refilled regions were again scanned with the same power and speed but with a perpendicular hatch

direction than that used previously to reduce internal stresses between subsequent layers.

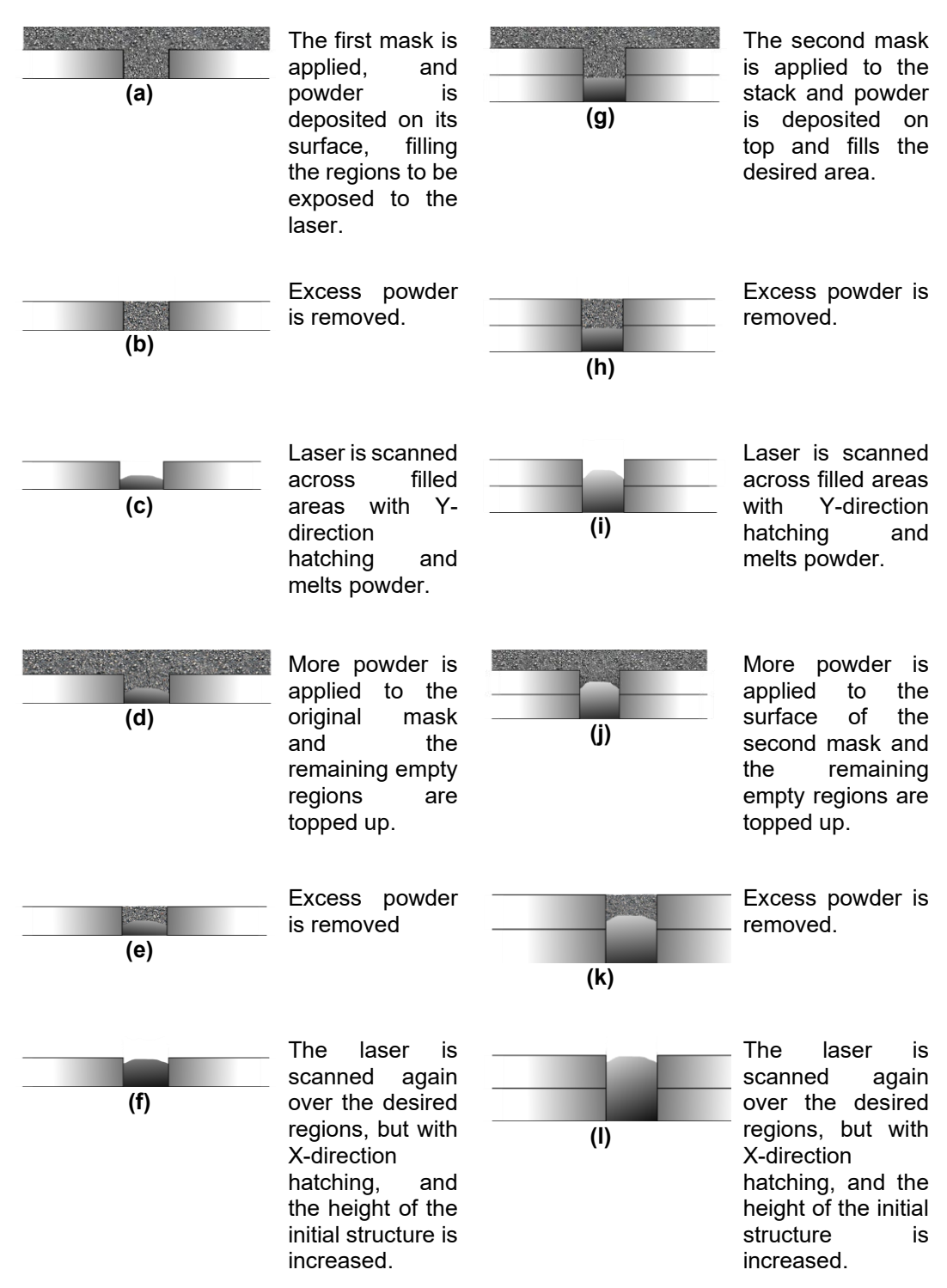


**Figure 20**: Powder deposition and growth processes of the additive manufacturing of TEGs. Two layers of deposition are shown, and this process is repeated with up to four masks.

After the laser has scanned and melted the powder, the area was wiped and a second mask was added. This process was repeated until four masks were used. Images of a single layer deposition process are given below, followed by the finished product after four mask layers were deposited.

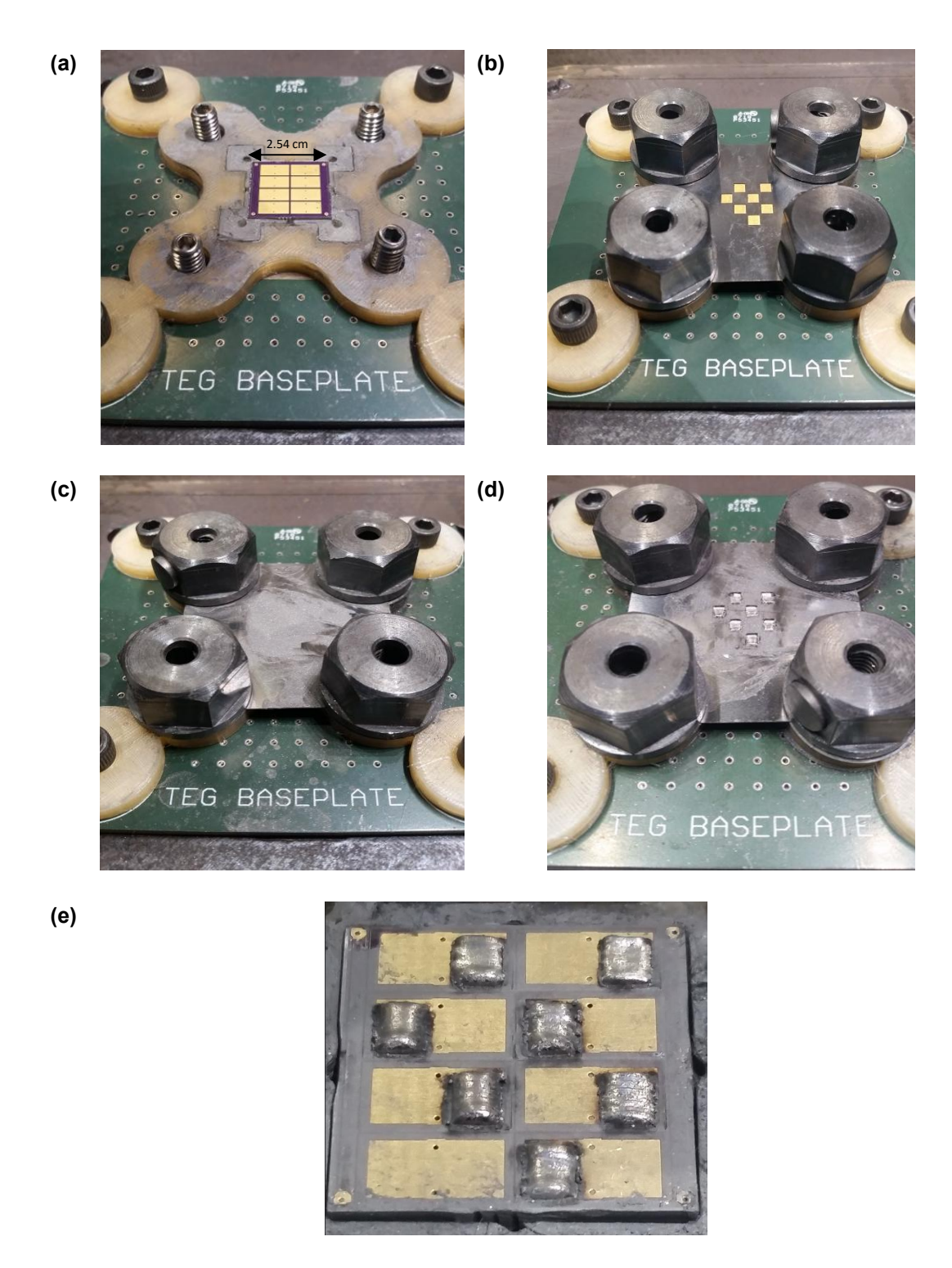


**Figure 21**: (a) Insertion of the PCB substrate into the TEG manufacturing assembly. (b) Application of the mask to the substrate. (c) Deposition of a single powder layer

on top of the mask. (d) Resolidified regions of the single powder layer after additive manufacturing. (e) Resolidified powder on substrate with mask removed.

#### 4.2 Morphology

## 4.2.1 Scanning Electron Microscopy (SEM)

The powder morphology was initially observed using scanning electron microscopy in order to gain an understanding of the powder grain sizes and deviation from conventionally spherical, AM powders. Images were taken of both the p-type and n-type powder samples on the JEOL-7000F Scanning Electron Microscope. The accelerating voltage was 15 kV and working distance of 10 mm.

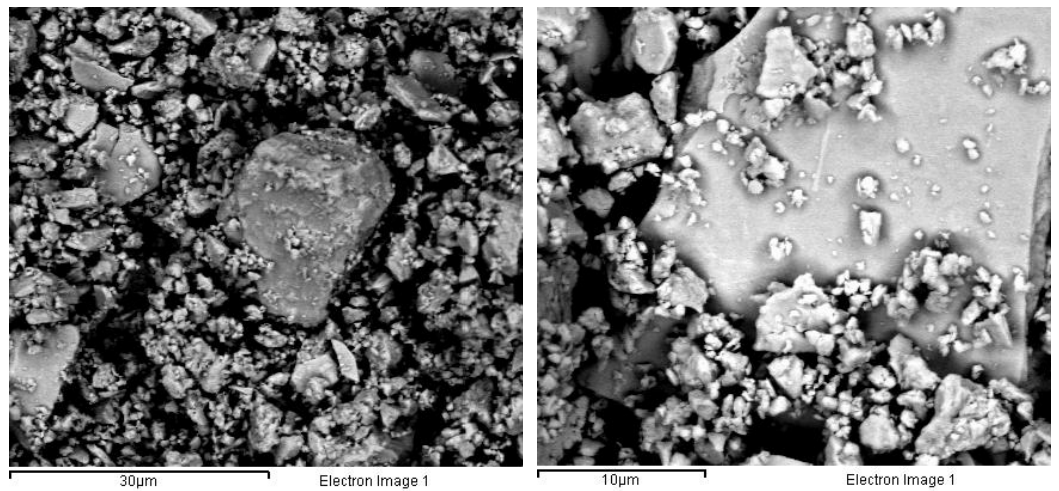


Figure 22: SEM images of (Left) p-type  $(Bi_{0.15}Sb_{0.85})_2Te_3$  and (Right) n-type  $Bi_2(Se_{0.17}Te_{0.83})_3$ .

# 4.2.2 Transmission Electron Microscopy (TEM)

TEM was performed to determine the presence of any amorphous phases that would be consistent with the presence of oxides [89]. Oxides

were contemplated to be of importance if their thickness was on the order of the wavelength of the laser light. This would mean that their contribution to scattering and attenuation would be significant as they would enter the regime of geometrical optics and would cause errors in the modeling of the light coupling into the powder. From the literature, oxides typically found on the surface of bulk bismuth telluride alloys occur in thicknesses of a few nm [89]. Thus, the confirmation of this thickness would allow for the neglection of the surface oxides in the optical portion of the laser-material model since the laser wavelength is 1080nm.

Individual powder grains were observed using the JEOL 2010F transmission electron microscope. The powder was separated in an ultrasonic bath of isopropanol and placed onto a copper grid. The accelerating voltage was 200 kV. The images were then analyzed with ImageJ software.

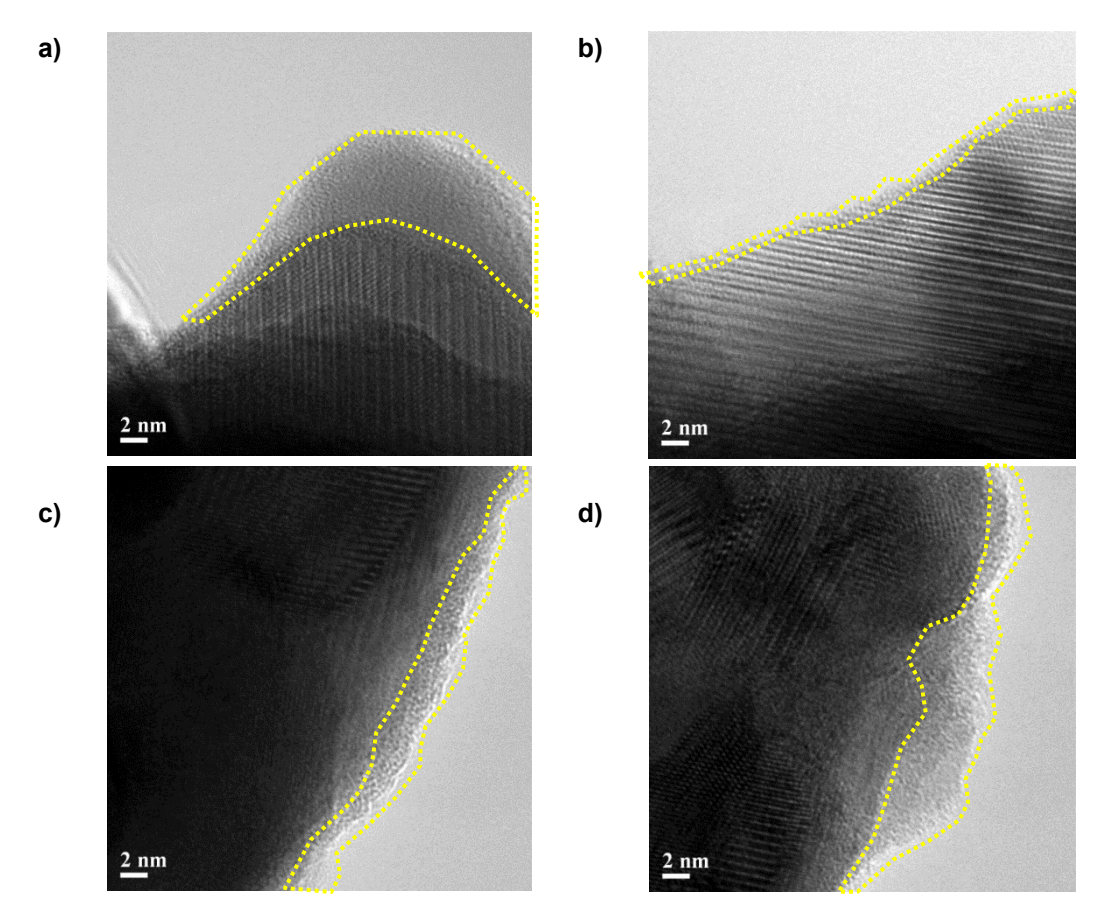


**Figure 23**: Images of (a)-(b) n-type and (c)-(d) p-type grains. Amorphous regions consistent with oxide growth are outlined in the dotted yellow lines.

As observed above, the native oxide thickness on both the p-type and n-type powders was within the range of 2-10nm therefore it is not expected to significantly affect the predicted laser process parameters.

## 4.2.3 Particle Size Analysis

The powder morphology was measured with a Mastersizer 3000 Particle Size Analyzer. It was suspended in liquid and measured before and after sieving with a 70  $\mu$ m pore size to attempt to remove particles that were larger than the powder layer thickness of 76  $\mu$ m. The volume percentages

assume contributions from particles of equivalent spherical volume to those that are irregularly shaped as outlined in [90]. The total volume is the sum volume of all particles observed, with the binned volume fractions according to diameter. This sample data is for the p-type (Bi<sub>0.15</sub>Sb<sub>0.85</sub>)<sub>2</sub>Te<sub>3</sub>.

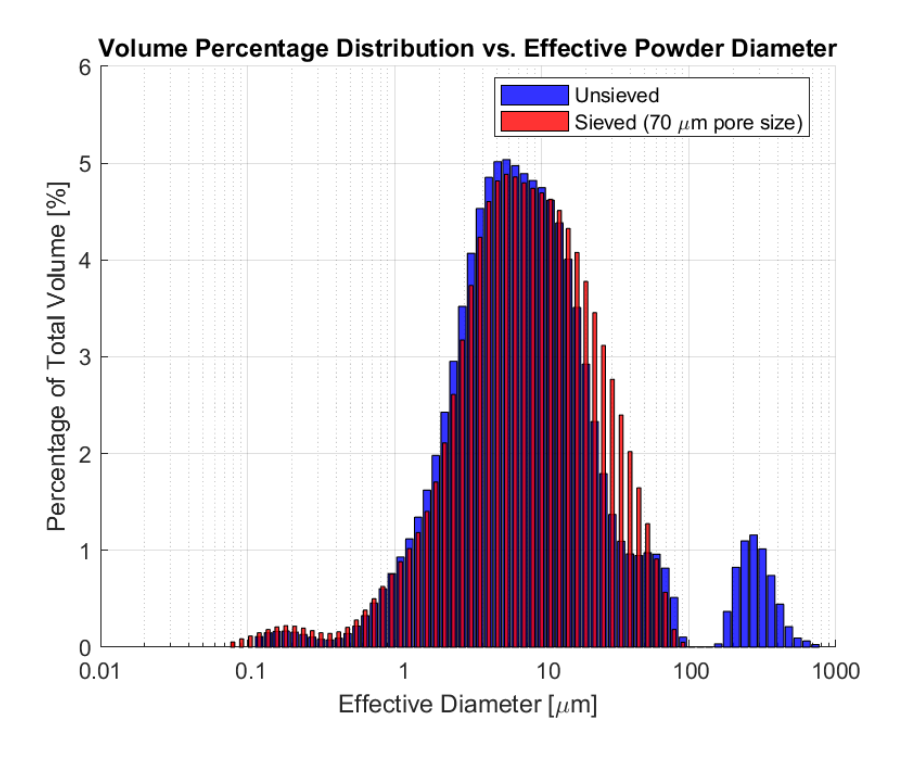


**Figure 24**: Powder particle diameter distribution according to percentage total volume of the observed sample.

# 4.3 Composition

### 4.3.1 X-Ray Diffraction (XRD)

The stoichiometry of the powders was first compared to a reference standard via XRD phase analysis using a Bruker SMART6000 CCD on a Bruker 3-circle D8 goniometer with a Rigaku RU-200 rotating anode x-ray

generator and parallel focusing optics. The powder patterns were taken to understand the initial stoichiometry of the powders before melting. These patterns were compared to those in literature with reference peak positions that best aligned with the experimental peaks. No cell refinement was performed, but the general peak positions corresponded best to the reference p-type and n-type powders that were taken from the literature.

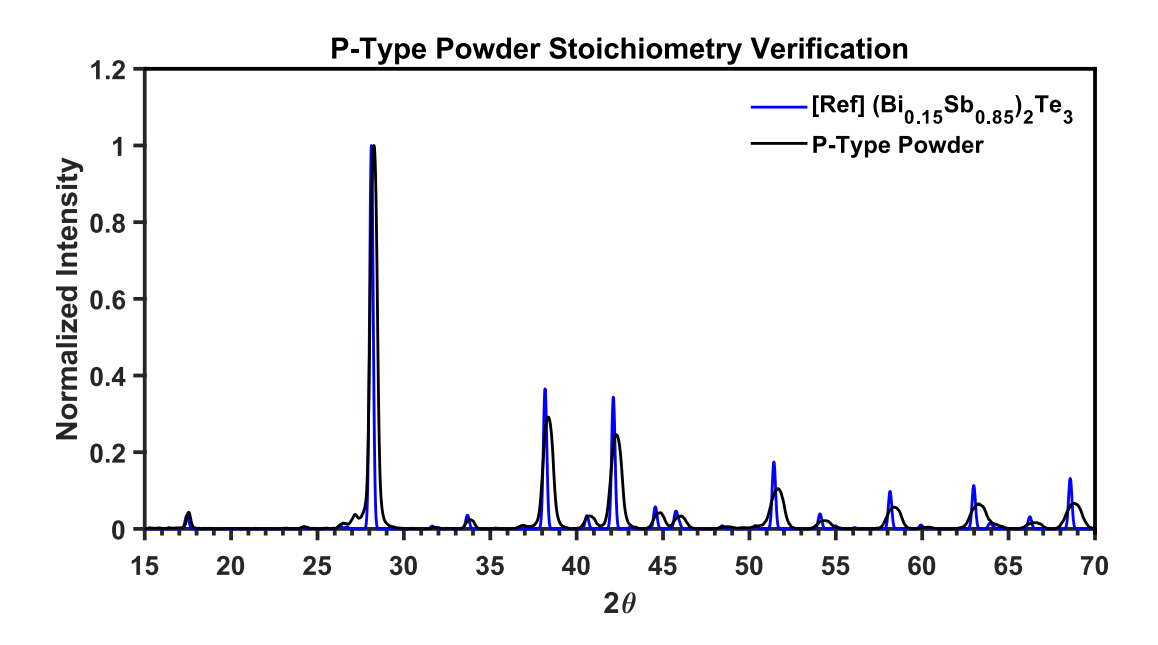
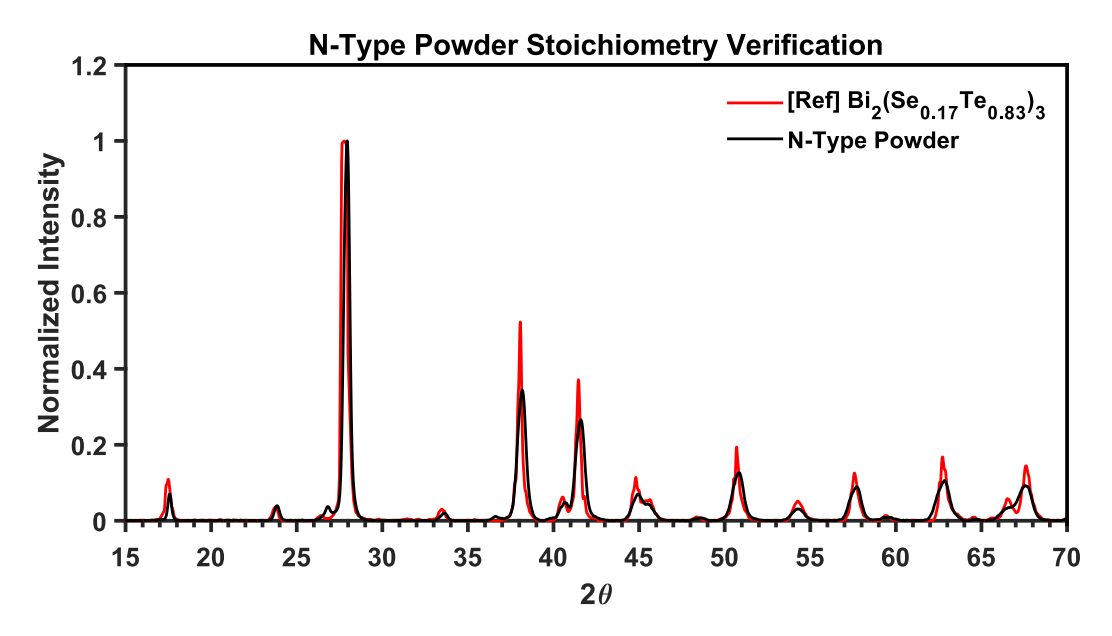


Figure 25: XRD powder pattern of (Bi<sub>0.15</sub>Sb<sub>0.85</sub>)<sub>2</sub>Te<sub>3</sub> for unmelted powder compared to reference [91].



**Figure 26:** XRD powder pattern of Bi<sub>2</sub>(Se<sub>0.17</sub>Te<sub>0.83</sub>)<sub>3</sub> for unmelted powder compared to reference [92].

As observed in the above figures, the experimental powder plot for the n-type material aligns better with its reference than the p-type. Therefore, the n-type is stoichiometry is most likely correct whereas the p-type may have slightly different proportions of bismuth and antimony due to the small offset in peak positions.

## 4.4 Thermal Properties

## 4.4.1 Differential Scanning Calorimetry (DSC)

Differential scanning calorimetry was performed on the p-type and n-type powders using the TGA/DSC 3+ LF/1100/537 by Metter Toledo with an Argon gas flow rate of 70ml/min to determine the enthalpy of melting. The latent heat of melting is an important parameter for the consideration of the laser parameters required for melting. A temperature ramp of 20

K/min was applied to bring the samples from ambient temperature up to 1000 K. The powder samples were weighed and put into 70  $\mu$ L alumina sample holders that were also weighed and initially measured for a baseline measurement. The mass of the p-type powder used was 128.42 mg and the n-type mass was 63.81 mg. The heat flow vs. time profiles were taken for each sample, and the baseline subtracted to yield the enthalpy vs temperature and enthalpy vs. time curves. Integrals of the melt peaks and data analysis were performed in Origin. Figure 27 and Figure 28 show the enthalpy valleys that correspond to the latent heat of melting in each material. The calculation of the latent heats of melting for each alloy system is given in Table 5.

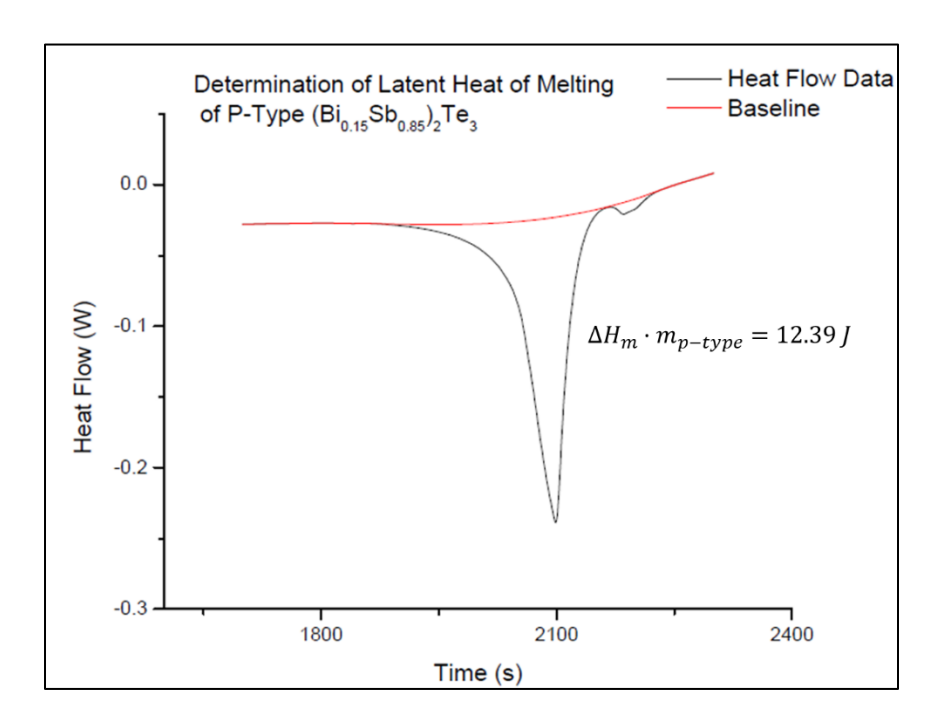


**Figure 27:** DSC of p-type  $(Bi_{0.15}Sb_{0.85})_2Te_3$  for the determination of  $\Delta H_m$ .

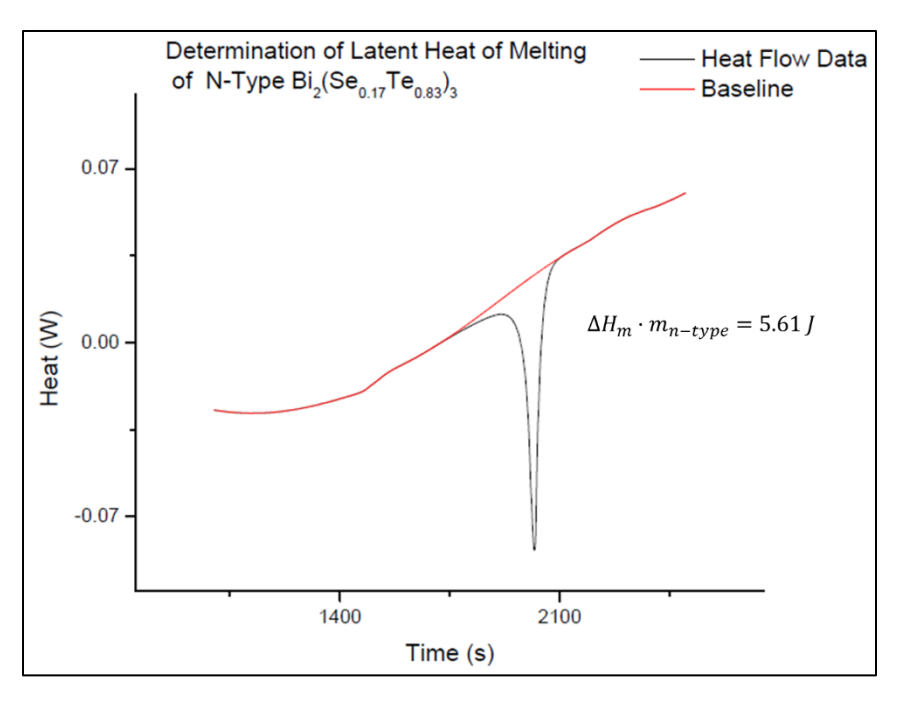


Figure 28: DSC of n-type  $Bi_2(Se_{0.17}Te_{0.83})_3$  for the determination of  $\Delta H_m$ .

Mass, Energy and Latent Heat of Melting for p-type and n-type Alloys				
	<i>m</i> [kg]	$\Delta H_m \cdot m$ [J]	$\Delta H_m$ [J/kg]	
p-type	1.284218·10 <sup>-4</sup>	12.39	9.65 x10 <sup>4</sup>	
n-type	6.38068 ·10 <sup>-5</sup>	5.61	8.79 x10 <sup>4</sup>	

**Table 5:** Experimentally determined mass, energy and latent heat of melting for ptype and n-type alloys.

## 5. Results

## 5.1 Composition

Next to the ability to simply melt and adhere these alloys to a substrate, the composition of the created structures is the most important property. If the stoichiometry of the powder is altered during the melt process, the material is expected to no longer have the thermoelectric properties of its bulk form and therefore may not perform adequately. A change in stoichiometry is possible and could come from loss of one of the elemental constituents of the materials due to evaporation during the laser heating process. A good indicator of which material will steadily evaporate first is the consideration of the vapor pressures of these containing elements. As the alloys studied are the p-type (Bi<sub>0.15</sub>Sb<sub>0.85</sub>)<sub>2</sub>Te<sub>3</sub> and the n-type Bi<sub>2</sub>(Se<sub>0.17</sub>Te<sub>0.83</sub>)<sub>3</sub>, it is useful to look at the vapor pressures of Bi, Sb, Se and Te as given in Figure 29.

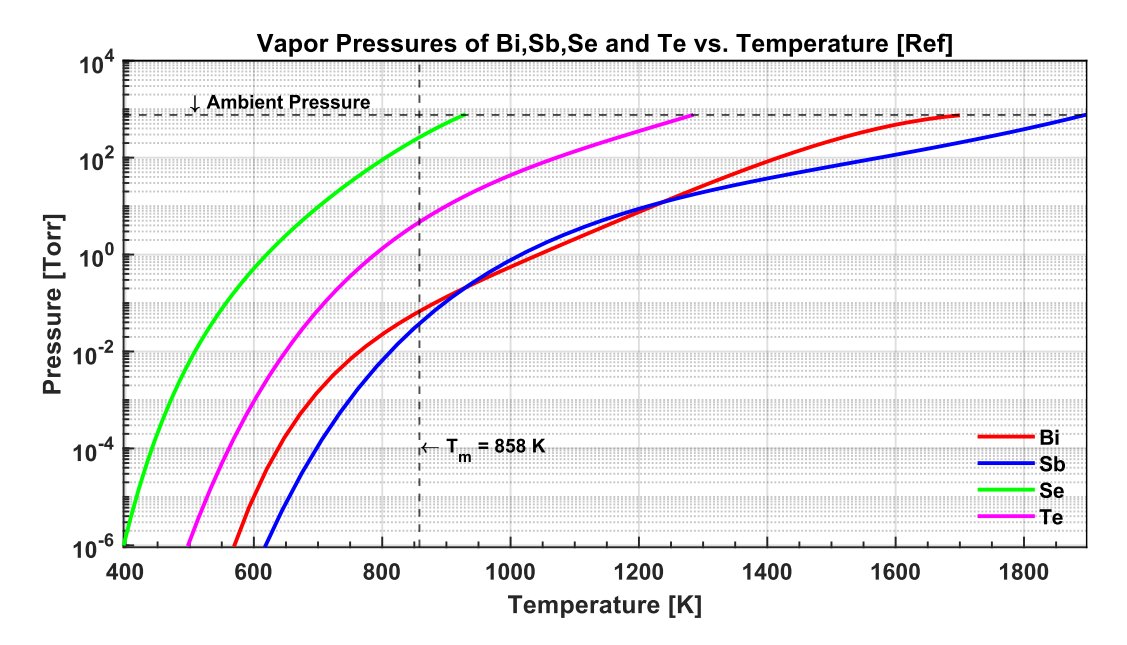


**Figure 29:** Vapor pressures of Bi, Sb, Se and Te vs. Temperature taken from [93]. Ambient pressure and the melt temperature are denoted as horizontal and vertical lines, respectively.

The consideration of the individual elemental vapor pressures deviates from the model assumption that each alloy has an effective boiling temperature and enthalpy of vaporization wherein all the elements evaporate stoichiometrically. This assumption was made for simplicity to make a first order approximation of the processing parameters. However, it is important to state that the operating pressure during the SLM process was kept at ambient and based on the plots in Figure 29, it is likely that material loss in the p-type Bi-Sb-Te system due to evaporation could be mainly attributed to loss of Te since it begins to steadily evaporate at a lower temperature. Likewise, it is assumed the n-type Bi-Se-Te alloy could see a decrease in its Se content.

#### 5.1.1 Energy Dispersive Spectroscopy (EDS)

EDS measurements were performed as a qualitative check on the two alloys that were processed with different powers and speeds, using parameters that were directly taken from use with other metallic powders such as Ti6Al4V. This was simply an observation of the effects of using unmodeled parameters for an initial test. The atomic percent of the constituent elements of each alloy are given in the tables below. The results provide the absolute atomic fraction of each element as well as the ratio of the assumed readily-evaporative element to the more stable ones.

P-Type Atomic Percentages from EDS for P-Type (Bi <sub>0.15</sub> Sb <sub>0.85</sub> ) <sub>2</sub> Te <sub>3</sub>								
Power [W]	Speed [m/s]	Linear Energy Density [J/m]	Bi atomic fraction	Sb atomic fraction	Te atomic fraction	Te: (Bi +Sb)		
powder		0	0.06	0.34	0.60	1.50		
50	2.5	20	0.05	0.40	0.55	1.22		
250	2.5	100	0.11	0.38	0.51	1.04		
250	1.5	166.67	0.11	0.46	0.43	0.75		

**Table 6:** Atomic fractions of the constituent atoms of resolidified (Bi<sub>0.15</sub>Sb<sub>0.85</sub>)<sub>2</sub>Te<sub>3</sub> at different powers and speeds obtained using EDS.

N-Type Atomic Percentages from EDS for N-Type Bi <sub>2</sub> (Se <sub>0.17</sub> Te <sub>0.83</sub> ) <sub>3</sub>								
Power [W]	Speed [m/s]	Linear Energy Density [J/m]	Bi atomic fraction	Se atomic fraction	Te atomic fraction	Se: (Bi+Te)		
None		0	0.40	0.10	0.50	0.11		
50	2.5	20	0.38	0.07	0.55	0.08		

**Table 7:** Atomic fractions of the constituent atoms of resolidified Bi<sub>2</sub>(Se<sub>0.17</sub>Te<sub>0.83</sub>)<sub>3</sub> at different powers and speeds obtained using EDS.

The linear energy density is simply obtained by dividing the power by the speed and allows both parameters to be combined. Based on the information given above, the ratio of Te to the Bi and Sb is seen to decrease in the p-type alloy with increasing energy density. Similarly for the n-type data, the same trend is observed for the Se content with respect to Bi and Te, although more datapoints should be taken to confirm this.

## 5.1.2 X-Ray Diffraction (XRD)

The following XRD results for the p-type and n-type materials are collected for only the power and speed combinations that yielded multilayer-built samples. These are 17W, 0.071m/s and 18W,0.075m/s in the p-type alloy and 16W,0.067m/s, 17W,0.071m/s and 18W,0.075m/s for the n-type alloy.

#### 5.1.2.1 P-Type Results

The p-type alloy, (Bi<sub>0.15</sub>Sb<sub>0.85</sub>)<sub>2</sub>Te<sub>3</sub>, exists in the functional chemical formula of (Bi<sub>x</sub>Sb<sub>1-x</sub>)<sub>2</sub>Te<sub>3</sub>. Below is a collection of literature data showing the transition from pure Bi<sub>2</sub>Te<sub>3</sub> to Sb<sub>2</sub>Te<sub>3</sub> by varying the ratios of bismuth and antimony while leaving the contribution of tellurium unchanged.

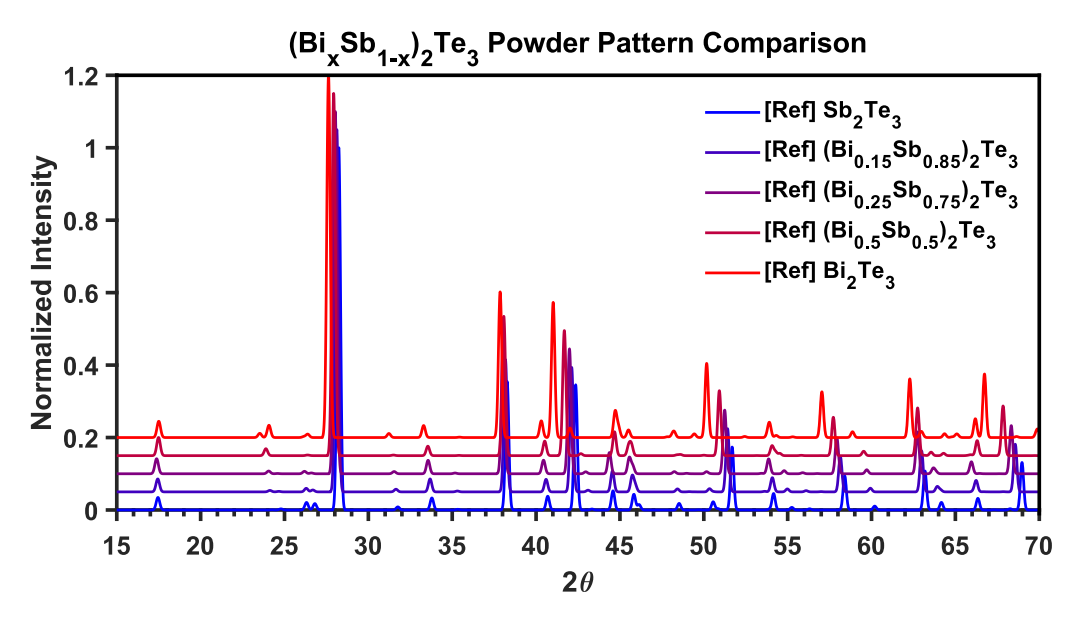
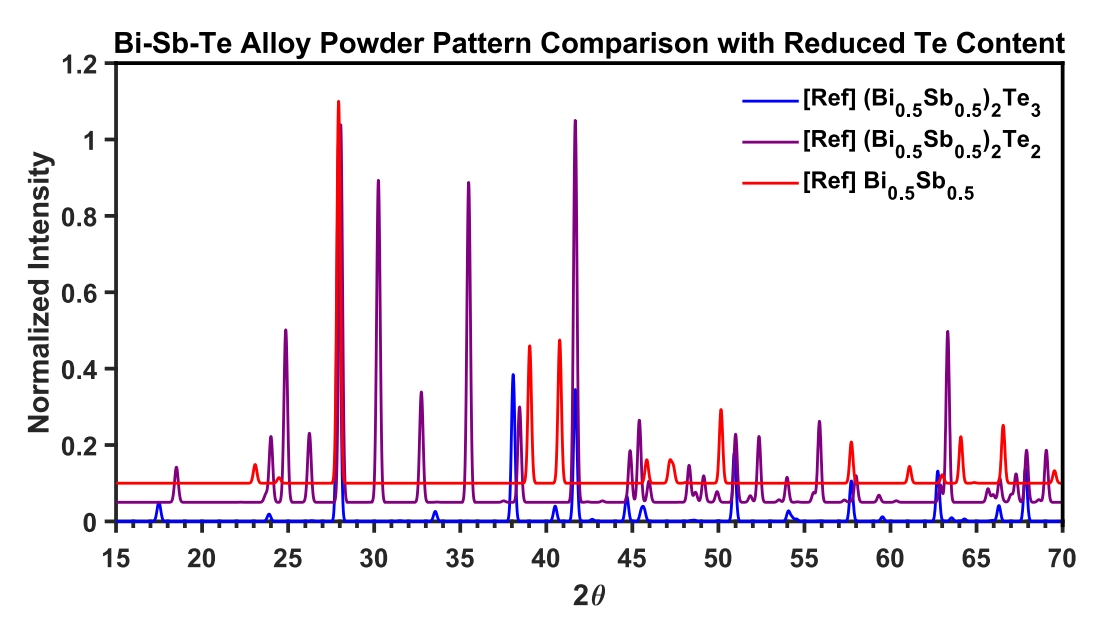


Figure 30: (Bi<sub>x</sub>Sb<sub>1-x</sub>)<sub>2</sub>Te<sub>3</sub> powder pattern comparison from literature data [91,94–96]

All the powder patterns in the above figure look relatively similar with regards to the number of peaks and their general locations. This indicates that as Sb is substituted for Bi and Bi<sub>2</sub>Te<sub>3</sub> transitions into Sb<sub>2</sub>Te<sub>3</sub>, there is not a significant effect on the crystal structure of the system. The pattern for (Bi<sub>0.5</sub>Sb<sub>0.5</sub>)<sub>2</sub>Te<sub>3</sub>, which is included in Figure 30, is plotted again in Figure 31 along with a pattern for (Bi<sub>0.5</sub>Sb<sub>0.5</sub>)<sub>2</sub>Te<sub>2</sub> which contains one less Te atom in its formula, and finally Bi<sub>0.5</sub>Sb<sub>0.5</sub> which is completely devoid of Te.



**Figure 31**: Bi-Sb-Te alloy powder pattern comparison from literature with reduced Te content [95,97].

It is important to note the differences in powder patterns for the  $(Bi_xSb_{1-x})_2Te_3$  alloy as it changes its Bi and Sb content versus a change in only the Te content as given by the differences in the above figures. This implies that altering the Te content will have much more radical consequences on the initial crystal structure. In fact, as noted in [95], the crystal structure of  $(Bi_{0.5}Sb_{0.5})_2Te_3$  is in the rhombohedral space group  $\overline{R} - 3m$  whereas the structure for  $(Bi_{0.5}Sb_{0.5})_2Te_2$  is of the primitive group  $\overline{P} - 3m$ .

Figure 32 depicts the powder patterns of the resolidified p-type material that was classified in Figure 25 as resembling the stoichiometry of (Bi<sub>0.15</sub>Sb<sub>0.85</sub>)<sub>2</sub>Te<sub>3</sub>. The pattern of the unmelted powder is provided there for reference as well. It is interesting to note that the powers and speeds used to melt the powder correspond to an almost identical linear energy density,

yet the powder melted at 18W seems to have more pronounced features corresponding with a reduction in Te. Therefore, it can be inferred that the power of the beam has a more significant effect on the temperature reached during the melt than the speed does.

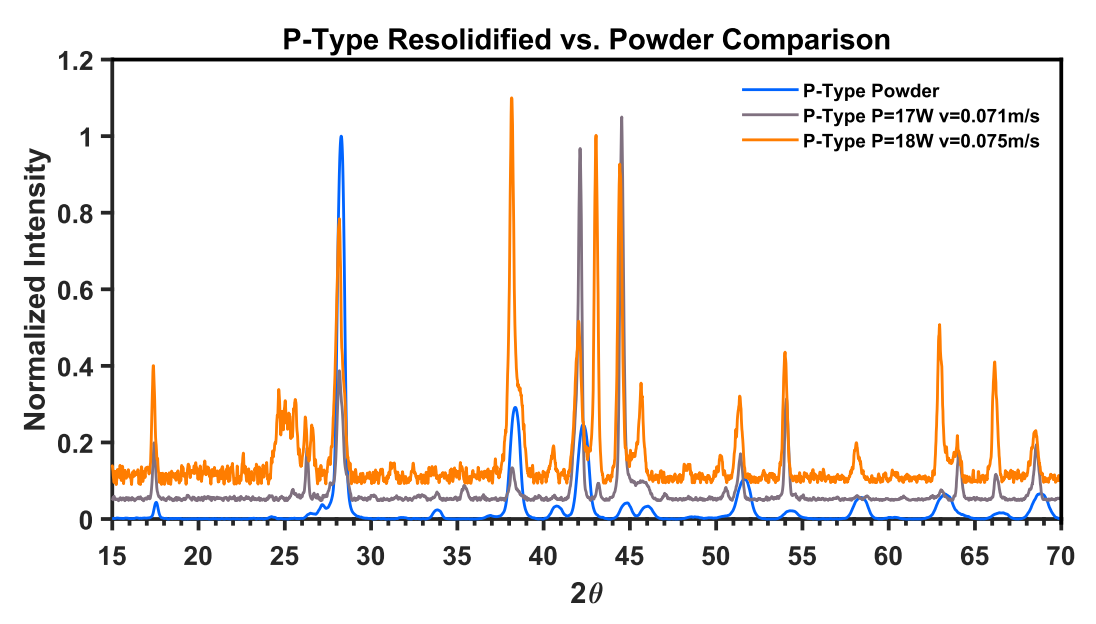


**Figure 32:** Powder patterns of resolidified p-type material at 17W, 0.071m/s and 18W, 0.075m/s overlaid with the pattern of the unmelted powder of stoichiometry (Bi<sub>0.15</sub>Sb<sub>0.85</sub>)<sub>2</sub>Te<sub>3</sub>.

Figure 33 combines the results of Figure 32 with the peak positions of the different alloys in Figure 31. The emergence of peaks between  $2\theta$  angles of 24 to  $26^{\circ}$  may be interpreted as a decrease in Te content upon melting and solidification, as observed by the reference peaks in the  $(Bi_{0.5}Sb_{0.5})_2Te_2$  system in that location. This along with the EDS data presented in the previous section for the p-type alloy melted at different powers and speeds are consistent with Te loss in this alloy system.

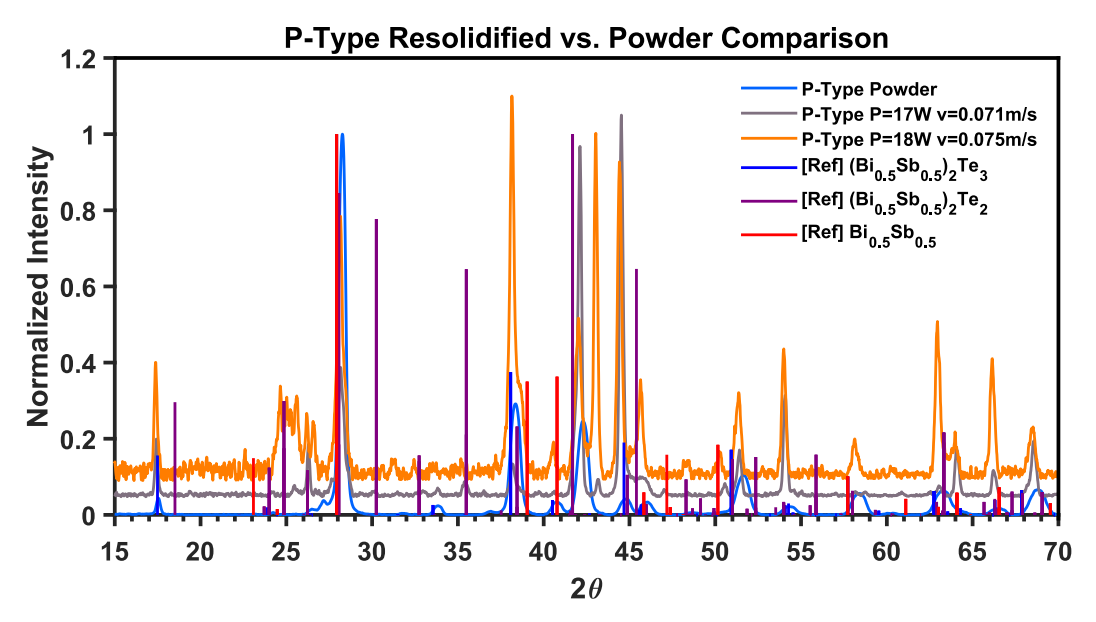


**Figure 33:** Overlay of Figure 32 with peak positions of Figure 31 to show the transition to a reduced Te alloy system during the melt process at the listed powers and speeds [95,97].

#### 5.1.2.2 N-Type Results

Like the p-type analysis in section 5.1.2.1, the n-type stoichiometry identified in Figure 26 is of the family of Bi<sub>2</sub>(Se<sub>y</sub>Te<sub>1-y</sub>)<sub>3</sub> alloys. The family of powder patterns obtained by varying *y* is obtained from various sources in Figure 34. Although the limited EDS data in the n-type system predicts a primary loss of Se, the XRD patterns in Figure 35 show significant texturing of phases that are both devoid of Se and Te. Two main characteristic peaks that do not occur in the unmelted powder are at 18.5°, which corresponds to pure Bi<sub>2</sub>Se<sub>3</sub>, and at 31.5°, which corresponds to the pure Bi<sub>2</sub>Te<sub>3</sub> system. These are better exemplified in the overlay plot in Figure 36. A texture analysis is necessary to determine all phases present, but the overall

impression is that within the n-type alloy Se and Te contents are mostly affected by the melt process, implying that the temperatures reached during manufacturing likely approach or exceed the vaporization temperatures at ambient for these elements at the powers and speeds listed.

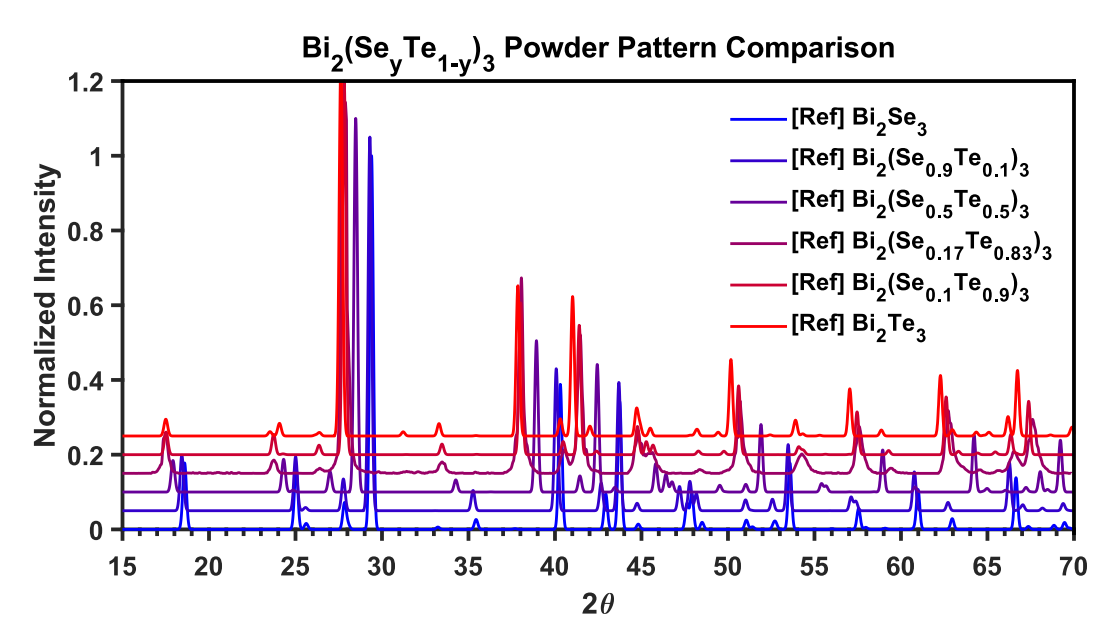


**Figure 34:** Bi<sub>2</sub>(Se<sub>y</sub>Te<sub>1-y</sub>)<sub>3</sub> powder pattern comparison from literature data **[92,94,98–100]**.

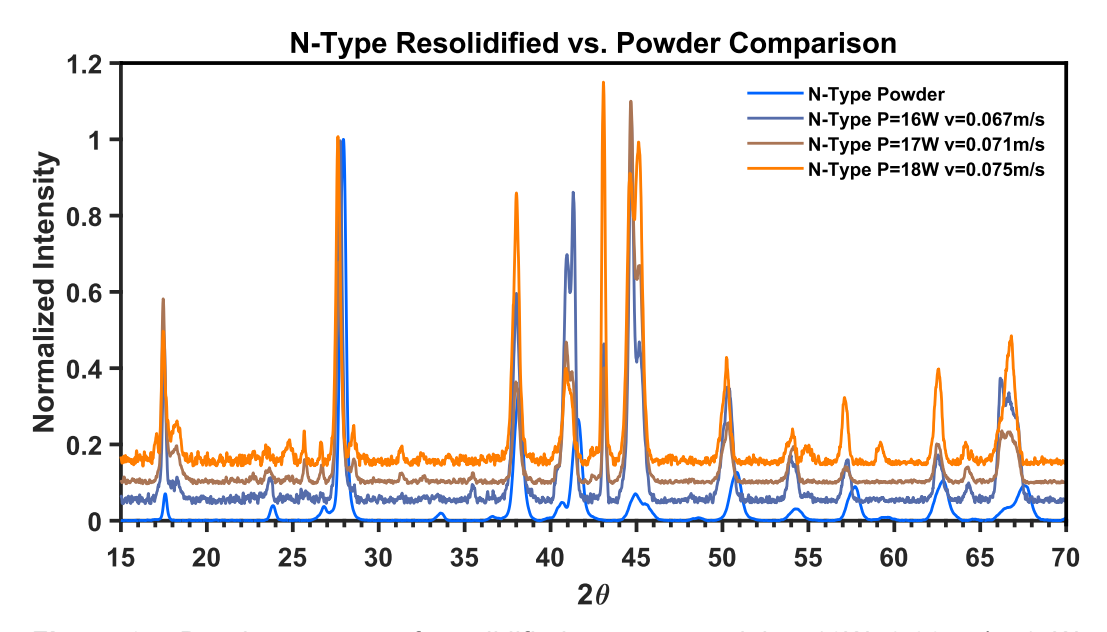


**Figure 35:** Powder patterns of resolidified n-type material at 16W, 0.067m/s, 17W, 0.071m/s and 18W, 0.075m/s overlaid with the pattern of the unmelted powder of stoichiometry Bi<sub>2</sub>(Se<sub>0.17</sub>Te<sub>0.83</sub>)<sub>3</sub>.

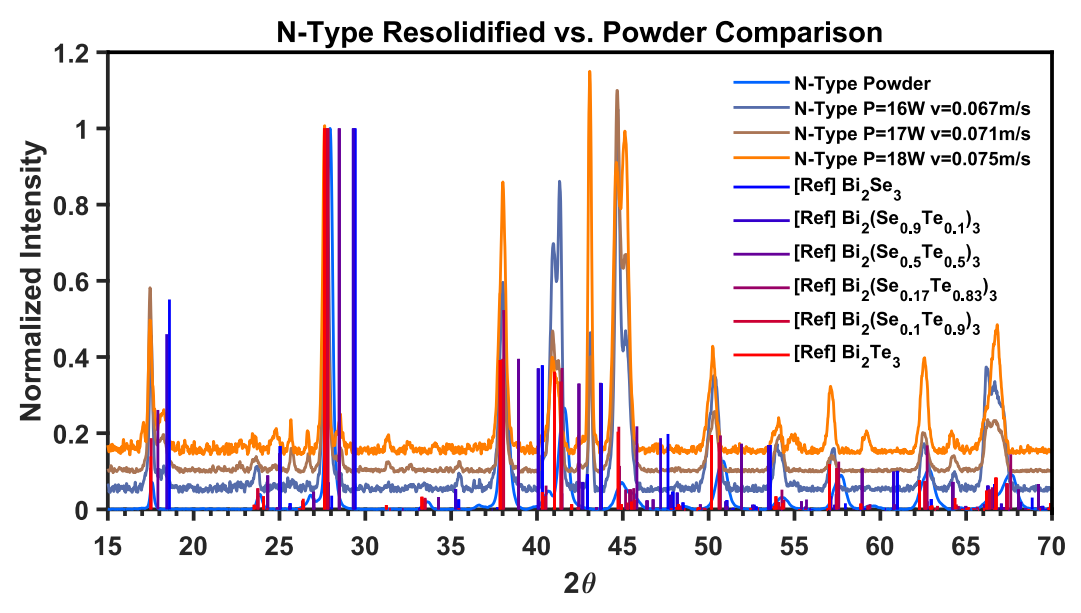


**Figure 36:** Overlay of Figure 35 with peak positions of Figure 34 to show the effects of varying the ratio of Se to Te during the melt process at the listed powers and speeds [92,94,98–100].

# 5.2 Relative Density

### 5.2.1 Porosity

The porosity of the p-type alloy system after melting and resolidification was measured using a custom-made Archimedes density setup with a sample that was manufactured with four layers detached from the PCB substrate. This was verified by the counting of pores in the remaining samples on that substrate that remained attached. These were counted by analyzing the pore size in ImageJ.

#### 5.2.1.1 Archimedes Density

The principle of the Archimedes density measurement is given by the following equation:

$$m_{dry} - m_{wet} = \rho_{water} V_{sample}$$
 [kg] (61)

With measurements of the mass both in air and submerged in water, the volume of the sample is then able to be isolated:

$$V_{sample} = \frac{m_{dry} - m_{wet}}{\rho_{water}}$$
 [m<sup>3</sup>] (62)

The effective density can then be calculated dividing the mass of the sample in air by its newly determined volume:

$$\rho_{eff} = \frac{m_{dry}}{V_{sample}} \qquad \left[\frac{kg}{m^3}\right] \quad (63)$$

Finally, using the theoretical bulk density of the sample from literature, the relative density factor can be calculated:

$$f_{rel} = \frac{\rho_{eff}}{\rho_{Theo}} \tag{64}$$

The factor given in equation (64) is analogous to the concept of the powder packing factor given in equation (7). The measurements performed on a ptype sample processed at 17W and 0.071 mm/s are given in Table 8.

Determination of Packing Factor and Porosity of p-type (Bi <sub>0.15</sub> Sb <sub>0.85</sub> ) <sub>2</sub> Te <sub>3</sub> Sample using Archimedes Density Test							
Measurement Number	m <sub>dry</sub>	m <sub>wet</sub>	ρ <sub>eff</sub> [kg/m³]	ρ <sub>Theo</sub> [kg/m³]	Relative Density Factor $(f_{rel})$	Porosity $(1-f_{rel})$	
1	34.6	28.6	5780	7662 [101]	0.754	0.246	
2	34.2	28.2	5700		0.744	0.256	
3	34.4	28.3	5600		0.731	0.269	
4	34.4	28.3	5690		0.743	0.257	

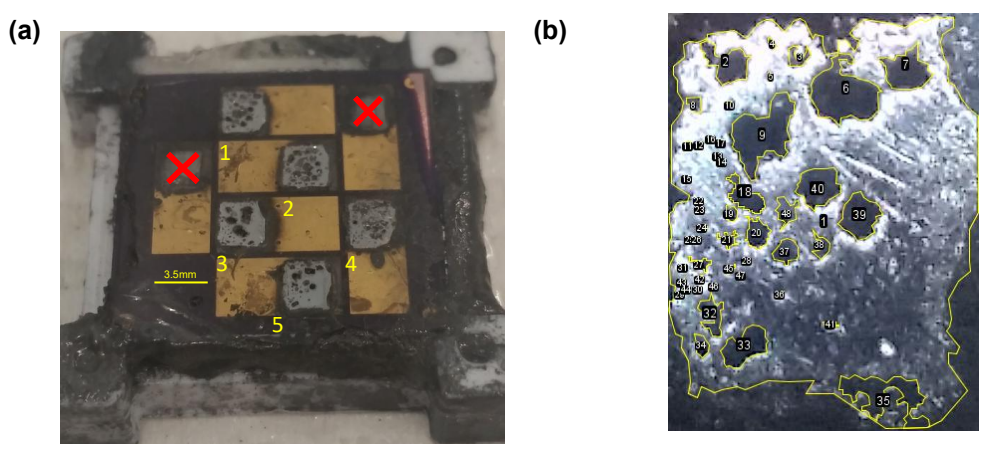
**Table 8:** Determination of Packing Factor and Porosity of p-type (Bi<sub>0.15</sub>Sb<sub>0.85</sub>)<sub>2</sub>Te<sub>3</sub> Sample using Archimedes Density Test. Reference bulk theoretical density taken from [101].

The average relative density was calculated to be **0.743**, making the porosity within the sample **0.257**.

#### 5.2.1.2 Image Processing

In order to perform thermoelectric testing, the remaining samples that adhered to the PCB substrate were coated with Crystalbond and polished until the planarized surfaces of the thermoelectric elements were exposed.

However, once the polishing was complete, it was observed that relatively large pores were present in the processed materials. Subsequently the total area of the pores was analyzed with the help of ImageJ software and is used to compare to the relative density determined by the Archimedes method. The average relative density among the five samples measured here was **0.69** which is only five percent less than that measured using the Archimedes method.



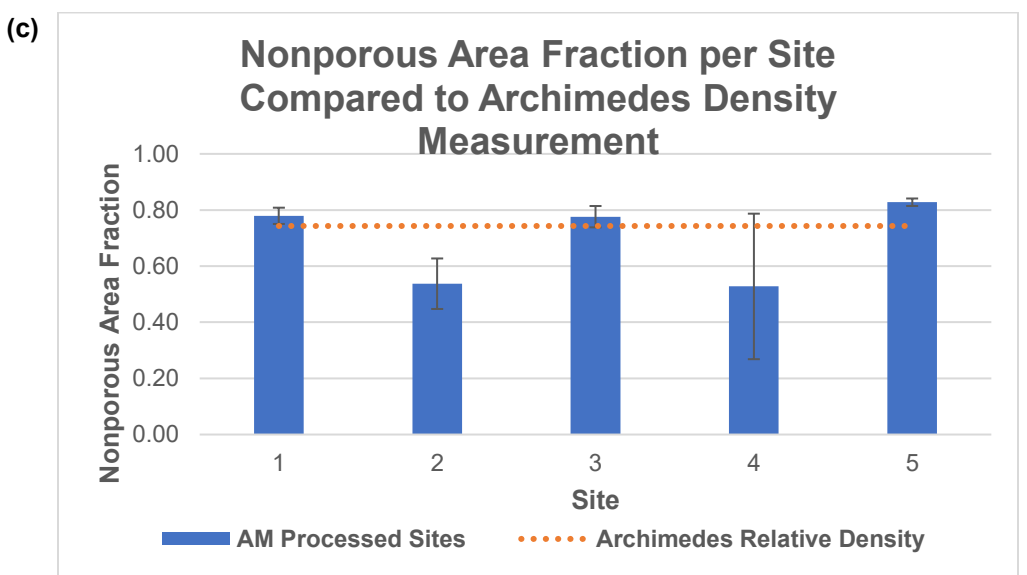


**Figure 37:** (a) P-type legs manufactured at 17W, 0.071 m/s. Two of the seven had detached, leaving five. (b) Sample image of site 5 processed in ImageJ. Here the areas of the porous regions were summed and compared to the nonporous region. (c) Nonporous area fraction per site compared to the relative density determined by the Archimedes method.

# 5.3 Morphology

Both halves of an attempted additively manufactured TEG are shown in Figure 38, although they were unable to be bonded to one another directly after the manufacturing process.

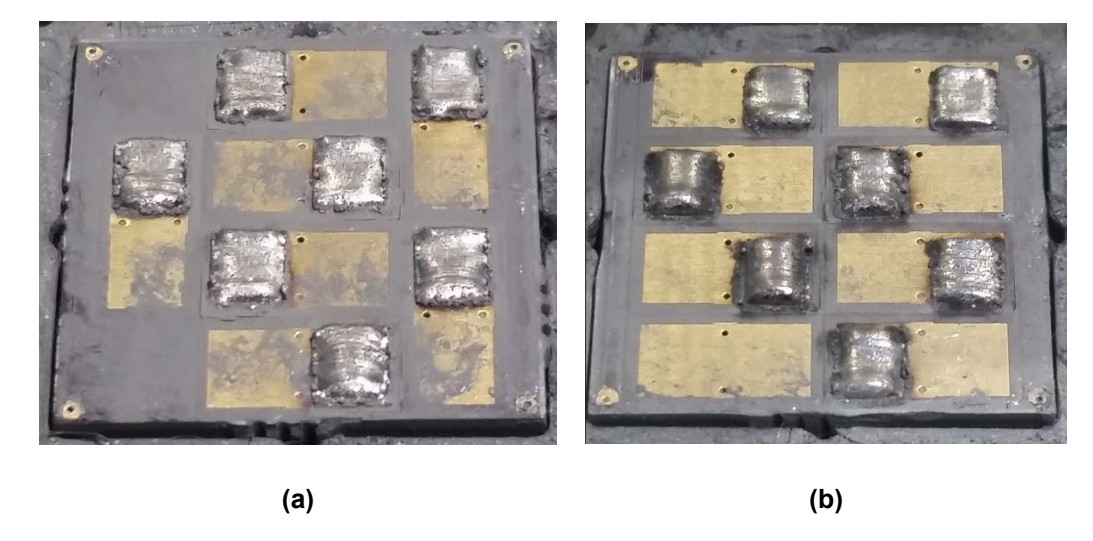


**Figure 38: (a)** P-type bismuth telluride on PCB, manufactured at P=17W and v=70mm/s. **(b)** N-type bismuth telluride on PCB, manufactured at P=17W and v=70mm/s. Designed to form a complete TEG when sandwiched together.

## 5.3.1 Optical Microscopy

The morphology of the resolidified squares was observed using optical microscopy. Completed p-type and n-type samples manufactured on a PCB substrate are given in Figure 39. The external surfaces of each type had angular features that were resultant from the rapid solidification process. It is also noteworthy that although the intention was to create rectangles, the precision of the sample shape seemed to be low. This is likely due to the nonuniformity of the powder grain sizes. Powder nonuniformity would permit the light to reach different depths at different locations in the layer and melt regions inconsistently.

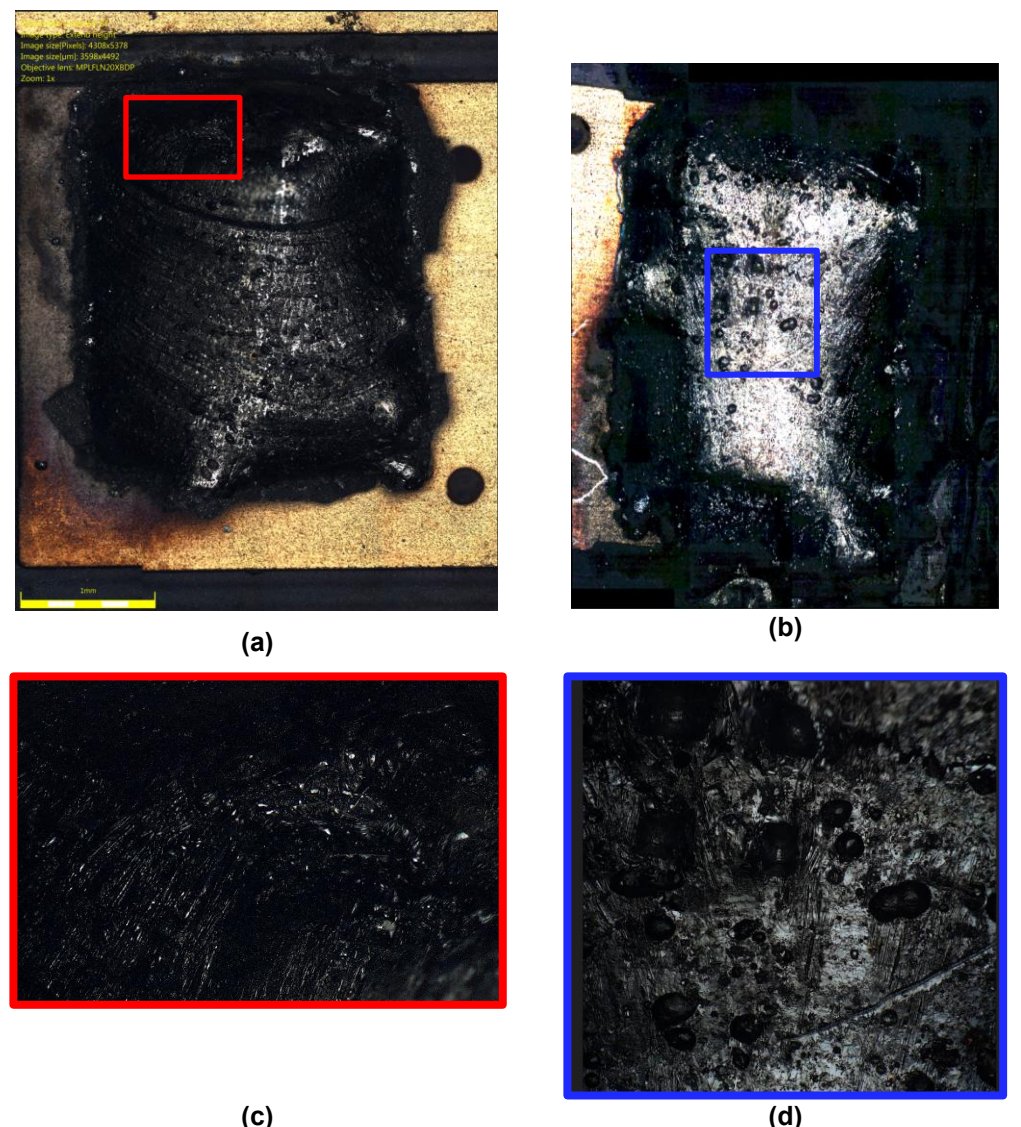


Figure 39: Stitched optical images of an (a) n-type and (b) p-type additively manufactured TEG element on a PCB substrate, with (c) and (d) being the respective enhanced regions denoted by their coloured outlines. Images were taken in segments using an Olympus DSX500 microscope and joined together with its accompanying software. (c) and (d) are corresponding to the selected regions in (a) and (b), respectively.

Additional images were taken of p-type samples that gave insight into surface features both on the top surface and at the substrate interface.

Figure 40 depicts the top surface of one such sample, where triangular surface features can be clearly observed. These features are interesting as they seem to manifest always during the SLM process but occur in different sizes depending on the power and speed combination used. The features created here are roughly 25-50 µm in size and smaller ones were created using larger power and speed parameters in the following section.

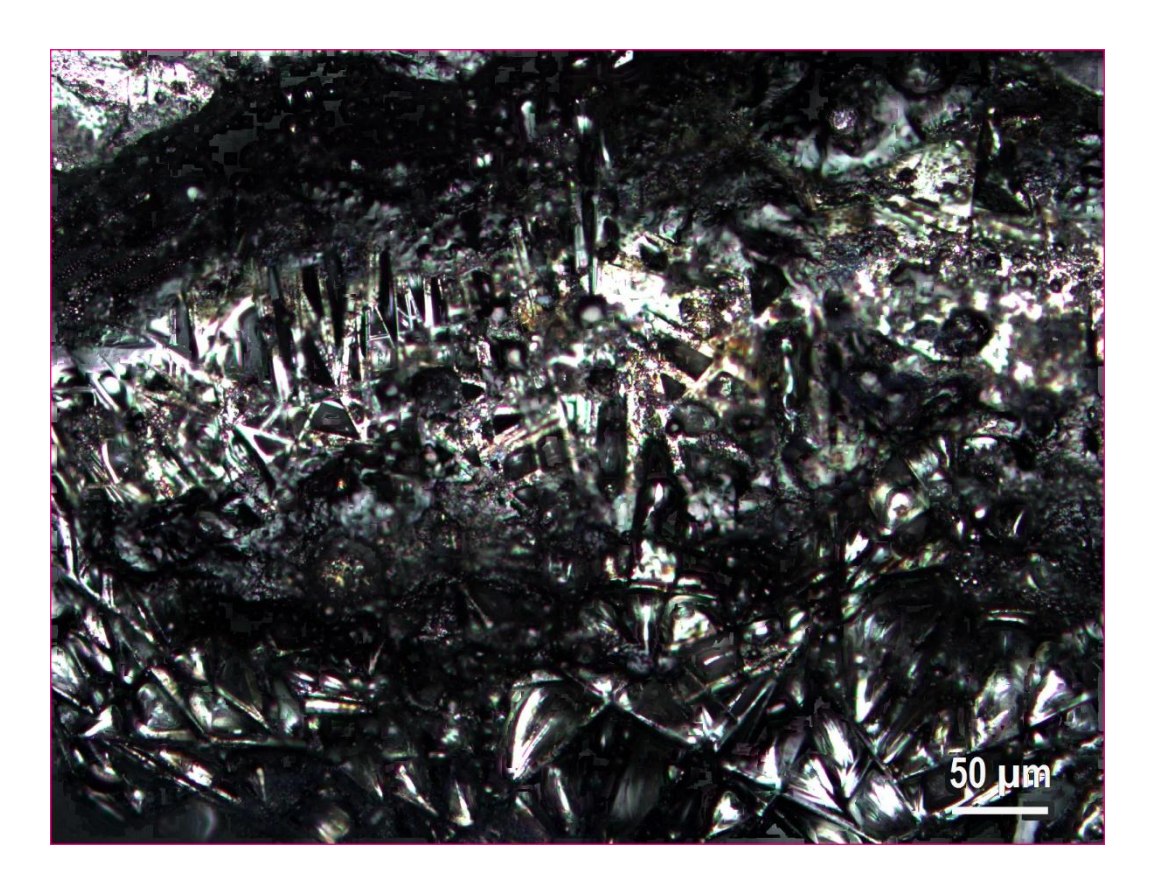
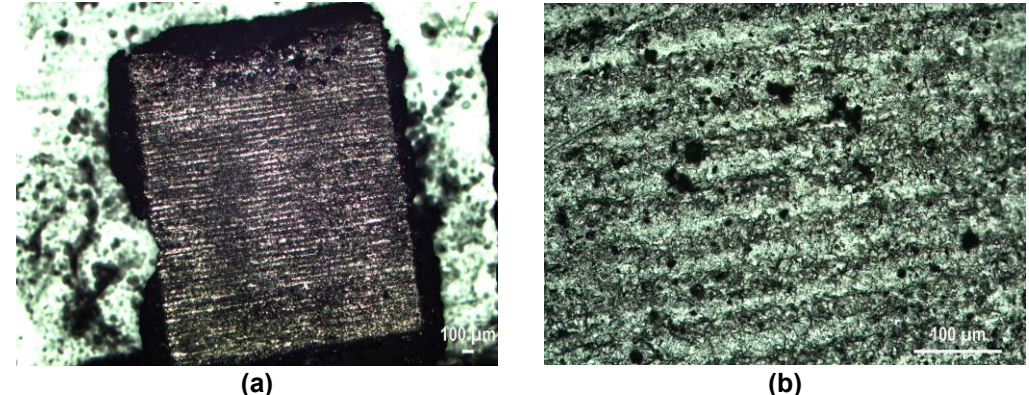


Figure 40: Stacked composite image of p-type sample created with 17W power and 70mm/s speed. Images taken at different focus levels using a Zeiss Axioplan 2 optical microscope. 15 images in total were taken and stack focused using ImageJ software.

The interface region of a fully intact p-type element was imaged after it readily detached from the PCB substrate. This gave insight into the

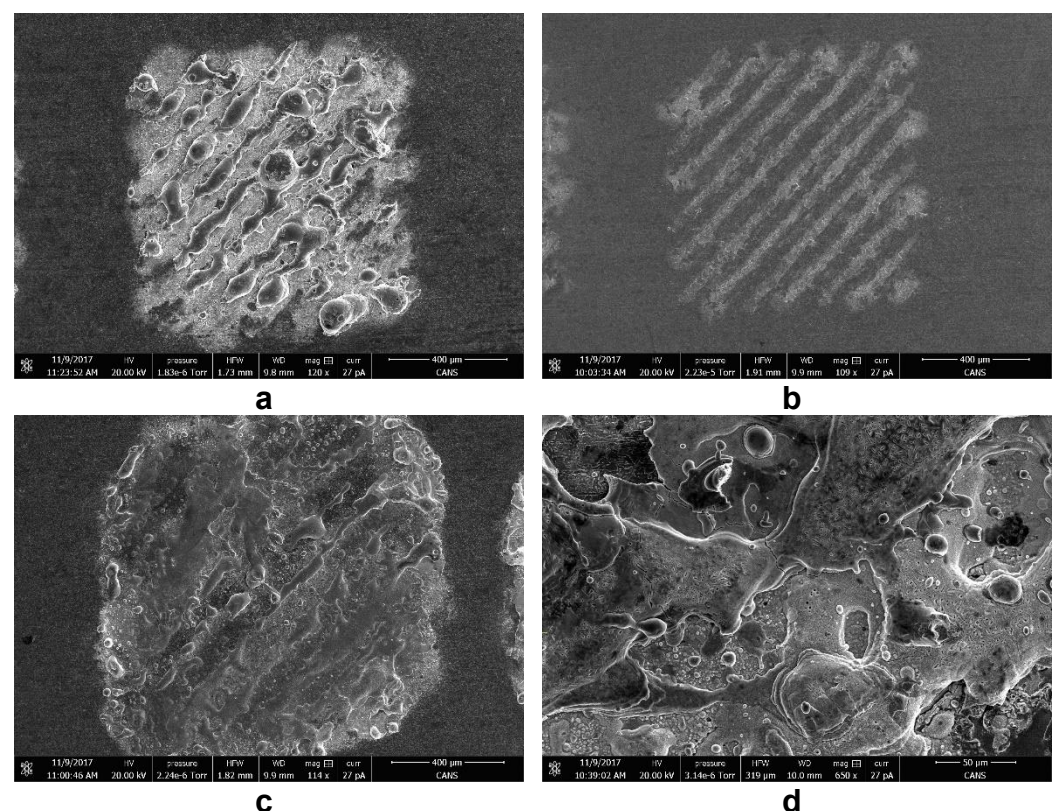
thickness of the melt tracks created for the first layer. The power and speed used were 17W and 70mm/s, respectively. The detaching of some samples from the PCB substrate was not fully investigated and could have been caused by numerous issues, such as surfactants on the powder or on the substrate, coefficient of thermal expansion mismatch between the powder and copper, or degree of surface roughness. One item that was interesting was that the hatch spacing could have been decreased to allow for more significant overlap between adjacent tracks. The implemented hatch spacing was equal to one laser diameter of 100µm. Although the samples were able to be created with some degree of success, it appears that at the current power and speed, a tightening of the hatch spacing by at least a factor of two may have produced more homogeneous samples.



**Figure 41**: (a) Interface of detached p-type element made at 17W, 70mm/s at 5X zoom. (b) 20X zoom of element in (a). Melt tracks clearly visible on initial layer with average track width of 33μm, measured using ImageJ software. Images were taken with a Zeiss Axioplan 2 optical microscope.

#### 5.3.2 Scanning Electron Microscopy

SEM was performed on additional samples that were created at different power and speed combinations. Both the p-type and n-type materials were imaged. Figures Figure 42 through Figure 45 show the microstructure for p-type and n-type samples created with laser power of 50W and 250W, and speeds of 1500 mm/s and 2500 mm/s. The power increases from left to right, and speed increases from top to bottom. Corresponding low and high resolution images are shown in the figures for each of the samples.



**c d Figure 42**: Lower resolution p-type samples manufactured at **a)** 50W, 1500 mm/s **b)**50W, 2500mm/s **c)** 250W, 1500mm/s **d)** 250W, 2500mm/s.

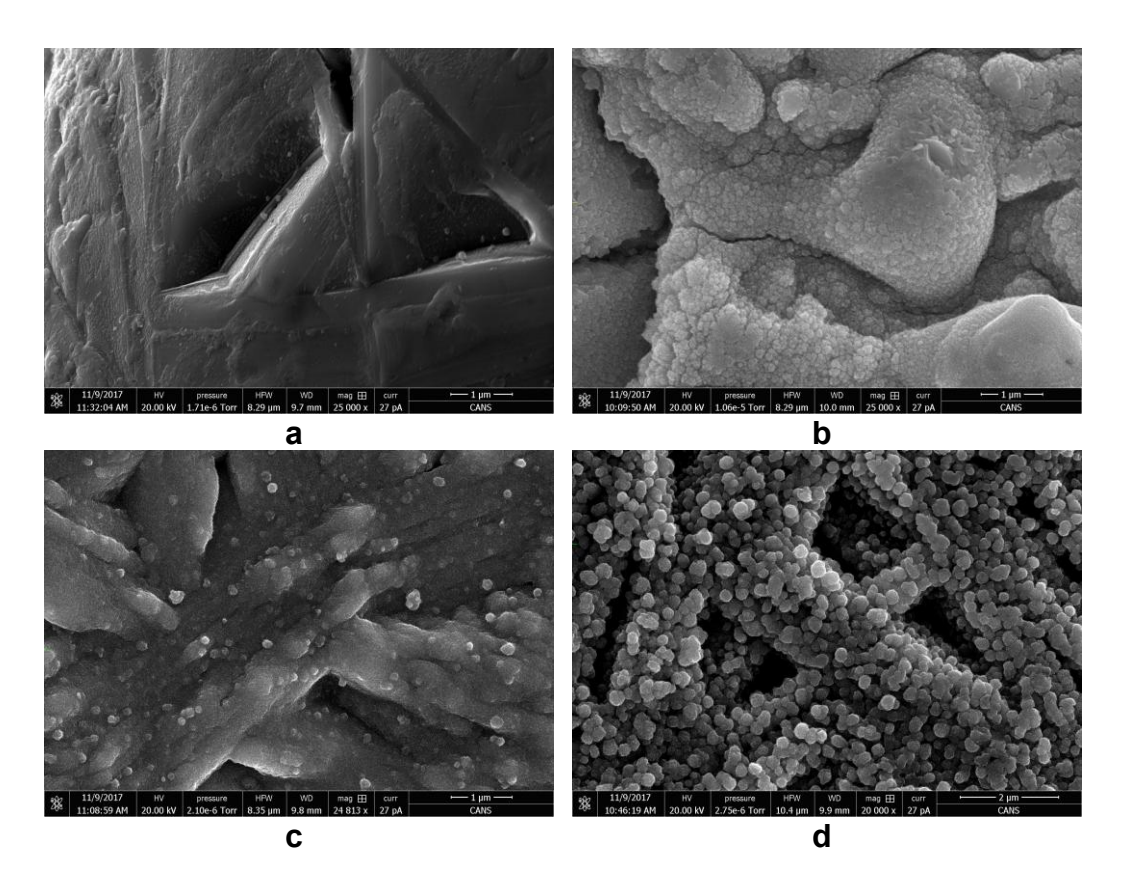
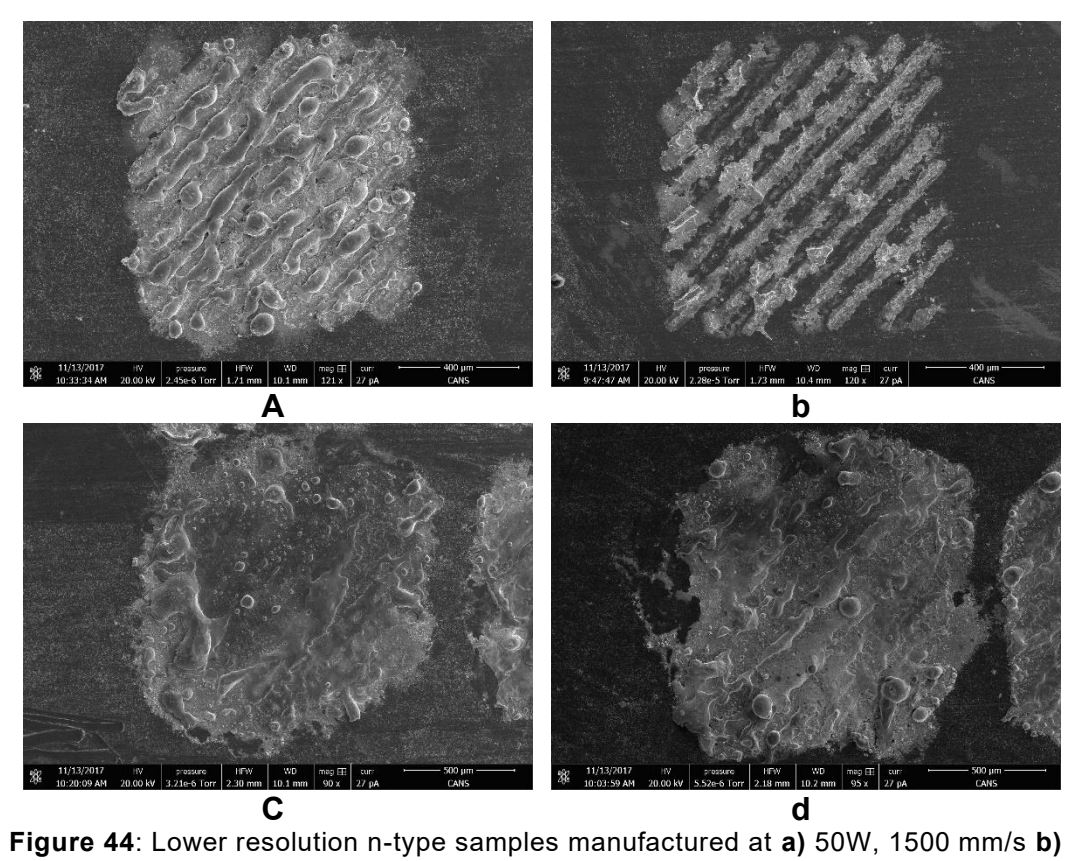


Figure 43: Higher resolution p-type samples manufactured at a) 50W, 1500 mm/s **b)** 50W, 2500mm/s **c)** 250W, 1500mm/s **d)** 250W, 2500mm/s.



**Figure 44**: Lower resolution n-type samples manufactured at **a)** 50W, 1500 mm/s **b)** 50W, 2500mm/s **c)** 250W, 1500mm/s **d)** 250W, 2500mm/s.

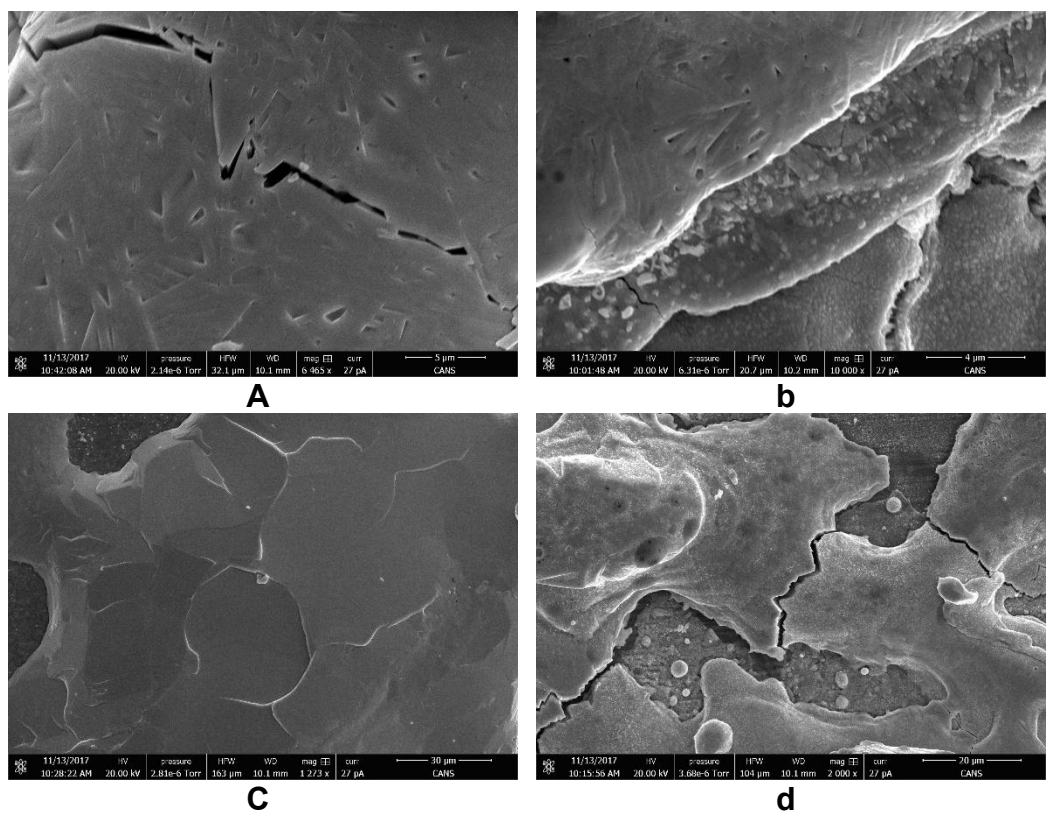


Figure 45: Higher resolution n-type samples manufactured at a) 50W, 1500 mm/s b) 50W, 2500mm/s c) 250W, 1500mm/s d) 250W, 2500mm/s.

Each of the samples created above are single layers of powder applied in squares of 1mm side length on a bulk copper substrate. A qualitative analysis of Figure 42 and Figure 44 illustrates that at any power, an increase in laser speed shows more defined melt tracks and thus less melting of intermediate material between lines. Higher power of course injects more lateral heat flow and thus can melt more material. The agglomeration of some of the powder at higher energy densities is a demonstration of the balling effect [49,102]. This is consistent with the use of a wide multimodal powder distribution that has grains ranging in size from

the nm to the hundreds of µm scale. Also the presence of surface oxides, which were detected in the TEM analysis, can contribute to balling as well by affecting the liquid surface tension during the solidification process [83].

The higher resolution images for both p-type and n-type material systems show the formation of triangular structures within the solidified portions. These appear similar to those observed in the optical microscopy image in Figure 40, although they are on the order of 1-2 µm in size. More investigation is needed as to how and why these occur, and if they enhance or hinder the thermoelectric performance of a device made using AM. The main differences between the samples containing the smaller features and those containing the larger ones are that the power was increased by up to a factor of 15 and the speed was increased by up to a factor of 50. One or likely both parameter increases led to the creation of smaller feature size.

# 5.4 Comparison to Model

From a traditional AM perspective, it is valuable to understand which power/speed combinations will lead to the production of a sample with minimal porosity. However, in this new space of thermoelectric materials, some porosity may actually improve performance [103] and therefore may be of use in the future. Lee *et al.* [104] modeled the effect of porosity on thermal and electrical transport properties and suggested that the time between scattering events for both phonons and electrons were affected by the inclusion of pores. They primarily focused on the inclusion of nanopores

in the SiGe material system and calculated the reduction of both the electrical and thermal conductivities versus porosity. The result was that there were regimes of porosity where the decrease in thermal conductivity exceeded that of the electrical conductivity and therefore, increased the ZT. Recent attempts at incorporating porosity into thermoelectric materials for ZT enhancement can also be found in the literature [105–108].

Nevertheless, the semi-analytical model assumes that the delivered energy corresponding to a specific power/speed combination will facilitate melting to the bottom of the melt pool with minimal mass loss due to evaporation occurring only at the material boiling point. In this regime, the saturated vapor pressure above the melt pool would be extremely close to that of the ambient environment, as dictated by the Clausius-Clapeyron relation [62]. Here, a minimal recoil pressure is assumed be imparted on the melt pool with little to no liquid expulsion being able to occur.

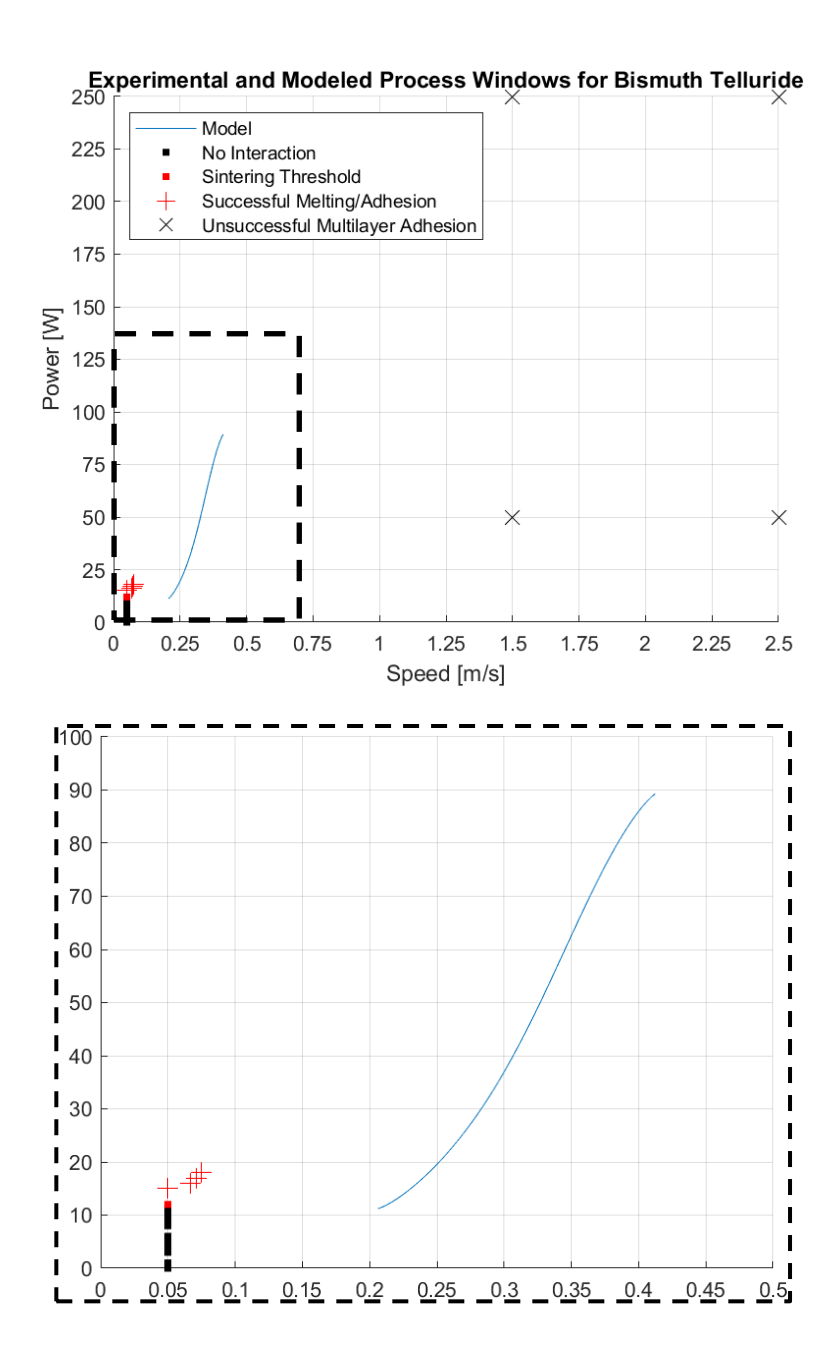


**Figure 46**: Experimental process parameters attempted in this work, as well as the modelled process window. (Top) All parameters included, (Bottom) Enhanced region shown in Top.

In terms of the present work, the model was developed after initial melting of bismuth telluride was attempted. Thus, the optimal process

parameters dictated by the model were not explicitly investigated but rather forecasted. This experimental work is captured in Figure 46. Here, the lowest power/speed combination that began sintering was 12W and 0.05 m/s, which is the lowest speed at which the laser can scan in the EOSINT M280 system. All powers below 12W were applied in combination with this speed with no change in the powder bed observed. This is denoted as the "No Interaction" dataset. At the sintering threshold, the powder darkened and solidified but did not look visibly melted. Powers applied above 15W at the 0.05m/s subsequently showed melting with a visible change in surface finish. The dataset labelled "Successful Melting/Adhesion" describes power and speed combinations in this work that led to the successful creation of multilayer p-type and n-type thermoelements. The "Unsuccessful" parameter set, while melting the initial layer to the substrate, did not allow for multilayered structures to be built with the application of subsequent powder layers. Likely, the power was too high such that most of the powder applied in the secondary layers was vaporized. It was noteworthy, however that the lower limit for the laser power of the modelled parameter set coincided well with the experimentally observed sintering threshold power to within one watt.

In the following paragraphs, comparisons to literature are provided for model validation. The two material systems utilized for this comparison will again be bismuth telluride and the well-characterized Ti6Al4V.

A recent article published by Headley et al [25] investigated the optimal process parameters for n-type bismuth telluride using a combination of experimentation and machine learning (ML). The experiments were carried out for a layer thickness of 35µm with a laser wavelength of 1070nm and spot size of 60µm. The substrate was bulk bismuth telluride ingot. The particle size distribution was estimated in this thesis using ImageJ and a sample image of the powder provided in the reference. An average particle size of 1.5µm was assumed when applying the semi-analytical model. A series of line scans at different speeds and powers were attempted in the reference and the resulting geometry of the melt pool was used with ML to predict the optimal process parameters. The goal was to obtain the lowest achievable porosity. The final values predicted by the ML algorithm were selected to be used instead with a 75µm layer thickness in order to achieve minimal porosity and to reduce build time. The model in this thesis was applied at both the 35 and 75µm to predict the complete melt of the powder at those layer thicknesses as shown in Figure 49.

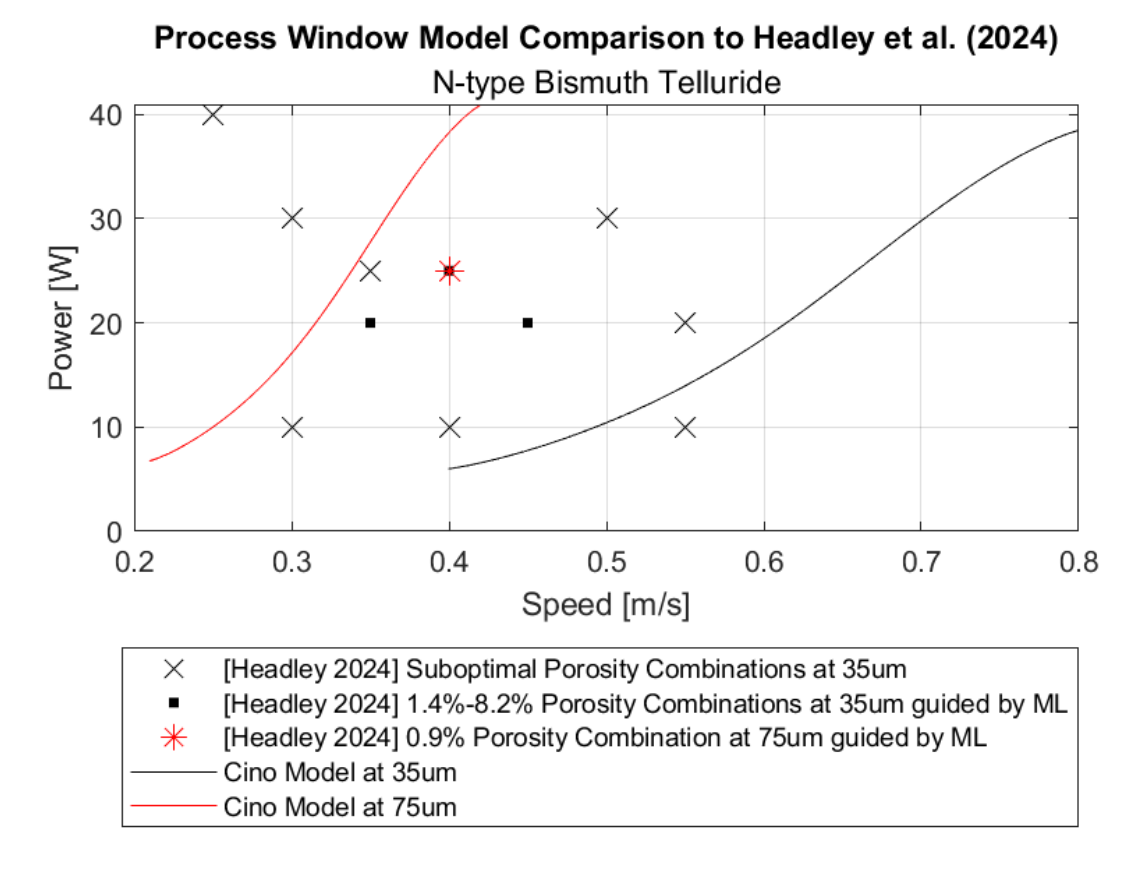


Figure 47: Semi-analytical model comparison to [25].

Headley predicted a power of 25W and 0.4 m/s for a layer thickness of 75µm. This also included values for hatch spacing, which the semi-analytical model does not account for, as it deals with only single melt tracks. The lowest porosity achieved was 0.9%. For the same layer thickness, the closest point to Headley's optimal combination in the proposed semi-analytical model is 25W and 0.34 m/s. This exercise was valuable as it illustrates the sensitivity of the process window prediction to the layer thickness.

The work of Shi *et al* [26] provides a second comparison to the bismuth telluride material system. Here, powder with an average particle size of

roughly 58µm was spread in 2mm layers on a stainless steel substrate and processed with a laser of 1070nm, similar to that of Headley. The spot size was 50µm.

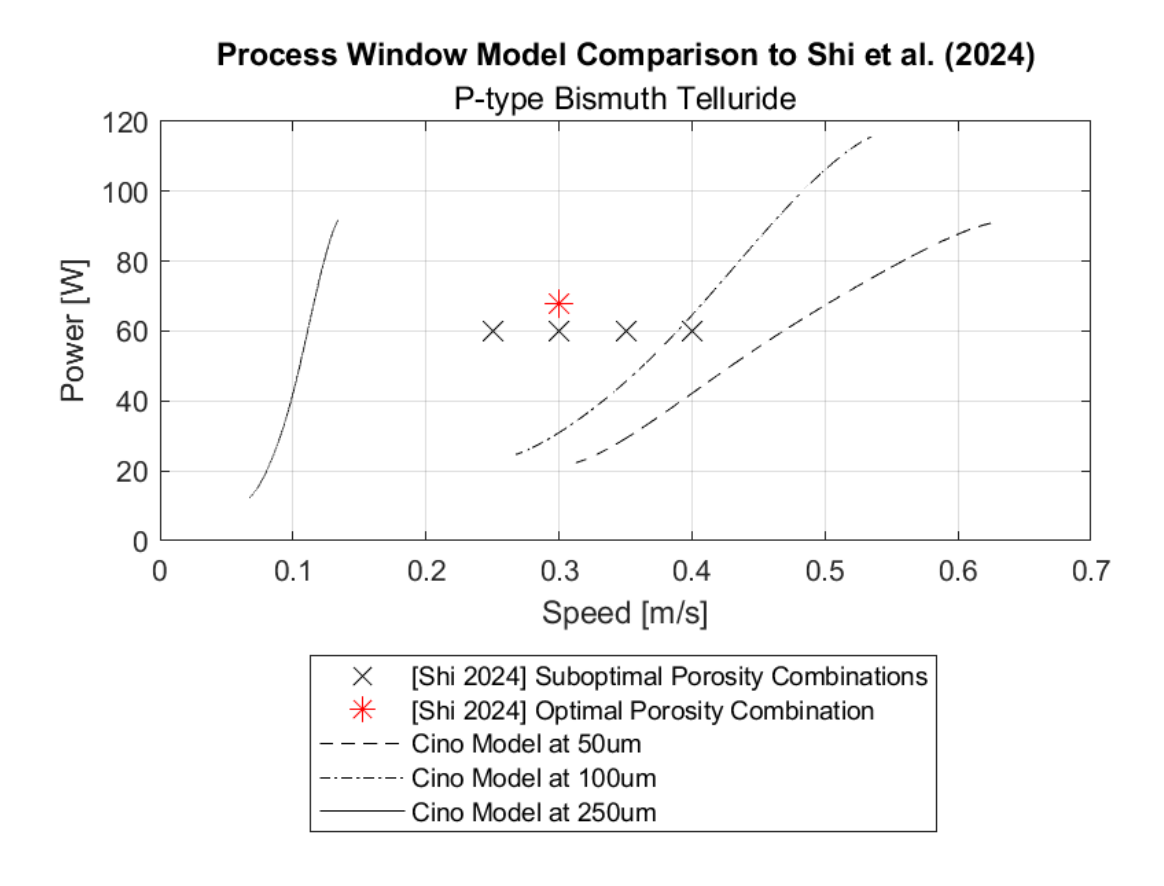
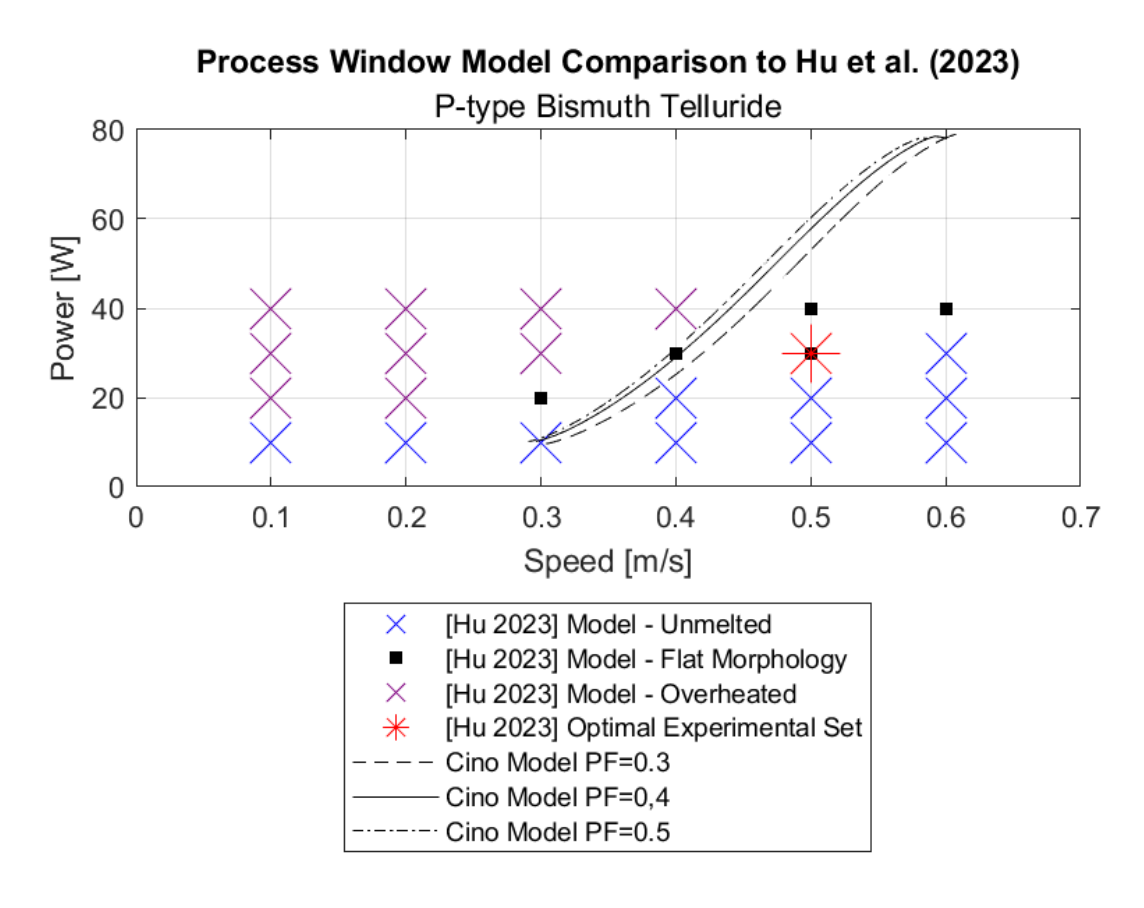


Figure 48: Semi-analytical model comparison to [26].

The reported layer thickness was optically large and it was mentioned that two laser passes were necessary to fully melt the powder at 2mm thickness. This thickness also was unable to be inserted into the semi-analytical model as it did not yield any suggested power/speed combinations that could facilitate complete melting without significant evaporative losses. Thus, since the author mentioned multiple passes to melt this layer, an intermediate layer thickness can be assumed where

partial melting may have occurred. The semi-analytical model in Figure 48 is applied for three partial-layer thicknesses of 50, 100, and 250µm powder, and the resulting process windows agree reasonably with experimentally observed combinations used in the reference. The minimal porosity reported here was 3.42%.

Finally, Hu et al [35] modelled bismuth telluride single melt tracks using COMSOL and iterated over a power and speed space of 10 to 40 W and 0.1 to 0.6m/s, respectively. They used a 1064nm laser with a 50µm radius. Their powder layer thickness was given as 36µm, and they provided a particle size distribution from which their powder absorption coefficient for a given packing factor could be calculated. From their numerical modeling, they used the resulting morphology of the individual tracks to predict an optimal parameter set. Their parameter datasets were separated into those that modelled unmelted, flat, or overheated track morphologies. The set labelled "flat" contained what the author deemed were the optimal parameters and resulted in a smooth top surface morphology. The set labelled "overheated" indicated that high intensity laser interaction had caused surface contouring consistent with the effects of recoil pressure and significant material evaporation. After modelling this space, they determined the combination of 30W, 0.5m/s to be optimal and used this to create their samples. This set of values yielded them a relative density of 97.4% when used experimentally. A comparison of their data to the model present in this work is given in Figure 49. Their powder packing factor was not given and thus a range of 0.3 to 0.5 was used for the semi-analytical model, which still showed good agreement.



**Figure 49**: Semi-analytical model comparison to numerically modelled (COMSOL) values and the decided upon optimal experimental set [35].

Since the porosity was almost eliminated in the work performed by Headley *et al*, the optimum process parameters predicted by ML seemed to be in the realm of those provided by the semi-analytical model. The low, but markedly higher residual porosity in the best sample prepared by Shi *et al* may be due to many factors including different powder morphology and

overly large layer thickness. Also, since no measurement was made for mass loss due to evaporation, it is also possible parameters were used that permitted full densification at the expense of some material ablation. The work of Hu was valuable as it used established numerical simulation software to iterate through a parameter space and showed that the semi-analytical model tended towards their optimal parameter set. The resulting process windows in each of the references above appear to capture possible power/speed combinations in each material system that used minimal porosity as a figure of merit.

For further validation purposes, the semi-analytical model was applied to the Ti6Al4V system for power/speed combinations yielding minimal porosity in literature.

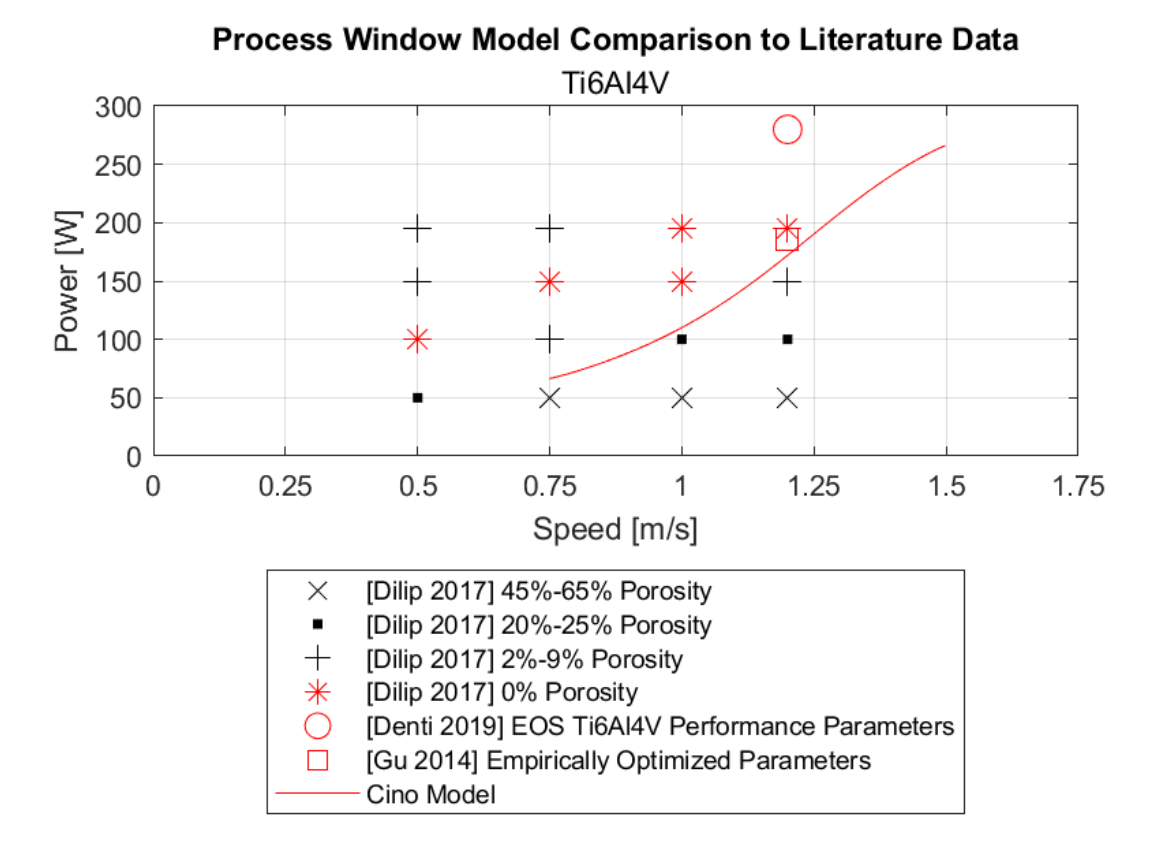


**Figure 50**: Semi-analytical model comparison to experimental, empirically modelled, and vendor-recommended parameters for Ti6Al4V [88,109,110].

The Ti6Al4V powder is a very prevalent material system studied in AM literature and has been reported upon frequently. Figure 50 includes experimental data from Dilip *et al* [88] that corresponds power/speed combinations with resultant porosity. Denti *et al* [109] experimented with the an EOSINT M290 machine and reported using the EOS recommended processing parameters for their Ti6Al4V powder. Finally, Gu *et al* [110] used empirical modeling to arrive at a power/speed combination that would yield near theoretical density to the underlying material system. All three references use a 30µm powder layer with similar powder morphology. The

applied semi-analytical model used the powder relative density – or packing factor – from Gu *et al*, as well as readily available material properties from [87]. As observed above, the experimental parameter sets yielding 0% porosity, as well as the empirically determined combination and EOS-recommended combination are all consistent with the semi-analytical model presented. The power and speed range predicted is clearly distinct from that of the vastly different, bismuth telluride system, and using minimal physical phenomena in the melt requirements, can predict within 11% of an experimentally observed optimal laser power value for the same experimentally observed speed.

To reiterate the versatility of the model, the key comparisons for both material systems are combined in the following figure.

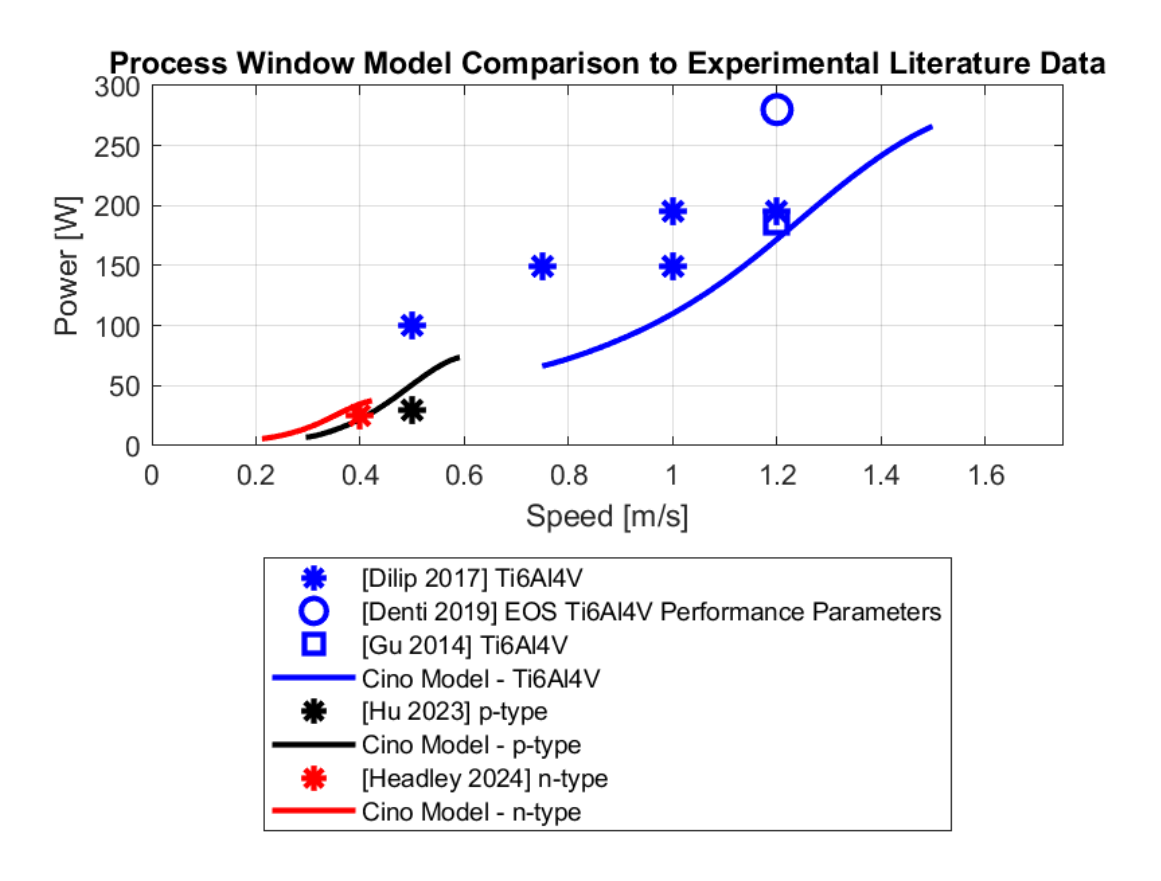


**Figure 51**: Combination of Bismuth Telluride and Ti6Al4V modeled process windows with corresponding experimental results from literature.

As mentioned above, the hatch spacing was a parameter that was reported and experimented with in the literature datasets that were presented, however the semi-analytical model did not take this into account. The proposed model currently deals only with single melt tracks on a powder bed. With some modifications to both the melt requirements and the geometry of the solid- and liquid-interacting beam components, this model may be able to be adapted in the future to include additional thermal phenomena as well as provide parameters that take hatch spacing into account.

#### 5.5 Thermoelectric Characterization

A preliminary set of measurements was carried out on the p-type material to determine its room temperature ZT. This was performed using a custom-made Harman Technique apparatus built within previous work [111]. The test system is based upon the work of Buist, where a bipolar, DC current is applied to the sample and the resulting voltage waveform provides the key voltages that can be used to calculate ZT [112]. Seven samples manufactured on a printed circuit board substrate were sputtered with 100nm each of titanium and gold and tested in a vacuum environment at 10<sup>-6</sup> Torr, at ambient temperature [113]. A DC current pulse of 200 mA was applied to each sample for 120s to develop a steady state thermoelectric voltage, and then the same pulse was applied again in reverse polarity after a 10s wait time. The voltages obtained from these two waveforms were then averaged to remove any influence of thermal offset voltages that would be present based on any asymmetry in the thermal transport geometry of the system.

The average measured room temperature ZT is presented in Figure 52 and compared to two other recent references that use almost the same stoichiometric p-type alloy as in this thesis [21,35]. The reference data uses material with stoichiometry given as Bi<sub>0.5</sub>Sb<sub>1.5</sub>Te<sub>3</sub> whereas the p-type stoichiometry used in this thesis slightly differs at (Bi<sub>0.15</sub>Sb<sub>0.85</sub>)<sub>2</sub>Te<sub>3</sub>. It has also been noted in the literature that a ZT of 1 is the minimum commercial

industry standard [42]. The propagated  $2\sigma$  uncertainty was calculated to be  $\pm 9\%$ . The relatively high room temperature ZT is promising, and further investigation should be carried out to determine its trend vs. temperature.

## Comparison of P-Type Bismuth Tellulride Room Temperature ZT Values Manufactured by SLM 1.4 1.3 1.2 1.1 1 0.9 8.0 0.7 0.6 0.5 0.4 0.3 0.2 0.1 0 Shi 2019 Cino 2024 Hu 2023 Reference

**Figure 52**: Comparison of room temperature ZT for p-type bismuth telluride samples manufactured by selective laser melting **[21,35]**. The error bar given represents ±9%.

## 6. Conclusions and Future Work

## 6.1 Contributions to Knowledge

The recognized usefulness of additive manufacturing in industry is gaining, and with this, there is a focus to understand and characterize novel

material systems so that new opportunities can present themselves for technological development. In the area of energy harvesting, thermoelectric devices are a definite contender for additive manufacturing given their bulk multilayered structures for heat transfer and electrical conduction. The initial idea to take powdered bismuth telluride that was not conducive to commercial laser powder bed fusion, was full of hurdles that could be representative of using any non-conventional powder system. These hurdles were methodically overcome to ultimately produce functioning thermoelectric devices.

The custom power delivery system outlined in section 4.1 allowed for the mitigation of many of these hurdles using a *design for manufacturing* approach. The randomized powder morphology that deviated from the conventional spherical morphology presented problems in obtaining uniform layer thickness, and good flowability. Widely used AM powders such as the Ti6Al4V alloy are available in spherical form with narrow particle size distributions and can be readily loaded into a hopper for uniform layer distribution on a powder bed. Since the bismuth telluride could not be readily spread, it was sieved and mixed with acetone to form a slurry. The uniform layer thickness was achieved by designing and applying solder stencils of uniform thickness such that repeatability can be maintained between layers. The masks were designed to be applied in a stackable formation, and to be fastened with quick-release nuts, a feature borrowed from machining. The

substrate that was selected to be printed upon was a customized, double layered printed circuit board. This was done to accommodate the thermoelectric since the PCB was designed with all of the necessary electrical pathways to form a finished TEG. Being double layered, it was able to be fitted with thermal vias to facilitate increased heat transfer from one side to the other in order to reach a uniform temperature quickly. In short, the customized powder delivery system was designed to allow for rapid prototyping of powdered thermoelectric material of arbitrary morphology, in a commercial laser powder bed fusion machine that would otherwise not be able to accommodate it during normal use. The customized substrate allowed for device manufacturing on a thermally and electrically functional substrate with incorporated contacts in lieu of the additional manufacturing that would have been required as seen in conventional TEG modules.

There are multiple aspects of the semi-analytical model that act as foundational points of knowledge moving forward. When determining the process parameters for a novel material system, it is important to have a deep understanding of the optical, thermal, and physical characteristics of the powder in question. If the infrastructure is available to the researcher to readily measure all these required characteristics, they should do so. However, this availability is not always guaranteed. Many of the material constants used within the modeling of this research were derived by

adjacent physical phenomena using temperature-averaged literature values for the material system. Examples of this include approximating the effective boiling temperature and latent heat of vaporization from effusion data and laser ablation thresholds, respectively. Regardless of the dependence on literature values, the rationale for the determination of effective optical and thermal material parameters proved to still produce useful predictions when applied to the semi-analytical model.

The model itself presented a unique method of analyzing the laser interaction with the powder. The intention was to obtain a process window for laser power and speed that could effectively melt a given powder of a given layer thickness. The separation of solid- and liquid-interacting beam components in a volumetric capacity was novel in that it proved to yield acceptable forecasting power. The melt process was analyzed for a representative volume, rather than for a macroscopic structure and the assumption that the melt time had to coincide with the laser interaction time over this volume was consistent with attempted process parameters that provided efficient melting. Looking at the laser interaction in this way allowed for the simplification of the energy delivery and distribution into the system. The gaussian beam was spatially and temporally integrated, and a single melt track width was imposed that was equivalent to the beam width, which was used in the selected AM process experiments. The core of the model was to leverage the energy deposited in the characteristic optical absorption depths of both the powder and the ensuing liquid layer that formed, with the thermal and optical requirements of the material contained within this representative volume. Its simplistic mathematical relationship allows for the quick determination of process windows that could be used as a guideline for exploratory research in an otherwise untested materials system for AM, and it is not impeded by the need for large computational power or sophisticated software.

Finally, for the bismuth telluride material system in question, it is evident that additive manufacturing has the potential to be a suitable process for bulk thermoelectric devices in the future. The main stoichiometry was maintained as optimal process parameters were approached, indicating that an additively manufactured TEG could still function with the thermoelectric properties of its bulk constituent materials. Any material loss that was observed occurred in a predictable manner, where lighter elements such as Se and Te were the first to reduce in concentration in samples that were created with higher delivered energy densities. The resulting triangular microstructures that were formed during the melt process contributed to a notable residual porosity that seemed to decrease the device thermal conductance without much detriment to the electrical conductance. This yielded an measured room temperature ZT of approximately unity, which is promising as it is the commercial benchmark value. Thermoelectrics represent a new paradigm for additive manufacturing, as their functionality is not only reliant on their structural and mechanical integrity, but also on their electronic properties. The utilization of the custom powder delivery system for low flowability powder, the customized PCB substrates, and the semi-analytical modeling scheme create a foundation for thermoelectric generator prototyping with any material system.

#### 6.2 Future Work

# 6.2.1 Proposed Modifications to the Semi-Analytical Model

The created process windows are limited in their accuracy due to both the fixed assumptions and impositions on the model, as well as the number of phenomena that have been unaccounted for. The model currently makes predictions assuming a single powder layer on a substrate, with the laser interacting on a single melt track. The model can be adapted to provide process windows for subsequent layers that are on solidified bulk materials rather than the initial metallic substrate. This would require solving the radiative transfer equation with the optical properties of the bulk material substituted for that of the substrate. A consideration for partial melting into the underlying solidified layer can be added to the energy balance for this consideration as well.

The individual melt track application can be expanded to include adjacent/overlapping melt tracks as well, and therefore, an estimation on

the effects of hatch spacing. The solid- and liquid-interacting beam portions would each forfeit a portion of their incident energy to a third area which would represent solidified material. Therefore, some assumptions as to the area of the beam that would be in contact with an adjacent, recently melted track, can additionally be considered with the areas that are in contact with the powder and forming liquid of the new melt track. This would require knowledge of the absorptivity, reflectivity, and absorption depth of the solid, as well as its thermal properties in the case of remelting during close hatch distances.

Currently, only radiation and evaporation at the boiling temperature are included as loss terms in the energy balance. This can be expanded to include terms such as convective surface losses, forced liquid convection due to recoil pressure and capillary action, as well as melt ejection which also results from the recoil pressure overcoming the liquid surface tension. Higher order effects such as plasma generation may also be able to be included, if simplified as well.

It would be useful to add a metric for determining the absolute proximity of experimentally observed optimal power and speed combinations to the modelled process window. One such metric could be the residual porosity of the system. To add a porosity model to the process window, the corresponding melt time to the modelled power and speed combination can be used in a mass balance to convert powder and

surrounding gas medium to and evaporating liquid with entrapped gas, and finally solidified bulk material. An estimation of how much vaporized liquid and entrapped gas can escape during the melt time, which again is influenced by the process parameters, can then allow for the calculation of the residual porosity in the system.

#### 6.2.2 Considerations for TEG Fabrication

If the gas atomization of thermoelectric powders is not widely pursued, the custom facility that was designed in this research will allow for their use in established powder bed systems. Automating this powder deposition process would improve yield in the future.

An attempt to build an entire thermoelectric module using constituent powders would also be a useful endeavour. Instead of prefabricating the substrates, they can be built from the bottom up using the LPBF process. Subsequently, electrodes could be built and finally the thermoelectric material. This could all be performed without breaking the print bed atmospheric seal so that exposure to contaminants and oxidation are minimized.

Now that bismuth telluride has been shown to maintain its thermoelectric properties after laser processing, the investigation of other thermoelectrics should be pursued. An evaluation with the semi-analytical model of the optical and thermal properties of a proposed powder can determine a rough

process window. This, in combination with the process window determination of powder on a solidified layer, can lead to a process for advanced AM segmented thermoelectric devices. Prospective materials should first be modelled for thermoelectric compatibility, and subsequently for thermal expansion mismatch. An emphasis should also be placed on searching for an appropriate diffusion barrier between adjacent materials, and if this barrier can be included in the AM process. One such material that should be considered would be MgSi due to its constituent elements' low vapor pressures.

Since this form of manufacturing involves laser interaction, the laser can also be used to post-process TEG materials after the initial melt process. A different parameter set may be able to be either empirically or semi-analytically modelled for a given material that would be used to anneal the thermoelectric after a layer deposition. Deliverables from this process could include a method for in-situ laser annealing, smoothing of physical features, decreasing porosity, and the introduction of stresses or strains into the system for thermoelectric enhancement.

#### 7. References

- [1] Lawrence Livermore National Laboratory, Estimated U.S. Energy Consumption in 2018, (2018). https://flowcharts.llnl.gov/content/assets/images/charts/Energy/Energ y\_2018\_United-States.png (accessed October 17, 2019).
- [2] D.M. Rowe, M.S. El-Genk, H.H. Saber, Modeling and optimization of segmented thermoelectric generators for terrestrial and space applications, in: Thermoelectr. Handb. Macro Nano, CRC Press, 2005: pp. 43–1.
- [3] Y.M. Belov, S.M. Maniakin, I.V. Morgunov, Review of Methods of Thermoelectric Materials Mass Production, Thermoelectr. Handb. Macro Nano (2005) 20–1.
- [4] S. LeBlanc, Thermoelectric generators: Linking material properties and systems engineering for waste heat recovery applications, Sustain. Mater. Technol. 1–2 (2014) 26–35. https://doi.org/10.1016/j.susmat.2014.11.002.
- [5] S. LeBlanc, S.K. Yee, M.L. Scullin, C. Dames, K.E. Goodson, Material and manufacturing cost considerations for thermoelectrics, Renew. Sustain. Energy Rev. 32 (2014) 313–327. https://doi.org/10.1016/j.rser.2013.12.030.
- [6] A. El-Desouky, M. Carter, M.A. Andre, P.M. Bardet, S. LeBlanc, Rapid processing and assembly of semiconductor thermoelectric materials for energy conversion devices, Mater. Lett. (n.d.). https://doi.org/10.1016/j.matlet.2016.07.152.
- [7] A. Montecucco, J. Siviter, A.R. Knox, The effect of temperature mismatch on thermoelectric generators electrically connected in series and parallel, Appl. Energy 123 (2014) 47–54. https://doi.org/10.1016/j.apenergy.2014.02.030.
- [8] D.M. Powell, M.T. Winkler, H.J. Choi, C.B. Simmons, D.B. Needleman, T. Buonassisi, Crystalline silicon photovoltaics: a cost analysis framework for determining technology pathways to reach baseload electricity costs, Energy Environ. Sci. 5 (2012) 5874–5883.
- [9] X.F. Zheng, C.X. Liu, Y.Y. Yan, Q. Wang, A review of thermoelectrics research – Recent developments and potentials for sustainable and

- renewable energy applications, Renew. Sustain. Energy Rev. 32 (2014) 486–503. https://doi.org/10.1016/j.rser.2013.12.053.
- [10] Y. Gelbstein, Z. Dashevsky, M.P. Dariel, Design, synthesis and characterization of graded n-type PbTe, in: Twenty-First Int. Conf. Thermoelectr. 2002 Proc. ICT 02, 2002: pp. 9–12. https://doi.org/10.1109/ICT.2002.1190253.
- [11] G.J. Snyder, T.S. Ursell, Thermoelectric Efficiency and Compatibility, Phys. Rev. Lett. 91 (2003) 148301. https://doi.org/10.1103/PhysRevLett.91.148301.
- [12] G.J. Snyder, E.S. Toberer, Complex thermoelectric materials, Nat. Mater. 7 (2008) 105–114. https://doi.org/10.1038/nmat2090.
- [13] S.R. Brown, S.M. Kauzlarich, F. Gascoin, G.J. Snyder, Yb14MnSb11: New High Efficiency Thermoelectric Material for Power Generation, Chem. Mater. 18 (2006) 1873–1877. https://doi.org/10.1021/cm060261t.
- [14] Z. Ouyang, D. Li, Modelling of segmented high-performance thermoelectric generators with effects of thermal radiation, electrical and thermal contact resistances, Sci. Rep. 6 (2016). http://www.ncbi.nlm.nih.gov/pmc/articles/PMC4823787/ (accessed November 16, 2016).
- [15] G. Min, D.M. Rowe, Ring-structured thermoelectric module, Semicond. Sci. Technol. 22 (2007) 880. https://doi.org/10.1088/0268-1242/22/8/009.
- [16] A. Schmitz, C. Stiewe, E. Müller, Preparation of Ring-Shaped Thermoelectric Legs from PbTe Powders for Tubular Thermoelectric Modules, J. Electron. Mater. 42 (2013) 1702–1706. https://doi.org/10.1007/s11664-012-2402-1.
- [17] N. Su, P. Zhu, Y. Pan, F. Li, B. Li, 3D-printing of shape-controllable thermoelectric devices with enhanced output performance, Energy 195 (2020). https://doi.org/10.1016/j.energy.2019.116892.
- [18] A. El-Desouky, A.L. Read, P.M. Bardet, M. Andre, S. LeBlanc, Selective Laser Melting of a Bismuth Telluride Thermoelectric Materials, (n.d.). http://sffsymposium.engr.utexas.edu/sites/default/files/2015/2015-86-ElDesouky.pdf (accessed November 17, 2016).

- [19] T. Zhang, M. Tewolde, K.-H. Kim, D.-M. Seo, J.P. Longtin, D.J. Hwang, Laser-assisted manufacturing of thermal energy devices, in: SPIE LASE, International Society for Optics and Photonics, 2016: pp. 973517–973517. http://proceedings.spiedigitallibrary.org/proceeding.aspx?articleid=25 04162 (accessed November 17, 2016).
- [20] Y. Kinemuchi, M. Mikami, I. Terasaki, W. Shin, Rapid synthesis of thermoelectric compounds by laser melting, Mater. Des. 106 (2016) 30–36.
- [21] J. Shi, H. Chen, S. Jia, W. Wang, 3D printing fabrication of porous bismuth antimony telluride and study of the thermoelectric properties, J. Manuf. Process. 37 (2019) 370–375. https://doi.org/10.1016/j.jmapro.2018.11.001.
- [22] Y. Du, J. Chen, Q. Meng, Y. Dou, J. Xu, S.Z. Shen, Thermoelectric materials and devices fabricated by additive manufacturing, Vacuum 178 (2020). https://doi.org/10.1016/j.vacuum.2020.109384.
- [23] R. Welch, D. Hobbis, G. Nolas, S. LeBlanc, Meso-, micro-, and nanostructures induced in bismuth telluride thermoelectric materials by laser additive manufacturing, in: Energy Harvest. Storage Mater. Devices Appl. X, SPIE, 2020: pp. 30–35. https://doi.org/10.1117/12.2558676.
- [24] M. Bian, Z. Xu, X. Tang, H. Jia, Y. Wang, A. Cabot, Solution-based 3D printed thermoelectric composite for custom-shaped thermoelectric generator applications, J. Alloys Compd. 976 (2024) 173202. https://doi.org/10.1016/j.jallcom.2023.173202.
- [25] C.V. Headley, R.J. Herrera del Valle, J. Ma, P. Balachandran, V. Ponnambalam, S. LeBlanc, D. Kirsch, J.B. Martin, The development of an augmented machine learning approach for the additive manufacturing of thermoelectric materials, J. Manuf. Process. 116 (2024) 165–175. https://doi.org/10.1016/j.jmapro.2024.02.045.
- [26] J. Shi, Z. Tong, C. Wang, B. Li, S. Cao, Y. Hu, Z. Wang, J. Peng, Predictable thermoelectric performance of directly synthesized Bi0.5Sb1.5Te3 using laser powder bed fusion additive manufacturing, Ceram. Int. 50 (2024) 2921–2930. https://doi.org/10.1016/j.ceramint.2023.11.035.
- [27] D. Khatamsaz, A. Molkeri, R. Couperthwaite, J. James, R. Arróyave, D. Allaire, A. Srivastava, Efficiently exploiting process-structure-

- property relationships in material design by multi-information source fusion, Acta Mater. 206 (2021) 116619.
- [28] T.G. Gallmeyer, S. Moorthy, B.B. Kappes, M.J. Mills, B. Amin-Ahmadi, A.P. Stebner, Knowledge of process-structure-property relationships to engineer better heat treatments for laser powder bed fusion additive manufactured Inconel 718, Addit. Manuf. 31 (2020) 100977.
- [29] D.L. McDowell, R.A. LeSar, The need for microstructure informatics in process–structure–property relations, MRS Bull. 41 (2016) 587–593.
- [30] G.B. Olson, Computational Design of Hierarchically Structured Materials, Science 277 (1997) 1237–1242. https://doi.org/10.1126/science.277.5330.1237.
- [31] W.J. Sames, F.A. List, S. Pannala, R.R. Dehoff, S.S. Babu, The metallurgy and processing science of metal additive manufacturing, Int. Mater. Rev. 61 (2016) 315–360. https://doi.org/10.1080/09506608.2015.1116649.
- [32] H.-S. Kim, S.-J. Hong, Thermoelectric properties of n-type 95%Bi2Te3–5%Bi2Se3 compounds fabricated by gas-atomization and spark plasma sintering, J. Alloys Compd. 586 (2014) S428–S431. https://doi.org/10.1016/j.jallcom.2013.05.163.
- [33] P. Dharmaiah, H.-S. Kim, C.-H. Lee, S.-J. Hong, Influence of powder size on thermoelectric properties of p-type 25% Bi2Te375% Sb2Te3 alloys fabricated using gas-atomization and spark-plasma sintering, J. Alloys Compd. 686 (2016) 1–8.
- [34] J.-G. Kwon, B. Madavali, Y.-E. Lee, S.-J. Jo, M. Shin, J.-W. Song, J.-W. Lee, S.-J. Hong, Realizing high thermoelectric properties through the development of bimodal microstructures using water atomized p-type Bi0.5Sb1.5Te3 alloys, Mater. Res. Bull. 177 (2024) 112823. https://doi.org/10.1016/j.materresbull.2024.112823.
- [35] Q. Hu, D. Luo, J. Guo, W. Qiu, 3D Printing of Bi2Te3-Based Thermoelectric Materials with High Performance and Shape Controllability, ACS Appl. Mater. Interfaces 15 (2023) 38623–38632. https://doi.org/10.1021/acsami.3c08116.
- [36] B. Chen, M. Kruse, B. Xu, R. Tutika, W. Zheng, M.D. Bartlett, Y. Wu, J.C. Claussen, Flexible thermoelectric generators with inkjet-printed bismuth telluride nanowires and liquid metal contacts, Nanoscale 11 (2019) 5222–5230.

- [37] K. Kato, H. Hagino, K. Miyazaki, Fabrication of Bismuth Telluride Thermoelectric Films Containing Conductive Polymers Using a Printing Method, J. Electron. Mater. 42 (2013) 1313–1318. https://doi.org/10.1007/s11664-012-2420-z.
- [38] A. Amin, R. Huang, D. Newbrook, V. Sethi, S. Yong, S. Beeby, I. Nandhakumar, Screen-printed bismuth telluride nanostructured composites for flexible thermoelectric applications, J. Phys. Energy 4 (2022) 024003.
- [39] M. Tewolde, G. Fu, D.J. Hwang, L. Zuo, S. Sampath, J.P. Longtin, Thermoelectric device fabrication using thermal spray and laser micromachining, J. Therm. Spray Technol. 25 (2016) 431–440.
- [40] F.R. Caliari, H. Lee, S. Sampath, Optimization of All-Oxide 2D Layered Thermoelectric Device Fabricated by Plasma Spray, J. Therm. Spray Technol. 29 (2020) 1815–1826. https://doi.org/10.1007/s11666-020-01085-8.
- [41] A.A. Baker, R. Thuss, N. Woollett, A. Maich, E. Stavrou, S.K. McCall, H.B. Radousky, Cold Spray Deposition of Thermoelectric Materials, JOM 72 (2020) 2853–2859. https://doi.org/10.1007/s11837-020-04151-2.
- [42] D.M. Rowe, Thermoelectrics Handbook: Macro to Nano, CRC Press, 2010.
- [43] M. Greifzu, R. Tkachov, L. Stepien, E. López, F. Brückner, C. Leyens, Laser Treatment as Sintering Process for Dispenser Printed Bismuth Telluride Based Paste, Materials 12 (2019) 3453. https://doi.org/10.3390/ma12203453.
- [44] H. Zhang, S. LeBlanc, Laser Additive Manufacturing Process Development for Bismuth Telluride Thermoelectric Material, J. Mater. Eng. Perform. 31 (2022) 6196–6204. https://doi.org/10.1007/s11665-022-07084-w.
- [45] A. El-Desouky, M. Carter, M. Mahmoudi, A. Elwany, S. LeBlanc, Influences of energy density on microstructure and consolidation of selective laser melted bismuth telluride thermoelectric powder, J. Manuf. Process. 25 (2017) 411–417.
- [46] Y. Mao, Y. Yan, K. Wu, H. Xie, Z. Xiu, J. Yang, Q. Zhang, C. Uher, X. Tang, Non-equilibrium synthesis and characterization of n-type Bi 2 Te 2.7 Se 0.3 thermoelectric material prepared by rapid laser melting and

- solidification, RSC Adv. 7 (2017) 21439–21445. https://doi.org/10.1039/C7RA02677C.
- [47] W.E. King, A.T. Anderson, R.M. Ferencz, N.E. Hodge, C. Kamath, S.A. Khairallah, A.M. Rubenchik, Laser powder bed fusion additive manufacturing of metals; physics, computational, and materials challenges, Appl. Phys. Rev. 2 (2015) 041304. https://doi.org/10.1063/1.4937809.
- [48] L. Thijs, F. Verhaeghe, T. Craeghs, J.V. Humbeeck, J.-P. Kruth, A study of the microstructural evolution during selective laser melting of Ti–6Al–4V, Acta Mater. 58 (2010) 3303–3312. https://doi.org/10.1016/j.actamat.2010.02.004.
- [49] D. Gu, Y. Shen, Balling phenomena in direct laser sintering of stainless steel powder: Metallurgical mechanisms and control methods, Mater. Des. 30 (2009) 2903–2910. https://doi.org/10.1016/j.matdes.2009.01.013.
- [50] A.B. Badiru, V.V. Valencia, D. Liu, Additive Manufacturing Handbook: Product Development for the Defense Industry, CRC Press, 2017.
- [51] L. Bian, N. Shamsaei, J. Usher, Laser-based Additive Manufacturing of Metal Parts: Modeling, Optimization, and Control of Mechanical Properties, CRC Press, 2017.
- [52] U.S. Bertoli, A.J. Wolfer, M.J. Matthews, J.-P.R. Delplanque, J.M. Schoenung, On the limitations of volumetric energy density as a design parameter for selective laser melting, Mater. Des. 113 (2017) 331–340.
- [53] K.G. Prashanth, S. Scudino, T. Maity, J. Das, J. Eckert, Is the energy density a reliable parameter for materials synthesis by selective laser melting?, Mater. Res. Lett. 5 (2017) 386–390.
- [54] W.M. Steen, J. Mazumder, Laser material processing, Springer Science & Business Media, 2010.
- [55] N.P. Lavery, S.G. Brown, J. Sienz, J. Cherry, F. Belblidia, A review of Computational Modelling of Additive Layer Manufacturing–multi-scale and multi-physics, Sustain. Des. Manuf. 651 (2014) 673.
- [56] W. King, A.T. Anderson, R.M. Ferencz, N.E. Hodge, C. Kamath, S.A. Khairallah, Overview of modelling and simulation of metal powder bed fusion process at Lawrence Livermore National Laboratory, Mater. Sci.

- Technol. 31 (2015) 957–968. https://doi.org/10.1179/1743284714Y.0000000728.
- [57] D. Rosenthal, Mathematical theory of heat distribution during welding and cutting, Weld. J. 20 (1941) 220–234.
- [58] H.E. Cline, Tr. Anthony, Heat treating and melting material with a scanning laser or electron beam, J. Appl. Phys. 48 (1977) 3895–3900.
- [59] H. Bikas, P. Stavropoulos, G. Chryssolouris, Additive manufacturing methods and modelling approaches: a critical review, Int. J. Adv. Manuf. Technol. 83 (2016) 389–405. https://doi.org/10.1007/s00170-015-7576-2.
- [60] D. Bäuerle, Laser Processing and Chemistry, Springer Science & Business Media, 2011.
- [61] A.J. Ghajar, Y.A.C. Dr, Heat and Mass Transfer: Fundamentals and Applications, McGraw-Hill Education, 2014.
- [62] D. Bäuerle, Laser Processing and Chemistry, Springer Science & Business Media, 2011.
- [63] A.V. Gusarov, J.-P. Kruth, Modelling of radiation transfer in metallic powders at laser treatment, Int. J. Heat Mass Transf. 48 (2005) 3423– 3434. https://doi.org/10.1016/j.ijheatmasstransfer.2005.01.044.
- [64] A.V. Gusarov, I. Yadroitsev, Ph. Bertrand, I. Smurov, Model of Radiation and Heat Transfer in Laser-Powder Interaction Zone at Selective Laser Melting, J. Heat Transf. 131 (2009) 072101-072101– 10. https://doi.org/10.1115/1.3109245.
- [65] D. Baillis, J.-F. Sacadura, Thermal radiation properties of dispersed media: theoretical prediction and experimental characterization, J. Quant. Spectrosc. Radiat. Transf. 67 (2000) 327–363. https://doi.org/10.1016/S0022-4073(99)00234-4.
- [66] J.R. Howell, M.P. Menguc, R. Siegel, M.P. Menguc, R. Siegel, Thermal Radiation Heat Transfer, CRC Press, 2015. https://doi.org/10.1201/b18835.
- [67] R.P. Chhabra, CRC handbook of thermal engineering, CRC press, 2017.

- [68] M. Tancrez, J. Taine, Direct identification of absorption and scattering coefficients and phase function of a porous medium by a Monte Carlo technique, Int. J. Heat Mass Transf. 47 (2004) 373–383.
- [69] F.L. Pedrotti, L.S. Pedrotti, L.M. Pedrotti, Introduction to Optics, Pearson Prentice Hall, 2007.
- [70] V.M. Glazov, S.N. Chizhevskaya, N.N. Glagoleva, Liquid semiconductors, PLENUM PRESS N. Y. 1969 362 P (1969).
- [71] F. Thümmler, R. Oberacker, An Introduction to Powder Metallurgy, Institute of Materials, 1993.
- [72] L.E. Criales, T. Özel, Temperature profile and melt depth in laser powder bed fusion of Ti-6Al-4V titanium alloy, Prog. Addit. Manuf. 2 (2017) 169–177.
- [73] I.A. Roberts, C.J. Wang, R. Esterlein, M. Stanford, D.J. Mynors, A three-dimensional finite element analysis of the temperature field during laser melting of metal powders in additive layer manufacturing, Int. J. Mach. Tools Manuf. 49 (2009) 916–923.
- [74] A. Hussein, L. Hao, C. Yan, R. Everson, Finite element simulation of the temperature and stress fields in single layers built without-support in selective laser melting, Mater. Des. 1980-2015 52 (2013) 638–647.
- [75] G.R. Hadley, Thermal conductivity of packed metal powders, Int. J. Heat Mass Transf. 29 (1986) 909–920.
- [76] A.V. Gusarov, T. Laoui, L. Froyen, V.I. Titov, Contact thermal conductivity of a powder bed in selective laser sintering, Int. J. Heat Mass Transf. 46 (2003) 1103–1109.
- [77] M. Rombouts, L. Froyen, A.V. Gusarov, E. Bentefour, C. Glorieux, Photopyroelectric measurement of thermal conductivity of metallic powders, J. Appl. Phys. 97 (2005). https://pubs.aip.org/aip/jap/article/97/2/024905/930563 (accessed November 1, 2024).
- [78] I.Y. Kashkooli, Z.A. Munir, The equilibrium and free surface sublimation pressures of oriented single crystals of bismuth telluride, J. Electrochem. Soc. 117 (1970) 248–250.

- [79] M. Stafe, A. Marcu, N.N. Puscas, Pulsed Laser Ablation of Solids: Basics, Theory and Applications, Springer Science & Business Media, 2013.
- [80] D.J. Heath, B. Mills, M. Feinaeugle, R.W. Eason, Rapid bespoke laser ablation of variable period grating structures using a digital micromirror device for multi-colored surface images, Appl. Opt. 54 (2015) 4984– 4988. https://doi.org/10.1364/AO.54.004984.
- [81] D.L. Greenaway, G. Harbeke, Band structure of bismuth telluride, bismuth selenide and their respective alloys, J. Phys. Chem. Solids 26 (1965) 1585–1604. https://doi.org/10.1016/0022-3697(65)90092-2.
- [82] N.P. Gorbachuk, V.R. Sidorko, Heat Capacity and Enthalpy of Bi 2 Si 3 and Bi 2 Te 3 in the Temperature Range 58-1012 K, Powder Metall. Met. Ceram. 43 (2004) 284–290.
- [83] I. Gibson, D. Rosen, B. Stucker, Additive Manufacturing Technologies: 3D Printing, Rapid Prototyping, and Direct Digital Manufacturing, 2nd ed., Springer-Verlag, New York, 2015. https://www.springer.com/gp/book/9781493921126 (accessed April 3, 2019).
- [84] J. Ready, Effects of High-Power Laser Radiation, Elsevier, 2012.
- [85] V. Alexiades, Mathematical Modeling Of Melting And Freezing Processes, Routledge, 2018.
- [86] G.G. Gladush, I. Smurov, Physics of Laser Materials Processing: Theory and Experiment, Springer-Verlag, Berlin Heidelberg, 2011. https://doi.org/10.1007/978-3-642-19831-1.
- [87] Z. Fan, F. Liou, Z. Fan, F. Liou, Numerical Modeling of the Additive Manufacturing (AM) Processes of Titanium Alloy, in: Titan. Alloys -Achiev. Enhanc. Prop. Divers. Appl., IntechOpen, 2012. https://doi.org/10.5772/34848.
- [88] J.J.S. Dilip, S. Zhang, C. Teng, K. Zeng, C. Robinson, D. Pal, B. Stucker, Influence of processing parameters on the evolution of melt pool, porosity, and microstructures in Ti-6Al-4V alloy parts fabricated by selective laser melting, Prog. Addit. Manuf. 2 (2017) 157–167. https://doi.org/10.1007/s40964-017-0030-2.
- [89] H. Bando, K. Koizumi, Y. Oikawa, K. Daikohara, V.A. Kulbachinskii, H. Ozaki, The time-dependent process of oxidation of the surface of

- Bi2Te3 studied by x-ray photoelectron spectroscopy, J. Phys. Condens. Matter 12 (2000) 5607.
- [90] M. Malvern Instruments Ltd, Mastersizer 3000 User Manual, Malvern Instrum. Ltd UK (2015).
- [91] C. Chen, B. Zhang, D. Liu, Z. Ge, Thermoelectric properties of CuyBixSb2- x- yTe3 alloys fabricated by mechanical alloying and spark plasma sintering, Intermetallics 25 (2012) 131–135.
- [92] J.J. Ritter, P. Maruthamuthu, Synthesis of Fine-Powder Polycrystalline Bi- Se- Te, Bi- Sb- Te, and Bi- Sb- Se- Te Alloys, Inorg. Chem. 36 (1997) 260–263.
- [93] C.L. Yaws, Handbook of vapor pressure: volume 4: inorganic compounds and elements, Gulf Professional Publishing, 1995.
- [94] V.R. Akshay, M.V. Suneesh, M. Vasundhara, Tailoring thermoelectric properties through structure and morphology in chemically synthesized n-type bismuth telluride nanostructures, Inorg. Chem. 56 (2017) 6264– 6274.
- [95] M.M. Stasova, N.K. Abrikosov, The radiographical analysis of the solid solution in system Bi-Sb-Te, Izv. Akad. Nauk SSSR Neorganicheskie Mater. 6 (1970) 1090.
- [96] T.L. Anderson, H.B. Krause, Refinement of the Sb <sub>2</sub> Te <sub>3</sub> and Sb <sub>2</sub> Te <sub>2</sub> Se structures and their relationship to nonstoichiometric Sb <sub>2</sub> Te <sub>3-y</sub> Se <sub>y</sub> compounds, Acta Crystallogr. B 30 (1974) 1307–1310. https://doi.org/10.1107/S0567740874004729.
- [97] W.F. Ehret, M.B. Abramson, The Nature of the Solid Phase in the System Antimony—Bismuth <sup>1</sup>, J. Am. Chem. Soc. 56 (1934) 385–388. https://doi.org/10.1021/ja01317a031.
- [98] C. Pérez Vicente, J.L. Tirado, K. Adouby, J.C. Jumas, A.A. Touré, G. Kra, X-ray Diffraction and <sup>119</sup> Sn Mössbauer Spectroscopy Study of a New Phase in the Bi <sub>2</sub> Se <sub>3</sub> –SnSe System: SnBi <sub>4</sub> Se <sub>7</sub>, Inorg. Chem. 38 (1999) 2131–2135. https://doi.org/10.1021/ic9812858.
- [99] J.F. Dumas, G. Brun, B. Liautard, J.C. Tedenac, M. Maurin, New contribution in the study of the Bi2Te3-Bi2Se3 system, Thermochim. Acta 122 (1987) 135–141. https://doi.org/10.1016/0040-6031(87)80113-2.

- [100] G.R. Miller, C. Li, C.W. Spencer, Properties of Bi <sub>2</sub> Te <sub>3</sub> -Bi <sub>2</sub> Se <sub>3</sub> Alloys, J. Appl. Phys. 34 (1963) 1398–1400. https://doi.org/10.1063/1.1729588.
- [101] B. Eisenmann, H. Schäfer, Sulfides, Selenides, Tellurides (Part 1), Springer Berlin Heidelberg, Berlin, Heidelberg, 1986. https://doi.org/10.1007/b19991.
- [102] S. Pal, M. Finšgar, R. Hudák, V. Rajťúková, T. Brajlih, N. Gubeljak, I. Drstvenšek, Mechanisms of defect formation in Ti-6Al-4V product during re-melting of layers in selective laser melting, J. Manuf. Process. 105 (2023) 260–275. https://doi.org/10.1016/j.jmapro.2023.09.044.
- [103] N.S. Lidorenko, O.M. Narva, L.D. Dudkin, R.S. Erofeev, Influence of porosity and intergrain-boundary quality on the electrical and thermal conductivities of semiconductive thermoelectric materials, Inorg Mater 6 (1970) 1853.
- [104] H. Lee, D. Vashaee, D.Z. Wang, M.S. Dresselhaus, Z.F. Ren, G. Chen, Effects of nanoscale porosity on thermoelectric properties of SiGe, J. Appl. Phys. 107 (2010). https://pubs.aip.org/aip/jap/article/107/9/094308/369855 (accessed January 14, 2025).
- [105] H. Chen, H. Xiang, F.-Z. Dai, J. Liu, Y. Lei, J. Zhang, Y. Zhou, High porosity and low thermal conductivity high entropy (Zr0. 2Hf0. 2Ti0. 2Nb0. 2Ta0. 2) C, J. Mater. Sci. Technol. 35 (2019) 1700–1705.
- [106] J. Feng, W. Wang, S. Huang, B. Jiang, B. Zhu, Y. Zhou, J. Cui, P. Lin, L. Xie, J. He, Porous Thermoelectric Zintl: YbCd<sub>2</sub>Sb<sub>2</sub>, ACS Appl. Energy Mater. 4 (2021) 913–920. https://doi.org/10.1021/acsaem.0c02825.
- [107] L. Yang, D. Huh, R. Ning, V. Rapp, Y. Zeng, Y. Liu, S. Ju, Y. Tao, Y. Jiang, J. Beak, High thermoelectric figure of merit of porous Si nanowires from 300 to 700 K, Nat. Commun. 12 (2021) 3926.
- [108] S. Li, W. Zhao, X.-L. Shi, L. Wang, S. Pan, G. Cheng, W.-D. Liu, M. Li, K. Guo, Z.-G. Chen, F. Pan, Designing cost-performance porous thermoelectric materials by interface engineering through atomic layer deposition, J. Mater. Sci. Technol. 214 (2025) 194–203. https://doi.org/10.1016/j.jmst.2024.06.037.

- [109] L. Denti, A. Sola, S. Defanti, C. Sciancalepore, F. Bondioli, Effect of powder recycling in laser-based powder bed fusion of Ti-6Al-4V, Manuf. Technol. 19 (2019) 190–196.
- [110] H. Gu, H. Gong, J.J.S. Dilip, D. Pal, A. Hicks, H. Doak, B. Stucker, Effects of powder variation on the microstructure and tensile strength of Ti6Al4V parts fabricated by selective laser melting, in: Proc. 25th Annu. Int. Solid Free. Fabr. Symp. Austin TX USA, 2014: pp. 4–6.
- [111] M.V. Cino, Design and Implementation of an Extensive Test Facility for Thermoelectric Materials and Devices, MASc Thesis, 2014.
- [112] R.J. Buist, A New Method for Testing Thermoelectric Materials and Devices, in: TE Technology, Inc., Arlington, Texas, USA, 1992. http://www.tetech.com/publications/pubs/ICT92RJB.pdf.
- [113] W.P. Lin, D.E. Wesolowski, C.C. Lee, Barrier/bonding layers on bismuth telluride (Bi2Te3) for high temperature thermoelectric modules, J. Mater. Sci. Mater. Electron. 22 (2011) 1313–1320. https://doi.org/10.1007/s10854-011-0306-0.
- [114] M.F. Modest, Radiative Heat Transfer, Academic Press, 2013.
- [115] J. Stewart, Calculus: Early Transcendentals, Thomson Brooks/Cole, 2008.
- [116] K. Cole, J. Beck, A. Haji-Sheikh, B. Litkouhi, Heat Conduction Using Greens Functions, Taylor & Francis, 2010.
- [117] H.S. Carslaw, J.C. Jaeger, Conduction of Heat in Solids, Clarendon Press, 1986.
- [118] D.W. Hahn, M.N. Özisik, Heat Conduction, John Wiley & Sons, 2012.
- [119] E.C. Titchmarsh, Introduction to the theory of Fourier integrals, (1948).
- [120] E.R. Hedrick, Tables of integrals and other mathematical data, New York, The Macmillan Company, 1957.

## 8. Appendices

#### A.1 Solution to the Radiative Transfer Equation

The Radiative Transfer Equation (RTE) describes the energy conservation along a given path r of light that enters a scattering and absorbing medium within an infinitesimally small solid angle  $d\Omega'$ . It is given in equation (A1.1).

$$\hat{\mathbf{s}} \cdot \nabla I(\mathbf{r}, \hat{\mathbf{s}}) = \kappa I_b(\mathbf{r}) - \beta I(\mathbf{r}, \hat{\mathbf{s}}) + \frac{\sigma_s}{4\pi} \int_{4\pi} I(\mathbf{r}, \hat{\mathbf{s}}') \Phi(\hat{\mathbf{s}}', \hat{\mathbf{s}}) d\Omega' \qquad \left[ \frac{W}{m^3} \right]$$
 (A1.1)

Where  $\kappa$  and  $\sigma_s$  are the absorption and scattering coefficients of the medium at a given wavelength. The scattering phase function  $\Phi(\hat{s}',\hat{s})$  represents the probability that light entering the medium from direction  $\hat{s}'$  will scatter in the direction of  $\hat{s}$ . For isotropic scattering, which is a reasonable assumption for a light interacting with powder, this function is equal to unity [63,64]. The emission term denoted by the subscript b can be omitted when solving the RTE for an incident laser intensity since the temperature of the medium is generally not high enough during the laser interaction time to contribute any significant radiation loss [114].

The terms on the right hand side in the RTE can be described in order as follows; the gain in intensity due to emission minus the sum of losses due to absorption and scattering outwards, plus the gain from inward

scattering [5]. Some simplifications can be performed to reduce equation (A1.1) into simpler notation as seen in [64]. The scattering albedo  $\omega$  for a given wavelength is related to the scattering and absorption coefficients through the following relation:

$$\omega = \frac{\sigma_{s}}{\beta} \tag{A1.2}$$

The reliability on the solid angle of incidence and scattering can be reduced based on the definition of a solid angle for in equation (A1.3) [114]. Here,  $\theta$  refers to the incident or scattering angle with respect to the surface normal, and  $\phi$  is the azimuthal angle. The direction vector  $\hat{s}$  is defined in [114] by equation (A1.4) and is composed of both  $\theta$  and  $\phi$ , where  $\hat{t}_1$  and  $\hat{t}_2$  are orthogonal unit vectors on the material surface. Gusarov makes a simplification by integrating the RTE over the  $2\pi$  azimuth component to place it only in terms of the incident and scattering angle [64].

$$\int_{4\pi} d\Omega = \int_{\phi=0}^{2\pi} \int_{\theta=0}^{\pi} \sin\theta d\theta d\phi$$
 [sr] (A1.3)

$$\hat{\mathbf{s}} = \cos\theta \hat{\mathbf{n}} + \sin\theta (\cos\phi \hat{\mathbf{t}}_1 + \sin\phi \hat{\mathbf{t}}_2)$$
(A1.4)

Taking the integral through  $\phi$  creates a new direction vector that is independent of azimuth angle, provided in equation (A1.5).

$$\hat{\mathbf{s}}_{new} = \cos\theta \,\hat{\mathbf{n}} \tag{A1.5}$$

Substituting equation (A1.2) and (A1.5) into equation (A1.1), integrating over the azimuth in the scattering term and removing the emission term, the RTE is updated below.

$$\hat{\mathbf{s}}_{new} \cdot \nabla I(\mathbf{r}, \hat{\mathbf{s}}_{new})$$

$$= -\beta I(\mathbf{r}, \hat{\mathbf{s}}_{new}) + \frac{\beta \omega}{4\pi}$$

$$\cdot \left(2\pi \int_{\theta'=0}^{\pi} I(\mathbf{r}, \hat{\mathbf{s}}'_{new}) \Phi(\hat{\mathbf{s}}'_{new}, \hat{\mathbf{s}}_{new}) \sin \theta' d\theta'\right)$$
(A1.6)

Dropping the vector notation, changing the path of r to simply the z-direction and substituting  $\mu = cos\theta$ , the one-dimensional RTE can be finally written as equation (A1.7) where again  $\mu'$  represents incident angle and  $\mu$  represents scattering angle. Updated versions of the solid angle from equation (A1.3) and phase function are also provided in terms of  $\mu$  in equations (A1.8) and (A1.9) respectively.

$$\mu \frac{dI(z,\mu)}{dz} = \beta \left\{ \frac{\omega}{2} \int_{-1}^{1} I(z,\mu') P(\mu',\mu) d\mu' - I(z,\mu) \right\} \qquad \left[ \frac{W}{m^3} \right] \quad (A1.7)$$

$$\int_{4\pi} d\Omega = \int_{\phi=0}^{2\pi} \int_{\mu=-1}^{1} d\mu d\phi \qquad [sr] \quad (A1.8)$$

$$P(\theta', \theta) = \frac{1}{2\pi} \int_0^{2\pi} P(\mu', \mu) d\phi = 1 \text{ for isotropic scattering}$$
 (A1.9)

The laser radiation is modelled as collimated incident radiation on the boundary surface. Beginning with the upper boundary condition at z=0, the general relationship between incident collimated radiation at a certain incident angle  $\theta_o$  and azimuth angle  $\phi_o$  is provided in equation (A1.10) from [114].

$$I(0,\mu,\phi) = Q_o \delta(\mu - \mu_o) \delta(\phi - \phi_o) \qquad \left[ \frac{W}{m^2 \cdot sr} \right] \quad (A1.10)$$

However, since the intensity is isotropic, both sides are integrated over  $2\pi$  in  $\phi$  to account for incidence from all azimuthal angles. This provides a top boundary condition independent of azimuth angle.

$$I(0,\mu) \cdot 2\pi = Q_o \delta(\mu - \mu_o) \qquad \left[\frac{W}{m^2}\right] \quad (A1.11)$$

Assuming normal incidence ( $\theta_0$ =0), this provides  $\mu_o = \cos(0) = 1$  and the upper boundary condition is therefore written as equation (A1.12),

$$I(0,\mu) = \frac{Q_o}{2\pi}\delta(\mu - 1) \qquad \qquad \mu > 0 \quad \left[\frac{W}{m^2}\right]$$
(A1.12)

where  $Q_o$  is the power density on the surface in  $\left[\frac{W}{m^2}\right]$ , and the possible angles of incidence correspond to  $\mu > 0$ . The bottom boundary condition is at the interface between the powder layer and the substrate surface. At the substrate, z=L and the corresponding boundary condition is given in equation (A1.13) where  $R_s$  is the reflectivity of the substrate.

$$I(L,\mu) = R_s I(L,-\mu) \qquad \qquad \mu < 0 \quad \left[\frac{W}{m^2}\right] \text{ (A1.13)}$$

The general solution to the RTE for collimated laser radiation normally incident at the top surface will be assumed to take the form in accordance with the two-flux method. The solution will have a forward collimated term, a backward reflected collimated term and a diffuse term [63,64,66,114]. This solution is given in equation (A1.14).

$$I(z,\mu) = I_{c+}(z,\mu) + I_{c-}(z,\mu) + F(z,\mu)$$
  $\left[\frac{W}{m^2}\right]$  (A1.14)

The above equation describes the superposition of collimated and diffuse terms and can be separated as such so that each component can be solved for independently.

## A.1.1. Collimated Component

The forward and backward normally incident collimated intensities are the respective first and second terms in equation (A1.14). Correspondingly, the forward and backward power densities as a function of depth into the z-direction are  $Q_+(z)$  and  $Q_-(z)$ . This creates two collimated solutions for the top and bottom surface involving the Dirac-delta function,  $\delta$ :

$$I_{c+}(z,\mu) = \frac{Q_{+}(z)}{2\pi}\delta(\mu - 1)$$
  $\mu > 0$   $\left[\frac{W}{m^2}\right]$  (A1.15)

$$I_{c-}(z,\mu) = \frac{Q_{-}(z)}{2\pi}\delta(\mu - 1) \qquad \qquad \mu < 0 \qquad \qquad \left[\frac{W}{m^2}\right] \tag{A1.16}$$

These power densities can be solved for by inserting each of these equations into the RTE given in equation (A1.7), however the integral term describing diffuse scattering will not be evaluated at this point. The contribution of the collimated beam portions to the diffuse component will be carried over to the diffuse solution to the RTE given in the following section. Again, this can be performed due to the principle of superposition. Performing the aforementioned substitutions, two separate equations are generated:

$$\mu \frac{dI_{c+}(z,\mu)}{dz} = \mu \left( \frac{\delta(\mu-1)}{2\pi} \frac{dQ_{+}(z)}{dz} \right) = -\beta \left( \frac{Q_{+}(z)}{2\pi} \delta(\mu-1) \right) \qquad \left[ \frac{W}{m^3} \right]$$
 (A1.17)

$$\mu \frac{dI_{c-}(z,\mu)}{dz} = \mu \left( \frac{\delta(\mu+1)}{2\pi} \frac{dQ_{-}(z)}{dz} \right) = -\beta \left( \frac{Q_{-}(z)}{2\pi} \delta(\mu+1) \right) \qquad \left[ \frac{W}{m^3} \right]$$
 (A1.18)

These simplify into the following equations, taking for the forward term  $\mu = \cos(0) = 1$  and for the backward term  $\mu = \cos(\pi) = -1$  due to reflection. Thus, the power densities are given as:

$$\frac{dQ_{+}(z)}{dz} = -\beta Q_{+}(z) \qquad \qquad \mu = \cos(0) = 1 \qquad \qquad \left[\frac{W}{m^3}\right]$$
 (A1.19)

$$\frac{dQ_{-}(z)}{dz} = +\beta Q_{-}(z) \qquad \qquad \mu = \cos(\pi) = -1 \qquad \left[\frac{W}{m^3}\right] \tag{A1.20}$$

Applying the boundary conditions in (A1.12) and (A1.13) to (A1.19) and (A1.20), respectively, the power densities can be solved for in the following manner:

$$\frac{dQ_{+}(z)}{Q_{+}(z)} = -\beta dz \qquad \left[\frac{W}{m^2}\right]$$
(A1.21)

$$Q_{+}(z) = C_{1}e^{-\beta z} + C_{2} \rightarrow Q_{+}(0) = Q_{o}e^{0} \rightarrow C_{1} = Q_{o}, C_{2}$$

$$= 0$$

$$\left[\frac{W}{m^{2}}\right] (A1.22)$$

$$Q_{+}(z) = Q_{o}e^{-\beta z} \qquad \left[\frac{W}{m^{2}}\right] \tag{A1.23}$$

Based on the back boundary condition being related to the forward collimated component, the backward component is solved for with the substitution of this boundary condition into the forward component solution defined above in (A1.23):

$$\frac{dQ_{-}(z)}{Q_{-}(z)} = \beta dz \qquad \left[\frac{W}{m^2}\right] \quad (A1.24)$$

$$Q_{-}(z) = C_3 e^{\beta z} + C_4$$
  $\left[\frac{W}{m^2}\right]$  (A1.25)

$$Q_{-}(L) = R_s Q_{+}(L) = R_s Q_o e^{-\beta L} = C_3 e^{\beta L} + C_4$$

$$\left[ \frac{W}{m^2} \right] \quad (A1.26)$$

$$\to C_3 = R_s Q_o e^{-2\beta L}, C_4 = 0$$

$$Q_{-}(z) = R_s Q_o e^{\beta z - 2\beta L}$$
 
$$\left[ \frac{W}{m^2} \right]$$
 (A1.27)

Thus the forward and reverse power densities that are present in the collimated terms of the solution have been solved for in equations (A1.23) and (A1.27).

### A.1.2. Diffuse Component

The diffuse contributions from the collimated sources above can now be calculated and included in the overall diffuse solution. Recall the RTE from equation (A1.7) written below but expanded.

$$\mu \frac{dI(z,\mu)}{dz} = \frac{\beta \omega}{2} \int_{-1}^{1} I(z,\mu') P(\mu',\mu) d\mu' - \beta I(z,\mu) \qquad \left[ \frac{W}{m^3} \right]$$
(A1.28)

The integral term in (A1.28) was omitted in the previous section because it calculates the contribution to diffuse radiation. The collimated term definitions given in equations (A1.15) and (A1.16) can be inserted into the integral term above with the limits of integration modified to allow incident angles of  $0 \le \mu' \le 1$  for the forward diffuse component and  $-1 \le \mu' \le 0$  for the backward diffuse component.

$$\begin{split} &\frac{\beta\omega}{2} \left\{ \int_{0}^{1} I_{c+}(z,\mu') P(\mu',\mu) d\mu' + \int_{-1}^{0} I_{c-}(z,\mu') P(\mu',\mu) d\mu' \right\} \\ &= \frac{\beta\omega}{2} \left\{ \int_{0}^{1} \left( \frac{Q_{+}(z)}{2\pi} \delta(\mu'-1) \right) P(\mu',\mu) d\mu' + \int_{-1}^{0} \left( \frac{Q_{-}(z)}{2\pi} \delta(\mu'+1) \right) P(\mu',\mu) d\mu' \right\} \end{split}$$

$$= \frac{\beta \omega}{2} \left\{ \frac{Q_{+}(z)}{2\pi} \int_{0}^{1} \delta(\mu' - 1) P(\mu', \mu) d\mu' + \frac{Q_{-}(z)}{2\pi} \int_{-1}^{0} \delta(\mu' + 1) P(\mu', \mu) d\mu' \right\}$$

$$= \frac{\beta \omega}{2} \left\{ \frac{Q_{+}(z)}{2\pi} P(1, \mu) + \frac{Q_{-}(z)}{2\pi} P(-1, \mu) \right\}$$
(A1.29)

Equation (A1.29) represents the contribution of the collimated components to diffuse scattering. The diffuse radiation solution to the RTE can now be solved for below by adding this term to the general RTE equation for the diffuse term,  $F(z, \mu)$ .

$$\mu \frac{dF(z,\mu)}{dz} = \frac{\beta \omega}{2} \left\{ \frac{Q_{+}(z)}{2\pi} P(1,\mu) + \frac{Q_{-}(z)}{2\pi} P(-1,\mu) \right\} + \frac{\beta \omega}{2} \int_{-1}^{1} F(z,\mu') P(\mu',\mu) d\mu' - \beta F(z,\mu)$$
 [\frac{W}{m^{3}}] (A1.30)

Continuing with the two-flux method, Gusarov proposes that the diffuse radiation can be approximated with a two term solution that is angularly dependent based on the forward and backward definitions above. This approximate solution is given below [64].

$$F(z,\mu) = F_{+}(z)H(\mu) + F_{-}(z)(1 - H(\mu)) \qquad \left[\frac{W}{m^{2}}\right]$$
(A1.31)

Here,  $H(\mu)$  is the Heaviside step function which acts to allow the forward (+) component to be nonzero for incident or scattered angles  $0 \le \mu \le 1$  and the backward (-) component to be negative for angles  $-1 \le \mu \le 0$ . Inserting

(A1.31) into the integral term of (A1.30) for incident angles allows the diffuse RTE solution to be further simplified.

$$\mu \frac{dF(z,\mu)}{dz} = \frac{\beta \omega}{2} \left\{ \frac{Q_{+}(z)}{2\pi} P(1,\mu) + \frac{Q_{-}(z)}{2\pi} P(-1,\mu) \right\}$$

$$+ \frac{\beta \omega}{2} \int_{-1}^{1} \left( F_{+}(z) H(\mu') + F_{-}(z) \left( 1 - H(\mu') \right) \right) P(\mu',\mu) d\mu' - \beta F(z,\mu)$$

$$\mu \frac{dF(z,\mu)}{dz} = \frac{\beta \omega}{2} \left\{ \frac{Q_{+}(z)}{2\pi} P(1,\mu) + \frac{Q_{-}(z)}{2\pi} P(-1,\mu) \right\} + \frac{\beta \omega}{2} \left( F_{+}(z) + F_{-}(z) \right) - \beta F(z,\mu)$$
(A1.32)

To obtain diffuse component for all *scattering* angles, the diffuse solution of (A1.31) can now be inserted into equation (A1.32) and an integral over the range  $-1 \le \mu \le 1$  must be performed.

$$\int_{-1}^{1} \mu \frac{dF(z,\mu)}{dz} d\mu = \frac{\beta \omega}{2} \left\{ \frac{Q_{+}(z)}{2\pi} \int_{-1}^{1} P(1,\mu) d\mu + \frac{Q_{-}(z)}{2\pi} \int_{-1}^{1} P(-1,\mu) d\mu \right\}$$

$$+ \frac{\beta \omega}{2} \left( F_{+}(z) + F_{-}(z) \right) \int_{-1}^{1} d\mu - \beta \int_{-1}^{1} F(z,\mu) d\mu$$
(A1.33)

However the substitution of the approximate diffuse solution (A1.31) now for scattered angles into (A1.33) necessitates the separation of integral ranges and creates two moment equation; one valid for  $0 \le \mu \le 1$  and the other for  $-1 \le \mu \le 0$ . Thus, (A1.33) is converted into the following two equations.

$$\int_0^1 \mu \frac{dF_+(z)}{dz} H(\mu) d\mu = \frac{\beta \omega}{2} \left\{ \frac{Q_+(z)}{2\pi} \int_0^1 P(1,\mu) d\mu + \frac{Q_-(z)}{2\pi} \int_0^1 P(-1,\mu) d\mu \right\}$$

$$+\frac{\beta\omega}{2}(F_{+}(z)+F_{-}(z))\int_{0}^{1}d\mu-\beta\int_{0}^{1}F_{+}(z)H(\mu)d\mu$$

$$\int_{-1}^{0} \mu \frac{dF_{-}(z)}{dz} (1 - H(\mu)) d\mu = \frac{\beta \omega}{2} \left\{ \frac{Q_{+}(z)}{2\pi} \int_{-1}^{0} P(1, \mu) d\mu + \frac{Q_{-}(z)}{2\pi} \int_{-1}^{0} P(-1, \mu) d\mu \right\}$$

$$+\frac{\beta\omega}{2}(F_{+}(z)+F_{-}(z))\int_{-1}^{0}d\mu-\beta\int_{-1}^{0}F_{-}(z)(1-H(\mu))d\mu$$

These further simplify below by evaluating the integrals:

$$\frac{1}{2}\frac{dF_{+}(z)}{dz} = \frac{\beta\omega}{2}\left\{\frac{Q_{+}(z)}{2\pi} + \frac{Q_{-}(z)}{2\pi}\right\} + \frac{\beta\omega}{2}\left(F_{+}(z) + F_{-}(z)\right) - \beta F_{+}(z)$$

$$-\frac{1}{2}\frac{dF_{-}(z)}{dz} = \frac{\beta\omega}{2}\left\{\frac{Q_{+}(z)}{2\pi} + \frac{Q_{-}(z)}{2\pi}\right\} + \frac{\beta\omega}{2}\left(F_{+}(z) + F_{-}(z)\right) - \beta F_{-}(z)$$

The above two equations can be factored and written in compact form:

$$\pm \frac{1}{2} \frac{dF_{\pm}(z)}{dz} = \beta \left( \frac{\omega}{2} \left( \frac{Q_{+}(z)}{2\pi} + \frac{Q_{-}(z)}{2\pi} + F_{+}(z) + F_{-}(z) \right) - F_{\pm}(z) \right)$$
(A1.34)

It is now time to introduce two dimensionless variables for length that will aid in the simplification of these moment equations.

$$\xi = \beta z \tag{A1.35}$$

$$\lambda = \beta L \tag{A1.36}$$

Equation (A1.35) normalizes any depth in the z-direction with the absorption coefficient  $\beta$  and (A1.36) does the same with the powder depth L. This

unitless depth  $\lambda$  is denoted as the optical thickness of the powder. These substitutions can be applied to equations (A1.23) and (A1.27) to normalize them as well:

$$Q_{+}(\xi) = Q_{o}e^{-\xi} \qquad \left[\frac{W}{m^{2}}\right] \quad (A1.37)$$

$$Q_{-}(\xi) = R_s Q_o e^{\xi - 2\lambda} \qquad \left[\frac{W}{m^2}\right] \quad (A1.38)$$

Equation (A1.40) can be normalized by introducing the dimensionless relationships for  $Q_{\pm}(\xi)$  and  $F_{\pm}(\xi)$ .

$$q_{\pm} = \frac{Q_{\pm}(\xi)}{Q_o} \tag{A1.39}$$

$$f_{\pm} = \frac{2\pi F_{\pm}(\xi)}{Q_o}$$
 (A1.40)

Substituting (A1.39) and (A1.40) into (A1.34) yield the following equation:

$$\pm \frac{1}{2} \left( \frac{Q_o}{2\pi} \right) \frac{df_{\pm}}{dz} = \beta \left( \frac{\omega}{2} \left( \frac{Q_o q_{+}}{2\pi} + \frac{Q_o q_{-}}{2\pi} + \frac{Q_o f_{+}}{2\pi} + \frac{Q_o f_{-}}{2\pi} \right) - \frac{Q_o f_{\pm}}{2\pi} \right)$$
(A1.41)

The derivative on the LHS of equation (A1.41) is in terms of z but needs to be in terms of  $\xi$  as defined in equation (A1.35). Therefore the following modification can be performed:

$$\frac{df_{\pm}}{dz} = \frac{df_{\pm}}{d\xi} \cdot \frac{d\xi}{dz} = \beta \frac{df_{\pm}}{d\xi}$$
 (A1.42)

Inserting (A1.42) into (A1.41) and dividing by the factor  $\frac{Q_0\beta}{2\pi}$  on both sides yields the dimensionless moment equations for  $\pm\frac{1}{2}\frac{df_\pm}{d\xi}$  which will be separated again below.

$$\frac{1}{2}\frac{df_{+}}{d\xi} = \frac{\omega}{2}(q_{+} + q_{-} + f_{+} + f_{-}) - f_{+}$$
(A1.43)

$$-\frac{1}{2}\frac{df_{-}}{d\xi} = \frac{\omega}{2}(q_{+} + q_{-} + f_{+} + f_{-}) - f_{-}$$
(A1.44)

Equations (A1.43) and (A1.44) can be added, as well as subtracted, to form two new differential equations of  $(f_+ - f_-)$  and  $(f_+ + f_-)$ , respectively. These manipulations are given in the following two equations, where both sides have also been multiplied by a factor of two to remove the  $\frac{1}{2}$  from the LHS and simplified.

$$\frac{d}{d\xi}(f_{+} - f_{-}) = 2\omega(q_{+} + q_{-}) + (2\omega - 2)(f_{+} + f_{-})$$
(A1.45)

$$\frac{d}{d\xi}(f_{+} + f_{-}) = -2(f_{+} - f_{-}) \tag{A1.46}$$

The second derivatives are then taken of the above two equations to yield:

$$\frac{d^2}{d\xi^2}(f_+ - f_-) = 2\omega \frac{d}{d\xi} (q_+ + q_-) + (2\omega - 2) \frac{d}{d\xi} (f_+ + f_-)$$
(A1.47)

$$\frac{d^2}{d\xi^2}(f_+ + f_-) = -2\frac{d}{d\xi}(f_+ - f_-)$$
(A1.48)

Inserting (A1.45) into (A1.48) and (A1.46) into (A1.47), and simplifying, the resulting second order differential equations are created:

$$\frac{d^2}{d\xi^2}(f_+ - f_-) = 2\omega \frac{d}{d\xi} (q_+ + q_-) + (4 - 4\omega)(f_+ - f_-)$$
(A1.49)

$$\frac{d^2}{d\xi^2}(f_+ + f_-) = -4\omega(q_+ + q_-) + (4 - 4\omega)(f_+ + f_-)$$
(A1.50)

Making the following substitutions:

$$y_1(\xi) = f_+ - f_- \tag{A1.51}$$

$$y_2(\xi) = f_+ + f_- \tag{A1.52}$$

Equations (A1.47) and (A1.48) can be written as two second-order nonhomogeneous linear differential equations (LDEs) in the form:

$$y_1'' - (4 - 4\omega)y_1 = 2\omega \frac{d}{d\xi} (q_+ + q_-)$$
(A1.53)

$$y_2'' - (4 - 4\omega)y_2 = -4\omega(q_+ + q_-)$$
(A1.54)

The right hand sides of the above two equations are composed entirely of the normalized functions  $q_+$  and  $q_-$ . These functions in terms of  $\xi$  are given below by inserting equations (A1.37) and (A1.38) into (A1.39). Their derivatives are provided as well.

$$q_{+} = \frac{Q_{+}(\xi)}{Q_{0}} = e^{-\xi} \tag{A1.55}$$

$$q_{-} = \frac{Q_{-}(\xi)}{Q_{o}} = R_{s}e^{\xi - 2\lambda}$$
 (A1.56)

$$\frac{dq_+}{d\xi} = -e^{-\xi} \tag{A1.57}$$

$$\frac{dq_{-}}{d\xi} = R_{s}e^{\xi - 2\lambda} = (R_{s}e^{-2\lambda})e^{\xi}$$
(A1.58)

The normalized  $q_{\pm}$  functions and their derivatives in equations (A1.55) to (A1.58) can be inserted into (A1.53) and (A1.54) for further simplification of the nonhomogeneous equations.

$$y_1'' - (4 - 4\omega)y_1 = -2\omega e^{-\xi} + 2\omega (R_s e^{-2\lambda})e^{\xi}$$
 (A1.59)

$$y_2'' - (4 - 4\omega)y_2 = -4\omega e^{-\xi} - 4\omega (R_s e^{-2\lambda})e^{\xi}$$
 (A1.60)

The solution to a second-order nonhomogeneous LDE, the general solution takes the form as:

$$y(\xi) = y_c(\xi) + y_p(\xi)$$
 (A1.61)

where  $y_c(\xi)$  is known as the complimentary solution that is obtained by equating the left hand sides of (A1.59) and (A1.60) to zero, and  $y_p(\xi)$  is a particular solution to these equations in their current form. The solutions will be obtained by the use of the Method of Undetermined Coefficients outlined in [115].

Beginning with the solution for  $y_1(\xi)$ , the complimentary solution is first framed by equating the LHS of (A1.59) to zero.

$$y_1'' - (4 - 4\omega)y_1 = 0 (A1.62)$$

The corresponding auxiliary equation to (A1.62) is written below and solved as:

$$r^{2} + 0 \cdot r - (4 - 4\omega) = 0$$

$$r^{2} - 4(1 - \omega) = 0$$

$$r^{2} = 4(1 - \omega)$$

$$r = +2\sqrt{1 - \omega}$$
(A1.63)

Therefore the solution to the complimentary equation for  $y_1(\xi)$  is given as:

$$y_{c1} = Ae^{-2\sqrt{1-\omega}\xi} + Be^{2\sqrt{1-\omega}\xi}$$
 (A1.64)

For the particular solution to  $y_1(\xi)$ , it is necessary to look at the form of the RHS of equation (A1.59) and model the solution accordingly. It is evident that this form will be a sum of exponentials as given below:

$$y_{p1} = A_p e^{-\xi} + B_p e^{\xi} \tag{A1.65}$$

The first and second derivatives of equation (A1.65) are derived in the following two equations.

$$y'_{p1} = -A_p e^{-\xi} + B_p e^{\xi} \tag{A1.66}$$

$$y_{p1}^{"} = A_p e^{-\xi} + B_p e^{\xi} \tag{A1.67}$$

Since the first derivative does not appear in equation (A1.59), only (A1.65) and (A1.67) need to be reinserted into it to obtain the particular solution. This is performed below and the resulting equation is factored to determine the unknowns  $A_p$  and  $B_p$ .

$$A_{p}e^{-\xi} + B_{p}e^{\xi} - (4 - 4\omega)(A_{p}e^{-\xi} + B_{p}e^{\xi}) = -2\omega e^{-\xi} + 2\omega(R_{s}e^{-2\lambda})e^{\xi}$$

$$A_{p}(4\omega - 3)e^{-\xi} + B_{p}(4\omega - 3)e^{\xi} = -2\omega e^{-\xi} + 2\omega(R_{s}e^{-2\lambda})e^{\xi}$$

$$A_{p} = -\frac{2\omega}{4\omega - 3} \quad \& \quad B_{p} = \frac{2\omega R_{s}e^{-2\lambda}}{4\omega - 3}$$
(A1.68)

With the unknowns determined, the particular solution is given as:

$$y_{p1} = -\frac{2\omega}{4\omega - 3}e^{-\xi} + \frac{2\omega R_s e^{-2\lambda}}{4\omega - 3}e^{\xi}$$
(A1.69)

Inserting equations (A1.64) and (A1.69) into (A1.61) yields the solution to  $y_1(\xi)$ , granted with two unknowns remaining; A and B.

$$y_1(\xi) = Ae^{-2\sqrt{1-\omega}\xi} + Be^{2\sqrt{1-\omega}\xi} - \frac{2\omega}{4\omega - 3}e^{-\xi} + \frac{2\omega R_s e^{-2\lambda}}{4\omega - 3}e^{\xi}$$
 (A1.70)

Pausing with  $y_1(\xi)$  and moving to  $y_2(\xi)$ , the same procedure can be followed to determine its complimentary and particular solutions. Conveniently, the complimentary solution will be easy to determine since setting the LHS of (A1.60) equal to zero yields the same result as previously found for  $y_1(\xi)$  in (A1.62).

$$y_2'' - (4 - 4\omega)y_2 = 0 (A1.71)$$

This automatically makes the zeroes for complimentary solution  $y_1(\xi)$  equal to those of  $y_2(\xi)$ , and thus its complimentary solution has the form of:

$$y_{c2} = Ce^{-2\sqrt{1-\omega}\xi} + De^{2\sqrt{1-\omega}\xi}$$
 (A1.72)

Again, looking at the RHS of (A1.60), the form of the particular solution for  $y_2(\xi)$  will also be the same sum of exponentials although naturally with different unknown coefficients.

$$y_{p2} = C_p e^{-\xi} + D_p e^{\xi} \tag{A1.73}$$

The first and second derivatives of the particular solution are given below as well.

$$y'_{p2} = -C_p e^{-\xi} + D_p e^{\xi} \tag{A1.74}$$

$$y_{p2}^{"} = C_p e^{-\xi} + D_p e^{\xi} \tag{A1.75}$$

Substitution of (A1.73) and (A1.75) into (A1.60) and simplifying leads to:

$$C_{v}e^{-\xi} + D_{v}e^{\xi} - (4 - 4\omega)(C_{v}e^{-\xi} + D_{v}e^{\xi}) = -4\omega e^{-\xi} - 4\omega(R_{s}e^{-2\lambda})e^{\xi}$$

$$C_{p}(4\omega - 3)e^{-\xi} + D_{p}(4\omega - 3)e^{\xi} = -4\omega e^{-\xi} - 4\omega (R_{s}e^{-2\lambda})e^{\xi}$$

$$C_p = -\frac{4\omega}{4\omega - 3}$$
 &  $D_p = -\frac{4\omega R_s e^{-2\lambda}}{4\omega - 3}$  (A1.76)

Therefore with the definitions of the unknowns in (A1.77), the particular solution for  $y_2(\xi)$  from (A1.73) is given as:

$$y_{p2} = -\frac{4\omega}{4\omega - 3}e^{-\xi} - \frac{4\omega R_s e^{-2\lambda}}{4\omega - 3}e^{\xi}$$
 (A1.77)

The general solution for  $y_2(\xi)$  can now be constructed by inserting (A1.72) and (A1.77) into (A1.61), again with the unknowns of C and D to still be determined.

$$y_2(\xi) = Ce^{-2\sqrt{1-\omega}\xi} + De^{2\sqrt{1-\omega}\xi} - \frac{4\omega}{4\omega - 3}e^{-\xi} - \frac{4\omega R_s e^{-2\lambda}}{4\omega - 3}e^{\xi}$$
(A1.78)

Making the appropriate substitutions for (A1.51) into (A1.70) and (A1.52) into (A1.78), the normalized sum and difference equations for  $f_{\pm}$  are obtained as follows:

$$f_{+} - f_{-} = Ae^{-2\sqrt{1-\omega}\xi} + Be^{2\sqrt{1-\omega}\xi} - \frac{2\omega}{4\omega - 3} \left( e^{-\xi} - R_{s}e^{\xi - 2\lambda} \right)$$
(A1.79)

$$f_{+} + f_{-} = Ce^{-2\sqrt{1-\omega}\xi} + De^{2\sqrt{1-\omega}\xi} - \frac{4\omega}{4\omega - 3} \left( e^{-\xi} + R_{s}e^{\xi - 2\lambda} \right)$$
(A1.80)

At this point isolated  $f_+$  and  $f_-$  equations are now attainable. The former is created by adding (A1.79) to (A1.80) and dividing by two, while the latter is created by the difference between these two equations and also dividing by two. These individual equations are given below as well as their derivatives.

$$f_{+} = \frac{A+C}{2}e^{-2\sqrt{1-\omega}\xi} + \frac{B+D}{2}e^{2\sqrt{1-\omega}\xi} - \frac{\omega}{4\omega-3}(3e^{-\xi} + R_{s}e^{\xi-2\lambda})$$
(A1.81)

$$f_{-} = \frac{C - A}{2} e^{-2\sqrt{1 - \omega}\xi} + \frac{D - B}{2} e^{2\sqrt{1 - \omega}\xi} - \frac{\omega}{4\omega - 3} (e^{-\xi} + 3R_s e^{\xi - 2\lambda})$$
(A1.82)

Dividing the positive first derivative of equation (A1.81) and the negative first derivative of equation (A1.82) by two yields:

$$\frac{1}{2}\frac{df_{+}}{d\xi} = \left(-\frac{A+C}{2}\sqrt{1-\omega}\right)e^{-2\sqrt{1-\omega}\xi} + \left(\frac{B+D}{2}\sqrt{1-\omega}\right)e^{2\sqrt{1-\omega}\xi} + \frac{\omega}{2}\frac{\left(3e^{-\xi}-R_{s}e^{\xi-2\lambda}\right)}{4\omega-3} \tag{A1.83}$$

$$-\frac{1}{2}\frac{df_{-}}{d\xi} = \left(\frac{C-A}{2}\sqrt{1-\omega}\right)e^{-2\sqrt{1-\omega}\xi} + \left(-\frac{D-B}{2}\sqrt{1-\omega}\right)e^{2\sqrt{1-\omega}\xi} - \frac{\omega\left(e^{-\xi} - 3R_{s}e^{\xi-2\lambda}\right)}{4\omega - 3}$$
(A1.84)

Inserting equations (A1.55), (A1.56), (A1.81) and (A1.82) into both (A1.43) and (A1.44), and simplifying, creates two new first derivative equations that are equivalent to (A1.83) and (A1.84). The simplification was performed with the aid of Maple numerical software.

$$\frac{1}{2}\frac{df_{+}}{d\xi} = \left(\frac{C\omega - C - A}{2}\right)e^{-2\sqrt{1-\omega}\xi} + \left(\frac{D\omega - D - B}{2}\right)e^{2\sqrt{1-\omega}\xi} + \frac{\omega\left(3e^{-\xi} - R_{s}e^{\xi - 2\lambda}\right)}{4\omega - 3} \tag{A1.85}$$

$$-\frac{1}{2}\frac{df_{-}}{d\xi} = \left(\frac{C\omega - C + A}{2}\right)e^{-2\sqrt{1-\omega}\xi} + \left(\frac{D\omega - D + B}{2}\right)e^{2\sqrt{1-\omega}\xi} - \frac{\omega\left(e^{-\xi} - 3R_se^{\xi - 2\lambda}\right)}{4\omega - 3} \tag{A1.86}$$

With (A1.85) equal to (A1.83) and (A1.86) equal to (A1.84), the corresponding factors in front of the exponential terms are equivalent and the third term in each pair of equations is identical. Therefore  $\mathcal{C}$  can be solved in terms of A, and  $\mathcal{D}$  in terms of B to reduce the number of unknowns in the general solution. Only one of these pairs of equations is necessary to obtain these new unknown definitions, and so choosing (A1.83) and (A1.85) leads to the following equations:

$$-\frac{A+C}{2}\sqrt{1-\omega} = \left(\frac{C\omega - C - A}{2}\right) \tag{A1.87}$$

$$\frac{B+D}{2}\sqrt{1-\omega} = \left(\frac{D\omega - D - B}{2}\right) \tag{A1.88}$$

This simplifies to:

$$C = \frac{A}{\sqrt{1 - \omega}} \tag{A1.89}$$

$$D = -\frac{B}{\sqrt{1 - \omega}} \tag{A1.90}$$

With the substitution of (A1.89) and (A1.90) into (A1.80), both the  $f_+ + f_-$  and the  $f_+ - f_-$  equations can now be written with only two unknowns present, A and B.

$$f_{+} - f_{-} = Ae^{-2\sqrt{1-\omega}\xi} + Be^{2\sqrt{1-\omega}\xi} - \frac{2\omega}{4\omega - 3} \left( e^{-\xi} - R_{s}e^{\xi - 2\lambda} \right)$$
 (A1.91)

$$f_{+} + f_{-} = \frac{A}{\sqrt{1 - \omega}} e^{-2\sqrt{1 - \omega}\xi} - \frac{B}{\sqrt{1 - \omega}} e^{2\sqrt{1 - \omega}\xi}$$

$$-\frac{4\omega}{4\omega - 3} \left( e^{-\xi} + R_{s} e^{\xi - 2\lambda} \right)$$
(A1.92)

The single  $f_+$  and  $f_-$  equations can also be updated from (A1.81) and (A1.82) with the new definitions of C and D in terms of A and B, respectively:

$$f_{+} = \frac{A}{2} \left( 1 + \frac{1}{\sqrt{1 - \omega}} \right) e^{-2\sqrt{1 - \omega}\xi} + \frac{B}{2} \left( 1 - \frac{1}{\sqrt{1 - \omega}} \right) e^{2\sqrt{1 - \omega}\xi}$$

$$- \frac{\omega}{4\omega - 3} \left( 3e^{-\xi} + R_{s}e^{\xi - 2\lambda} \right)$$
(A1.93)

$$f_{-} = \frac{A}{2} \left( \frac{1}{\sqrt{1 - \omega}} - 1 \right) e^{-2\sqrt{1 - \omega}\xi} - \frac{B}{2} \left( \frac{1}{\sqrt{1 - \omega}} + 1 \right) e^{2\sqrt{1 - \omega}\xi}$$

$$- \frac{\omega}{4\omega - 3} \left( e^{-\xi} + 3R_{s}e^{\xi - 2\lambda} \right)$$
(A1.94)

It is now time to invoke boundary conditions for the diffuse radiation component to solve the above two equations. For the dimensionalized function,  $F(z, \mu)$ , Gusarov provides the upper and lower boundary conditions as the two following equations, respectively.

$$F(L,\mu) = R_s F(L,-\mu) \qquad \qquad \mu < 0 \qquad \qquad \left[\frac{W}{m^2}\right] \quad (A1.96)$$

Taking the nondimensionalized equivalents of (A1.95) and (A1.96) in terms of  $f_{\pm}(\xi)$  with the help of (A1.40) allows the boundary conditions to be redefined below:

$$f_{-}(\lambda) = R_s f_{+}(\lambda)$$
  $\mu < 0$   $\left[\frac{W}{m^2}\right]$  (A1.98)

The top boundary condition given in equation (A1.97) can first be inserted into the standalone equation for  $f_+$  in (A1.93) with  $\xi = 0$ . Simplifying the resulting equation provides function of A in terms of B.

$$0 = \frac{A}{2} \left( 1 + \frac{1}{\sqrt{1 - \omega}} \right) e^{-2\sqrt{1 - \omega}(0)} + \frac{B}{2} \left( 1 - \frac{1}{\sqrt{1 - \omega}} \right) e^{2\sqrt{1 - \omega}(0)}$$
$$-\frac{\omega}{4\omega - 3} \left( 3e^{-0} + R_s e^{0 - 2\lambda} \right)$$

$$0 = \frac{A}{2} \left( 1 + \frac{1}{\sqrt{1 - \omega}} \right) + \frac{B}{2} \left( 1 - \frac{1}{\sqrt{1 - \omega}} \right) - \frac{\omega}{4\omega - 3} \left( 3 + R_s e^{-2\lambda} \right)$$

$$A = \frac{\left(\frac{2\omega}{4\omega - 3}\left(3 + R_s e^{-2\lambda}\right) - B\left(1 - \frac{1}{\sqrt{1 - \omega}}\right)\right)}{\left(1 + \frac{1}{\sqrt{1 - \omega}}\right)}$$
(A1.99)

Inserting the bottom boundary condition at  $\xi = \lambda$  from (A1.98) into both equations (A1.91) and (A1.92) yields:

$$f_{+}(\lambda) - R_{s}f_{+}(\lambda) = Ae^{-2\sqrt{1-\omega}\lambda} + Be^{2\sqrt{1-\omega}\lambda} - \frac{2\omega}{4\omega - 3} \left(e^{-\lambda} - R_{s}e^{\lambda - 2\lambda}\right)$$
(A1.100)

$$f_{+}(\lambda) + R_{s}f_{+}(\lambda) = \frac{A}{\sqrt{1-\omega}}e^{-2\sqrt{1-\omega}\lambda} - \frac{B}{\sqrt{1-\omega}}e^{2\sqrt{1-\omega}\lambda} - \frac{4\omega}{4\omega-3}\left(e^{-\lambda} + R_{s}e^{\lambda-2\lambda}\right)$$
 (A1.101)

Isolating the LHS of both of the above equations for  $f_+(\lambda)$  then allows for the solution of the unknown B by subtracting the resultant two equations and inserting (A1.99) for A.

$$f_{+}(\lambda) = \frac{\left(Ae^{-2\sqrt{1-\omega}\lambda} + Be^{2\sqrt{1-\omega}\lambda} - \frac{2\omega}{4\omega - 3}(e^{-\lambda} - R_se^{\lambda - 2\lambda})\right)}{1 - R_s}$$

$$f_{+}(\lambda) = \frac{\left(\frac{A}{\sqrt{1-\omega}}e^{-2\sqrt{1-\omega}\lambda} - \frac{B}{\sqrt{1-\omega}}e^{2\sqrt{1-\omega}\lambda} - \frac{4\omega}{4\omega - 3}(e^{-\lambda} + R_se^{\lambda - 2\lambda})\right)}{1 + R_s}$$

$$B = \frac{2\omega \left(e^{\lambda}(1-R_s)(1+R_s)(1+a-\omega)\left(e^{2a\lambda}\right) - \left(R_s + 3\left(e^{2\lambda}\right)\right)\left((1-R_s)a + (1+R_s)(\omega-1)\right)\right)}{(4\omega - 3)(e^{2\lambda})\left((\omega(1+R_s) - 2(1+a))(e^{4a\lambda}) - 2(a-1) - \omega(1+R_s)\right)}$$
(A1.102)

The above solution for B can now be inserted into (A1.99) to obtain the solution for the unknown A. A substitution of  $a = \sqrt{1 - \omega}$  has been implemented in equations (A1.102) and (A1.103) to reduce their size.

$$A = \frac{2\omega(e^{2a\lambda})\Big(\Big(R_s + 3(e^{2\lambda})\Big)\Big((\omega(1+R_s) - 2)a - 2(1-\omega)\Big)\Big(e^{2a\lambda}\Big) + \omega a(1-R_s)(1+R_s)e^{\lambda}\Big)}{(4\omega - 3)(e^{2\lambda})\Big(\Big(\omega(1+R_s) - 2(1+a)\Big)(e^{4a\lambda}) - 2(a-1) - \omega(1+R_s)\Big)(1+a)}$$
(A1.103)

# A.1.3. Full RTE Solution

With the unknowns now solved for in terms of known variables, the solution to the RTE can be formulated from the definition of heat flux given in [64,114] restated below:

$$Q = 2\pi \int_{-1}^{1} I(z,\mu)\mu d\mu$$
 (A1.104)

Inserting (A1.14), (A1.15), and (A1.16) into (A1.104) and simplifying leads to:

$$Q = 2\pi \left\{ \int_{-1}^{1} \left( \frac{Q_{+}(z)}{2\pi} \delta(\mu - 1) + \frac{Q_{-}(z)}{2\pi} \delta(\mu + 1) + F_{+}(z) H(\mu) + F_{-}(z) (1 - H(\mu)) \right) \mu d\mu \right\}$$

$$Q = 2\pi \left\{ \frac{Q_{+}(z)}{2\pi} \int_{0}^{1} \mu \delta(\mu - 1) d\mu + \frac{Q_{-}(z)}{2\pi} \int_{-1}^{0} \mu \delta(\mu + 1) d\mu + F_{+}(z) \int_{0}^{1} \mu H(\mu) d\mu + F_{-}(z) \int_{-1}^{0} \mu (1 - H(\mu)) d\mu \right\}$$

$$Q = Q_{+} - Q_{-} + \pi F_{+} - \pi F_{-} \tag{A1.105}$$

Finally, the dimensionless solution to heat flux is obtained by dividing the above equation by  $Q_o$  and applying the definitions for each dimensionless term according to (A1.39) and (A1.40) [64]:

$$q = q(\xi) = \frac{Q}{Q_o} = q_+ - q_- + \frac{f_+ - f_-}{2}$$
(A1.106)

Equation (A1.106) is the solution to the RTE that yields heat flux as a function of dimensionless depth into the powder. The definitions of all the above terms will be re-stated in the equations below for ease:

$$q_{+} = e^{-\xi} \tag{A1.107}$$

$$q_{-} = R_{\rm s} e^{\xi - 2\lambda} \tag{A1.108}$$

$$f_{+} - f_{-} = Ae^{-2a\xi} + Be^{2a\xi} - \frac{2\omega}{4\omega - 3} \left( e^{-\xi} - R_{s}e^{\xi - 2\lambda} \right)$$
 (A1.109)

$$A = \frac{2\omega(e^{2a\lambda})\left(\left(R_s + 3(e^{2\lambda})\right)\left((\omega(1+R_s) - 2)a - 2(1-\omega)\right)\left(e^{2a\lambda}\right) + \omega a(1-R_s)(1+R_s)e^{\lambda}\right)}{(4\omega - 3)(e^{2\lambda})\left(\left(\omega(1+R_s) - 2(1+a)\right)(e^{4a\lambda}) - 2(a-1) - \omega(1+R_s)\right)(1+a)}$$
(A1.110)

$$B = \frac{2\omega \left(e^{\lambda}(1-R_s)(1+R_s)(1+a-\omega)(e^{2a\lambda}) - \left(R_s + 3(e^{2\lambda})\right)((1-R_s)a + (1+R_s)(\omega-1))\right)}{(4\omega - 3)(e^{2\lambda})((\omega(1+R_s) - 2(1+a))(e^{4a\lambda}) - 2(a-1) - \omega(1+R_s))}$$
(A1.111)

$$a = \sqrt{1 - \omega} \tag{A1.112}$$

$$\xi = \beta z \tag{A1.113}$$

$$\lambda = \beta L \tag{A1.114}$$

Where  $\beta$  is the powder absorption coefficient, L is the powder depth,  $R_s$  is the substrate reflectivity, and  $\omega$  is the scattering albedo of the powder which is equal to its bulk reflectivity,  $R_b$  [64].

Two useful items arise from the dimensionless solution  $q(\xi)$ . These are the absorptivity of the powder layer and the volumetric heat source within the powder due to the laser. The absorptivity of the powder is determined by evaluating the amount of flux at the powder-substrate interface and subtracting it from the flux incident at the top powder surface. This is evaluated and simplified below, where  $B_p$  is the absorptivity of the powder alone:

$$B_{p} = \frac{A}{2} (1 - e^{-2a\lambda}) + \frac{B}{2} (1 - e^{2a\lambda}) + \left(\frac{R_{b}}{4R_{b} - 3} - 1\right) (R_{s}e^{-2\lambda} + e^{-\lambda}(1 - R_{s}) - 1)$$
(A1.115)

In the above equation,  $B_p = q(0) - q(\lambda)$  where the terms on the RHS are the evaluations of equation (A1.106) at  $\xi = 0$  and  $\xi = \lambda$ , respectively, using the

definitions from (A1.113) and (A1.114). The coefficients *A* and *B* were also fully defined in equations (A1.103) and (A1.102), respectively. The absorptivity is not explicitly stated in the final form of the volumetric heat source equation but is good to know when calculating how much of the laser energy was coupled into the system. Its effect is still included, however, when the volumetric heat source is applied as it is consequential of the derivation.

The function that defines volumetric heat source is created using the negative derivative of (A1.106) with respect to  $\xi$ . It is given below [64]:

$$-\frac{dq}{d\xi} = a(Ae^{-2a\xi} - Be^{2a\xi}) + (e^{-\xi} + R_s e^{\xi - 2\lambda}) \left(1 - \frac{R_b}{4R_b - 3}\right)$$
 [-] (A1.116)

Equation (A1.116) is constructed from dimensionless variables and must be modified with the help of the derivative of (A1.35) via the chain rule to be put in units of [m<sup>-1</sup>].

$$-\frac{dq}{dz} = -\frac{dq}{d\xi} \cdot \frac{d\xi}{dz} = -\beta \frac{dq}{d\xi} |_{\xi = \beta z}$$
 [m<sup>-1</sup>] (A1.117)

This finally yields the general form of the volumetric heating equation based on the solution of the RTE:

$$I(x, y, z, t) = I(x, y, t) \cdot \beta \left( -\frac{dq}{d\xi} |_{\xi = \beta z} \right) \qquad \left[ \frac{W}{m^3} \right] \quad (A1.118)$$

where I(x,y,t) is the surface intensity in  $\left[\frac{w}{m^2}\right]$  and  $\beta$  is the absorption coefficient in  $[m^{-1}]$ .

### A.2 Green's Function Solution Derivation

The analytical modeling of laser-material interactions with respect to the propagation of heat can best be performed by the use of Green's functions [62,86]. Green's functions (GFs) are used in many aspects of physics, and specifically in heat transfer, represent the temperature response to a unit point heat source spontaneously generated at point  $(x_1, y_1, z_1)$  and at time  $t_1$  on a point of interest at (x, y, z) at time  $t \ge t_1$ . It is written with the notation  $G(x, y, z, t \mid x_1, y_1, z_1, t_1)$  where the coordinates on the left describe the response and those on the right describe the impulse [116]. The effectiveness of this method is limited to boundary conditions of constant temperature, constant flux, or convection. Radiation and higher order boundary conditions have not been used in the literature due to their difficulty to implement. Also, the effect of phase change is unable to be accounted for explicitly, so the results are based purely on heat conduction. Nevertheless, the isothermal regions generated by this method provide insight into the temperature field surrounding the laser heat source, as well as an implicit determination of the melt width due to that temperature field.

One of the greatest features of Green's functions is that their form in higher dimensions is obtained by a multiplication of one-dimensional Green's functions [117]. For example, the powder bed in SLM can be considered an infinite medium in the x – and y – directions, and as a slab

of finite thickness in the z-direction. Therefore, the appropriate functions for two one-dimensional infinite media are multiplied together and then subsequently multiplied by the function for a one-dimensional finite medium. The following will derive the equations necessary to create the three-dimensional Green's function solution for steady-state heat equation.

### A.2.1. Dimensionless Numbers

The use of dimensionless numbers proves to be a powerful tool to reduce the number of symbols during derivations and to increase the efficiency of numerical calculations by working with smaller quantities. For modeling of the heat equation, Bäuerle proposes substitutions for the spatial and time dimensions, as well as for some other properties [62]. These are given in Table 9.

## Common Dimensionless Variables Normalized to Laser Radius $\omega_{\chi}$

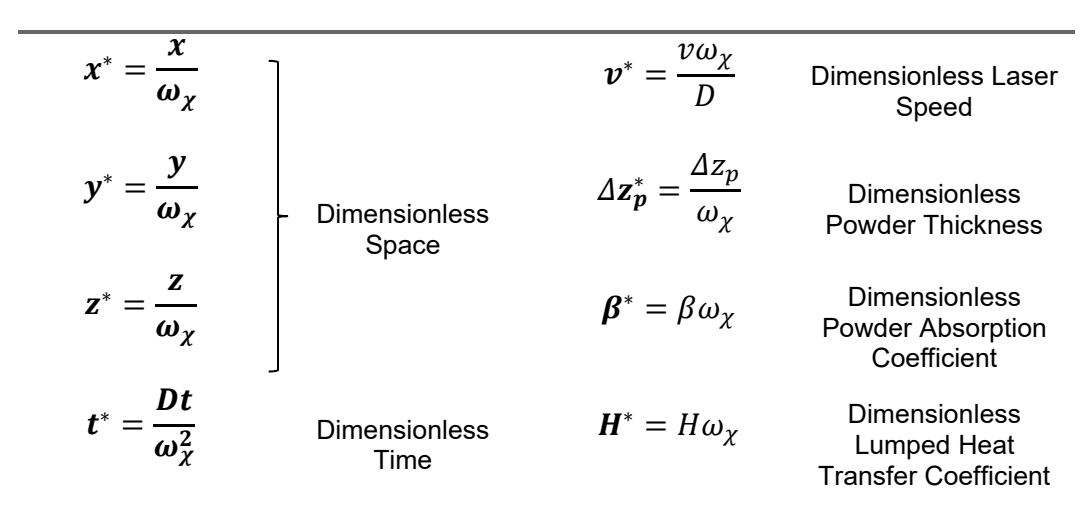


**Table 9:** Common dimensionless variables to use during the solution of the heat equation for laser-material interactions.

It is important to add a few clarifications for some of the symbols found in Table 9. The factor of normalization is a characteristic length of the system, in this case it is the laser radius  $\omega_\chi$  which was defined in section 3.1.3.1, but could be any characteristic length of the system [62]. The character D represents the thermal diffusivity of either powder or liquid and will usually include a "p" or "L" subscript denoting it as such. The equation for the dimensionless powder absorption coefficient from the solution of the RTE can also be applied to the bulk solid or liquid absorption coefficient from the Lambert-Beer law by simply substituting  $\alpha^*$  and  $\beta^*$  and  $\alpha$  for  $\beta$ , respectively. The lumped heat transfer coefficient, written as H, is a combination of the heat transfer coefficient and the thermal conductivity of whatever surface is being considered. It is given as:

$$H = \frac{h}{k} \tag{A2.1}$$

The dimensionless quantities given above will be used throughout the derivation of the three-dimensional Green's function equation and can be consulted as a reference.

### A.2.2. 1-D Green's Function in an Infinite Domain in

#### **Dimensionless Coordinates**

As stated previously, the powder bed can be treated as an infinite slab in x and y that has finite thickness in the z-direction. The Green's function

(GF) for each dimension can be derived separately and then combined as a product to form the three-dimensional solution. To begin the derivation in the x- and y-directions, the nonhomogeneous heat equation is first presented in one dimension in equation (A2.2).

$$\frac{\partial^2 T}{\partial x^2} + \frac{g(x,t)}{k} = \frac{1}{D} \frac{\partial T}{\partial t} \qquad \left[ \frac{K}{m^2} \right] \quad (A2.2)$$

The above equation must first be converted into dimensionless variables with the help of the chain rule and Table 9.

$$\frac{\partial T}{\partial x} = \frac{\partial T}{\partial x^*} \cdot \frac{\partial x^*}{\partial x} = \frac{1}{\omega_x} \frac{\partial T}{\partial x^*}$$
 [A2.3)

$$\frac{\partial^2 T}{\partial x^2} = \frac{\partial}{\partial x} \left( \frac{\partial T}{\partial x} \right) = \frac{\partial}{\partial x} \left( \frac{1}{\omega_{\chi}} \frac{\partial T}{\partial x^*} \right) = \frac{1}{\omega_{\chi}} \frac{\partial}{\partial x^*} \left( \frac{\partial x^*}{\partial x} \cdot \frac{\partial T}{\partial x^*} \right) = \frac{1}{\omega_{\chi}^2} \frac{\partial^2 T}{\partial x^{*2}}$$
 
$$\left[ \frac{K}{m^2} \right]$$
 (A2.4)

$$\frac{\partial T}{\partial t} = \frac{\partial T}{\partial t^*} \cdot \frac{\partial t^*}{\partial t} = \frac{D}{\omega_\chi^2} \frac{\partial T}{\partial t^*}$$
 (A2.5)

Substituting equations (A2.3) to (A2.5) into (A2.2) and changing the heat source term g(x,t) into its nondimensionalized counterpart, the 1-D heat equation with dimensionless variables is given below:

$$\frac{1}{\omega_{\chi}^{2}} \frac{\partial^{2} T}{\partial x^{*2}} + \frac{g(x^{*}, t^{*})}{k} = \frac{1}{\omega_{\chi}^{2}} \frac{\partial T}{\partial t^{*}} \qquad \left[\frac{K}{m^{2}}\right]$$
(A2.6)

Simplifying the above equation, the familiar form of the 1-D nonhomogeneous heat equation is presented in equation (A2.7). The

equation is now strictly in terms of units of temperature as the positional and time variables have been nondimensionalized.

$$\frac{\partial^2 T}{\partial x^{*2}} + \frac{\omega_{\chi}^2}{k} g(x^*, t^*) = \frac{\partial T}{\partial t^*}$$
 [K] (A2.7)

Hahn *et al* describes that to determine the GF for a given geometry, the solution to the homogeneous heat equation must be obtained in the form of a kernel of integration [118]. Beginning with equation (A2.7) and removing the heat source term, the 1-D homogeneous heat equation is portrayed below with a change in nomenclature from T to  $\Psi$  over the infinite domain of the dimensionless  $x^*$ .

$$\frac{\partial^2 \Psi}{\partial x^{*2}} = \frac{\partial \Psi}{\partial t^*}$$
 [K] (A2.8)

The initial conditions are given as a function of  $x^*$ :

$$\Psi(x^*, t^* = 0) = F(x^*)$$
  $-\infty < x^* < \infty$  [K] (A2.9)

The solution will proceed with the separation of variables method as outlined in [118]. First a general trial solution is presented:

$$\Psi(\mathbf{x}^*, \mathbf{t}^*) = X(\mathbf{x}^*)\Theta(\mathbf{t}^*)$$
 [K] (A2.10)

Taking the appropriate derivatives of the above trial solution, applying them to equation (A2.8), and separating the variables yields:

$$\frac{\partial^2 \Psi(\mathbf{x}^*, \mathbf{t}^*)}{\partial \mathbf{x}^{*2}} = \frac{\partial^2 X(\mathbf{x}^*)}{\partial \mathbf{x}^{*2}} \Theta(\mathbf{t}^*)$$
 [K] (A2.11)

$$\frac{\partial \Psi(\mathbf{x}^*, \mathbf{t}^*)}{\partial \mathbf{t}^*} = X(\mathbf{x}^*) \frac{\partial \Theta(\mathbf{t}^*)}{\partial \mathbf{t}^*}$$
 [K] (A2.12)

$$\frac{\partial^2 X(\mathbf{x}^*)}{\partial \mathbf{x}^{*2}} \Theta(\mathbf{t}^*) = X(\mathbf{x}^*) \frac{\partial \Theta(\mathbf{t}^*)}{\partial \mathbf{t}^*}$$
 [-] (A2.13)

$$\frac{1}{X(\mathbf{x}^*)} \frac{\partial^2 X(\mathbf{x}^*)}{\partial \mathbf{x}^{*2}} = \frac{1}{\Theta(\mathbf{t}^*)} \frac{\partial \Theta(\mathbf{t}^*)}{\partial \mathbf{t}^*}$$
 [-] (A2.14)

The PDE of (A2.8) has now been converted into two ODEs in equation (A2.14). This will be rewritten below and the variables of dimensionless time and space in the brackets will be dropped for simplicity.

$$\frac{1}{X}\frac{\partial^2 X}{\partial x^{*2}} = \frac{1}{\Theta}\frac{\partial \Theta}{\partial t^*} = -v^2 \tag{A2.15}$$

$$\frac{\partial^2 X}{\partial x^{*2}} + \nu^2 X = 0 \tag{A2.16}$$

$$\frac{\partial \theta}{\partial t^*} + \nu^2 \theta = 0 \tag{A2.17}$$

The respective trial solutions to equations (A2.16) and (A2.17) are given below:

$$X(x^*) = A_1(v)\cos(vx^*) + B_1(v)\sin(vx^*)$$
 (A2.18)

$$\Theta(\mathbf{t}^*) = C_1 e^{-\nu^2 \mathbf{t}^*} \tag{A2.19}$$

The coefficients  $A_1$  and  $B_1$  are both functions of the ODE solution variable,  $\nu$ . Since the domain is infinite and equation (A2.18) is a sum of a sine and cosine term, an integral of all possible values for  $\nu$  is needed for the complete solution. Therefore, inserting equations (A2.18) and (A2.19) into equation (A2.10) and integrating over all values of  $\nu$ , the general trial solution becomes:

$$\Psi(\mathbf{x}^*, \mathbf{t}^*) = \int_{\nu=0}^{\infty} (A_1(\nu) \cos(\nu \mathbf{x}^*) + B_1(\nu) \sin(\nu \mathbf{x}^*)) C_1 e^{-\nu^2 \mathbf{t}^*} d\nu$$
 [K] (A2.20)

The coefficients can be combined for simplification to yield:

$$\Psi(\mathbf{x}^*, \mathbf{t}^*) = \int_{\nu=0}^{\infty} (A_2(\nu) \cos(\nu \mathbf{x}^*) + B_2(\nu) \sin(\nu \mathbf{x}^*)) e^{-\nu^2 t^*} d\nu$$
 [K] (A2.21)

where

$$A_2(\nu) = A_1(\nu)C_1 \text{ and } B_2(\nu) = B_1(\nu)C_1$$
 (A2.22)

The initial condition from equation (A2.9) can be applied to the updated solution in (A2.21) to determine the unknown coefficients.

$$\Psi(x^*, 0) = F(x^*)$$

$$= \int_{v=0}^{\infty} (A_2(v) \cos(vx^*))$$

$$+ B_2(v) \sin(vx^*) dv$$
[K] (A2.23)

The integral in (A2.23) has the form of a *Fourier integral* and its coefficients therefore can be expressed analytically as in the following two equations [119].

$$A_2(\nu) = \frac{1}{\pi} \int_{-\infty}^{\infty} F(x_1^*) \cos(\nu x_1^*) dx_1^*$$
 (A2.24)

$$B_2(\nu) = \frac{1}{\pi} \int_{-\infty}^{\infty} F(x_1^*) \sin(\nu x_1^*) dx_1^*$$
 (A2.25)

The variable of integration in each of (A2.24) and (A2.25) is now that of the space domain, although it has been altered to be  $x_1^*$  to indicate that for each  $\nu$  considered, the coefficients depend upon the integration of the spatial domain with a dummy variable before being inserted into the general solution with respect to a desired position in  $x^*$ . Substituting these two coefficient solutions into (A2.23) yields:

$$F(\mathbf{x}^*) = \int_{\nu=0}^{\infty} \left( \frac{1}{\pi} \int_{-\infty}^{\infty} F(\mathbf{x}_1^*) \cos(\nu \mathbf{x}_1^*) \cos(\nu \mathbf{x}^*) d\mathbf{x}_1^* \right) + \frac{1}{\pi} \int_{-\infty}^{\infty} F(\mathbf{x}_1^*) \sin(\nu \mathbf{x}_1^*) \sin(\nu \mathbf{x}^*) d\mathbf{x}_1^*$$
[K] (A2.26)

The trigonometry in (A2.26) can be further simplified by the use of standard trigonometric identities that are widely available and thus the initial conditions can now be written as:

$$F(\mathbf{x}^*) = \int_{\nu=0}^{\infty} \left( \frac{1}{\pi} \int_{-\infty}^{\infty} F(\mathbf{x}_1^*) \cos(\nu(\mathbf{x}^* - \mathbf{x}_1^*)) d\mathbf{x}_1^* \right) d\nu$$
 [K] (A2.27)

Equating (A2.23) to (A2.27) for  $F(x^*)$  and recognizing that the integrands are necessarily equal provides:

$$A_{2}(\nu)\cos(\nu x^{*}) + B_{2}(\nu)\sin(\nu x^{*})$$

$$= \frac{1}{\pi} \int_{-\infty}^{\infty} F(x_{1}^{*})\cos(\nu(x^{*} - x_{1}^{*})) dx_{1}^{*}$$
(A2.28)

This allows for an update of the initial trial solution in equation (A2.21) to have the form:

$$\Psi(\mathbf{x}^*, \mathbf{t}^*) = \int_{\nu=0}^{\infty} \left(\frac{1}{\pi} \int_{-\infty}^{\infty} F(\mathbf{x}_1^*) \cos(\nu(\mathbf{x}^*) - \mathbf{x}_1^*)\right) d\mathbf{x}_1^* e^{-\nu^2 t^*} d\nu$$
[K] (A2.29)

The integration in the above equation can be rearranged in the following way:

$$\Psi(\mathbf{x}^*, \mathbf{t}^*) = \frac{1}{\pi} \int_{-\infty}^{\infty} F(\mathbf{x}_1^*) \left[ \int_{\nu=0}^{\infty} e^{-\nu^2 t^*} \cos(\nu (\mathbf{x}^* - \mathbf{x}_1^*)) \, d\nu \right] d\mathbf{x}_1^*$$
 [K] (A2.30)

The term in the square brackets in equation (A2.30) can be simplified with the help of identity *863.3* from [120]:

$$\int_{\nu=0}^{\infty} e^{-\nu^2 t^*} \cos(\nu (x^* - x_1^*)) \, d\nu = \frac{\sqrt{\pi}}{2\sqrt{t^*}} e^{-\frac{(x^* - x_1^*)^2}{4t^*}} \tag{A2.31}$$

Substituting (A2.31) into (A2.30) and simplifying, the solution to the homogeneous heat equation finally becomes:

$$\Psi(\mathbf{x}^*, \mathbf{t}^*) = \int_{-\infty}^{\infty} \frac{1}{\sqrt{4\pi \mathbf{t}^*}} e^{-\frac{(\mathbf{x}^* - \mathbf{x}_1^*)^2}{4\mathbf{t}^*}} F(\mathbf{x}_1^*) d\mathbf{x}_1^*$$
 [K] (A2.32)

The above solution to the homogeneous problem can be rewritten in terms of the GF kernel multiplied by the initial condition, that is:

$$\Psi(\mathbf{x}^*, \mathbf{t}^*) = \int_{-\infty}^{\infty} G^*(\mathbf{x}^*, \mathbf{t}^* | \mathbf{x}_1^*, 0) F(\mathbf{x}_1^*) d\mathbf{x}_1^*$$
 [K] (A2.33)

Thus, the solution to the homogeneous version of the problem yields the GF evaluated at  $t_1^* = 0$  [118]. For later use in the Green Function Solution Equation (GFSE), the general 1-D GF in an infinite domain evaluated for  $0 \le t_1^* \le t^*$  is obtained by replacing  $t^*$  with  $t^* - t_1^*$ :

$$G^*(\mathbf{x}^*, \mathbf{t}^* | \mathbf{x}_1^*, \mathbf{t}_1^*) = \frac{1}{\sqrt{4\pi(\mathbf{t}^* - \mathbf{t}_1^*)}} e^{-\frac{(\mathbf{x}^* - \mathbf{x}_1^*)^2}{4(\mathbf{t}^* - \mathbf{t}_1^*)}}$$
(A2.34)

The asterisk notation is used with the *G* as well to clarify that it has been derived with dimensionless components and it itself is also a dimensionless quantity.

With respect to SLM as previously mentioned, the x- and y-dimensions are both considered to extend to infinity. As such, each 1-D GF is provided below by a simple variable change.

$$G_{x}^{*}(x^{*}, t^{*} | x_{1}^{*}, t_{1}^{*}) = \frac{1}{\sqrt{4\pi(t^{*} - t_{1}^{*})}} e^{-\frac{(x^{*} - x_{1}^{*})^{2}}{4(t^{*} - t_{1}^{*})}}$$
(A2.35)

$$G_{\mathbf{y}}^{*}(\mathbf{y}^{*}, \mathbf{t}^{*} | \mathbf{y}_{1}^{*}, \mathbf{t}_{1}^{*}) = \frac{1}{\sqrt{4\pi(\mathbf{t}^{*} - \mathbf{t}_{1}^{*})}} e^{-\frac{(\mathbf{y}^{*} - \mathbf{y}_{1}^{*})^{2}}{4(\mathbf{t}^{*} - \mathbf{t}_{1}^{*})}}$$
(A2.36)

## A.2.3. 1-D Green's Function in a Finite Domain in

#### **Dimensionless Coordinates**

The GF for a finite domain, such as the depth of a powder bed in the z-direction, will now be derived. The procedure is the same wherein the homogeneous version of the heat equation is used, however since the domain is finite, there exist boundary conditions which need to be converted to their homogeneous equivalents. The nondimensionalized heat equation is again presented below, but with the variable  $z^*$  instead of  $x^*$ .

$$\frac{\partial^2 T}{\partial \mathbf{z}^{*2}} + \frac{\omega_{\chi}^2}{k} g(\mathbf{z}^*, \mathbf{t}^*) = \frac{\partial T}{\partial \mathbf{t}^*}$$
 [K] (A2.37)

The one-dimensional domain that will be used for this derivation is given in Figure 53.

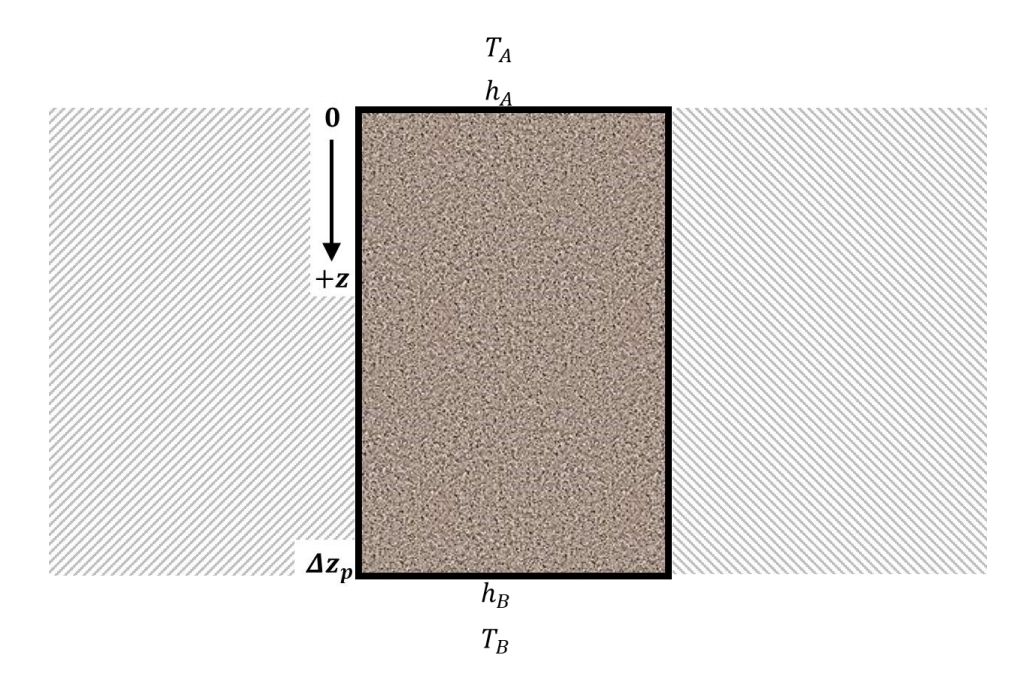


**Figure 53:** 1-D finite domain representing an infinitesimally thin slice of the powder bed. The hatched regions signify the only direction considered is the positive z-direction, which in this case moves downwards from the top surface.

In the above figure,  $\Delta z_p$  is the powder depth,  $h_A$  and  $h_B$  are the respective heat transfer coefficients of the top and bottom surfaces, and  $T_A$  and  $T_B$  are the top and bottom surrounding temperatures. The top temperature would typically be the ambient temperature in the build chamber and the bottom temperature would be the top surface temperature of the preceding power layer or baseplate. The boundary conditions at the top and bottom of the plate as demonstrated above are presented below in equation form and must be nondimensionalized before proceeding. The

sign conventions used in this case are consistent with the flow of heat in the negative direction, as without laser interaction, heat would flow up from the build plate and out of the top powder surface by convection.

$$k\frac{\partial T}{\partial z}|_{z=0} = h_A T(0,t) - h_A T_A \qquad \left[\frac{W}{m^2}\right] \quad (A2.38)$$

$$k\frac{\partial T}{\partial z}|_{z=\Delta z_p} = -h_B T(\Delta z_p, t) + h_B T_B \qquad \left[\frac{W}{m^2}\right] \quad (A2.39)$$

The above two boundary conditions can be nondimensionalized using the same process applied in equation (A2.3), with again the normalization constant being the laser radius  $\omega_{\gamma}$ .

$$\frac{\partial T}{\partial z} = \frac{\partial T}{\partial \mathbf{z}^*} \cdot \frac{\partial \mathbf{z}^*}{\partial z} = \frac{1}{\omega_{\chi}} \frac{\partial T}{\partial \mathbf{z}^*} \qquad \left[ \frac{K}{m} \right] \quad (A2.40)$$

Applying (A2.40) to equations (A2.38) and (A2.39), and simplifying, provides the boundary conditions in terms of a dimensionless z variable. It will also be shown that the heat transfer coefficient can be made into a dimensionless quantity with the help of equation (A2.1) and Table 9. Beginning with the top boundary condition:

$$k\frac{\partial T}{\partial z}|_{z=0} = h_A T(0,t) - h_A T_A$$

$$\frac{\partial T}{\partial z} = \frac{h_A}{k} T - \frac{h_A}{k} T_A$$

$$\frac{\partial T}{\partial z} = H_A T - H_A T_A$$

$$\frac{1}{\omega_{\chi}} \frac{\partial T}{\partial \mathbf{z}^*} = H_A T - H_A T_A$$

$$\frac{\partial T}{\partial \mathbf{z}^*} = H_A \omega_{\chi} T - H_A \omega_{\chi} T_A$$

$$\frac{\partial T}{\partial \mathbf{z}^*}|_{\mathbf{z}^* = \mathbf{0}} = \mathbf{H}_A^* T - \mathbf{H}_A^* T_A$$
[K] (A2.41)

The bottom boundary condition is nondimensionalized in the same manner:

$$k\frac{\partial T}{\partial z}|_{z=\Delta z_p} = -h_B T(\Delta z_p, t) + h_B T_B$$

$$\frac{\partial T}{\partial z} = \frac{-h_B}{k} T + \frac{h_B}{k} T_B$$

$$\frac{\partial T}{\partial z} = -H_B T + H_B T_B$$

$$\frac{1}{\omega_\chi} \frac{\partial T}{\partial z^*} = -H_B T + H_B T_B$$

$$\frac{\partial T}{\partial z^*} = -H_B \omega_\chi T + H_B \omega_\chi T_B$$

$$\Delta z_p^* = \frac{\Delta z_p}{\omega_\chi}$$

$$\frac{\partial T}{\partial z^*}|_{z^*=\Delta z_p^*} = -H_B^* T + H_B^* T_B$$
[K] (A2.43)

It is convenient to rewrite equations (A2.41) and (A2.43) with the terms including the temperature variable on one side and the constant terms on

the other. This will help when converting them into their homogeneous equivalents for the GF derivation.

$$\frac{\partial T}{\partial \mathbf{z}^*}|_{\mathbf{z}^*=\mathbf{0}} - \mathbf{H}_A^* T = -\mathbf{H}_A^* T_A$$
 [K] (A2.44)

$$\frac{\partial T}{\partial \boldsymbol{z}^*}|_{\boldsymbol{z}^* = \boldsymbol{\Delta} \boldsymbol{z}_p^*} + \boldsymbol{H}_B^* T = \boldsymbol{H}_B^* T_B$$
 [K] (A2.45)

The initial condition is given again as a function of the position variable. In this case it will be a constant temperature such that:

$$T(z,0) = F(z) = F(z^*) = T_0$$
 [K] (A2.46)

As with the derivation of the GF in the infinite domain, it is necessary to start with the homogeneous form of the heat equation. The nomenclature of T will again be converted to  $\Psi$  to indicate it is the homogeneous solution being sought.

$$\frac{\partial^2 \Psi}{\partial \mathbf{z}^{*2}} = \frac{\partial \Psi}{\partial \mathbf{t}^*}$$
 [K] (A2.47)

However, since this is a finite domain the boundary conditions must be applied in their homogeneous form. Thus equations (A2.44) and (A2.45) are rewritten as:

$$\frac{\partial \Psi}{\partial \mathbf{z}^*}|_{\mathbf{z}^*=\mathbf{0}} - \mathbf{H}_A^* \Psi = 0 \rightarrow \frac{\partial \Psi}{\partial \mathbf{z}^*}|_{\mathbf{z}^*=\mathbf{0}} = \mathbf{H}_A^* \Psi$$
 [K] (A2.48)

$$\frac{\partial \Psi}{\partial \mathbf{z}^*}|_{\mathbf{z}^* = \mathbf{\Delta} \mathbf{z}_p^*} + \mathbf{H}_B^* \Psi = 0 \rightarrow \frac{\partial \Psi}{\partial \mathbf{z}^*}|_{\mathbf{z}^* = \mathbf{\Delta} \mathbf{z}_p^*} = -\mathbf{H}_B^* \Psi$$
 [K] (A2.49)

The method of separation of variables will again be used, starting with the general solution of:

$$\Psi(\mathbf{z}^*, \mathbf{t}^*) = Z(\mathbf{z}^*)\Theta(\mathbf{t}^*)$$
 [K] (A2.50)

Substituting (A2.50) into (A2.47) and simplifying, the PDE is converted into two ODEs:

$$\frac{1}{Z}\frac{\partial^2 Z}{\partial z^{*2}} = \frac{1}{\Theta}\frac{\partial \Theta}{\partial t^*} = -\nu^2 \tag{A2.51}$$

$$\frac{\partial^2 Z}{\partial z^{*2}} + \nu^2 Z = 0 \tag{A2.52}$$

$$\frac{\partial \Theta}{\partial \mathbf{t}^*} + \nu^2 \Theta = 0 \tag{A2.53}$$

The assumed solution that satisfies equation (A2.52) in the positional variable,  $z^*$ , and its first derivative are given as:

$$Z(\mathbf{z}^*, \nu) = A_1 \sin(\nu \mathbf{z}^*) + B_1 \cos(\nu \mathbf{z}^*)$$
 (A2.54)

$$\frac{\partial Z}{\partial \mathbf{z}^*} = \nu A_1 \cos(\nu \mathbf{z}^*) - \nu B_1 \sin(\nu \mathbf{z}^*)$$
(A2.55)

The general Z solution is first simplified using equations (A2.48), (A2.50), (A2.54) and (A2.55) all evaluated at  $\mathbf{z}^* = 0$ .

$$\frac{\partial \Psi(\boldsymbol{z}^*, \boldsymbol{t}^*)}{\partial \boldsymbol{z}^*}|_{\boldsymbol{z}^*=\boldsymbol{0}} = \boldsymbol{H}_A^* \Psi(0, \boldsymbol{t}^*)$$

$$\frac{\partial Z}{\partial \mathbf{z}^*}|_{\mathbf{z}^*=\mathbf{0}}\Theta(\mathbf{t}^*) = \mathbf{H}_A^* Z(0, \nu)\Theta(\mathbf{t}^*)$$

$$\frac{\partial Z}{\partial z^*}|_{z^*=0} = H_A^* Z(0, \nu)$$

$$Z(0, \nu) = A_1 \sin(\nu(0)) + B_1 \cos(\nu(0))$$

$$Z(0, \nu) = B_1$$

$$\frac{\partial Z}{\partial z^*}|_{z^*=0} = \nu A_1 \cos(\nu(0)) - \nu B_1 \sin(\nu(0))$$

$$\frac{\partial Z}{\partial z^*}|_{z^*=0} = \nu A_1$$

$$H_A^* Z(0, \nu) = \nu A_1$$

$$H_A^* B_1 = \nu A_1$$

$$A_1 = \frac{H_A^* B_1}{\nu}$$
(A2.56)

Therefore, the top boundary condition has removed the coefficient  $A_1$  from the general solution. At this point, the bottom boundary condition can be invoked by evaluating equations (A2.49), (A2.50), (A2.54), (A2.55) at  $\mathbf{z}^* = \Delta \mathbf{z}_p^*$  and using the substitution for  $A_1$  from (A2.56).

$$\frac{\partial \Psi(\mathbf{z}^*, \mathbf{t}^*)}{\partial \mathbf{z}^*} |_{\mathbf{z}^* = \Delta \mathbf{z}_p^*} = -H_B^* \Psi(\Delta \mathbf{z}_p^*, \mathbf{t}^*)$$

$$\frac{\partial Z}{\partial \mathbf{z}^*} |_{\mathbf{z}^* = \Delta \mathbf{z}_p^*} \Theta(\mathbf{t}^*) = -H_B^* Z(\Delta \mathbf{z}_p^*) \Theta(\mathbf{t}^*)$$

$$\frac{\partial Z}{\partial \mathbf{z}^*} |_{\mathbf{z}^* = \Delta \mathbf{z}_p^*} = -H_B^* Z(\Delta \mathbf{z}_p^*)$$

$$Z(\Delta \mathbf{z}_n^*, \mathbf{v}) = A_1 \sin(\mathbf{v} \Delta \mathbf{z}_n^*) + B_1 \cos(\mathbf{v} \Delta \mathbf{z}_n^*)$$

$$Z(\Delta \mathbf{z}_{p}^{*}, \nu) = \frac{H_{A}^{*}B_{1}}{\nu} \sin(\nu \Delta \mathbf{z}_{p}^{*}) + B_{1}\cos(\nu \Delta \mathbf{z}_{p}^{*})$$

$$\frac{\partial Z}{\partial \mathbf{z}^{*}}|_{\mathbf{z}^{*} = \Delta \mathbf{z}_{p}^{*}} = \nu A_{1}\cos(\nu \Delta \mathbf{z}_{p}^{*}) - \nu B_{1}\sin(\nu \Delta \mathbf{z}_{p}^{*})$$

$$\frac{\partial Z}{\partial \mathbf{z}^{*}}|_{\mathbf{z}^{*} = \Delta \mathbf{z}_{p}^{*}} = H_{A}^{*}B_{1}\cos(\nu \Delta \mathbf{z}_{p}^{*}) - \nu B_{1}\sin(\nu \Delta \mathbf{z}_{p}^{*})$$

$$-H_{B}^{*}Z(\Delta \mathbf{z}_{p}^{*}) = -H_{B}^{*}\left(\frac{H_{A}^{*}B_{1}}{\nu}\sin(\nu \Delta \mathbf{z}_{p}^{*}) + B_{1}\cos(\nu \Delta \mathbf{z}_{p}^{*})\right)$$

$$H_{A}^{*}B_{1}\cos(\nu \Delta \mathbf{z}_{p}^{*}) - \nu B_{1}\sin(\nu \Delta \mathbf{z}_{p}^{*})$$

$$= -H_{B}^{*}\left(\frac{H_{A}^{*}B_{1}}{\nu}\sin(\nu \Delta \mathbf{z}_{p}^{*}) + B_{1}\cos(\nu \Delta \mathbf{z}_{p}^{*})\right)$$

$$H_{A}^{*}B_{1}\cos(\nu \Delta \mathbf{z}_{p}^{*}) - \nu B_{1}\sin(\nu \Delta \mathbf{z}_{p}^{*})$$

$$= \frac{-H_{B}^{*}H_{A}^{*}B_{1}}{\nu}\sin(\nu \Delta \mathbf{z}_{p}^{*}) - H_{B}^{*}B_{1}\cos(\nu \Delta \mathbf{z}_{p}^{*})$$

$$H_{A}^{*}B_{1}\cos(\nu \Delta \mathbf{z}_{p}^{*}) + H_{B}^{*}B_{1}\cos(\nu \Delta \mathbf{z}_{p}^{*})$$

$$= \frac{-H_{B}^{*}H_{A}^{*}B_{1}}{\nu}\sin(\nu \Delta \mathbf{z}_{p}^{*}) + \nu B_{1}\sin(\nu \Delta \mathbf{z}_{p}^{*})$$

$$B_{1}\cos(\nu \Delta \mathbf{z}_{p}^{*}) (H_{A}^{*} + H_{B}^{*}) = B_{1}\sin(\nu \Delta \mathbf{z}_{p}^{*})\left(\nu - \frac{H_{B}^{*}H_{A}^{*}}{\nu}\right)$$

$$\frac{\sin(\nu \Delta \mathbf{z}_{p}^{*})}{\cos(\nu \Delta \mathbf{z}_{p}^{*})} = \frac{(H_{A}^{*} + H_{B}^{*})}{\left(\nu - \frac{H_{B}^{*}H_{A}^{*}}{\nu}\right)}$$

$$\tan(\nu \Delta \mathbf{z}_{p}^{*}) = \frac{\nu(H_{A}^{*} + H_{B}^{*})}{(\nu^{2} - H_{A}^{*}H_{A}^{*})}$$

$$(A2.57)$$

Thus the application of the bottom boundary condition has led to the determination of a transcendental equation for the ODE variable,  $\nu$ , that

depends on the normalized depth of the finite region and the top and bottom normalized heat transfer coefficients. This equation, (A2.57), will be revisited later in the derivation. At this point, the solution for the *Z* component has been simplified to become:

$$Z(\mathbf{z}^*, \nu) = B_1 \left( \frac{\mathbf{H}_A^*}{\nu} \sin(\nu \mathbf{z}^*) + \cos(\nu \mathbf{z}^*) \right)$$
(A2.58)

The solution of the  $\Theta$  component which satisfies equation (A2.53) is assumed to be:

$$\Theta(\mathbf{t}^*) = C_1 e^{-\nu^2 \mathbf{t}^*} \tag{A2.59}$$

Applying equations (A2.58) and (A2.59) to (A2.50) yields the updated general solution:

$$\Psi(\mathbf{z}^*, \mathbf{t}^*) = B_1 C_1 \left( \frac{\mathbf{H}_A^*}{\nu} \sin(\nu \mathbf{z}^*) + \cos(\nu \mathbf{z}^*) \right) e^{-\nu^2 \mathbf{t}^*}$$
 [K] (A2.60)

Since this equation contains a sum of a sine and cosine, the complete solution involves an infinite sum of  $\nu$  values. Therefore, it is necessary to change  $\nu$  into  $\nu_n$  and combine  $B_1C_1$  into a single coefficient,  $C_n$ :

$$\Psi(\mathbf{z}^*, \mathbf{t}^*) = \sum_{n=1}^{\infty} C_n \left( \frac{\mathbf{H}_A^*}{\nu_n} \sin(\nu_n \mathbf{z}^*) + \cos(\nu_n \mathbf{z}^*) \right) e^{-\nu_n^2 \mathbf{t}^*}$$
 [K] (A2.61)

This coefficient can be solved for by invoking the initial conditions provided in equation (A2.46).

$$\Psi(\mathbf{z}^*, 0) = F(\mathbf{z}^*) = \sum_{n=1}^{\infty} C_n \left( \frac{\mathbf{H}_A^*}{\nu_n} \sin(\nu_n \mathbf{z}^*) + \cos(\nu_n \mathbf{z}^*) \right)$$
 [K] (A2.62)

The form of equation (A2.62) is that of a Fourier series expansion, where  $v_n$  are called *eigenvalues* of the solution. Thus, using the principle of orthogonality, both sides of this equation can first be multiplied by the term in brackets and integrated over the entire domain [118]. An arbitrary eigenvalue will be used in the multiplication, denoted as  $v_m$ .

$$\int_{0}^{\Delta \mathbf{z}_{p}^{*}} F(\mathbf{z}^{*}) \left( \frac{\mathbf{H}_{A}^{*}}{\nu_{m}} \sin(\nu_{m} \mathbf{z}^{*}) + \cos(\nu_{m} \mathbf{z}^{*}) \right) d\mathbf{z}^{*}$$

$$= \sum_{n=1}^{\infty} \int_{0}^{\Delta \mathbf{z}_{p}^{*}} C_{n} \left( \frac{\mathbf{H}_{A}^{*}}{\nu_{n}} \sin(\nu_{n} \mathbf{z}^{*}) + \cos(\nu_{n} \mathbf{z}^{*}) \right) \left( \frac{\mathbf{H}_{A}^{*}}{\nu_{m}} \sin(\nu_{m} \mathbf{z}^{*}) + \cos(\nu_{m} \mathbf{z}^{*}) \right) d\mathbf{z}^{*}$$
(A2.63)

By orthogonality, the RHS of equation (A2.63) is equal to zero for every eigenvalue where the subscript  $n \neq m$  upon summing. Therefore, the only value that satisfies this nontrivial solution is n = m. Upon simplifying and using this characteristic, the unknown coefficient  $C_n$  can be determined:

$$\int_0^{\Delta \mathbf{z}_p^*} F(\mathbf{z}^*) \left( \frac{\mathbf{H}_A^*}{\nu_n} \sin(\nu_n \mathbf{z}^*) + \cos(\nu_n \mathbf{z}^*) \right) d\mathbf{z}^* = \int_0^{\Delta \mathbf{z}_p^*} C_n \left( \frac{\mathbf{H}_A^*}{\nu_n} \sin(\nu_n \mathbf{z}^*) + \cos(\nu_n \mathbf{z}^*) \right)^2 d\mathbf{z}^*$$

$$C_{n} = \frac{\int_{0}^{\Delta z_{p}^{*}} F(\mathbf{z}^{*}) \left(\frac{\mathbf{H}_{A}^{*}}{\nu_{n}} \sin(\nu_{n} \mathbf{z}^{*}) + \cos(\nu_{n} \mathbf{z}^{*})\right) d\mathbf{z}^{*}}{\int_{0}^{\Delta z_{p}^{*}} \left(\frac{\mathbf{H}_{A}^{*}}{\nu_{n}} \sin(\nu_{n} \mathbf{z}^{*}) + \cos(\nu_{n} \mathbf{z}^{*})\right)^{2} d\mathbf{z}^{*}}$$
(A2.64)

The integral in the denominator of equation (A2.64) can be explicitly evaluated and further simplified by considering the transcendental solution derived earlier in equation (A2.57), as well as the identity  $\cos^2(\theta) = \frac{1}{1+\tan^2(\theta)}$ . There are many intermediate steps to this simplification, so an equation-solving software package (MAPLE) was used to yield:

$$C_{n} = \frac{\int_{0}^{\Delta z_{p}^{*}} F(\mathbf{z}^{*}) \left( \frac{\mathbf{H}_{A}^{*}}{\nu_{n}} \sin(\nu_{n} \mathbf{z}^{*}) + \cos(\nu_{n} \mathbf{z}^{*}) \right) d\mathbf{z}^{*}}{\frac{1}{2} \left( \frac{\Delta z_{p}^{*} \left( \nu_{n}^{2} + \mathbf{H}_{A}^{*}^{2} \right)}{\nu_{n}^{2}} + \frac{\left( \mathbf{H}_{A}^{*} + \mathbf{H}_{B}^{*} \right) \left( \nu_{n}^{2} + \mathbf{H}_{A}^{*} \mathbf{H}_{B}^{*} \right)}{\nu_{n}^{2} \left( \nu_{n}^{2} + \mathbf{H}_{B}^{*}^{2} \right)} \right)}$$
(A2.65)

The simplified denominator expression is referred to as the *norm* of the eigenfunction [118]. Before reinserting this new expression for  $C_n$  into the general homogeneous solution defined previously, two changes will be made for clarification. The first is that since the integral is performed over the entire domain regardless of what position in the overall solution is being considered, the variable  $\mathbf{z}^*$  will be changed to  $\mathbf{z}_1^*$  to make this distinction. Secondly, the norm will be represented by the function identifier  $N(\nu_n)$ .

$$N(\nu_n) = \frac{1}{2} \left( \frac{\Delta \mathbf{z}_p^* (\nu_n^2 + \mathbf{H}_A^{*2})}{\nu_n^2} + \frac{(\mathbf{H}_A^* + \mathbf{H}_B^*)(\nu_n^2 + \mathbf{H}_A^* \mathbf{H}_B^*)}{\nu_n^2 (\nu_n^2 + \mathbf{H}_B^{*2})} \right)$$
(A2.66)

This finally leads to:

$$C_n = \frac{\int_0^{\Delta z_p^*} F(\mathbf{z_1^*}) \left(\frac{\mathbf{H_A^*}}{\nu_n} \sin(\nu_n \mathbf{z_1^*}) + \cos(\nu_n \mathbf{z_1^*})\right) d\mathbf{z_1^*}}{N(\nu_n)}$$
(A2.67)

With the coefficient  $C_n$  now fully defined, it can be substituted into the general solution of (A2.61) and simplified to yield:

$$\Psi(\mathbf{z}^{*}, \mathbf{t}^{*}) = \int_{0}^{\Delta \mathbf{z}_{p}^{*}} \sum_{n=1}^{\infty} \frac{\left(\frac{H_{A}^{*}}{\nu_{n}} \sin(\nu_{n} \mathbf{z}^{*}) + \cos(\nu_{n} \mathbf{z}^{*})\right) \left(\frac{H_{A}^{*}}{\nu_{n}} \sin(\nu_{n} \mathbf{z}_{1}^{*}) + \cos(\nu_{n} \mathbf{z}_{1}^{*})\right) e^{-\nu_{n}^{2} t^{*}} F(\mathbf{z}_{1}^{*}) d\mathbf{z}_{1}^{*}}{N(\nu_{n})}$$
[K] (A2.68)

The terms in the brackets can be represented by the following substitution:

$$Z(\mathbf{z}^*, \nu_n) = \left(\frac{H_A^*}{\nu_n} \sin(\nu_n \mathbf{z}^*) + \cos(\nu_n \mathbf{z}^*)\right)$$
(A2.69)

which makes the homogenous solution now:

$$\Psi(\mathbf{z}^*, \mathbf{t}^*) = \int_0^{\Delta z_p^*} \sum_{n=1}^{\infty} \frac{Z(\mathbf{z}^*, \nu_n) Z(\mathbf{z}_1^*, \nu_n) e^{-\nu_n^2 \mathbf{t}^*}}{N(\nu_n)} F(\mathbf{z}_1^*) d\mathbf{z}_1^* \qquad [K] \quad (A2.70)$$

As performed in section A.2.2, equation (A2.33), the homogeneous solution can again be represented as the integral the product of the GF evaluated at  $t_1^* = 0$  and the function  $F(z_1^*)$  [116,118].

$$\Psi(\mathbf{z}^*, \mathbf{t}^*) = \int_0^{\Delta \mathbf{z}_p^*} G^*(\mathbf{z}^*, \mathbf{t}^* | \mathbf{z}_1^*, 0) \cdot F(\mathbf{z}_1^*) d\mathbf{z}_1^*$$
 [K] (A2.71)

Therefore, the GF for a finite domain, in this case in the z-direction, is obtained by replacing  $t^*$  with  $t^* - t_1^*$ . The final form of the GF along with all the necessary supplementary equations are provided below.

$$G_{\mathbf{z}}^{*}(\mathbf{z}^{*}, \mathbf{t}^{*} | \mathbf{z}_{1}^{*}, \mathbf{t}_{1}^{*}) = \sum_{n=1}^{\infty} \frac{Z(\nu_{n}, \mathbf{z}^{*})Z(\nu_{n}, \mathbf{z}_{1}^{*})e^{-\nu_{n}^{2}(\mathbf{t}^{*} - \mathbf{t}_{1}^{*})}}{N(\nu_{n})}$$
(A2.72)

$$Z(\mathbf{z}^*, \nu_n) = \left(\frac{\mathbf{H}_A^*}{\nu_n} \sin(\nu_n \mathbf{z}^*) + \cos(\nu_n \mathbf{z}^*)\right)$$
(A2.73)

$$N(\nu_n) = \frac{1}{2} \left( \frac{\Delta \mathbf{z}_p^* (\nu_n^2 + {H_A^*}^2)}{\nu_n^2} + \frac{(H_A^* + H_B^*)(\nu_n^2 + {H_A^*}H_B^*)}{\nu_n^2 (\nu_n^2 + {H_B^*}^2)} \right)$$
(A2.74)

$$\tan(\nu_n \Delta \mathbf{z}_p^*) = \frac{\nu_n (\mathbf{H}_A^* + \mathbf{H}_B^*)}{(\nu_n^2 - \mathbf{H}_B^* \mathbf{H}_A^*)}$$
(A2.75)

## A.2.4. Green's Function Solution Equation (GFSE) in

#### **Dimensionless Coordinates**

The GFs derived so far can be used to determine the temperature of a system within a Green's Function Solution Equation (GFSE). This equation considers the effects of the initial conditions, the source heating term, and the boundary conditions. It will be derived as a general solution in dimensionless variables that can be applicable to one-, two-, or three-dimensional problems. For relevance to the current research, the three-dimensional in the Cartesian system case will be derived. The derivation begins by stating the heat equation as used previously, however it now

includes a term for the fin effect, which can be useful in situations that involve moving coordinate systems.

$$\nabla^2 T(x, y, z, t) + \frac{g(x, y, z, t)}{k} - m^2 T(x, y, z, t) = \frac{1}{D} \frac{\partial T(x, y, z, t)}{\partial t} \qquad \left[\frac{K}{m^2}\right] \quad (A2.76)$$

The initial conditions can be stated as:

$$T(x, y, z, 0) = F(x, y, z)$$
 [K] (A2.77)

The boundary conditions will be assumed to be applied perpendicular to the xy plane, and thus parallel to the z-axis, which increases downward from the top surface. This orientation is considered for the infinite slab-like system that has a finite thickness, similar to that of a powder bed. Thus the generalized boundary conditions for this scenario are:

$$\frac{\partial T}{\partial z}|_{z=0} - \frac{h_A}{k} T(0, t) = -\frac{h_A}{k} T_A \qquad \left[\frac{K}{m}\right]$$
 (A2.78)

$$\frac{\partial T}{\partial z}|_{z=\Delta z_p} + \frac{h_B}{k} T(\Delta z_p, t) = \frac{h_B}{k} T_B \qquad \left[\frac{K}{m}\right] \tag{A2.79}$$

which can be further simplified due to equation (A2.1):

$$\frac{\partial T}{\partial z}|_{z=0} - \mathbf{H}_A T(0,t) = -\mathbf{H}_A T_A \qquad \left[\frac{K}{m}\right] \tag{A2.80}$$

$$\frac{\partial T}{\partial z}|_{z=\Delta z_p} + \boldsymbol{H}_B T (\Delta z_p, t) = \boldsymbol{H}_B T_B \qquad \left[\frac{K}{m}\right] \tag{A2.81}$$

In equation (A2.76), the Laplacian operator,  $\nabla^2$ , is used for the second order spatial derivatives and the fin coefficient,  $m^2$ , is a constant with units of [m<sup>-2</sup>]. The boundary conditions used are identical to those from the finite

domain GF derivation in section A.2.3, with the subscript *A* representing the top boundary and *B* representing the bottom boundary. It is necessary to first put all these equations in terms of dimensionless variables with the help of Table 9.

The Laplacian will be converted to a form using its dimensionless equivalent with help from the following derivation:

$$\nabla = \frac{\partial}{\partial x} + \frac{\partial}{\partial y} + \frac{\partial}{\partial z} = \frac{\partial}{\partial x^*} \frac{\partial x^*}{\partial x} + \frac{\partial}{\partial y^*} \frac{\partial y^*}{\partial y} + \frac{\partial}{\partial z^*} \frac{\partial z^*}{\partial z}$$
 [m<sup>-1</sup>]

$$\nabla^* = \frac{\partial}{\partial x^*} + \frac{\partial}{\partial y^*} + \frac{\partial}{\partial z^*}$$

$$\frac{\partial x^*}{\partial x} = \frac{\partial y^*}{\partial y} = \frac{\partial z^*}{\partial z} = \frac{1}{\omega_x}$$
 [m<sup>-1</sup>]

$$\nabla = \frac{1}{\omega_{\mathsf{Y}}} \nabla^*$$
 [m<sup>-1</sup>]

$$\nabla^2 = \nabla \cdot \nabla = \frac{1}{\omega_{\chi}} \nabla^* \cdot \frac{1}{\omega_{\chi}} \nabla^* = \frac{1}{\omega_{\chi}^2} \nabla^{*2}$$
 [m<sup>-2</sup>] (A2.82)

The time derivative can be converted identically as given in equation (A2.5), and provided again below:

$$\frac{\partial T}{\partial t} = \frac{\partial T}{\partial t^*} \cdot \frac{\partial t^*}{\partial t} = \frac{D}{\omega_{\gamma}^2} \frac{\partial T}{\partial t^*} \qquad \left[\frac{K}{s}\right] \tag{A2.83}$$

Using all the above conversions, the simplified heat equation with dimensionless variables is given as:

$$\nabla^{*2}T(x^*, y^*, z^*, t^*) + \frac{\omega_\chi^2}{k}g(x^*, y^*, z^*, t^*) - m^{*2}T(x^*, y^*, z^*, t^*) = \frac{\partial T(x^*, y^*, z^*, t^*)}{\partial t^*}$$
 [K] (A2.84)

where the dimensionless fin coefficient is included as  $m^{*2} = m^2 \omega_\chi^2$ . The initial conditions become:

$$T(x^*, y^*, z^*, \mathbf{0}) = F(x^*, y^*, z^*)$$
 [K] (A2.85)

The boundary conditions for  $t^* > 0$  become:

$$\frac{\partial T(x^*, y^*, z^*, t^*)}{\partial z^*}|_{z^*=0} - H_A^* T(x^*, y^*, 0, t^*) = -H_A^* T_A$$
 [K] (A2.86)

$$\frac{\partial T(\mathbf{x}^*, \mathbf{y}^*, \mathbf{z}^*, \mathbf{t}^*)}{\partial \mathbf{z}^*}|_{\mathbf{z}^* = \Delta \mathbf{z}_p^*} + H_B^* T(\mathbf{x}^*, \mathbf{y}^*, \Delta \mathbf{z}_p^*, \mathbf{t}^*) = H_B^* T_B$$
 [K] (A2.87)

Before proceeding, it is necessary to introduce the GF *auxiliary equation* which has the same form as the heat equation. As outlined by Beck *et al*, all GFs satisfy an *auxiliary equation* in which the heat source is replaced by a term involving Dirac delta functions, which symbolizes an impulse occurring within the dimensions of the system at some time  $t_1^*$  [116]. It is important first to note that the dimensions of the GF are dependent on the spatial dimensionality of the system being modelled. However, the normalized GFs are dimensionless in entirety. This is illustrated in Table 10.

Model Spatial Units of G Units of  $G^*$  Dimensions

1 (eg. <i>x</i> )	$m^{-1}$	-
2 (eg. <i>x,y</i> )	$m^{-2}$	-
3 (eg. x, y, z)	$m^{-3}$	-

Table 10: Dimensional dependency of GFs on the spatial dimensions of the model.

The implications of Table 10 are that the units of the auxiliary equation will change depending on the spatial dimensions of the model. For example, the auxiliary equation for three spatial dimensions is given by equation (A2.88). The units of this equation are [m<sup>-5</sup>] which includes the three-dimensional GF of units [m<sup>-3</sup>] multiplied by various factors and operators which contain units of [m<sup>-2</sup>]. The Dirac delta function has units of [m<sup>-1</sup>] for spatial variables and [s<sup>-1</sup>] for time. Thus, to achieve the same units as the other terms in the equation, the term containing the product of the spatial and temporal delta functions must always be divided by the thermal diffusivity, *D*, in the dimensional case.

$$\nabla^{2}G + \frac{1}{D}\delta(x - x_{1})\delta(y - y_{1})\delta(z - z_{1})\delta(t - t_{1}) - m^{2}G = \frac{1}{D}\frac{\partial G}{\partial t}$$
 [m<sup>-5</sup>] (A2.88)

When nondimensionalizing the variables of the auxiliary equation, both the GF itself and all its containing variables are unitless. Therefore, the entire equation has no units whatsoever once the normalization has been applied. It follows that the term containing the product of Dirac delta functions of dimensionless variables must now contain no factor in front of it to satisfy

the units of the system. The normalized GF auxiliary equation is given below:

$$\nabla^{*2}G^* + \delta(x^* - x_1^*)\delta(y^* - y_1^*)\delta(z^* - z_1^*)\delta(t^* - t_1^*) - m^{*2}G^* = \frac{\partial G^*}{\partial t^*}$$
(A2.89)

The boundary conditions for the normalized auxiliary equation are:

$$\frac{\partial G^*(x^*, y^*, z^*, t^*)}{\partial z^*}|_{z^*=0} = H_A^* G^*(x^*, y^*, \mathbf{0}, t^*)$$
 (A2.90)

$$\frac{\partial G^{*}(x^{*}, y^{*}, z^{*}, t^{*})}{\partial z^{*}}|_{z^{*} = \Delta z_{p}^{*}} = -H_{B}^{*}G^{*}(x^{*}, y^{*}, \Delta z_{p}^{*}, t^{*})$$
(A2.91)

The GFSE derivation begins with applying the principle of reciprocity of the GF to the nondimensional auxiliary equation. This principle is given as [116]:

$$G^{*}(x^{*}, y^{*}, z^{*}, t^{*} \mid x_{1}^{*}, y_{1}^{*}, z_{1}^{*}, t_{1}^{*})$$

$$= G^{*}(x_{1}^{*}, y_{1}^{*}, z_{1}^{*}, -t_{1}^{*} \mid x^{*}, y^{*}, z^{*}, -t^{*})$$
(A2.92)

Applying (A2.92) to (A2.89) and making the substitutions  $(x_1^*, y_1^*, z_1^*, -t_1^*)$  for  $(x^*, y^*, z^*, t^*)$  and  $(x^*, y^*, z^*, -t^*)$  for  $(x_1^*, y_1^*, z_1^*, t_1^*)$  yields:

$$\nabla^{*2}G^* + \delta(x_1^* - x^*)\delta(y_1^* - y^*)\delta(z_1^* - z^*)\delta(-t_1^* + t^*) - m^{*2}G^* = -\frac{\partial G^*}{\partial t_1^*}$$
(A2.93)

It is then necessary to express equation (A2.84) in terms of  $(x_1^*, y_1^*, z_1^*, t_1^*)$ 

$$\nabla^{*2}T(x_{1}^{*}, y_{1}^{*}, z_{1}^{*}, t_{1}^{*}) + \frac{\omega_{\chi}^{2}}{k}g(x_{1}^{*}, y_{1}^{*}, z_{1}^{*}, t_{1}^{*}) - m^{*2}T(x_{1}^{*}, y_{1}^{*}, z_{1}^{*}, t_{1}^{*})$$

$$= \frac{\partial T(x_{1}^{*}, y_{1}^{*}, z_{1}^{*}, t_{1}^{*})}{\partial t_{1}^{*}}$$
[K] (A2.94)

Multiplying (A2.93) by T and (A2.94) by  $G^*$ , dropping the variable notation in brackets in the T variable for simplicity, and subtracting the former from the latter yields:

$$G^* \nabla^{*2} T - T \nabla^{*2} G^* + G^* \frac{\omega_{\chi}^2}{k} g(\mathbf{x}_1^*, \mathbf{y}_1^*, \mathbf{z}_1^*, \mathbf{t}_1^*)$$

$$- T \delta(\mathbf{x}_1^* - \mathbf{x}^*) \delta(\mathbf{y}_1^* - \mathbf{y}^*) \delta(\mathbf{z}_1^* - \mathbf{z}^*) \delta(-\mathbf{t}_1^* + \mathbf{t}^*)$$

$$= G^* \frac{\partial T}{\partial \mathbf{t}_1^*} + T \frac{\partial G^*}{\partial \mathbf{t}_1^*}$$
(A2.95)

where the fin terms cancel each other after the subtraction. The RHS of (A2.95) can be further simplified as it is simply the expression of the product rule for derivatives:

$$G^* \nabla^{*2} T - T \nabla^{*2} G^* + G^* \frac{\omega_{\chi}^2}{k} g(\mathbf{x}_1^*, \mathbf{y}_1^*, \mathbf{z}_1^*, \mathbf{t}_1^*)$$

$$- T \delta(\mathbf{x}_1^* - \mathbf{x}^*) \delta(\mathbf{y}_1^* - \mathbf{y}^*) \delta(\mathbf{z}_1^* - \mathbf{z}^*) \delta(-\mathbf{t}_1^* + \mathbf{t}^*) \qquad [K] \quad (A2.96)$$

$$= \frac{\partial (G^* T)}{\partial \mathbf{t}_1^*}$$

Equation (A2.96) must then be integrated over the three spatial dimensions and over time. The integrals will be in the form of:

$$\int_{t_1^*=0}^{t^*+\varepsilon} \int_{x_1^*=-\infty}^{\infty} \int_{y_1^*=-\infty}^{\infty} \int_{z_1^*=0}^{\Delta z_p^*} dx_1^* dy_1^* dz_1^* dt_1^*$$
 [K] (A2.97)

Where the limits of integration in each spatial dimension are in accordance with the infinite slab description given earlier. The integral in time contains the upper limit  $t^* + \varepsilon$  where  $\varepsilon$  is currently defined as an arbitrarily small

positive number. Applying this integral to equation (A2.96) and simplifying gives:

$$\int_{t_{1}^{*}=0}^{t^{*}+\varepsilon} \int_{x_{1}^{*}=-\infty}^{\infty} \int_{y_{1}^{*}=-\infty}^{\infty} \int_{z_{1}^{*}=0}^{\Delta z_{p}^{*}} (G^{*}\nabla^{*2}T - T\nabla^{*2}G^{*}) dx_{1}^{*}dy_{1}^{*}dz_{1}^{*}dt_{1}^{*} 
+ \frac{\omega_{\chi}^{2}}{k} \int_{t_{1}^{*}=0}^{t^{*}+\varepsilon} \int_{x_{1}^{*}=-\infty}^{\infty} \int_{y_{1}^{*}=-\infty}^{\infty} \int_{z_{1}^{*}=0}^{\Delta z_{p}^{*}} G^{*}g(x_{1}^{*}, y_{1}^{*}, z_{1}^{*}, t_{1}^{*}) dx_{1}^{*}dy_{1}^{*}dz_{1}^{*}dt_{1}^{*} 
- T(x^{*}, y^{*}, z^{*}, t^{*}) = \left[ \int_{x_{1}^{*}=-\infty}^{\infty} \int_{y_{1}^{*}=-\infty}^{\infty} \int_{y_{1}^{*}=-\infty}^{\Delta z_{p}^{*}} (G^{*}T) dx_{1}^{*}dy_{1}^{*}dz_{1}^{*} \right]_{t_{1}^{*}=0}^{t^{*}=t^{*}+\varepsilon}$$
(A2.98)

The term  $T(x^*, y^*, z^*, t^*)$  on the LHS of equation results from the integration in time and space of the term containing the product of Dirac delta functions. Isolating for this term begins to yield the form of the GFSE:

$$T(\mathbf{x}^{*}, \mathbf{y}^{*}, \mathbf{z}^{*}, \mathbf{t}^{*})$$

$$= -\left[\int_{x_{1}^{*}=-\infty}^{\infty} \int_{y_{1}^{*}=-\infty}^{\infty} \int_{z_{1}^{*}=0}^{\Delta z_{p}^{*}} (G^{*}T) dx_{1}^{*} dy_{1}^{*} dz_{1}^{*}\right]_{t_{1}^{*}=0}^{t_{1}^{*}=t^{*}+\varepsilon}$$

$$+ \frac{\omega_{\chi}^{2}}{k} \int_{t_{1}^{*}=0}^{t^{*}+\varepsilon} \int_{x_{1}^{*}=-\infty}^{\infty} \int_{y_{1}^{*}=-\infty}^{\infty} \int_{z_{1}^{*}=0}^{\Delta z_{p}^{*}} G^{*}g(x_{1}^{*}, y_{1}^{*}, z_{1}^{*}, t_{1}^{*}) dx_{1}^{*} dy_{1}^{*} dz_{1}^{*} dt_{1}^{*}$$

$$+ \int_{t_{1}^{*}=0}^{t^{*}+\varepsilon} \int_{x_{1}^{*}=-\infty}^{\infty} \int_{y_{1}^{*}=-\infty}^{\infty} \int_{z_{1}^{*}=0}^{\Delta z_{p}^{*}} (G^{*}\nabla^{*2}T - T\nabla^{*2}G^{*}) dx_{1}^{*} dy_{1}^{*} dz_{1}^{*} dt_{1}^{*}$$

$$(A2.99)$$

Focusing on the first term on the RHS of equation (A2.99), this can be expanded with the help of equation (A2.92) and represented as:

$$-\left[\int_{x_{1}^{*}=-\infty}^{\infty}\int_{y_{1}^{*}=-\infty}^{\infty}\int_{z_{1}^{*}=0}^{\Delta z_{p}^{*}}(G^{*}T)dx_{1}^{*}dy_{1}^{*}dz_{1}^{*}\right]_{t_{1}^{*}=0}^{t_{1}^{*}=t^{*}+\varepsilon}$$

$$=-\int_{x_{1}^{*}=-\infty}^{\infty}\int_{y_{1}^{*}=-\infty}^{\infty}\int_{z_{1}^{*}=0}^{\Delta z_{p}^{*}}G^{*}(x^{*},y^{*},z^{*},t^{*}|x_{1}^{*},y_{1}^{*},z_{1}^{*},t^{*}+\varepsilon)T(x_{1}^{*},y_{1}^{*},z_{1}^{*},t^{*}+\varepsilon)dx_{1}^{*}dy_{1}^{*}dz_{1}^{*} \qquad [K] \quad (A2.100)$$

$$+\int_{x_{1}^{*}=-\infty}^{\infty}\int_{y_{1}^{*}=-\infty}^{\infty}\int_{z_{1}^{*}=0}^{\Delta z_{p}^{*}}G^{*}(x^{*},y^{*},z^{*},t^{*}|x_{1}^{*},y_{1}^{*},z_{1}^{*},0)T(x_{1}^{*},y_{1}^{*},z_{1}^{*},0)dx_{1}^{*}dy_{1}^{*}dz_{1}^{*}$$

GFs operate under the assertion of causality, which states that the effect of the impulse cannot take place before the impulse has been applied [116]. Therefore, since  $t^* + \varepsilon > t^*$ , the first term on the RHS of equation (A2.100) must be unequivocally equal to zero as it describes the time of the impulse occurring after the effect has been observed. The remaining second term on the right can be further simplified because  $T(x_1^*, y_1^*, z_1^*, \mathbf{0})$  is simply the expression for the initial conditions of the system, given earlier as equation (A2.85), evaluated at  $(x_1^*, y_1^*, z_1^*)$ . The fully simplified first term of the GFSE represents the contribution from the *initial conditions* and becomes:

$$-\left[\int_{x_{1}^{*}=-\infty}^{\infty}\int_{y_{1}^{*}=-\infty}^{\infty}\int_{z_{1}^{*}=0}^{\Delta z_{p}^{*}}(G^{*}T)dx_{1}^{*}dy_{1}^{*}dz_{1}^{*}\right]_{t_{1}^{*}=0}^{t_{1}^{*}=t^{*}+\varepsilon}$$

$$=\int_{x_{1}^{*}=-\infty}^{\infty}\int_{y_{1}^{*}=-\infty}^{\infty}\int_{z_{1}^{*}=0}^{\Delta z_{p}^{*}}G^{*}(x^{*},y^{*},z^{*},t^{*}|x_{1}^{*},y_{1}^{*},z_{1}^{*},0)F(x_{1}^{*},y_{1}^{*},z_{1}^{*})dx_{1}^{*}dy_{1}^{*}dz_{1}^{*}$$
[K] (A2.101)

The second term on the RHS of (A2.99) is the contribution of the *source* term and will be left unmodified at this point. The third and final term describes the role of the boundary conditions. Remembering that the geometry considered is that of an infinite slab of finite thickness, the only boundaries are on the infinite planes of  $z^* = 0$  and  $z^* = \Delta z_p^*$ , where again  $\Delta z_p^*$  is the dimensionless thickness of the powder layer. It is first important to note that this third term of (A2.99) can therefore be changed using Green's Theorem from a volume integral to a surface integral [116]:

$$\int_{t_{1}^{*}=0}^{t^{*}+\varepsilon} \int_{x_{1}^{*}=-\infty}^{\infty} \int_{y_{1}^{*}=-\infty}^{\Delta z_{p}^{*}} (G^{*}\nabla^{*2}T - T\nabla^{*2}G^{*}) dx_{1}^{*}dy_{1}^{*}dz_{1}^{*}dt_{1}^{*}$$

$$= \int_{t_{1}^{*}=0}^{t^{*}+\varepsilon} \int_{x_{1}^{*}=-\infty}^{\infty} \int_{y_{1}^{*}=-\infty}^{\infty} \left(G^{*}\frac{\partial T}{\partial z_{1}^{*}}|_{z_{1}^{*}=0}\right)$$

$$- T\frac{\partial G^{*}}{\partial z_{1}^{*}}|_{z_{1}^{*}=0} dx_{1}^{*}dy_{1}^{*}dt_{1}^{*} \qquad [K] \quad (A2.102)$$

$$+ \int_{t_{1}^{*}=0}^{t^{*}+\varepsilon} \int_{x_{1}^{*}=-\infty}^{\infty} \int_{y_{1}^{*}=-\infty}^{\infty} \left(G^{*}\frac{\partial T}{\partial z_{1}^{*}}|_{z_{1}^{*}=\Delta z_{p}^{*}}\right)$$

$$- T\frac{\partial G^{*}}{\partial z_{1}^{*}}|_{z_{1}^{*}=\Delta z_{p}^{*}} dx_{1}^{*}dy_{1}^{*}dt_{1}^{*}$$

The boundary conditions for both the heat equation and the auxiliary equation are simplified and restated below in terms of the variables  $(x_1^*, y_1^*, z_1^*, t_1^*)$ :

$$\frac{\partial T(x_1^*, y_1^*, z_1^*, t_1^*)}{\partial z_1^*} |_{z_1^* = 0} = H_A^* (T(x_1^*, y_1^*, 0, t_1^*) - T_A)$$
 [K] (A2.103)

$$\frac{\partial T(x_1^*, y_1^*, z_1^*, t_1^*)}{\partial z_1^*} \Big|_{z_1^* = \Delta z_p^*} = -H_B^* \Big( T(x_1^*, y_1^*, \Delta z_p^*, t_1^*) - T_B \Big)$$
 [K] (A2.104)

$$\frac{\partial G^*(x^*, y^*, z^*, t^* \mid x_1^*, y_1^*, z_1^*, t_1^*)}{\partial z_1^*} \big|_{z_1^* = 0} = H_A^* G^*(x^*, y^*, z^*, t^* \mid x_1^*, y_1^*, 0, t_1^*)$$
(A2.105)

$$\frac{\partial G^{*}(x^{*}, y^{*}, z^{*}, t^{*} \mid x_{1}^{*}, y_{1}^{*}, z_{1}^{*}, t_{1}^{*})}{\partial z_{1}^{*}}|_{z_{1}^{*} = \Delta z_{p}^{*}} = -H_{B}^{*}G^{*}(x^{*}, y^{*}, z^{*}, t^{*} \mid x_{1}^{*}, y_{1}^{*}, \Delta z_{p}^{*}, t_{1}^{*})$$
(A2.106)

The boundary condition contribution to the GFSE in equation (A2.102) will now be simplified. Equations (A2.103) and (A2.105) can be substituted into the bracketed portion of the first term on the RHS. This simplification yields:

$$G^* \frac{\partial T}{\partial z_1^*} |_{z_1^*=0} - T \frac{\partial G^*}{\partial z_1^*} |_{z_1^*=0}$$

$$= G^*(x^*, y^*, z^*, t^* \mid x_1^*, y_1^*, 0, t_1^*) H_A^*(T(x_1^*, y_1^*, 0, t_1^*)$$

$$- T_A)$$

$$- T(x_1^*, y_1^*, 0, t_1^*) H_A^*G^*(x^*, y^*, z^*, t^* \mid x_1^*, y_1^*, 0, t_1^*)$$

$$= -G^*(x^*, y^*, z^*, t^* \mid x_1^*, y_1^*, 0, t_1^*) H_A^*T_A$$

$$[K] \quad (A2.107)$$

$$= -G^*(x^*, y^*, z^*, t^* \mid x_1^*, y_1^*, 0, t_1^*) H_A^*T_A$$

Similarly, the bracketed portion of the second term in (A2.102) can be simplified with the help of equations (A2.104) and (A2.106):

$$G^* \frac{\partial T}{\partial z_1^*} |_{z_1^* = \Delta z_p^*} - T \frac{\partial G^*}{\partial z_1^*} |_{z_1^* = \Delta z_p^*}$$

$$= G^* (x^*, y^*, z^*, t^* \mid x_1^*, y_1^*, \Delta z_p^*, t_1^*) \left( -H_B^* (T(x_1^*, y_1^*, \Delta z_p^*, t_1^*) - T_B) \right)$$

$$- T(x_1^*, y_1^*, \Delta z_p^*, t_1^*) \left( -H_B^* G^* (x^*, y^*, z^*, t^* \mid x_1^*, y_1^*, \Delta z_p^*, t_1^*) \right)$$

$$= G^* (x^*, y^*, z^*, t^* \mid x_1^*, y_1^*, \Delta z_p^*, t_1^*) H_B^* T_B$$
[K] (A2.108)

Therefore, equation (A2.102) is finally simplified to become:

$$\int_{t_{1}^{*}=0}^{t^{*}+\varepsilon} \int_{x_{1}^{*}=-\infty}^{\infty} \int_{y_{1}^{*}=-\infty}^{\infty} \int_{z_{1}^{*}=0}^{\Delta z_{p}^{*}} (G^{*}\nabla^{*2}T - T\nabla^{*2}G^{*}) dx_{1}^{*}dy_{1}^{*}dz_{1}^{*}dt_{1}^{*}$$

$$= -H_{A}^{*}T_{A} \int_{t_{1}^{*}=0}^{t^{*}+\varepsilon} \int_{x_{1}^{*}=-\infty}^{\infty} \int_{y_{1}^{*}=-\infty}^{\infty} G^{*}(x^{*}, y^{*}, z^{*}, t^{*} \mid x_{1}^{*}, y_{1}^{*}, 0, t_{1}^{*}) dx_{1}^{*}dy_{1}^{*}dt_{1}^{*} \qquad [K] \quad (A2.109)$$

$$+ H_{B}^{*}T_{B} \int_{t_{1}^{*}=0}^{t^{*}+\varepsilon} \int_{x_{1}^{*}=-\infty}^{\infty} \int_{y_{1}^{*}=-\infty}^{\infty} G^{*}(x^{*}, y^{*}, z^{*}, t^{*} \mid x_{1}^{*}, y_{1}^{*}, \Delta z_{p}^{*}, t_{1}^{*}) dx_{1}^{*}dy_{1}^{*}dt_{1}^{*}$$

where again the dimensionless heat transfer coefficient and surrounding temperature of the top surface at  $\mathbf{z}_1^* = \mathbf{0}$  are given respectively by  $\mathbf{H}_A^*$  and  $T_A$ . Similarly, the same respective quantities for the bottom surface at  $\mathbf{z}_1^* = \Delta \mathbf{z}_p^*$  are written as  $\mathbf{H}_B^*$  and  $T_B$ .

The terms of the GFSE, which was initially presented in equation (A2.99) have been found to produce the temperature in the following relationship in a three-dimensional Cartesian system:

$$T(\mathbf{x}^*, \mathbf{y}^*, \mathbf{z}^*, \mathbf{t}^*) = T_{initial\ conditions} + T_{source} + T_{boundary\ conditions}$$
 [K] (A2.110)

The first and third terms of equation (A2.110) were simplified respectively in equations (A2.101) and (A2.109). The second term will remain relatively unchanged as it appeared in equation (A2.99). The final step is to take the limit as  $\varepsilon \to 0$  in the time integral, to yield the final form of the nondimensional GFSE. Therefore, the fully derived GFSE with dimensionless variables is given in equation (A2.111).

$$T(x^{*}, y^{*}, z^{*}, t^{*})$$

$$= \int_{x_{1}^{*}=-\infty}^{\infty} \int_{y_{1}^{*}=-\infty}^{\Delta z_{p}^{*}} G^{*}(x^{*}, y^{*}, z^{*}, t^{*} | x_{1}^{*}, y_{1}^{*}, z_{1}^{*}, 0) F(x_{1}^{*}, y_{1}^{*}, z_{1}^{*}) dx_{1}^{*} dy_{1}^{*} dz_{1}^{*}$$

$$+ \frac{\omega_{\chi}^{2}}{k} \int_{t_{1}^{*}=0}^{t^{*}} \int_{x_{1}^{*}=-\infty}^{\infty} \int_{y_{1}^{*}=-\infty}^{\Delta z_{p}^{*}} G^{*}(x^{*}, y^{*}, z^{*}, t^{*} | x_{1}^{*}, y_{1}^{*}, z_{1}^{*}, t_{1}^{*}) g(x_{1}^{*}, y_{1}^{*}, z_{1}^{*}, t_{1}^{*}) dx_{1}^{*} dy_{1}^{*} dz_{1}^{*} dt_{1}^{*}$$

$$- H_{A}^{*} T_{A} \int_{t_{1}^{*}=0}^{t^{*}} \int_{x_{1}^{*}=-\infty}^{\infty} \int_{y_{1}^{*}=-\infty}^{\infty} G^{*}(x^{*}, y^{*}, z^{*}, t^{*} | x_{1}^{*}, y_{1}^{*}, 0, t_{1}^{*}) dx_{1}^{*} dy_{1}^{*} dt_{1}^{*}$$

$$+ H_{B}^{*} T_{B} \int_{t_{1}^{*}=0}^{t^{*}} \int_{x_{1}^{*}=-\infty}^{\infty} \int_{y_{1}^{*}=-\infty}^{\infty} G^{*}(x^{*}, y^{*}, z^{*}, t^{*} | x_{1}^{*}, y_{1}^{*}, \Delta z_{p}^{*}, t_{1}^{*}) dx_{1}^{*} dy_{1}^{*} dt_{1}^{*}$$

The GFSE that has been presented was derived for use with the infinite slab geometry which is representative of a powder bed. The boundary conditions that were implemented were of the general form of:

$$k\frac{\partial T}{\partial z}|_{z=s_i} \mp h_i T(x, y, s_i, t) = \mp f_i(x, y, s_i, t) \qquad \left[\frac{W}{m^2}\right]$$
(A2.112)

Given in dimensionless variables, the above equation is changed to:

$$k\frac{\partial T}{\partial \mathbf{z}^*}|_{\mathbf{z}^*=\mathbf{s}_i^*} \mp \omega_{\chi} h_i T(\mathbf{x}^*, \mathbf{y}^*, \mathbf{s}_i^*, \mathbf{t}^*) = \mp \omega_{\chi} f_i(\mathbf{x}^*, \mathbf{y}^*, \mathbf{s}_i^*, \mathbf{t}^*) \qquad \left[\frac{W}{m}\right] \quad (A2.113)$$

Here,  $s_i^*$  represents the  $i^{th}$  surface coordinate and  $f_i(x^*, y^*, s_i^*, t^*)$  is a function depending on the boundary condition considered. For convective boundary conditions, as were used in the above derivation,  $f_i(\mathbf{x}^*, \mathbf{y}^*, \mathbf{s}_i^*, \mathbf{t}^*) = h_i T_{\mathbf{s}_i^*}$ , where  $T_{\mathbf{s}_i^*}$  is the surrounding temperature at that surface. For an imposed flux,  $f_i(x^*, y^*, s_i^*, t^*) = q(s_i, t)$ . For simplicity, only the variable  $s_i^st$  is included in the function description but in multidimensional systems the other variables may be included as well. This explanation is important because the boundary condition of constant temperature modifies the GFSE slightly. To convert the general boundary condition of equation (A2.113) into one that uses a constant temperature, k must be set equal to zero and  $h_i$  equal to 1 W/(m<sup>2</sup>K). This yields:

$$T(x^*, y^*, s_i^*, t^*) = f_i(x^*, y^*, s_i^*, t^*) = T_{s_i^*}$$
 [K] (A2.114)

Beck *et al* describes fully how to derive the GFSE with the constant temperature boundary condition, and the final result will be given below for both cases using the  $f_i$  nomenclature [116].

$$T(x^*, y^*, z^*, t^*) \qquad [K] \quad (A2.115)$$

$$= \int_{x_1^* = -\infty}^{\infty} \int_{y_1^* = -\infty}^{\infty} \int_{z_1^* = 0}^{\Delta z_p^*} G^*(x^*, y^*, z^*, t^* | x_1^*, y_1^*, z_1^*, 0) F(x_1^*, y_1^*, z_1^*) dx_1^* dy_1^* dz_1^*$$

$$+ \frac{\omega_X^2}{k} \int_{t_1^* = 0}^{t^*} \int_{x_1^* = -\infty}^{\infty} \int_{y_1^* = -\infty}^{\infty} \int_{z_1^* = 0}^{\Delta z_p^*} G^*(x^*, y^*, z^*, t^* | x_1^*, y_1^*, z_1^*, t_1^*) g(x_1^*, y_1^*, z_1^*, t_1^*) dx_1^* dx_1^* dx_1^*$$

$$- \sum_{i=1}^2 \int_{t_1^* = 0}^{t^*} \int_{x_1^* = -\infty}^{\infty} \int_{y_1^* = -\infty}^{\infty} \int_{y_1^* = -\infty}^{\infty} f_i(x_1^*, y_1^*, z_1^*, t_1^*) \frac{\partial G^*(x^*, y^*, z^*, t^* | x_1^*, y_1^*, z_1^*, t_1^*)}{\partial z_1^*} |_{z_1^*}$$
For constant temperature boundary conditions
$$T(x^*, y^*, z^*, t^*)$$

$$= \int_{x_1^* = -\infty}^{\infty} \int_{y_1^* = -\infty}^{\infty} \int_{z_1^* = 0}^{\Delta z_p^*} G^*(x^*, y^*, z^*, t^* | x_1^*, y_1^*, z_1^*, dx_1^* dx_1^* dx_1^* dx_1^*$$

$$+ \frac{\omega_X^2}{k} \int_{t_1^* = 0}^{t^*} \int_{x_1^* = -\infty}^{\infty} \int_{y_1^* = -\infty}^{\Delta z_p^*} G^*(x^*, y^*, z^*, t^* | x_1^*, y_1^*, z_1^*, t_1^*) g(x_1^*, y_1^*, z_1^*, t_1^*) dx_1^* dy_1^* dz_1^* dt_1^*$$

$$+ \frac{\omega_X^2}{k} \sum_{t=1}^2 \int_{t_1^* = 0}^{t^*} \int_{x_1^* = -\infty}^{\infty} \int_{y_1^* = -\infty}^{\infty} f_i(x_1^*, y_1^*, z_1^*, t_1^*) G^*(x^*, y^*, z^*, t^* | x_1^*, y_1^*, z_1^*, t_1^*) dx_1^* dy_1^* dt_1^*$$
For all other boundary conditions

# A.2.5. GFSE for a Moving Coordinate System in

#### **Dimensionless Coordinates**

The GF derivation to this point has been for a *transient* system. For the specific case of selective laser melting, the laser can be considered as stationary with the powder moving at a fixed velocity underneath it. The arrangement described here is that of a *quasistationary* (QS) system. The benefit of approaching the powder bed as a QS system is that a constant

melt pool geometry can be determined with clearly defined regions of fixed temperature. It is not truly steady state because the temperature at any fixed point on the powder bed will fluctuate with time during the heating and cooling process. However, in terms of a moving coordinate system as time approaches infinity, the temperature in space is perceived as constant to the external observer.

The heat equation for a solid moving with velocity v in the positive x-direction is given below [116,118]:

$$\frac{\partial^2 T}{\partial x^2} + \frac{\partial^2 T}{\partial y^2} + \frac{\partial^2 T}{\partial z^2} + \frac{g(x, y, z, t)}{k} = \frac{1}{D} \frac{\partial T}{\partial t} + \frac{v}{D} \frac{\partial T}{\partial x} \qquad \left[\frac{K}{m^2}\right]$$
(A2.117)

Equation (A2.117) can be nondimensionalized with the help of Table 9 and equations (A2.3) to (A2.5). The normalization constant is again the laser radius,  $\omega_{\gamma}$ . The nondimensionalized terms will be restated below:

$$\frac{\partial T}{\partial x} = \frac{1}{\omega_{\chi}} \frac{\partial T}{\partial x^{*}} \qquad \frac{\partial T}{\partial y} = \frac{1}{\omega_{\chi}} \frac{\partial T}{\partial y^{*}} \qquad \frac{\partial T}{\partial z} = \frac{1}{\omega_{\chi}} \frac{\partial T}{\partial z^{*}} \qquad \left[\frac{K}{m}\right] \quad (A2.118)$$

$$\frac{\partial^{2}T}{\partial x^{2}} = \frac{1}{\omega_{\chi}^{2}} \frac{\partial^{2}T}{\partial x^{*2}} \qquad \frac{\partial^{2}T}{\partial y^{2}} = \frac{1}{\omega_{\chi}^{2}} \frac{\partial^{2}T}{\partial y^{*2}} \qquad \frac{\partial^{2}T}{\partial z^{2}} = \frac{1}{\omega_{\chi}^{2}} \frac{\partial^{2}T}{\partial z^{*2}} \qquad \left[\frac{K}{m^{2}}\right] \quad (A2.119)$$

$$\frac{\partial T}{\partial t} = \frac{D}{\omega_{\chi}^{2}} \frac{\partial T}{\partial t^{*}} \qquad \left[\frac{K}{s}\right] \quad (A2.120)$$

The relevant terms from equations (A2.118) to (A2.120) can be substituted into (A2.117) and then simplified in order to yield the heat equation variables for a moving system with dimensionless variables.

$$\frac{1}{\omega_{\chi}^{2}} \frac{\partial^{2}T}{\partial x^{*2}} + \frac{1}{\omega_{\chi}^{2}} \frac{\partial^{2}T}{\partial y^{*2}} + \frac{1}{\omega_{\chi}^{2}} \frac{\partial^{2}T}{\partial z^{*2}} + \frac{g(x^{*}, y^{*}, z^{*}, t^{*})}{k}$$

$$= \frac{1}{D} \frac{D}{\omega_{\chi}^{2}} \frac{\partial T}{\partial t^{*}} + \frac{v}{D} \frac{1}{\omega_{\chi}} \frac{\partial T}{\partial x^{*}}$$

$$\frac{\partial^{2}T}{\partial x^{*2}} + \frac{\partial^{2}T}{\partial y^{*2}} + \frac{\partial^{2}T}{\partial z^{*2}} + \frac{\omega_{\chi}^{2}}{k} g(x^{*}, y^{*}, z^{*}, t^{*}) = \frac{\partial T}{\partial t^{*}} + \frac{\omega_{\chi}v}{D} \frac{\partial T}{\partial x^{*}}$$

$$\frac{\partial^{2}T}{\partial x^{*2}} + \frac{\partial^{2}T}{\partial y^{*2}} + \frac{\partial^{2}T}{\partial z^{*2}} + \frac{\omega_{\chi}^{2}}{k} g(x^{*}, y^{*}, z^{*}, t^{*}) = \frac{\partial T}{\partial t^{*}} + v^{*} \frac{\partial T}{\partial x^{*}} \qquad [K] \quad (A2.121)$$

The extra term on the RHS of equation (A2.121) makes it unsuitable to be solved by the GFSE in its current form. It is recommended in the literature to apply a variable transform to the general solution so that it can then be analyzed using GFs [116,118]. The transform is given as:

$$T(x, y, z, t) = W(x, y, z, t)e^{\frac{vx}{2D} - \frac{v^2t}{4D}}$$
 [K] (A2.122)

The above equation is expressed in terms of dimensionless variables again with the help of Table 9:

$$T(x^*, y^*, z^*, t^*) = W(x^*, y^*, z^*, t^*)e^{\frac{v^*x^*}{2} - \frac{v^{*2}t^*}{4}}$$
 [K] (A2.123)

In order to apply equation (A2.121) to (A2.123), each term must first be derived in terms of the W variable change. For simplicity, the variable listing of  $(x^*, y^*, z^*, t^*)$  will be dropped. The following were computed using MAPLE software:

$$\frac{\partial T}{\partial x^*} = \left(\frac{v^*}{2}\right) W e^{\frac{v^* x^*}{2} - \frac{v^{*2} t^*}{4}} + \frac{\partial W}{\partial x^*} e^{\frac{v^* x^*}{2} - \frac{v^{*2} t^*}{4}}$$
 [K] (A2.124)

$$\frac{\partial^2 T}{\partial x^{*2}} = \left(\frac{v^*}{2}\right)^2 W e^{\frac{v^* x^*}{2} - \frac{v^{*2} t^*}{4}} + v \frac{\partial W}{\partial x^*} e^{\frac{v^* x^*}{2} - \frac{v^{*2} t^*}{4}} + \frac{\partial^2 W}{\partial x^{*2}} e^{\frac{v^* x^*}{2} - \frac{v^{*2} t^*}{4}}$$
 [K] (A2.125)

$$\frac{\partial^2 T}{\partial \mathbf{v}^{*2}} = \frac{\partial^2 W}{\partial \mathbf{v}^{*2}} e^{\frac{\mathbf{v}^* \mathbf{x}^*}{2} - \frac{\mathbf{v}^{*2} \mathbf{t}^*}{4}}$$
 [K] (A2.126)

$$\frac{\partial^2 T}{\partial z^{*2}} = \frac{\partial^2 W}{\partial z^{*2}} e^{\frac{v^* x^*}{2} - \frac{v^{*2} t^*}{4}}$$
 [K] (A2.127)

$$\frac{\partial T}{\partial t^*} = -\left(\frac{v^*}{2}\right)^2 W e^{\frac{v^*x^*}{2} - \frac{v^{*2}t^*}{4}} + \frac{\partial W}{\partial t^*} e^{\frac{v^*x^*}{2} - \frac{v^{*2}t^*}{4}}$$
 [K] (A2.128)

Inserting equations (A2.124) to (A2.128) into (A2.121) and simplifying yields:

$$\frac{\partial^2 W}{\partial \boldsymbol{x}^{*2}} + \frac{\partial^2 W}{\partial \boldsymbol{v}^{*2}} + \frac{\partial^2 W}{\partial \boldsymbol{z}^{*2}} + \frac{\omega_{\chi}^2}{k} g(\boldsymbol{x}^*, \boldsymbol{y}^*, \boldsymbol{z}^*, \boldsymbol{t}^*) e^{-\frac{\boldsymbol{v}^* \boldsymbol{x}^*}{2} + \frac{\boldsymbol{v}^{*2} \boldsymbol{t}^*}{4}} = \frac{\partial W}{\partial \boldsymbol{t}^*}$$
[K] (A2.129)

Equation (A2.129) is now the heat equation defined in terms of the transformed variable, W, which is conducive to being solved in the GFSE. Assuming initial conditions in the form of equation (A2.85) and considering the variable substitution of (A2.123), the transformed initial conditions are presented as:

$$T(x^*, y^*, z^*, \mathbf{0}) = W(x^*, y^*, z^*, \mathbf{0})e^{\frac{v^*x^*}{2}} = F(x^*, y^*, z^*)$$
 [K] (A2.130)

$$W(x^*, y^*, z^*, \mathbf{0}) = F(x^*, y^*, z^*)e^{-\frac{v^*x^*}{2}}$$
 [K] (A2.131)

Similarly, the general boundary conditions of the infinite slab geometry in the form of equation (A2.113) can be converted in the derivation below:

$$k \frac{\partial T}{\partial \mathbf{z}^*}|_{\mathbf{z}^* = \mathbf{s}_i^*} \mp \omega_{\chi} h_i T(\mathbf{x}^*, \mathbf{y}^*, \mathbf{s}_i^*, \mathbf{t}^*) = \mp \omega_{\chi} f_i(\mathbf{x}^*, \mathbf{y}^*, \mathbf{s}_i^*, \mathbf{t}^*) \qquad \left[\frac{W}{m}\right]$$

$$\frac{\partial T}{\partial \mathbf{z}^*} = \frac{\partial W}{\partial \mathbf{z}^*} e^{\frac{\mathbf{v}^* \mathbf{x}^*}{2} - \frac{\mathbf{v}^{*2} \mathbf{t}^*}{4}}$$
 [K]

$$k \frac{\partial W}{\partial \mathbf{z}^{*}}|_{\mathbf{z}^{*}=\mathbf{s}_{i}^{*}} e^{\frac{\mathbf{v}^{*}\mathbf{x}^{*}}{2} - \frac{\mathbf{v}^{*}\mathbf{z}^{*}}{4}} + \omega_{\chi} h_{i} W(\mathbf{x}^{*}, \mathbf{y}^{*}, \mathbf{s}_{i}^{*}, \mathbf{t}^{*}) e^{\frac{\mathbf{v}^{*}\mathbf{x}^{*}}{2} - \frac{\mathbf{v}^{*}\mathbf{z}^{*}}{4}}$$

$$= \mp \omega_{\gamma} f_{i}(\mathbf{x}^{*}, \mathbf{y}^{*}, \mathbf{s}_{i}^{*}, \mathbf{t}^{*})$$

$$k \frac{\partial W}{\partial z^*}|_{z^* = s_i^*} \mp \omega_{\chi} h_i W(x^*, y^*, s_i^*, t^*) = \mp \omega_{\chi} f_i(x^*, y^*, s_i^*, t^*) e^{-\frac{v^* x^*}{2} + \frac{v^{*2} t^*}{4}} \quad \left[\frac{W}{m}\right]$$

$$k \frac{\partial W}{\partial \boldsymbol{z}^*}|_{\boldsymbol{z}^* = \boldsymbol{s}_i^*} \mp \omega_{\chi} h_i W(\boldsymbol{x}^*, \boldsymbol{y}^*, \boldsymbol{s}_i^*, \boldsymbol{t}^*) = \mp \omega_{\chi} \boldsymbol{f}_i^*(\boldsymbol{x}^*, \boldsymbol{y}^*, \boldsymbol{s}_i^*, \boldsymbol{t}^*) \quad \left[\frac{W}{m}\right] \quad (A2.132)$$

The sign convention selected for the terms in the general boundary condition equation (A2.132) is dependant on the geometry of the system. The boundary condition function  $f_i(x^*, y^*, s_i^*, t^*)$  has been combined with the exponent factor that resulted from the variable transform. This is given by:

$$f_{i}^{*}(x^{*}, y^{*}, s_{i}^{*}, t^{*}) = f_{i}(x^{*}, y^{*}, s_{i}^{*}, t^{*})e^{-\frac{v^{*}x^{*}}{2} + \frac{v^{*2}t^{*}}{4}} \qquad \left[\frac{W}{m^{2}}\right]$$
(A2.133)

With the conversion of the boundary conditions into a form containing the W variable transform, the GFSE for the moving slab can be provided analogously as in equations (A2.115) and (A2.116).

$$\begin{split} W(x^*,y^*,z^*,t^*) &= \int_{x_1^*=-\infty}^{\infty} \int_{y_1^*=-\infty}^{4z_p^*} G^*(x^*,y^*,z^*,t^*|x_1^*,y_1^*,z_1^*,0) F(x_1^*,y_1^*,z_1^*) e^{-\frac{v^*x_1^*}{2}} dx_1^* dy_1^* dz_1^* \\ &+ \frac{\omega_x^2}{k} \int_{t_1^*=0}^{t^*} \int_{x_1^*=-\infty}^{\infty} \int_{y_1^*=-\infty}^{2} \int_{z_1^*=0}^{4z_p^*} G^*(x^*,y^*,z^*,t^*|x_1^*,y_1^*,z_1^*,t_1^*) g(x_1^*,y_1^*,z_1^*,t_1^*) e^{-\frac{v^*x_1^*}{2}} \frac{v^{*2}t_1^*}{4} dx_1^* dy_1^* dz \\ &- \sum_{i=1}^2 \int_{t_1^*=0}^{t^*} \int_{x_1^*=-\infty}^{\infty} \int_{y_1^*=-\infty}^{\infty} \int_{y_1^*=-\infty}^{\infty} \int_{t_1^*=0}^{t^*} \int_{t_1^*=0}^{t^*} \int_{y_1^*=-\infty}^{\infty} \int_{y_1^*=-\infty}^{t^*} \int_{t_1^*=0}^{t^*} \int_{x_1^*=-\infty}^{\infty} \int_{y_1^*=-\infty}^{2} \int_{t_1^*=0}^{t^*} \int_{x_1^*=0}^{\infty} \int_{x_1^*=0}^{\infty} G^*(x^*,y^*,z^*,t^*|x_1^*,y_1^*,z_1^*) e^{-\frac{v^*x_1^*}{2}} \frac{\partial G^*(x^*,y^*,z^*,t^*|x_1^*,y_1^*,z_1^*,t_1^*)}{\partial z_1^*} \Big|_{z_1^*=s_1^*} dx_1^* dy_1^* dz_1^* \\ &+ \frac{\omega_x^2}{k} \int_{t_1^*=0}^{t^*} \int_{x_1^*=-\infty}^{\infty} \int_{y_1^*=-\infty}^{\infty} \int_{y_1^*=-\infty}^{dx_1^*} \int_{x_1^*=0}^{t^*} G^*(x^*,y^*,z^*,t^*|x_1^*,y_1^*,z_1^*,t_1^*) g(x_1^*,y_1^*,z_1^*,t_1^*) e^{-\frac{v^*x_1^*}{2}} \frac{v^*x_1^*}{4} dx_1^* dy_1^* dz_1^* dt_1^* \\ &+ \frac{\omega_x^2}{k} \sum_{i=1}^{t^*} \int_{t_1^*=0}^{\infty} \int_{x_1^*=-\infty}^{\infty} \int_{y_1^*=-\infty}^{dx_1^*} \int_{x_1^*=0}^{t^*} G^*(x^*,y^*,z^*,t^*|x_1^*,y_1^*,z_1^*,t_1^*) g(x_1^*,y_1^*,z_1^*,t_1^*) e^{-\frac{v^*x_1^*}{2}} \frac{v^*x_1^*}{4} dx_1^* dy_1^* dz_1^* dt_1^* \\ &+ \frac{\omega_x^2}{k} \sum_{i=1}^{t^*} \int_{t_1^*=0}^{t^*} \int_{x_1^*=-\infty}^{\infty} \int_{y_1^*=-\infty}^{dx_1^*} \int_{x_1^*=0}^{t^*} G^*(x^*,y^*,z^*,t^*) \frac{v^*x_1^*}{4} G^*(x^*,y^*,z^*,t^*) \frac{v^*x_1^*}{4} G^*(x^*,y^*,z^*,t^*) \frac{v^*x_1^*}{4} \frac{v^*x_1^*}{4} \int_{x_1^*=0}^{t^*x_1^*} dx_1^* dy_1^* dz_1^* dt_1^* \\ &+ \text{For all other boundary conditions} \end{split}$$

#### A.2.6. Laser Source Term in Dimensionless Coordinates

The source term can be defined for many different beam shapes and attenuation factors as outlined in *Bäuerle et. al* [62]. For the purposes of the current research, a Gaussian beam as outlined in section 3.1.3.1 will be used and the attenuation due to the Lambert-Beer law (LB) and the Radiative Transfer Equation (RTE) will be applied in separate cases.

Thus, the general form of the *stationary* Gaussian source incident on the xy-plane is given below where f(z) is the attenuation function:

$$g(x, y, z, t) = \frac{\chi P}{\pi \omega_{\chi}^{2}} e^{-\chi \left(\frac{x^{2} + y^{2}}{\omega_{\chi}^{2}}\right)} f(z) \qquad \left[\frac{W}{m^{3}}\right] \tag{A2.137}$$

The attenuation function that characterizes the Lambert-Beer law is given as:

$$f_{LB}(z) = A\alpha e^{-\alpha z}$$
 [m<sup>-1</sup>] (A2.138)

where  $\alpha$  is the absorption coefficient in units of [m<sup>-1</sup>] and the material absorptivity, A, is included. This law is described in the literature and mentioned earlier in section 3.1.1.1.1 [62,79,84,86]. Substituting equation (A2.138) into (A2.137) and converting all the spatial variables into their dimensionless counterparts with the help of Table 9 yields the source term for the Gaussian beam with Lambert-Beer attenuation:

$$g_{LB}(\mathbf{x}^*, \mathbf{y}^*, \mathbf{z}^*, \mathbf{t}^*) = \frac{A\alpha\chi P}{\pi\omega_{\chi}^2} e^{-\chi(x^{*2} + y^{*2})} e^{-\alpha^* \mathbf{z}^*} \qquad \left[\frac{W}{m^3}\right] \text{ (A2.139)}$$

The RTE must be considered as well because SLM is performed with powders that lie on metallic substrates. As outlined in Appendix A.1, the RTE considers attenuation as well as scattering and reflection from the bottom surface. It allows a second chance for the laser to be absorbed into the powder especially in optically thin layers where the underlying material

has a high reflectivity. The attenuation function for the RTE is more involved than that of the Lambert-Beer law and was derived specifically in Appendix A.1 and is summarized again below.

The solution to the RTE is given by combining equations (A1.106) to (A1.109). It represents the absorptivity at any normalized depth within the powder-substrate system of  $\xi$ . This depth is defined in the product of the absorption coefficient  $\beta$  and z. The variable  $\omega$ , which was used previously, represents the bulk material reflectivity and has been replaced by  $R_b$  for clarity and distinction from the laser radius.

$$q(\xi) = e^{-\xi} - R_s e^{\xi - 2\lambda} + \frac{1}{2} \left( A e^{-2a\xi} + B e^{2a\xi} - \frac{2R_b}{4R_b - 3} \left( e^{-\xi} - R_s e^{\xi - 2\lambda} \right) \right)$$
 (A2.140)

The negative derivative of  $q(\xi)$  is used to form the attenuation function that contributes to volumetric heating:

$$-\frac{dq}{d\xi} = a\left(Ae^{-2a\xi} - Be^{2a\xi}\right) + \left(e^{-\xi} + R_s e^{\xi - 2\lambda}\right) \left(1 - \frac{R_b}{4R_b - 3}\right)$$
 (A2.141)

with the coefficients defined as:

$$= \frac{2R_{b}(e^{2a\lambda})((R_{s}+3(e^{2\lambda}))((R_{b}(1+R_{s})-2)a-2(1-R_{b}))(e^{2a\lambda})+R_{b}a(1-R_{s})(1+R_{s})e^{\lambda})}{(4R_{b}-3)(e^{2\lambda})((R_{b}(1+R_{s})-2(1+a))(e^{4a\lambda})-2(a-1)-R_{b}(1+R_{s}))(1+a)}$$
(A2.142)

$$=\frac{2R_{b}\left(e^{\lambda}(1-R_{s})(1+R_{s})(1+a-R_{b})\left(e^{2a\lambda}\right)-\left(R_{s}+3\left(e^{2\lambda}\right)\right)\left((1-R_{s})a+(1+R_{s})(R_{b}-1)\right)\right)}{(4R_{b}-3)(e^{2\lambda})\left((R_{b}(1+R_{s})-2(1+a))(e^{4a\lambda})-2(a-1)-R_{b}(1+R_{s})\right)}$$
(A2.143)

$$a = \sqrt{1 - R_b} \tag{A2.144}$$

$$\lambda = \beta \Delta z_p \tag{A2.145}$$

$$\xi = \beta z \tag{A2.146}$$

$$\frac{d\xi}{dz} = \beta \tag{A2.147}$$

The attenuation function for the RTE in terms of the dimensional variable z is obtained by applying the chain rule to equation (A2.141) with the help of (A2.147).

$$f_{RTE}(z) = -\frac{dq}{dz} = -\frac{dq}{d\xi} \cdot \frac{d\xi}{dz} = \beta \left( -\frac{dq}{d\xi} |_{\xi = \beta z} \right)$$
 [m<sup>-1</sup>] (A2.148)

Substituting the RHS of (A2.141) into equation (A2.148) and evaluating at  $\xi = \beta z$  as instructed above, provides the semi-expanded representation of the dimensional RTE attenuation function:

$$f_{RTE}(z) = \beta \left( a \left( A e^{-2a\beta z} - B e^{2a\beta z} \right) + \left( e^{-\beta z} \right) +$$

Finally, with the help of Table 9, the variable z in equation (A2.149) can be put into its dimensionless form:

$$f_{RTE}(\mathbf{z}^*) = \beta \left( a \left( A e^{-2a\beta^* \mathbf{z}^*} - B e^{2a\beta^* \mathbf{z}^*} \right) + \left( e^{-\beta^* \mathbf{z}^*} \right) + \left($$

The optical thickness  $\lambda$  as defined in equation (A2.145) **does not need to be put into its dimensionless form** as it is already a dimensionless constant that does not change with position in a fixed slab. Thus,  $\lambda = \lambda^*$ , and this can be verified by using the normalized values found in Table 9 as well. Finally, the dimensionless source term using the RTE attenuation function above is given below in analogy to equation (A2.139):

$$g_{RTE}(\mathbf{x}^*, \mathbf{y}^*, \mathbf{z}^*, \mathbf{t}^*) = \frac{\beta \chi P}{\pi \omega_{\chi}^2} e^{-\chi (\mathbf{x}^{*2} + \mathbf{y}^{*2})} \left( a \left( A e^{-2a\beta^* \mathbf{z}^*} - B e^{2a\beta^* \mathbf{z}^*} \right) + \left( e^{-\beta^* \mathbf{z}^*} \right) + \left$$

Two important aspects about these derivations must be noted at this point. The first is that the absorptivity factor which is present in the Lambert-Beer source is not explicitly present in the RTE source. This is because the effects of absorptivity are already included in the RTE solution. Specifically, an integral over the thickness of the powder layer for equation (A2.149) would yield the absorptivity of the system. Secondly, both equations (A2.139) and (A2.151) still contain dimensional absorption coefficients as multiplicative factors outside of their exponentials, while inside their respective exponentials these coefficients are nondimensional. This will be

remedied once the source term is placed into the GFSE, where it is multiplied by a factor of  $\frac{\omega_\chi^2}{k}$ . Equation (A2.135) can be consulted as an example of the implementation of this factor. One of the terms from the square of the laser radius will be repositioned in the source term to multiply with the absorption coefficient, either  $\alpha$  or  $\beta$ , to produce its dimensionless counterpart  $\alpha^*$  or  $\beta^*$ , respectively.

### A.2.7. Final Form of the GFSE

All of the derivations presented until this point can now be utilized to form the GFSE for the infinite slab geometry in three dimensions. The first step is to construct the three-dimensional GF by multiplying equations (A2.35), (A2.36) and (A2.72) together.

$$G^{*}(x^{*}, y^{*}, z^{*}, t^{*} \mid x_{1}^{*}, y_{1}^{*}, z_{1}^{*}, t_{1}^{*})$$

$$= G_{x}^{*}(x^{*}, t^{*} \mid x_{1}^{*}, t_{1}^{*})G_{y}^{*}(y^{*}, t^{*} \mid y_{1}^{*}, t_{1}^{*})G_{z}^{*}(z^{*}, t^{*} \mid z_{1}^{*}, t_{1}^{*})$$
(A2.152)

$$G^{*}(\boldsymbol{x}^{*}, \boldsymbol{y}^{*}, \boldsymbol{z}^{*}, \boldsymbol{t}^{*} \mid \boldsymbol{x}_{1}^{*}, \boldsymbol{y}_{1}^{*}, \boldsymbol{z}_{1}^{*}, \boldsymbol{t}_{1}^{*})$$

$$= \frac{1}{4\pi(\boldsymbol{t}^{*} - \boldsymbol{t}_{1}^{*})} e^{\frac{(\boldsymbol{x}^{*} - \boldsymbol{x}_{1}^{*})^{2} + (\boldsymbol{y}^{*} - \boldsymbol{y}_{1}^{*})^{2}}{4(\boldsymbol{t}^{*} - \boldsymbol{t}_{1}^{*})}} \sum_{n=1}^{\infty} \frac{Z(\boldsymbol{z}^{*}, \nu_{n})Z(\boldsymbol{z}_{1}^{*}, \nu_{n})e^{-\nu_{n}^{2}(\boldsymbol{t}^{*} - \boldsymbol{t}_{1}^{*})}}{N(\nu_{n})}$$
(A2.153)

where again:

$$Z(\mathbf{z}^*, \nu_n) = \left(\frac{\mathbf{H}_A^*}{\nu_n} \sin(\nu_n \mathbf{z}^*) + \cos(\nu_n \mathbf{z}^*)\right)$$
(A2.154)

$$N(\nu_n) = \frac{1}{2} \left( \frac{\Delta \mathbf{z}_p^* (\nu_n^2 + \mathbf{H}_A^{*2})}{\nu_n^2} + \frac{(\mathbf{H}_A^* + \mathbf{H}_B^*)(\nu_n^2 + \mathbf{H}_A^* \mathbf{H}_B^*)}{\nu_n^2 (\nu_n^2 + \mathbf{H}_B^{*2})} \right)$$
(A2.155)

$$\tan(\nu_n \Delta z_p^*) = \frac{\nu_n (H_A^* + H_B^*)}{(\nu_n^2 - H_B^* H_A^*)}$$
(A2.156)

The GFSE for the infinite slab geometry for the moving coordinate system is composed of the initial conditions term, the source term, and the boundary conditions term as outlined in equations (A2.134) and (A2.135). The form of the GFSE here, however, will be based on that of (A2.135) as the GF in the z-direction was derived using convective boundary conditions.

The initial conditions term in the moving coordinate system will be solved for first. The initial temperature within the powder bed is assumed to be constant such that:

$$F(x^*, y^*, z^*) = F(x_1^*, y_1^*, z_1^*) = T_0$$
 [K] (A2.157)

From equation (A2.135), the initial conditions term is given as:

$$W_{in}(\mathbf{x}^*, \mathbf{y}^*, \mathbf{z}^*, \mathbf{t}^*)$$

$$= \int_{x_1^* = -\infty}^{\infty} \int_{y_1^* = -\infty}^{\infty} \int_{z_1^* = 0}^{\Delta z_p^*} G^*(\mathbf{x}^*, \mathbf{y}^*, \mathbf{z}^*, \mathbf{t}^* | \mathbf{x}_1^*, \mathbf{y}_1^*, \mathbf{z}_1^*, \mathbf{0}) F(\mathbf{x}_1^*, \mathbf{y}_1^*, \mathbf{z}_1^*) e^{-\frac{v^* \mathbf{x}_1^*}{2}} d\mathbf{x}_1^* d\mathbf{y}_1^* d\mathbf{z}_1^*$$
[K] (A2.158)

In the above equation, it is necessary to evaluate the GF at  $t_1^* = 0$ . Combining equations (A2.153) to (A2.155), (A2.157), (A2.158), and (A2.123), and simplifying with the help of MAPLE software, the initial condition term is given as:

$$T_{in}(\mathbf{x}^*, \mathbf{y}^*, \mathbf{z}^*, \mathbf{t}^*) = W_{in}(\mathbf{x}^*, \mathbf{y}^*, \mathbf{z}^*, \mathbf{t}^*) e^{\frac{\mathbf{v}^* \mathbf{x}^*}{2} - \frac{\mathbf{v}^{*2} \mathbf{t}^*}{4}}$$
 [K] (A2.159)

$$T_{in}(\mathbf{x}^*, \mathbf{y}^*, \mathbf{z}^*, \mathbf{t}^*)$$

$$= T_o \sum_{n=1}^{\infty} \left( \frac{2(\mathbf{H}_A^* \sin(\nu_n \mathbf{z}^*) + \nu_n \cos(\nu_n \mathbf{z}^*))(\mathbf{H}_A^* (1 - \cos(\nu_n \Delta \mathbf{z}_p^*)) + \nu_n \sin(\nu_n \Delta \mathbf{z}_p^*))(\nu_n^2 + \mathbf{H}_B^{*2})}{\nu_n \left( \Delta \mathbf{z}_p^* \nu_n^4 + \nu_n^2 \left( \mathbf{H}_A^* + \mathbf{H}_B^* + \Delta \mathbf{z}_p^* (\mathbf{H}_A^{*2} + \mathbf{H}_B^{*2}) \right) + \mathbf{H}_A^* \mathbf{H}_B^* (\mathbf{H}_A^* (1 + \mathbf{H}_B^* \Delta \mathbf{z}_p^*) + \mathbf{H}_B^*)} \right)^{e^{-\nu_n^2 t^*}}$$
[K] (A2.160)

Equation (A2.160) can be further simplified by grouping the terms according to equations (A2.154) and (A2.155). This yields the more compact version of:

$$T_{in}(\mathbf{x}^*, \mathbf{y}^*, \mathbf{z}^*, \mathbf{t}^*) = T_o \sum_{n=1}^{\infty} \left( \frac{Z(\mathbf{z}^*, \nu_n) e^{-\nu_n^2 t^*}}{N(\nu_n)} \int_0^{\Delta z_p^*} Z(\mathbf{z}_1^*, \nu_n) d\mathbf{z}_1^* \right)$$
 [K] (A2.161)

Equation (A2.161) represents the transient effects of the initial conditions. It can be put into its quasistationary form by taking its limit as  $t^* \to \infty$ . Since  $t^*$  only occurs within its exponential, and the exponent is negative, the limit is equal to zero. This is intuitive since the initial conditions of a system operating at a steady or quasistationary state should tend toward zero as time approaches infinity.

$$T_{in_{QS}}(\mathbf{x}^*, \mathbf{y}^*, \mathbf{z}^*, \infty) = T_o \sum_{n=1}^{\infty} \left( \frac{Z(\mathbf{z}^*, \nu_n) e^{-\nu_n^2 \infty}}{N(\nu_n)} \int_0^{\Delta \mathbf{z}_p^*} Z(\mathbf{z}_1^*, \nu_n) d\mathbf{z}_1^* \right) = 0$$
 [K] (A2.162)

Moving on from the initial condition term, the convective boundary condition terms will now be determined for the top and bottom surfaces of the slab. At the top surface,  $z^* = 0$ , the convective boundary condition is given as:

$$\frac{\partial T(\mathbf{x}^*, \mathbf{y}^*, \mathbf{z}^*, \mathbf{t}^*)}{\partial \mathbf{z}^*} \big|_{\mathbf{z}^* = \mathbf{0}} - H_A^* T(\mathbf{x}^*, \mathbf{y}^*, \mathbf{0}, \mathbf{t}^*) = -H_A^* T_A$$

$$= \frac{\omega_{\chi}}{k} f_1(\mathbf{x}^*, \mathbf{y}^*, \mathbf{0}, \mathbf{t}^*)$$
[K] (A2.163)

This boundary condition term in the moving coordinate system GFSE is:

$$W_{TOP}(\boldsymbol{x}^*, \boldsymbol{y}^*, \boldsymbol{z}^*, \boldsymbol{t}^*) = \frac{\omega_{\chi}}{k} \int_{t_1^* = 0}^{t^*} \int_{y_1^* = -\infty}^{\infty} \int_{y_1^* = -\infty}^{\infty} f_1(x_1^*, y_1^*, \boldsymbol{0}, t_1^*) e^{-\frac{v^* x_1^*}{2} + \frac{v^{*2} t_1^*}{4}} G^*(\boldsymbol{x}^*, \boldsymbol{y}^*, \boldsymbol{z}^*, \boldsymbol{t}^* \mid x_1^*, y_1^*, \boldsymbol{0}, t_1^*) dx_1^* dy_1^* dt_1^*$$
[K] (A2.164)

Again invoking equation (A2.123) and using (A2.163), (A2.164) and (A2.153) evaluated at  $\mathbf{z}_1^* = \mathbf{0}$ , the top boundary condition contribution is given as:

$$T_{TOP}(\mathbf{x}^*, \mathbf{y}^*, \mathbf{z}^*, \mathbf{t}^*) = W_{TOP}(\mathbf{x}^*, \mathbf{y}^*, \mathbf{z}^*, \mathbf{t}^*) e^{\frac{\mathbf{v}^* \mathbf{x}^*}{2} - \frac{\mathbf{v}^{*2} \mathbf{t}^*}{4}}$$
 [K] (A2.165)

$$T_{TOP}(\boldsymbol{x}^*, \boldsymbol{y}^*, \boldsymbol{z}^*, \boldsymbol{t}^*)$$

$$=-H_{A}^{*}T_{A}\sum_{n=1}^{\infty}\left(\frac{2(H_{A}^{*}\sin(\nu_{n}z^{*})+\nu_{n}\cos(\nu_{n}z^{*}))(\nu_{n}^{2}+H_{B}^{*}{}^{2})(1-e^{-\nu_{n}^{2}t^{*}})}{\nu_{n}\left(\Delta z_{p}^{*}\nu_{n}^{4}+\nu_{n}^{2}\left(H_{A}^{*}+H_{B}^{*}+\Delta z_{p}^{*}(H_{A}^{2}+H_{B}^{2}\right)\right)+H_{A}^{*}H_{B}^{*}\left(H_{B}^{*}+H_{A}^{*}(1+\Delta z_{p}^{*}H_{B}^{*})\right)\right)}\right)$$
[K] (A2.166)

This boundary condition can be simplified with the help of equations (A2.154) and (A2.155) as well to yield the compact form of:

$$T_{TOP}(\mathbf{x}^*, \mathbf{y}^*, \mathbf{z}^*, \mathbf{t}^*) = -\mathbf{H}_A^* T_A \sum_{n=1}^{\infty} \left( \frac{Z(\mathbf{z}^*, \nu_n)}{\nu_n^2 N(\nu_n)} (1 - e^{-\nu_n^2 t^*}) \right)$$
 [K] (A2.167)

Taking the limit as  $t^* \to \infty$  provides the quasistationary top boundary contribution in the moving coordinate system:

$$T_{TOP_{QS}}(\mathbf{x}^*, \mathbf{y}^*, \mathbf{z}^*, \infty) = -\mathbf{H}_A^* T_A \sum_{n=1}^{\infty} \left( \frac{Z(\mathbf{z}^*, \nu_n)}{\nu_n^2 N(\nu_n)} \right)$$
 [K] (A2.168)

Similarly, the bottom boundary contribution is constructed in the same way, with the condition given at  $z^* = \Delta z_p^*$ :

$$\frac{\partial T(\boldsymbol{x}^*, \boldsymbol{y}^*, \boldsymbol{z}^*, \boldsymbol{t}^*)}{\partial \boldsymbol{z}^*} |_{\boldsymbol{z}^* = \Delta \boldsymbol{z}_p^*} + \boldsymbol{H}_B^* T(\boldsymbol{x}^*, \boldsymbol{y}^*, \Delta \boldsymbol{z}_p^*, \boldsymbol{t}^*) = \boldsymbol{H}_B^* T_B$$

$$= \frac{\omega_{\chi}}{k} f_2(\boldsymbol{x}^*, \boldsymbol{y}^*, \Delta \boldsymbol{z}_p^*, \boldsymbol{t}^*)$$
[K] (A2.169)

where

$$W_{BOTTOM}(\boldsymbol{x}^*, \boldsymbol{y}^*, \boldsymbol{z}^*, \boldsymbol{t}^*)$$

$$= \frac{\omega_{\chi}}{k} \int_{t_1^*=0}^{t^*} \int_{x_1^*=-\infty}^{\infty} \int_{y_1^*=-\infty}^{\infty} f_2(x_1^*, y_1^*, \Delta z_p^*, t_1^*) e^{-\frac{v^* x_1^*}{2} + \frac{v^{*2} t_1^*}{4}} G^*(\boldsymbol{x}^*, \boldsymbol{y}^*, \boldsymbol{z}^*, \boldsymbol{t}^* \mid \boldsymbol{x}_1^*, \boldsymbol{y}_1^*, \Delta z_p^*, t_1^*) dx_1^* dy_1^* dt} \begin{bmatrix} K \end{bmatrix} (A2.170)$$

By using the same procedure as that for the top boundary, the contribution from the bottom term is given as:

$$T_{BOTTOM}(\mathbf{x}^*, \mathbf{y}^*, \mathbf{z}^*, \mathbf{t}^*) = W_{BOTTOM}(\mathbf{x}^*, \mathbf{y}^*, \mathbf{z}^*, \mathbf{t}^*) e^{\frac{\mathbf{v}^* \mathbf{x}^*}{2} - \frac{\mathbf{v}^{*2} \mathbf{t}^*}{4}}$$
 [K] (A2.171)

$$T_{BOTTOM}(\boldsymbol{x}^*, \boldsymbol{y}^*, \boldsymbol{z}^*, \boldsymbol{t}^*)$$

$$=H_{B}^{*}T_{B}\sum_{n=1}^{\infty}\left(\frac{2(H_{A}^{*}\sin(\nu_{n}\mathbf{z}^{*})+\nu_{n}\cos(\nu_{n}\mathbf{z}^{*}))(H_{A}^{*}\sin(\nu_{n}\Delta\mathbf{z}_{p}^{*})+\nu_{n}\cos(\nu_{n}\Delta\mathbf{z}_{p}^{*}))(\nu_{n}^{2}+H_{B}^{*2})(1-e^{-\nu_{n}^{2}t^{*}})}{\nu_{n}^{2}\left(\Delta\mathbf{z}_{p}^{*}\nu_{n}^{4}+\nu_{n}^{2}(H_{A}^{*}+H_{B}^{*}+\Delta\mathbf{z}_{p}^{*}(H_{A}^{*}^{2}+H_{B}^{*2}^{2})\right)+H_{A}^{*}H_{B}^{*}\left(H_{B}^{*}+H_{A}^{*}(1+\Delta\mathbf{z}_{p}^{*}H_{B}^{*})\right)}\right)$$
[K] (A2.172)

Simplifying the above equation with the help of (A2.154) and (A2.155) again provides the compact form of the bottom boundary contribution:

 $T_{BOTTOM}(\boldsymbol{x}^*, \boldsymbol{y}^*, \boldsymbol{z}^*, \boldsymbol{t}^*)$ 

$$= H_B^* T_B \sum_{n=1}^{\infty} \left( \frac{Z(\mathbf{z}^*, \nu_n) Z(\Delta \mathbf{z}_{p}^*, \nu_n)}{\nu_n^2 N(\nu_n)} (1 - e^{-\nu_n^2 t^*}) \right)$$
 [K] (A2.173)

To obtain the quasistationary state, the limit as  $t^* \to \infty$  is again evaluated, yielding:

$$T_{BOTTOM_{QS}}(\boldsymbol{x}^*, \boldsymbol{y}^*, \boldsymbol{z}^*, \infty) = \boldsymbol{H}_{\boldsymbol{B}}^* T_B \sum_{n=1}^{\infty} \left( \frac{Z(\boldsymbol{z}^*, \nu_n) Z(\boldsymbol{\Delta} \boldsymbol{z}_{\boldsymbol{p}}^*, \nu_n)}{\nu_n^2 N(\nu_n)} \right) \quad [K] \text{ (A2.174)}$$

The final and most involved term to obtain is the contribution from the source. The source term under consideration is that of the RTE from equation (A2.151), and is restated below. The variable  $t^*$  has been dropped from the notation of the source since it does not explicitly appear due to the source being stationary in the new moving coordinate system.

$$g_{RTE}(\mathbf{x}^*, \mathbf{y}^*, \mathbf{z}^*, \mathbf{t}^*) = g_{RTE}(\mathbf{x}^*, \mathbf{y}^*, \mathbf{z}^*) = I_o g_x(\mathbf{x}^*) g_y(\mathbf{y}^*) g_z(\mathbf{z}^*)$$

$$= I_o e^{-\chi \left(\mathbf{x}^{*2} + \mathbf{y}^{*2}\right)} \left( a \left( A e^{-2a\beta^* \mathbf{z}^*} - B e^{2a\beta^* \mathbf{z}^*} \right) + \left( e^{-\beta^* \mathbf{z}^*} \quad \left[ \frac{W}{m^3} \right] \right)$$

$$+ R_s e^{\beta^* \mathbf{z}^* - 2\lambda} \left( 1 - \frac{R_b}{4R_b - 3} \right)$$
(A2.175)

where

$$I_o = \frac{\beta \chi P}{\pi \omega_\chi^2}$$
 
$$\left[ \frac{W}{m^3} \right]$$
 (A2.176) 
$$g(x^*) = e^{-\chi x^{*2}}$$

$$g(\mathbf{y}^*) = e^{-\chi {y^*}^2}$$
 (A2.178)

$$g(\mathbf{z}^*) = a(Ae^{-2a\boldsymbol{\beta}^*\mathbf{z}^*} - Be^{2a\boldsymbol{\beta}^*\mathbf{z}^*}) + (e^{-\boldsymbol{\beta}^*\mathbf{z}^*} + R_se^{\boldsymbol{\beta}^*\mathbf{z}^*-2\lambda})\left(1 - \frac{R_b}{4R_b - 3}\right)$$
(A2.179)

Considering the laser source and the three-dimensional GF defined for the infinite slab in equation (A2.153), The source term in the GFSE for the moving system from (A2.135) is given as:

$$W_{SOURCE}(x^*, y^*, z^*, t^*) = \frac{\omega_{\chi}^2}{k} \int_{t_1^*=0}^{t^*} \int_{x_1^*=-\infty}^{\infty} \int_{y_1^*=-\infty}^{\Delta z_p^*} \int_{z_1^*=0}^{\Delta z_p^*} G^*(x^*, y^*, z^*, t^* | x_1^*, y_1^*, z_1^*, t_1^*) g(x_1^*, y_1^*, z_1^*, t_1^*) e^{-\frac{v^* x_1^*}{2} + \frac{v^{*2} t_1^*}{4}} dx_1^* dy_1^* dz_1^*$$
[K (A2.180)

The total contribution, as determined previously for the initial conditions and boundary conditions, is obtained by inserting the evaluated integral above into equation (A2.123):

$$T_{SOURCE}(\mathbf{x}^*, \mathbf{y}^*, \mathbf{z}^*, \mathbf{t}^*) = W_{SOURCE}(\mathbf{x}^*, \mathbf{y}^*, \mathbf{z}^*, \mathbf{t}^*) e^{\frac{\mathbf{v}^* \mathbf{x}^*}{2} - \frac{\mathbf{v}^{*2} \mathbf{t}^*}{4}}$$
 [K (A2.181)

Before writing the source term according to the process above, it is important to note that unlike for the initial and boundary conditions, there is no analytical quasistationary solution for the source term. This is because the integral in the variable  $t_1^*$  is only able to be computed numerically. Thus, the final form of this term will be left as an integral. This solution is obtained by lengthy manipulation in MAPLE software by the evaluation of the above equations. It was then simplified with help from (A2.154) and (A2.155) as done previously as well.

 $T_{SOURCE}(\boldsymbol{x}^*, \boldsymbol{y}^*, \boldsymbol{z}^*, \boldsymbol{t}^*)$ 

$$= \frac{\omega_{\chi}^{2}}{k} I_{o} \sum_{n=1}^{\infty} \left( \frac{Z(\mathbf{z}^{*}, \nu_{n})}{N(\nu_{n})} \left[ \int_{0}^{\Delta z_{p}^{*}} Z(\mathbf{z}_{1}^{*}, \nu_{n}) g_{z}(\mathbf{z}_{1}^{*}) d\mathbf{z}_{1}^{*} \right] \left\{ \int_{0}^{t^{*}} \frac{e^{-\frac{\chi \left( \left( \mathbf{x}^{*} - \mathbf{v}^{*} \left( \mathbf{t}^{*} - \mathbf{t}_{1}^{*} \right) \right)^{2} + \mathbf{y}^{*} 2\right)}}{1 + 4\chi \left( \mathbf{t}^{*} - \mathbf{t}_{1}^{*} \right)} e^{-\nu_{n}^{2} \left( \mathbf{t}^{*} - \mathbf{t}_{1}^{*} \right)} d\mathbf{t}_{1}^{*} \right\} \right) [K] \quad (A2.182)$$

The source term defined in (A2.182) has been integrated through the  $x_1^*$  and  $y_1^*$  in their respective infinite domains. Thus, the x- and y-contributions to the source disappear from the above equation. However, the integral in  $z_1^*$  has been left unevaluated and thus the z-contribution from the source remains. The argument of the integral is composed of equations (A2.154) and (A2.179) evaluated at  $z^* = z_1^*$ . The eigenvalues are obtained as previously mentioned by:

$$\tan(\nu_n \Delta z_p^*) = \frac{\nu_n (H_A^* + H_B^*)}{(\nu_n^2 - H_B^* H_A^*)}$$
(A2.183)

To obtain the source term contribution at any point  $(x^*, y^*, z^*, t^*)$ , both integrals in  $z_1^*$  and  $t_1^*$  equation (A2.182) can be evaluated numerically, although the former does have an analytical solution. It was condensed into shorter notation to save space. The *quasistationary solution* is arrived at by means of a variable transform. If the following substitution is applied to equation (A2.182):

$$\varepsilon = t^* - t_1^* \tag{A2.184}$$

$$d\varepsilon = -dt_1^* \tag{A2.185}$$

The limits of the original integral are converted as follows:

$$\boldsymbol{t}_{1}^{*} = 0 \rightarrow \boldsymbol{\varepsilon} = \boldsymbol{t}^{*} \tag{A2.186}$$

$$\boldsymbol{t}_{1}^{*} = \boldsymbol{t}^{*} \rightarrow \boldsymbol{\varepsilon} = \boldsymbol{0} \tag{A2.187}$$

Evaluating as  $t^* \to \infty$  for the above two limits creates new limits of integration:

$$t_1^* = 0 \rightarrow \lim_{t^* \to \infty} \varepsilon = \infty$$
 (A2.188)

$$\boldsymbol{t}_{1}^{*} = \boldsymbol{t}^{*} \rightarrow \lim_{\boldsymbol{t}^{*} \to \infty} \boldsymbol{\varepsilon} = \boldsymbol{0}$$
 (A2.189)

Due to the negative sign in equation (A2.185) the integral and its limits can be flipped according to the following representation.

$$\lim_{t^* \to \infty} \int_0^{t^*} dt_1^* = -\lim_{t^* \to \infty} \int_{t^*}^0 d\varepsilon = \lim_{t^* \to \infty} \int_0^{t^*} d\varepsilon = \int_0^\infty d\varepsilon$$
 (A2.190)

Applying the above variable change creates an integral that is easier to evaluate numerically:

$$T_{SOURCE_{OS}}(\boldsymbol{x}^*, \boldsymbol{y}^*, \boldsymbol{z}^*, \infty)$$

$$= \frac{\omega_{\chi}^{2}}{k} I_{o} \sum_{n=1}^{\infty} \left( \frac{Z(\mathbf{z}^{*}, \nu_{n})}{N(\nu_{n})} \left[ \int_{\mathbf{0}}^{\Delta z_{p}^{*}} Z(\mathbf{z}_{1}^{*}, \nu_{n}) g_{z}(\mathbf{z}_{1}^{*}) d\mathbf{z}_{1}^{*} \right] \left\{ \int_{\mathbf{0}}^{\infty} \frac{e^{-\frac{\chi((x^{*} - \nu^{*} \varepsilon)^{2} + y^{*}^{2})}{1 + 4\chi \varepsilon}}}{1 + 4\chi \varepsilon} e^{-\nu_{n}^{2} \varepsilon} \right] \left[ K \text{ (A2.191)} \right]$$

Thus, all the terms of GFSE for the moving infinite slab have been determined with dimensionless variables and the final equation is given as follows for both the transient and quasistationary cases:

$$T(x^{*}, y^{*}, z^{*}, t^{*}) = T_{in} + T_{SOURCE} + T_{TOP} + T_{BOTTOM}$$

$$[K] \quad (A2.192)$$

$$T(x^{*}, y^{*}, z^{*}, t^{*})$$

$$= T_{o} \sum_{n=1}^{\infty} \left( \frac{Z(z^{*}, v_{n})e^{-v_{n}^{2}t^{*}}}{N(v_{n})} \int_{0}^{\Delta z_{p}^{*}} Z(z_{1}^{*}) dz_{1}^{*} \right)$$

$$+ \frac{\omega_{\chi}^{2}}{k} I_{o} \sum_{n=1}^{\infty} \left( \frac{Z(z^{*}, v_{n})}{N(v_{n})} \left[ \int_{0}^{\Delta z_{p}^{*}} Z(z_{1}^{*}, v_{n}) g_{z}(z_{1}^{*}) dz_{1}^{*} \right] \left\{ \int_{0}^{t^{*}} \frac{e^{-\frac{\chi(\left(x^{*}-v^{*}(t^{*}-t_{1}^{*})}\right)^{2}+y^{*2}}\right) - v_{n}^{2}(t^{*}-t_{1}^{*})}{1 + 4\chi(t^{*}-t_{1}^{*})} dt_{1}^{*}} \right\}$$

$$- H_{A}^{*} T_{A} \sum_{n=1}^{\infty} \left( \frac{Z(z^{*}, v_{n})}{v_{n}^{2}N(v_{n})} (1 - e^{-v_{n}^{2}t^{*}}) \right) + H_{B}^{*} T_{B} \sum_{n=1}^{\infty} \left( \frac{Z(z^{*}, v_{n})Z(\Delta z_{p}^{*}, v_{n})}{v_{n}^{2}N(v_{n})} (1 - e^{-v_{n}^{2}t^{*}}) \right)$$
For the transient case (finite  $t^{*}$ )

$$T(\boldsymbol{x}^{*},\boldsymbol{y}^{*},\boldsymbol{z}^{*},\infty) = T_{SOURCE_{QS}} + T_{TOP_{QS}} + T_{BOTTOM_{QS}}$$

$$T(\boldsymbol{x}^{*},\boldsymbol{y}^{*},\boldsymbol{z}^{*},\infty)$$

$$= \frac{\omega_{\chi}^{2}}{k} I_{o} \sum_{n=1}^{\infty} \left( \frac{Z(\boldsymbol{z}^{*},\nu_{n})}{N(\nu_{n})} \left[ \int_{0}^{\Delta \boldsymbol{z}_{p}^{*}} Z(\boldsymbol{z}_{1}^{*},\nu_{n}) g_{z}(\boldsymbol{z}_{1}^{*}) \, d\boldsymbol{z}_{1}^{*} \right] \left\{ \int_{0}^{\infty} \frac{e^{-\frac{\chi((\boldsymbol{x}^{*}-\boldsymbol{v}^{*}\boldsymbol{\varepsilon})^{2}+\boldsymbol{y}^{*2})}{1+4\chi\boldsymbol{\varepsilon}}} e^{-\nu_{n}^{2}\boldsymbol{\varepsilon}} d\boldsymbol{\varepsilon} \right\} \right\}$$

$$-\boldsymbol{H}_{A}^{*}T_{A} \sum_{n=1}^{\infty} \left( \frac{Z(\boldsymbol{z}^{*},\nu_{n})}{\nu_{n}^{2}N(\nu_{n})} \right) + \boldsymbol{H}_{B}^{*}T_{B} \sum_{n=1}^{\infty} \left( \frac{Z(\boldsymbol{z}^{*},\nu_{n})Z(\Delta \boldsymbol{z}_{p}^{*},\nu_{n})}{\nu_{n}^{2}N(\nu_{n})} \right)$$
For the quasistationary case as  $\boldsymbol{t}^{*} \to \infty$ 

The individual functions within the integrals are again stated for reference:

$$Z(\mathbf{z}^*, \nu_n) = \left(\frac{\mathbf{H}_A^*}{\nu_n} \sin(\nu_n \mathbf{z}^*) + \cos(\nu_n \mathbf{z}^*)\right)$$
(A2.196)

$$N(\nu_n) = \frac{1}{2} \left( \frac{\Delta \mathbf{z}_p^* (\nu_n^2 + \mathbf{H}_A^{*2})}{\nu_n^2} + \frac{(\mathbf{H}_A^* + \mathbf{H}_B^*)(\nu_n^2 + \mathbf{H}_A^* \mathbf{H}_B^*)}{\nu_n^2 (\nu_n^2 + \mathbf{H}_B^{*2})} \right)$$
(A2.197)

$$\tan(\nu_n \Delta z_p^*) = \frac{\nu_n (H_A^* + H_B^*)}{(\nu_n^2 - H_B^* H_A^*)}$$
(A2.198)

$$H^* = \frac{\omega_{\chi}}{k} h \tag{A2.199}$$

$$I_o = \frac{\beta \chi P}{\pi \omega_{\chi}^2} \qquad \left[ \frac{W}{m^3} \right] \tag{A2.200}$$

$$g_z(\mathbf{z}^*) = a(Ae^{-2a\boldsymbol{\beta}^*\mathbf{z}^*} - Be^{2a\boldsymbol{\beta}^*\mathbf{z}^*}) + (e^{-\boldsymbol{\beta}^*\mathbf{z}^*})$$
(A2.201)

$$+R_s e^{\beta^* \mathbf{z}^* - 2\lambda} \left(1 - \frac{R_b}{4R_b - 3}\right)$$

$$=\frac{2R_{b}(e^{2a\lambda})\left(\left(R_{s}+3(e^{2\lambda})\right)\left((R_{b}(1+R_{s})-2)a-2(1-R_{b})\right)\left(e^{2a\lambda}\right)+R_{b}a(1-R_{s})(1+R_{s})e^{\lambda}\right)}{(4R_{b}-3)(e^{2\lambda})\left(\left(R_{b}(1+R_{s})-2(1+a)\right)(e^{4a\lambda})-2(a-1)-R_{b}(1+R_{s})\right)(1+a)}$$

$$=\frac{2R_{b}\left(e^{\lambda}(1-R_{s})(1+R_{s})(1+a-R_{b})\left(e^{2a\lambda}\right)-\left(R_{s}+3\left(e^{2\lambda}\right)\right)\left((1-R_{s})a+(1+R_{s})(R_{b}-1)\right)\right)}{(4R_{b}-3)(e^{2\lambda})\left((R_{b}(1+R_{s})-2(1+a))(e^{4a\lambda})-2(a-1)-R_{b}(1+R_{s})\right)}$$

$$a = \sqrt{1 - R_b} \tag{A2.204}$$

$$\lambda = \beta \Delta z_p = \beta^* \Delta z_p^* \tag{A2.205}$$

In a separate exercise, the GFSE was derived for an assumed constant temperature boundary between the powder and build plate on the bottom while keeping the convective boundary on the top of the powder bed. This GFSE is given below.

$$T(\boldsymbol{x}^*, \boldsymbol{y}^*, \boldsymbol{z}^*, \infty) = T_{SOURCE_{QS}} + T_{TOP_{QS}} + T_{BOTTOM_{QS}}$$

$$T(\boldsymbol{x}^*, \boldsymbol{y}^*, \boldsymbol{z}^*, \infty)$$

$$= \frac{\omega_{\chi}^2}{k} I_o \sum_{n=1}^{\infty} \left( \frac{Z(\boldsymbol{z}^*, \nu_n)}{N(\nu_n)} \left[ \int_{\boldsymbol{0}}^{\Delta \boldsymbol{z}_p^*} Z(\boldsymbol{z}_1^*, \nu_n) g_z(\boldsymbol{z}_1^*) \, d\boldsymbol{z}_1^* \right] \left\{ \int_{\boldsymbol{0}}^{\infty} \frac{e^{-\frac{\chi((\boldsymbol{x}^* - \boldsymbol{v}^* \boldsymbol{\varepsilon})^2 + \boldsymbol{y}^{*2})}{1 + 4\chi \boldsymbol{\varepsilon}}} e^{-\nu_n^2 \boldsymbol{\varepsilon}} d\boldsymbol{\varepsilon} \right\} \right)$$

$$-\boldsymbol{H}_A^* T_A \sum_{n=1}^{\infty} \left( \frac{Z(\boldsymbol{z}^*, \nu_n) \sin{(\nu_n \Delta \boldsymbol{z}_p^*)}}{\nu_n^2 N(\nu_n)} \right) + T_B \sum_{n=1}^{\infty} \left( \frac{Z(\boldsymbol{z}^*, \nu_n)}{\nu_n N(\nu_n)} \right)$$
For the quasistationary case as  $\boldsymbol{t}^* \to \infty$